CHEMICAL REVIEWS

Subscriber access provided by V. Vernadsky | National Library of Ukraine

Nanoalloys: From Theory to Applications of Alloy Clusters and Nanoparticles

Riccardo Ferrando, Julius Jellinek, and Roy L. Johnston

Chem. Rev., **2008**, 108 (3), 845-910 • DOI: 10.1021/cr040090g

Downloaded from http://pubs.acs.org on December 24, 2008

More About This Article

Additional resources and features associated with this article are available within the HTML version:

- Supporting Information
- Links to the 10 articles that cite this article, as of the time of this article download
- Access to high resolution figures
- Links to articles and content related to this article
- Copyright permission to reproduce figures and/or text from this article

View the Full Text HTML

ACS Publications
High quality. High impact.

Chemical Reviews is published by the American Chemical Society. 1155 Sixteenth Street N.W., Washington, DC 20036

CHEMICAL REVIEWS

Volume 108, Number 3

Nanoalloys: From Theory to Applications of Alloy Clusters and Nanoparticles

Riccardo Ferrando,*,† Julius Jellinek,‡ and Roy L. Johnston§

Dipartimento di Fisica, Universita di Genova, INFM and IMEM/CNR, Via Dodecaneso 33, Genova, I16146, Italy, Chemistry Division,|| Argonne National Laboratory, Argonne, Illinois 60439, and School of Chemistry, University of Birmingham, Edgbaston, Birmingham, B15 2TT, United Kingdom

Received November 27, 2006

Contents

* To whom correspondence should be addressed. Phone: +39010 3536214. Fax: +39010 311066. E-mail: ferrando@fisica.unige.it.
† Universita di Genova.
‡ Argonne National Laboratory.
§ University of Birmingham.
|| As of October 1, 2007, Chemical Sciences and Engineering Division.

10.1021/cr040090g CCC: $71.00 © 2008 American Chemical Society
Published on Web 03/12/2008

1. Introduction

1.1. General Aspects

1.1.1. Clusters

Clusters or nanoparticles are aggregates of between a few and many millions of atoms or molecules. They may consist of identical atoms, or molecules, or two or more different species and can be studied in a number of media, such as molecular beams, the vapor phase, and colloidal suspensions, and isolated in inert matrices or on surfaces.[1−5]

Interest in clusters arises, in part, because they constitute a new type of material which may have properties which are distinct from those of individual atoms and molecules or bulk matter. An important reason for the interest in clusters is the size-dependent evolution of their properties,[4,6,7] such as their structure. In fact, both the geometric shape and the energetic stability of clusters may drastically change with size. For example, it is known that alkali-metal clusters, with sizes of up to thousands of atoms (and also smaller clusters of Cu and Ag), conform to the jellium model in that certain nuclearities are relatively stable (the so-called *magic sizes*) due to their having filled electronic shells.[5,8] By contrast, clusters of transition metals and some main-group metals (e.g., Al, Ca, and Sr) generally exhibit magic sizes which correspond to clusters consisting of concentric polyhedral shells (*geometric shells*) of atoms, where the relative stability of a given cluster is determined by the competition between packing and surface energy effects.[2,5]

Also from the point of view of applications, there is continuing interest in metal clusters because of potential applications in fields such as catalysis and nanoelectronics (e.g., in single-electron tunneling devices).[4]

1.1.2. Nanoalloys

In materials science, the range of properties of metallic systems can be greatly extended by taking mixtures of elements to generate intermetallic compounds and alloys. In many cases, there is an enhancement in specific properties upon alloying due to synergistic effects, and the rich diversity of compositions, structures, and properties of metallic alloys has led to widespread applications in electronics, engineering, and catalysis. The desire to fabricate materials with well-defined, controllable properties and structures on the nanometer scale coupled with the flexibility afforded by intermetallic materials has generated interest in bimetallic and trimetallic nanoclusters, which will be referred to as *alloy nanoclusters* or *nanoalloys* in the following discussion.

As for bulk alloys, a very wide range of combinations and compositions are possible for nanoalloys. Bimetallic nanoalloys (A_mB_n) can be generated with, more or less, controlled size ($m + n$) and composition (m/n). The cluster structures and degree of A−B segregation or mixing may depend on the method and conditions of cluster generation (type of cluster source, temperature, pressure, etc.). Nanoalloys can

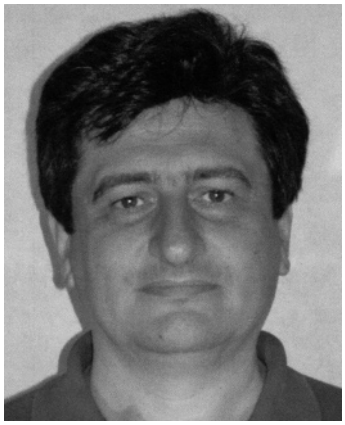

Riccardo Ferrando received his Laurea degree in Physics cum laude in 1988 and received his Ph.D. degree in Physics in 1993 from the University of Genova, Italy. In 1993/1994 he was a postdoctoral fellow at the CRMC2/CNRS in Marseille, France, thanks to a fellowship from the French Ministry of Education. From 1995 on he was a staff member at the Physics Department of the University of Genova, first as Researcher and then as Associate Professor in Physics of Matter. He has been a Visiting Professor at Los Alamos National Laboratory (USA) and the Blaise Pascal University (Clemont-Ferrand, France). His research interests lie in theoretical and computational condensed matter physics and chemistry ranging from the theory of stochastic processes (escape rate theories) to surface diffusion of atoms and aggregates and crystal growth. More recently he has focused his interest in the computational modeling of nanoparticles, with special attention to their structural properties and growth dynamics. He is the author of about 120 papers in peer-reviewed journals.

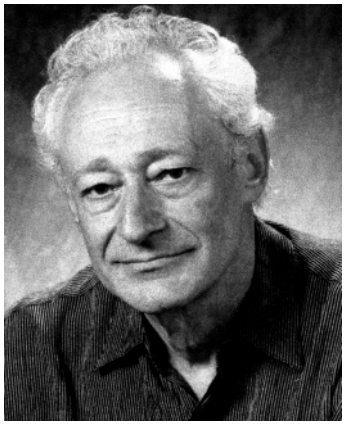

Julius Jellinek was born in the republic of Ukraine of the former Soviet Union. He graduated with distinction in theoretical high-energy physics from the University of Uzhgorod, Ukraine, in 1969. From 1969 to 1972 he continued postgraduate studies at the same university. In 1976 he immigrated to Israel, where in 1983 he received his Ph.D. degree in Theoretical Chemical Physics from the Weizmann Institute. The same year, as a Chaim Weizmann Fellow, he came to the University of Chicago to work with Steve Berry. In 1986 he joined the Chemistry Division of the Argonne National Laboratory to lead the theoretical component of the Cluster Studies Group. He was the Group Leader of that group from 2000 to 2005. He has received a number of awards, the latest of which is The University of Chicago Medal for Distinguished Performance at Argonne National Laboratory (2005). Currently, he is a Senior Scientist at the Chemical Sciences and Engineering Division of the Argonne National Laboratory and a Senior Fellow at The University of Chicago/Argonne Computation Institute. His main interests and activities lie in the broad area of finite systems and phenomena (atomic and molecular clusters, nanosystems, nanophenomena) and include fundamental conceptual developments as well as modeling and numerical simulations. He is the editor of the book, *Theory of Atomic and Molecular Clusters* (Springer, 1999).

be generated in a variety of media, such as cluster beams, colloidal solutions, immobilized on surfaces, or inside pores.

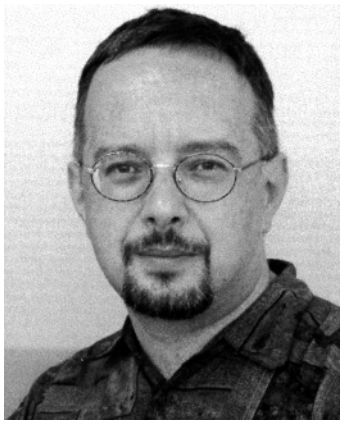

Roy L. Johnston is Professor of Computational Chemistry at the University of Birmingham, United Kingdom. He received his B.A. (1983) and D.Phil. (1986) degrees from the University of Oxford. His D.Phil. work, on theoretical aspects of cluster molecules, was carried out under the supervision of Professor D. Michael P. Mingos, FRS. From 1987 to 1989 he was a SERC/NATO postdoctoral fellow, working with Professor Roald Hoffmann at Cornell University on theoretical solid-state chemistry and with Professor Dennis Lichtenberger at the University of Arizona on gas-phase and surface photoelectron spectroscopy. He returned to the United Kingdom in 1989 as a Royal Society University Research Fellow at the University of Sussex, where he collaborated with Professor John Murrell on the development and application of many-body potentials for modeling clusters, surfaces, and solids. He was appointed to a lectureship in inorganic chemistry at the University of Birmingham in 1995 and promoted to Senior Lecturer in 2002, Reader in 2003, and Chair in 2006. His research interests lie in theoretical and computational chemistry with particular recent interest being the application of genetic algorithms and other evolutionary techniques to optimization problems in cluster chemistry, crystallography, and protein folding and study of the geometric and electronic structures and segregation properties of bimetallic nanoclusters (nanoalloys). He is the author of the book "Atomic and Molecular Clusters" (Taylor & Francis, 2002) and a Fellow of the Royal Society of Chemistry.

One of the major reasons for interest in alloy nanoparticles is the fact that their chemical and physical properties may be tuned by varying the composition and atomic ordering as well as the size of the clusters. In fact, nanoalloys may display not only magic sizes but also magic compositions, i.e., compositions at which the alloy nanoclusters present a special stability. Surface structures, compositions, and segregation properties[9,10] of nanoalloys are of interest as they are important in determining chemical reactivity and especially catalytic activity.[11,12] Nanoalloys are also of interest as they may display structures and properties which are distinct from those of the pure elemental clusters: the structures of binary clusters may be quite different from the structures of the corresponding pure clusters of the same size; synergism is sometimes observed in catalysis by bimetallic nanoalloys. They may also display properties which are distinct from the corresponding bulk alloys due to finite size effects, e.g., there are examples of pairs of elements (such as iron and silver) which are immiscible in the bulk but readily mix in finite clusters.[13]

1.1.3. Isomerism in Nanoalloys

From a theoretical point of view, nanoalloys are a fascinating challenge due to the complexity of their energy landscape. In fact, on going from pure metal clusters to bimetallic nanoalloys there is an increase in complexity due to the presence of two different types of atoms, which leads to the possibility of isomers based on the permutation of unlike atoms as well as the regular geometrical isomers (with different skeletal structures). Jellinek introduced the term

"homotops" to describe A_mB_n alloy cluster structures with a fixed number of atoms ($N = m + n$) and composition (m/n ratio) which have the same geometrical arrangement of atoms but differ in the way in which the A- and B-type atoms are arranged.[14−18]

As the number of homotops rises combinatorially with cluster size, global optimization (in terms of both geometrical isomers and homotops) is an extremely difficult task. Ignoring point group symmetry, a single geometrical isomer of an N-atom AB cluster will give rise to homotops,

$$ {}^{N}P_{A,B} = \frac{N!}{N_A!N_B!} = \frac{N!}{N_A!(N - N_A)!} \quad (1) $$

where N is the total number of atoms, N_A is the number of atoms of type A and N_B is the number of atoms of type B. For a 20-atom $A_{10}B_{10}$ cluster, for example, there are 184 756 homotops, though many may be symmetry equivalent. The total number of homotops of any composition for a given structural isomer is 2^N, which for a 20-atom cluster is approximately 10^6.

In addition to geometrical isomers and homotops, the term "composomers" has been introduced by Johnston and Belchior to refer to compositional isomers, i.e., clusters with the same number of atoms ($N = N_A + N_B$) and geometrical (skeletal) structure but different compositions (N_A/N_B).[19]

1.2. Types and Structures of Nanoalloys

Generally speaking, nanoalloys can be classified according to their mixing pattern (also named chemical ordering) and geometric structure.

1.2.1. Mixing Patterns

Four main types of mixing patterns (shown in Figure 1) can be identified for nanoalloys.

Core−shell segregated nanoalloys (Figure 1a) consist of a shell of one type of atom (B) surrounding a core of another (A), though there may be some mixing between the shells. This mixing pattern is common to a large variety of systems, as we shall see in the following sections. In this review, these clusters will be denoted $A_{core}B_{shell}$.

Subcluster segregated nanoalloys (Figure 1b) consist of A and B subclusters, which may share a mixed interface (left) or may only have a small number of A−B bonds (right). This mixing pattern is, in principle, possible, but we do not know of any specific example.

Mixed A−B nanoalloys (Figure 1c) may be either ordered (left) or random (i.e., a solid solution, right). Random mixed nanoalloys are often termed "alloyed" nanoparticles in the literature, but we shall not use this term in the following, preferring the terms "mixed" or "intermixed" and specifying whether mixing is ordered or random. The intermixed pattern is common to many systems.

Multishell nanoalloys (Figure 1d) may present layered or onion-like alternating −A−B−A− shells. Metastable structures of this type were observed in simulations of the growth of Cu−Ag, Ni−Ag and Pd−Ag clusters;[20] there has also been evidence in favor of stable A−B−A and A−B−A−B arrangements for Co−Rh and Pd−Pt clusters, respectively.[21,22] Very recently, three-shell Pd−Au nanoparticles have been experimentally produced.[23] These nanoparticles present an intermixed core, an Au-rich intermediate shell, and a Pd-rich outer shell.

1.2.2. Geometric Structures

By analogy with pure metal clusters (see, for example, ref 5), for nanoalloys several structural types are possible.

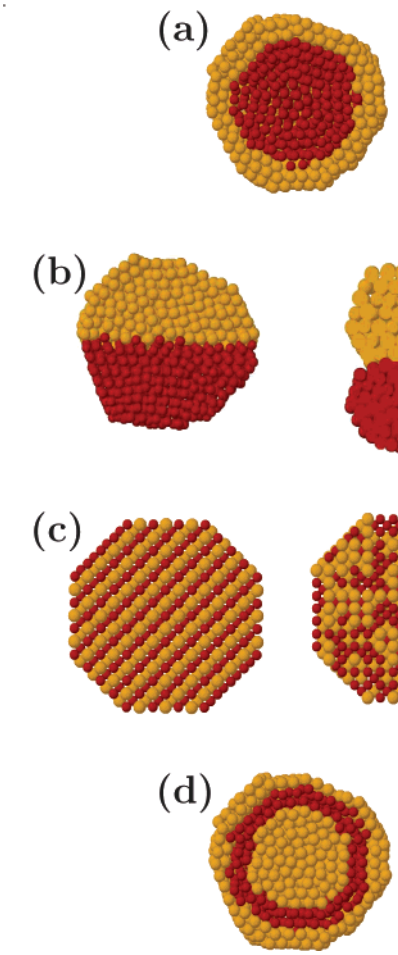

Figure 1. Schematic representation of some possible mixing patterns: core−shell (a), subcluster segregated (b), mixed (c), three shell (d). The pictures show cross sections of the clusters.

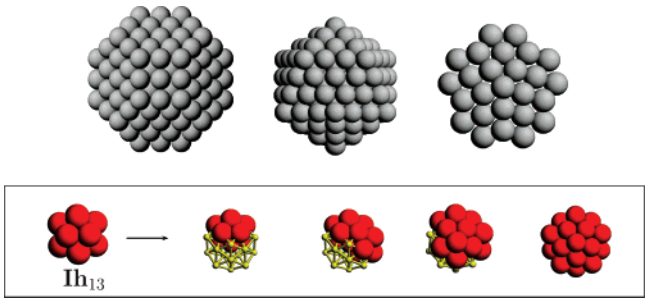

Figure 2. (Top row, from left to right) fcc truncated octahedron, icosahedron, and truncated decahedron. (Bottom row) Polyicosahedral cluster composed of interpenetrating elementary icosahedra of 13 atoms,[24] here indicated by Ih_{13}. Polyicosahedral structures are a subfamily of polytetrahedral structures because the elementary icosahedron is composed of 4-atom tetrahedra.

Crystalline structures are fragments of bulk crystals (see Figure 2). In the case of the fcc bulk lattice, crystalline clusters may take the form of octahedra or truncated octahedra. Noncrystalline structures are also possible, such as icosahedra, decahedra, polytetrahedra, and polyicosahedra (see Figure 2). Generally speaking, noncrystalline structures may take compact shapes with an efficient packing of atoms. This efficient packing is however obtained at the expense of some internal strain due to nonoptimal interatomic distances in the structure. The strain energy is proportional to the cluster volume, so that noncrystalline structures become unfavorable for large sizes.[5] Icosahedra, polytetra-

hedra, and polyicosahedra tend to be more favorable for nanoalloys than for pure metal clusters. This is especially true when the size mismatch between atomic species is large, and small atoms can be accommodated inside the cluster to reduce the compressive strain which is typical of these structures.[24] A striking example has been obtained in the optimization of a model of Cu−Au clusters of size 55,[25] in which the lowest energy structure of the pure Au cluster is not icosahedral, but a single copper impurity is sufficient to stabilize the icosahedral structure of $Au_{54}Cu_1$. Electronic shell closure effects may operate in synergy to further enhance the stability of specific structural motifs. Examples are found in Cu−Ag clusters of size 40, in which a specific core−shell polyicosahedral structure is stabilized[26] due to electronic effects, and in icosahedral Pb_{13}, which increases its energetic stability and HOMO−LUMO gap when the smaller Mg atom is substituted for the internal Pb atom.[27]

1.2.3. Factors Influencing Segregation, Mixing, and Ordering in Nanoalloys

The degree of segregation/mixing and atomic ordering in A_mB_n nanoalloys depends on the following factors.

(1) Relative strengths of A−A, B−B, and A−B bonds. To a first approximation, if A−B bonds are strongest, this favors mixing; otherwise, segregation is favored, with the species forming strongest homonuclear bonds tending to be at the center (core) of the cluster.

(2) Surface energies of bulk elements A and B. The element with lowest surface energy tends to segregate to the surface.

(3) Relative atomic sizes. Smaller atoms tend to occupy the more sterically confined core, especially in icosahedral clusters, where the core undergoes compression.

(4) Charge transfer. Electron transfer from less to more electronegative elements favors mixing.

(5) Strength of binding to surface ligands (surfactants). For supported or passivated clusters, the element that binds most strongly to the support or ligands may be pulled out toward the surface.

(6) Specific electronic/magnetic effects. Certain sizes, compositions, and/or segregation arrangements may be stabilized by electronic shell structure (as in the jellium model) or electron spin interactions.

We note that the observed atomic arrangement for a particular A−B nanoalloy depends critically on the balance of the factors outlined above as well as on the preparation method and experimental conditions.

1.3. Passivated, Coated, and Supported Nanoalloys

Nanoalloys may also be classified as "free"/"bare" or "passivated"/"coated" (where the surface is stabilized by coordination to surfactant molecules or ligands). Free/bare clusters are generally created in the gas phase or molecular beams, while passivated clusters are generated in both the gas phase and solution. Nanoalloys may also be "supported" on surfaces or inside porous materials.

1.3.1. Passivated Clusters and Colloids

In the size regime of clusters ranging from nanometer to micrometer dimensions lies the class of metal "colloids", some of which have been known for many centuries.[28−30] Stained glass windows, dating back as far as medieval times, provide beautiful examples of colors which are caused by the suspension of small colloidal particles of copper, silver, and gold in the glass. In fact, the use of colloidal metals in coloring glass probably dates back as far as the ancient Egyptians, and Cleopatra is reputed to have used cosmetics prepared from colloidal gold. The Romans also used colloidal gold to produce pink-tinted glass.

One problem with studying bare metal clusters (such as those created in cluster beams) is that it could be difficult to isolate and handle them on a preparative scale like conventional molecules. To enable the investigation of approximately uniformly sized clusters and exploit cluster properties in device applications, it is necessary to protect ("passivate") them with a ligand shell as this avoids coalescence at high cluster densities. Two types of stabilization can be distinguished:[31] electrostatic stabilization due to Coulombic repulsion between nanoparticles, arising from the electrical double layer of ions adsorbed at the particle surface (e.g., when preparing sodium citrate gold sols), and steric stabilization due to the coordination of bulky organic molecules, such as polymers, block copolymers, bulky P, N, and S donors, etc.

1.3.2. Supported Nanoalloys

Nanoparticles can also be deposited (from solution or the gas phase, where size selection may be possible) onto a substrate (such as graphite, silicon, or an inorganic oxide) or in an inert gas matrix. While such experiments allow individual clusters to be studied by microscopic techniques, it is difficult to infer the geometric or electronic structure of a free cluster from that of the corresponding surface-supported cluster since such clusters may be perturbed by the substrate. The same caveat applies to the study of thin films and crystals of ligand-passivated clusters.

1.3.3. Bimetallic Transition-Metal Carbonyl Clusters

Since the 1960s, transition-metal carbonyl clusters (i.e., clusters of transition metals which are stabilized by the surface coordination of carbon monoxide (CO) molecules) have been extensively studied.[29,32−35] More recently, this work has encompassed large transition-metal carbonyl clusters (with tens or even hundreds of atoms) as well as bimetallic and trimetallic clusters. Although not the subject of this review, a brief discussion is presented here of the bonding in transition-metal carbonyl clusters. In section 5 some of the experimental results obtained for bimetallic nanoparticles will be compared with those of the carbonyl-coated analogues.

In transition-metal carbonyl clusters, the surface-bound CO molecules generally bind via the carbon atom to one metal (terminal), two metals (edge binding), or three metals (face binding), though higher coordination modes and some distorted binding (e.g., involving both the C and O atoms) are also known. The high strength of metal−CO binding arises from donation of electron density from a filled (σ symmetry) carbon-based lone pair orbital into an empty metal orbital and the "back-donation" of electron density from filled metal d orbitals into one or both of the empty CO antibonding (π^*) molecular orbitals. This strong M−CO bonding, which reflects the strong binding of CO to bulk metal surfaces, has an important consequence for bimetallic metal carbonyl clusters since it can compete with the cohesive and surface energy terms to determine whether a particular metal will segregate to the surface or the core of a cluster or if a mixed configuration is energetically preferred.[36] An example of a bimetallic transition-metal carbonyl cluster, $[Ni_{24}Pt_{14}(CO)_{44}]^{4-}$, consisting of a capped octahedral Pt_{14} core surrounded by a shell of Ni atoms is shown in Figure 3.[37]

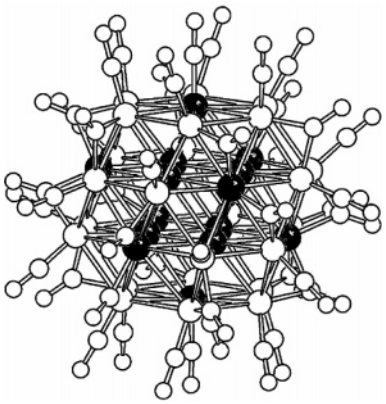

Figure 3. Molecular structure of a $[Ni_{24}Pt_{14}(CO)_{44}]^{4-}$ metal−carbonyl cluster. The Pt atoms (black spheres) are mostly inside a Ni cage. (From ref 37. Reproduced by permission of The Royal Society of Chemistry.)

Bimetallic transition-metal carbonyl clusters have been extensively investigated as homogeneous catalysts (in solution, though it is often uncertain as to whether the active catalyst is in fact the cluster or a monometallic decomposition product) and (with more success) precursors for surface- or micropore-supported heterogeneous catalysts, generally after thermal removal of most or all of the passivating CO ligands (see refs 38−41 and references therein). Examples of these studies are listed in section 6.

1.4. Applications of Nanoalloys

Nanoalloys have already been utilized in a number of technologically important areas, ranging from catalysis (e.g., catalytic converters in automobiles and electrochemical fuel cells) to optoelectronic, magnetic, and even medical applications.

1.4.1. Catalysis

The properties, including the catalytic activity, of metals may be modified and fine tuned by alloying, i.e., forming bimetallic solids.[42,43] The same is true for small metal particles and clusters, and the field of alloy nanocatalysis is currently attracting a lot of attention.[12,39,41,43−46] According to Schmid,[45] in the field of catalysis, the mutual influence of different neighboring atoms can lead to catalytic behavior which is different (and often better) than that of the monometallic clusters, i.e., "synergistic effects" are observed. Layered (core−shell) bimetallic clusters offer fascinating prospects for the design of new catalysts. Bimetallic catalysts containing Pt with Ir or Re have found extensive use in the reforming of petrochemicals, while bimetallic and trimetallic clusters containing Pt, Pd, and other metals are of importance in automobile catalytic converters.

Electrocatalysis. Bimetallic nanoparticles have a long pedigree in the field of electrocatalysis. Sinfelt and colleagues developed supported bimetallic cluster catalysts while working at Exxon in the 1960s,[43] while Pt and Pt-containing bimetallic nanoparticle catalysts were employed in commercial prototype phosphoric acid fuel cells as early as the 1970s.[47,48] Petrow and Allen pioneered (and patented in 1974) the preparation of bimetallic nanoparticle electrocatalysts by adsorbing colloidal precursors onto carbon black, followed by thermal decomposition or hydrogen reduction.[48] For a discussion of the many applications of bimetallic nanoparticles in electrocatalysis (i.e., in fuel cell applications) the reader is referred to recent reviews by Markovic et al.[49] and Russell and Rose[50] and an older review by Bönnemann and Brijoux.[51]

Examples of the application of nanoalloys in catalysis and electrocatalysis are given in section 6.

1.4.2. Optical Properties

As long ago as 1857, Michael Faraday made the remarkable observation that in gold colloids "... the gold is reduced in exceedingly fine particles which becoming diffused, produce a beautiful fluid... the various preparations of gold whether ruby, green, violet or blue... consist of that substance in a metallic divided state".[28] We now understand the colors of colloidal suspensions or sols in terms of strong absorption bands in the visible region of the spectrum caused by plasmons. While for small metal clusters the electronic spectrum consists of a number of well-defined lines, corresponding to transitions between well-separated, quantized energy levels (vide infra), in medium-sized and large metal clusters a single "surface plasmon" mode carries 100% of the oscillator strength, so one observes a single peak in the electronic spectrum.[30] The surface plasmon is due to extensive electronic correlation and corresponds to a collective excitation of weakly bound electrons relative to the ionic cores, i.e., the correlated motion of the cluster's itinerant electrons in the attractive field due to the positively charged ionic cores.

Mie[52] developed a classical electrodynamical model to quantify the collective excitation of electrons in metallic particles.[53,54] A similar approach (the Drude model) has also been applied to bulk metals. According to Mie theory, the absorption cross-section $\sigma(\omega)$ (where ω is the frequency of the incident light) of a nanoparticle embedded in a medium of known dielectric constant ϵ_m is given by

$$\sigma(\omega) = \frac{4\pi\omega}{c\epsilon_m^{1/2}} \mathrm{Im}[\alpha(\omega)] \quad (2)$$

where Im denotes the imaginary part, c is the speed of light, and $\alpha(\omega)$ is the polarizability of the nanoparticle. For a homogeneous spherical nanoparticle of radius R and dielectric function $\epsilon(\omega)$

$$\alpha(\omega) = \epsilon_m R^3 \frac{\epsilon(\omega) - \epsilon_m}{\epsilon(\omega) + 2\epsilon_m} \quad (3)$$

whereas for a binary core−shell spherical particle $\alpha(\omega)$ is given by

$$\alpha(\omega) = \epsilon_m R^3 \frac{(\epsilon_2 - \epsilon_m)(\epsilon_1 + 2\epsilon_2) + f_v(\epsilon_1 - \epsilon_2)(\epsilon_m + 2\epsilon_2)}{(\epsilon_1 + 2\epsilon_m)(\epsilon_1 + 2\epsilon_2) + 2f_v(\epsilon_2 - \epsilon_m)(\epsilon_1 - \epsilon_2)} \quad (4)$$

where $\epsilon_1(\omega)$ and $\epsilon_2(\omega)$ are the dielectric functions of the core and the shell metal, respectively, and f_v is the volume fraction of the core ($f_v = R_c^3/R^3$, where R_c is the core radius).[55]

The surface plasmon described here is strictly known as the dipolar surface plasmon since it causes an electric dipole at the surface of the cluster. The dipolar plasmon is dominant at cluster radii $R \ll \lambda$ (the wavelength of the exciting radiation). There are other higher multipole resonances, but these are generally less intense than the dipolar plasmon.

For nonspherical particles, better agreement with experiment is achieved using numerical approaches, such as the discrete dipole approximation, which has been applied extensively by Schatz and co-workers to study noble-metal

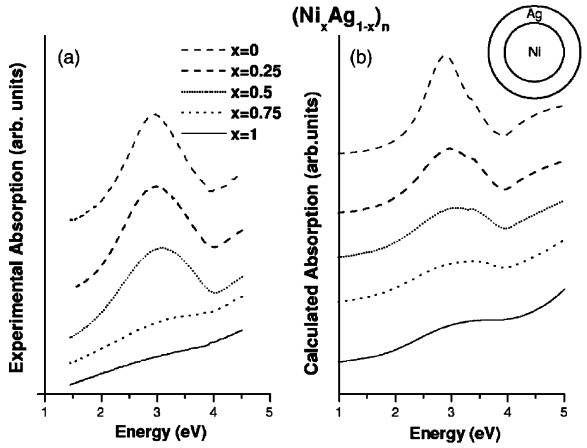

Figure 4. Experimental (a) and calculated (b) absorption spectra of NiAg particles. A $Ni_{core}Ag_{shell}$ structure is assumed in the calculations, so that the absorption spectrum is given by eqs 2 and 4. (Reprinted with permission from ref 60. Copyright 2003 American Physical Society.)

clusters.[56] For smaller particles (at present limited to on the order of hundreds of atoms) DFT calculations can be used to obtain more accurate simulations of plasmon spectra.[57] DFT calculations on smaller clusters (e.g., from a few to some tens of atoms) confirm the breakdown of the plasmon model for these small clusters with the optical spectra having multiple peaks, i.e., resembling those of typical molecules.[58] At a higher level of theory, for clusters with up to 10 atoms, time-dependent DFT calculations can also be performed to obtain optical spectra via calculation of dynamic polarizabilities.[59]

Gaudry et al.[60] measured the absorption spectra of NiAg clusters (with a diameter of about 2.7 nm) and compared their results to eq 4 using for ϵ_1 and ϵ_2 the dielectric functions of the bulk metals. Assuming a $Ni_{core}Ag_{shell}$ arrangement, they obtained a good agreement for the position of the absorption peak, which showed a slight blue shift with increasing Ni proportion in the clusters (a mixed arrangement would have given a red shift). The calculated peak widths were however smaller than the experimental ones. This effect was attributed to a shortening of the electron mean free path in nanoparticles compared to the bulk mean free path. After including this effect in the dielectric functions, a good overall agreement between experimental and theoretical spectra was obtained (see Figure 4).

The absorption characteristics of colloidal metal particles are very complex depending on the electronic structure of the metal, the size of the cluster, the type of plasmon (conduction vs valence electrons, dipole vs quadrupolar, etc.), the dielectric constant of the medium (matrix) in which the metal particles are suspended/embedded, and the nature of the cluster surface−matrix interaction. At higher concentrations of colloidal particles (e.g., in particle arrays), there may also be interference effects, i.e., coupling between the individual particles. Other light scattering effects, such as opalescence, can also be observed.

Regarding the optical properties of nanoalloys, the most widely studied system is probably Ag−Au, where the shape and frequency of the plasmon resonance has been shown to vary considerably with composition and the degree of segregation or mixing.[54,61,62] Further details on the optical properties of Ag−Au and other nanoalloys are given in section 5.

1.4.3. Magnetic Properties

There has been much recent interest in granular materials formed by embedding clusters in a solid host. When embedded in nonmagnetic metals, or even insulators, magnetic 3d metal clusters (e.g., of Cr, Fe, Co, and Ni or mixtures of these metals) are known to exhibit the phenomenon of giant magneto-resistance (GMR) with a change in resistance upon application of a magnetic field of as much as 50% for Fe clusters embedded in Ag.[63] Such GMR materials show considerable promise for applications as magnetic sensors and magnetic recording and have led to the study of bimetallic nanoalloys formed between magnetic 3d metals and nonmagnetic 4d (e.g., Rh, Pd, Ag) or 5d metals (e.g., Pt, Au).

The combination of 3d metals (e.g., Co and Ni) with large local magnetic moments and 4d metals (e.g., Rh) with strong spin−orbit coupling may be an effective way of obtaining a high magnetic moment and anisotropy which is required in high-density magnetic recording.[21] Similarly, the 3d−5d Fe−Pt and Co−Pt nanoalloys are also candidates for ultrahigh density magnetic recording media due to their high magnetic anisotropy with associated high magnetic susceptibility and coercivity. Further discussion of the magnetism of nanoalloys is presented in section 5.

1.4.4. Biodiagnostics

In the past decade, there has been tremendous growth in the use of nanoparticles and other nanostructures in biodiagnostics—molecular diagnostics for biomedical applications, e.g., for bioconjugation, as cellular labels, and in assays for gases, metal ions, and DNA/protein markers for disease.[64,65] In this respect, nanoparticles offer the possibility of enhanced robustness, sensitivity, and selectivity. A brief introduction (in the context of nanoalloys) is presented here; for further details the interested reader is directed to a recent review of the field by Rossi and Mirkin.[65]

Because of their tunability (of composition and ordering as well as size and shape), bimetallic nanoalloys show considerable promise as biodiagnostic agents. Mirkin and colleagues used $Ag_{core}Au_{shell}$ nanoparticles (50−100 nm diameter) as tunable colorimetric probes for DNA detection, making use of the variation of the surface plasmon with the composition and ordering and the sharp melting transitions of nanoparticle-labeled DNA.[66] For the 50 nm particles, sensitivities in detecting the target DNA ranged from 5 nM to 50 pM (though the best competing assays had sensitivities as low as 600 fM).[65] Greatly improved sensitivities for scanometric detection of DNA has been achieved by coating Au particles with Ag (in a chip-based assay system), resulting in amplification of the target signal and detection of concentrations as low as 100 aM.[65] Combining Au and magnetic nanoparticles (in the bio-bar-code amplification technique), detection down to 500 zM (10 DNA strands in solution) has been reported.[65,67]

2. Methods for Generating Nanoalloys

Bimetallic clusters can be generated in a variety of ways, in the gas phase, in solution, supported on a substrate, or in a matrix. Many of the methods and media for studying nanoalloys are the same as for pure monometallic clusters,[1,4,68] though there may be added complexities. For further details, readers are directed to a number of reviews of synthetic methods for mono- and bimetallic (and multim-

etallic) nanoclusters[31,46,68−70] and to the articles cited for specific nanoalloy systems in section 5.

2.1. Molecular Beams

The development of molecular beam techniques has enabled the study of "free" clusters in an interaction-free environment: the so-called "cluster beam".[71,72]

Clusters are generated in a cluster source with cluster generation consisting of the processes of vaporization (production of atoms or molecules in the gas phase), nucleation (initial condensation of atoms or molecules to form a cluster nucleus, growth (addition of more atoms or molecules to the initially formed nucleus), and coalescence/aggregation (the merging of small clusters to form larger clusters). As well as growing, clusters can also shrink by evaporation or fragmentation. In many cluster beam experiments, the initially generated clusters are subjected to supersonic expansion. Isenthalpic and adiabatic expansion of the clusters from a (relatively) high-pressure condensation region through a narrow nozzle into a vacuum results in cooling and further condensation until a narrow beam of clusters (with high velocities but a narrow velocity distribution) is formed. In the "free jet" region, there are virtually no collisions between clusters and their properties can be studied in isolation.[4]

A variety of different cluster sources are available with the type of source depending on how refractory or volatile the metals are. Depending on the nature and conditions of the source, different size distributions of clusters may be generated.

Most modern day metal cluster sources are of the gas condensation type. These include the following.[1,4,5,8,71−73]

(1) Laser vaporization. For bimetallic nanoparticles, a single alloy rod target, mixed metallic powders, or two monometallic targets are vaporized by the incident laser beam.

(2) Pulsed arc cluster ion source. Vaporization of the mono- or bimetallic targets is achieved by passing an intense electrical discharge through them.

(3) Ion sputtering. Clusters are produced by bombarding the metal target with high-energy inert gas ions (generally Kr^+ or Xe^+) with bombardment energies in the range 10−30 keV and currents of approximately 10 mA.

(4) Magnetron sputtering. Argon plasma is ignited over a target by applying either a dc or a rf potential and confined by a magnetic field. Ar^+ ions in the plasma are then accelerated onto the target, resulting in sputtering.

After vaporization, condensation of clusters can be achieved by letting the metallic vapors collide with a cold inert carrier gas and expansion through a nozzle (see, for example, ref 74).

2.2. Chemical Reduction

Colloidal metallic particles are generally produced by chemical reduction of metal salts dissolved in an appropriate solvent in the presence of surfactant (e.g., citrate, alkylthiols, or thioethers) or polymeric ligands (e.g., polyvinylpyrrolidone, PVP), which passivates the cluster surface.[31,70] This approach, which was first published by Faraday in 1857,[28] was developed and standardized by the work of Turkevich, since the 1950s.[75] A colloidal metal particle can be described in terms of a metallic core surrounded by a ligand shell. Alkylthiols ($CH_3(CH_2)_nSH$) and thioethers ($CH_3(CH_2)_nS(CH_2)_mCH_3$) form particularly stable colloidal particles with late transition metals (M = Ag, Au, Pd, Pt) due to the strength of the M−S bond (especially for gold).

Turkevich proposed a mechanism for the stepwise formation of colloidal nanoclusters based on nucleation, growth, and subsequent agglomeration. Modern analytical experiments have shown that this mechanism is essentially correct, generally proceeding via a "seed" particle (which may be smaller than 1 nm in diameter) which is relatively stable to dissolution but acts as a nucleus for further growth ("ripening").[75]

Colloid preparation can be single phase or two phase, where colloids form at the interface between an aqueous layer (in which the metal salt is dissolved) and an organic layer (containing the surfactant and reducing agent).[76] They can also be generated by using inverse micelles. An inverse micelle is a hollow, spherical species, the inner surface of which is made chemically attractive to metal ions (e.g., the ionic head groups of surfactant molecules) while the hydrocarbon chains interact with the surrounding organic solvent. Control of average particle size and size distribution can be achieved by tuning the preparation conditions (solvent, surfactant, reducing agent, etc.) or varying the size of the inverse micelles. The solubility properties of the metal colloids can be varied by changing the nature of the passivating ligands.[31] Thus, lipid-soluble metal colloids are produced by coordinating lipophilic ligands, generating "organosols" in organic solvents. On the other hand, water-soluble "hydrosols" are obtained by passivating the cluster with hydrophilic ligands. In addition, metal hydrosols stabilized by zwitterionic surfactants (which are capable of self-aggregation) are encapsulated in organic double layers.

2.2.1. Co-Reduction

Bimetallic colloids can readily be prepared by chemical reduction of the appropriate mixture of salts in the solution phase using reducing agents such as $NaBH_4$, N_2H_4 (hydrazine), and H_2 gas.[31,46,51,69,70,77] During the reduction process, the metal species with the highest redox potential generally precipitates first, forming a core on which the second component is deposited as a shell.[69] The order of deposition can be changed by performing the reduction in the presence of a ligand (surfactant) that bonds significantly more strongly to the metal with the higher redox potential, stabilizing the inverse-core−shell arrangement. As an example, co-reduction of Ag and Pd generally leads to $Pd_{core}Ag_{shell}$ clusters due to the higher redox potential of Pd. Co-reduction in the presence of ammonia, however, leads to formation of the reverse $Ag_{core}Pd_{shell}$ cluster because of the stronger binding of NH_3 to Pd than to Ag.[69] For metal ions with similar redox potentials and metals with relatively large enthalpies of mixing, alloyed bimetallic particles can be generated.[69,78]

Matijević and co-workers have shown that a shell of the double salt $Ni(CO_3)\cdot Ni(OH)_2$ can be precipitated onto the surface of manganese carbonate cubes.[69,79] Calcination of the resulting powder forms the core−shell bimetallic oxide cluster $(Mn_2O_3)_{core}(NiO)_{shell}$, which is reduced in H_2 at 350 °C for 6 h to produce $Mn_{core}Ni_{shell}$ bimetallic particles with cubic morphologies (see Figure 5).[69,79] Similar methods have been used to deposit a shell of tin hydroxide onto an ellipsoidal core of hematite (α-Fe_2O_3). Calcination at 750 °C converts the outer shell into SnO_2, with further reduction by H_2 at 350 °C generating particles with a Fe core and Sn outer shell, which also have a Fe_3Sn_2 boundary

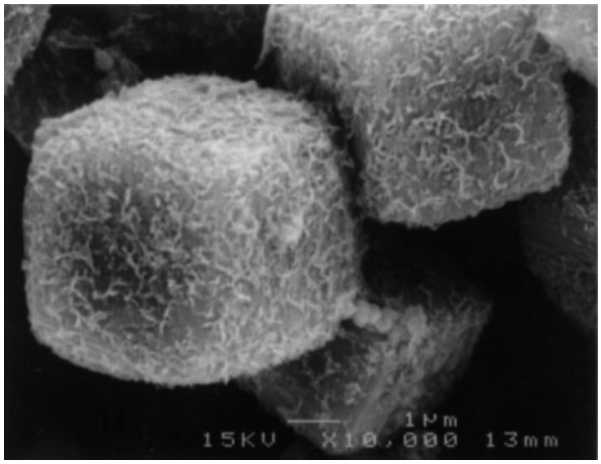

Figure 5. SEM image of cubic $Mn_{core}Ni_{shell}$ particles. The original Mn_2O_3 cubes coated with a shell of NiO were reduced in a stream of hydrogen for 6 h at 350 °C. (From ref 69. Reproduced by permission of The Royal Society of Chemistry on behalf of the Centre National de la Recherche Scientifique.)

phase. It is interesting to note that SnO_2 cannot be reduced to Sn metal by H_2 in the absence of hematite, which indicates that the initial reduction generates Fe metal, some of which reduces the SnO_2 to Sn.[69,80]

2.2.2. Successive Reduction: Reaction of Preformed Clusters

Atoms of one metal can be deposited onto a preformed cluster of another metal via the "seed-germ" process—a term introduced by Schmid and colleagues wherein a cluster without passivating ligands (or with weakly coordinated surfactant molecules) undergoes a second reduction step in the presence of salts of the other metal.[12,29,45] The so-called "living metal polymer" description[31,81] is analogous to the seed-germ description, though it emphasizes the link to the well-known organic living polymers. Watzky and Finke postulated that it should be possible to use the living metal polymer idea to generate, for example, all possible onion-like layered nanoparticle structures for a trimetallic A−B−C system.[81]

2.2.3. Reduction of Co-Complexes

Another way of making bimetallic particles is to reduce complexes which contain both of the metal species.[70] This approach has been used, for example, to generate Pd−Ag and Pt−Ag nanoparticles.[82]

2.3. Thermal Decomposition of Transition-Metal Complexes

The thermal decomposition of low-valent transition-metal complexes (usually organometallic compounds and clusters or labile noble-metal salts) has been used to synthesize many mono- and bimetallic nanoparticles, particularly of the more noble metals.[31,39,83] Improved results are obtained if thermolysis is performed in the presence of stabilizing ligands such as PVP.[84]

Thomas, Johnson, and co-workers recently generated bimetallic nanoparticles, such as Ru_6Pd_6, Ru_6Sn, $Ru_{10}Pt_2$, Ru_5Pt, $Ru_{12}Cu_4$, and $Ru_{12}Ag_4$, by the gentle thermolysis (e.g., heating to approximately 200 °C in vacuo for 2 h) of precursor organometallic clusters (typically with carbonyl and phosphine ligands) which are anchored within silica micropores with typical pore diameters of 3−30 nm[41] (see Figure 6). As the bare metal particles have the same low number of metal atoms as the precursor complexes, they are very small (1−1.5 nm diameter), so that all of the metal atoms are on the surface and potentially able to act as catalytic sites. These nanocatalysts were found to exhibit high catalytic activities and frequently high selectivities for a number of single-step low-temperature (333−373 K) hydrogenations.[41] Due to their tethering to the silica support, the catalysts were found to retain their high activity for longer periods than colloidal catalysts, which are prone to coalescence and sintering. XAS (EXAFS and XANES) studies have shown that, as expected, the nanocatalyst particles are coordinated to the silica via the oxygen atoms.

Rao and colleagues reported that Pd−Ag and Cu−Pd colloids of varying compositions have been produced by the alcohol reduction of solutions containing $AgNO_3/PdO_x$ and CuO_x/PdO_x.[77] Pt−Ag colloids have been prepared by $NaBH_4$ reduction of oxalate salts and Cu−Pd colloids by thermal decomposition of acetate mixtures in high-boiling solvents. Bare nanoalloys (e.g., Ni−Cu, Ag−Au, Ni−Pd, and Cu−Pd) have been generated by thermal evaporation of the metals in a vacuum. XPS measurements of core-level binding energies show that shifts (relative to the bulk metals) have contributions due to size effects as well as mixing.[85]

2.4. Ion Implantation

Metal nanoclusters embedded in insulating matrices are of interest for optical, magnetic, and catalytic properties. It is particularly noteworthy that the third-order susceptibility $\chi^{(3)}$ of the metal clusters is greater than that of the matrix and the resulting increase of the intensity-dependent refractive index could be useful for optical switching.[86] The sequential implantation of two different metal ions has been used to generate implanted bimetallic clusters, for example, generation of solid−solution Ag−Au, Cu−Pd, and Cu−Au nanoalloys by ion implantation in silica using M^+ ion beams with energies of approximately 100 keV (see ref 86 and references therein).

2.5. Electrochemical Synthesis

This is a very versatile method of generating mono- and bimetallic nanoparticles in solution[31] with much of the work in this area being due to Reetz and co-workers.[87] Bimetallic Pd−Ni, Fe−Co, and Fe−Ni nanocolloids have been prepared using two sacrificial bulk metallic anodes in a single electrolysis cell.[88] Bimetallic clusters of metals, such as Pt, Rh, Ru, and Mo, which are less soluble as anodes, can be generated by electrochemically reducing their salts at the cathode. Core−shell layered bimetallic nanoparticles (e.g., $Pt_{core}Pd_{shell}$[89]) can also be produced electrochemically, where, as Bönnemann and Richards pointed out, the Pt core can be regarded as a "living metal polymer" on which the Pd atoms are deposited[31] (see Figure 7).

In electrochemical synthesis, more reactive metals can act as the reducing agents for more noble metals, e.g., the Fe^{2+}/Fe^0 couple has an electrode potential $E^0 = -0.45$ V, while that for $[PdCl_4]^{2-}/Pd^0$ is +0.59 V. Pd-coated Fe nanoparticles have been generated in this way.[90]

2.5.1. Electrodeposition at Liquid–Liquid Interfaces

Formation of nanoparticulate noble metals (particularly Ag, Au, Pd, and Pt) by electrodeposition at the interface between

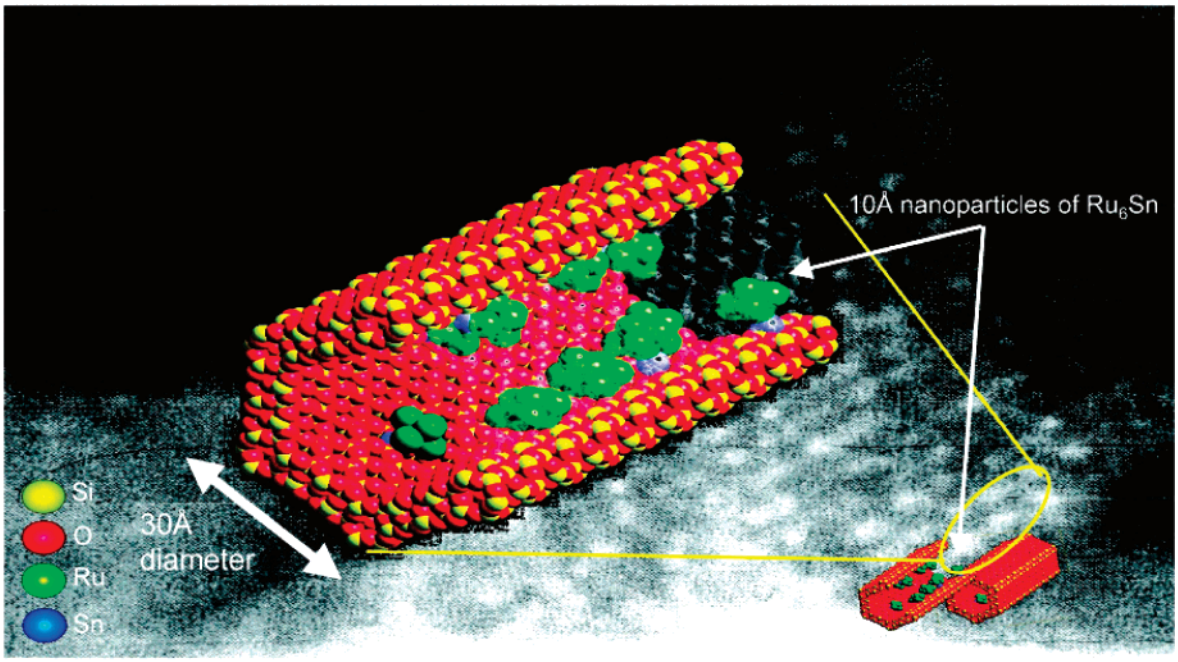

Figure 6. Computer graphic illustration of Ru_6Sn nanoparticles adsorbed in a zeolite−superimposed on an enlarged SEM image of the same system. (Reprinted with permission from ref 41. Copyright American Chemical Society.)

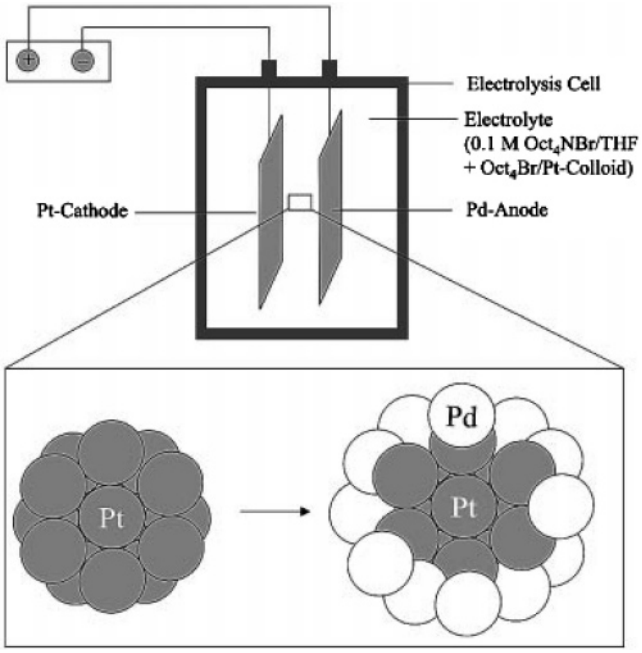

Figure 7. Schematic representation of an electrolysis cell for the preparation of layered PdPt nanocolloids. (Reprinted with permission from ref 31. Copyright 2001 Wiley-VCH.)

two immiscible liquids (typically hydrocarbon and aqueous phases) is of interest because of the smooth nature of the interface and the lack of electrode surface effects.[91,92] At the oil−water interface, because of the high interfacial tension (which is lowered by the nanoparticles), supramolecular assembly is highly dynamic, so that errors (defects) can be corrected rapidly.[76] Recent experiments by Dryfe and colleagues have shown that Pd nanoparticles are more readily formed than Pt (which requires a greater overpotental), despite the greater nobility of Pt, perhaps due to the greater surface energy of Pt.[93] Seeding by Pd particles has been found to promote Pt deposition. Co-deposition of Pd and Pt has also been studied, SEM and XRD analyses indicating 200−500 nm aggregates composed of smaller (less than 4 nm) particles.[93] EDX measurements have shown that both metals are present in the deposits, though it is not yet known whether this corresponds to independent Pd and Pt clusters or whether Pd−Pt nanoalloys have been formed.

2.6. Radiolysis

Radiolysis of aqueous solutions is an efficient method for reducing metal ions in order to generate mono- and bimetallic transition-metal clusters, and has been used to synthesize (among others) Ag−Au, Cu−Ag, Pd−Ag, Pt−Ag, Pd−Au, Pt−Au, Cu−Pd, and Ni−Pt nanoalloys.[94−99] In the radiolytic method, γ-ray irradiation of water leads to solvated electrons which subsequently reduce the metal ions. The metals then coalesce to form clusters. On radiolysis of aqueous solutions of two metals, the more noble metal is reduced preferentially but formation of core−shell or alloyed nanoparticles depends on the rate of radiolysis (which depends on the γ-ray dose), the relative concentrations of the two metals, the rate of interion electron transfer, and the nature of the ligands which are coordinated to the metal ions.[95,96] Higher dose rates favor mixing over core−shell formation, though for some systems (e.g., Cu−Pd, Ni−Pt, and Pt−Ag) mixing can take place even at moderately low dose rates, often with atomic ordering (e.g., Cu_3Pd, CuPd, and Ni_3Pt superlattices have been identified).[95]

Radiolysis has also been used to graft bimetallic clusters (e.g., Pt−Ru and Ni−Ru) onto metal (Ti or Ni) electrodes used in the chlorine−soda process.[100] A number of radiolytically alloyed bi- and trimetallic clusters (e.g., Cu−Au, Ni−Pt, Ag−Au, Cu−Ag, and Cu−Pd−Ag) have been deposited on silver halide emulsions and shown good activity as development centers for high-resolution photographic development.[95]

2.7. Sonochemical Synthesis

Mizukoshi et al. reported the synthesis of 8 nm diameter $Au_{core}Pd_{shell}$ nanoparticles (as measured by TEM and EDX)

induced by irradiation of an aqueous solution of Au(III) and Pd(II) ions by high-intensity ultrasound.[101] Morphological differences between the results of sonochemical and radiochemical cluster generation suggest that formation of a core−shell structure (and smaller nanoparticles) is influenced by the characteristics of the sonochemical experiment: the effective stirring, microjet stream, and shock wave (due to the collapse of cavitation bubbles).[101] More recently, Kan et al. have shown that successive deposition is more effective than simultaneous deposition for the sonogeneration of core−shell Au−Pd nanoalloys.[102]

2.8. Biosynthesis

It is known that biomineralization arises from the control of mineral growth by biomolecules,[103] often via formation of nanoparticles or nanocrystals which are subsequently organized on longer length scales due to the self-assembly of templating macromolecules.[104] Biomineralization is of technological interest because of the desire for bottom-up manufacture of devices on the nanometer scale.

2.8.1. Biomimetic Synthesis

The analogy with biology has inspired the development of a variety of biomimetic synthetic methods for the organization of inorganic materials on the nanoscale.[103,105]

As has recently been stated by Brayner et al.,[104] numerous biological systems, such as proteins, polysaccharides, DNA, or combinatorial phage display peptide libraries, have already been used to direct the growth of nanoparticles. (The interested reader can find further references to this work in ref 104.) For example, Mertig and co-workers reported the use of S layers (which are regular, quasi-2D protein crystals with thickness ranging from 5 to 15 nm which can be recrystallized in vitro to give sheets and tube-shaped crystals), extracted from *Bacillus sphaericus* NCTC9602, as a template for the growth of arrays of Pt or Pd nanoparticles, via in situ chemical reduction and electron-beam-induced growth in a TEM apparatus.[106] To date, to the best of our knowledge, no bimetallic clusters have been synthesized in this way.

Recently, Rotello and co-workers reported the construction of nanocomposite materials consisting of FePt nanoparticles and DNA with the assembly of the preformed nanoparticles mediated by the DNA.[107] These nanoparticle−DNA aggregates have increased interparticle spacing, which has been found to alter the magnetic properties of the assemblies.

2.8.2. In-Vivo Biogeneration of Nanoparticles

It is known that certain microbes, on their own, can reduce metal salts to their zerovalent metallic states.[108] Macaskie and co-workers used bacterial hydrogenases to reduce aqueous Pd(II) to cell-bound Pd(0) nanoparticles of variable size (some as small as 5 nm).[109] These particles were found to be ferromagnetic and have high catalytic activity in hydrogenation as well as for reduction of Cr(VI) to Cr(III) under conditions where the bacteria alone or chemically reduced Pd nanoparticles were ineffective.[110] These biogenerated nanoparticles offer the possibility for bioremediation of industrial wastes, reclamation of precious metals (e.g., Pd and Pt), and formation of high-quality "Bio-Pd^0" catalysts for use in hydrogen fuel cells and other applications.[109] Interestingly, a Pd−Au hybrid crystal has recently been biomanufactured from the bottom up (Macaskie and coworkers, unpublished). The "biosynthesis" of Ni−Ti clusters has recently been reported, where the 2−5 nm particles were generated by reduction of a solution of Ni and Ti ions mixed with a suspension of powdered milled alfalfa.[111]

3. Experimental Techniques for Characterization of Nanoalloys

A variety of experimental techniques, including mass spectrometry, diffraction, microscopy, and numerous spectroscopies, have been applied to characterize and study the properties of mono- and bimetallic nanoparticles.[70,112,113] The following section gives a brief overview of some of the most commonly applied techniques.

3.1. Mass Spectrometry

Mass spectrometry is used to study the mass abundance of clusters in a cluster molecular beam by deflecting them (according to their mass) in an electric field after they have been ionized, generally by electron impact or laser ionization. Mass abundances occasionally show peaks which are intense relative to their neighbors. These "magic numbers" can often be explained in terms of extra thermodynamic or kinetic stability at these particular sizes, which may be due to electronic or atomic packing effects.[8,114,115]

3.2. Diffraction

X-ray and electron diffraction can be performed on single nanoparticles or arrays of nanoparticles. XRD has been particularly widely used to study surface-supported nanoparticles, affording information on structure, crystallinity, lattice spacing (and hence some information on the degree of mixing or segregation, provided that the lattice spacings of the two metals are distinct), particle size, and qualitative chemical composition information[116] (see Figure 8). Electron diffraction, on the other hand, has been more widely used for molecular beams of clusters. Although interpretation of the electron diffraction results is complex, information on the geometry, average size, and temperature of the nanoparticles may be obtained.[117,118]

3.3. Microscopy

For metal nanoparticles deposited or adsorbed onto a substrate, it is important to know the degree of aggregation, size, size distribution, and morphology of the particles. Microscopies of various types can be used to obtain this and other information.

3.3.1. Electron Microscopy

Electron microscopy is particularly useful for studying nanoparticles as the electron beam can be focused down to very small dimensions.[113]

Transmission electron microscopy (TEM), in which the electrons pass through the sample, generally requires the nanoparticles to be dispersed onto an electron-transparent substrate, such as a thin carbon-coated microgrid. TEM is particularly useful because of the high contrast between the metal atoms (especially heavy metals) and any passivating organic molecules or polymers.

High-resolution TEM (HRTEM, HREM) offers resolution down to the Ångstrom level and enables information to be obtained on the structure (atomic packing) rather than just

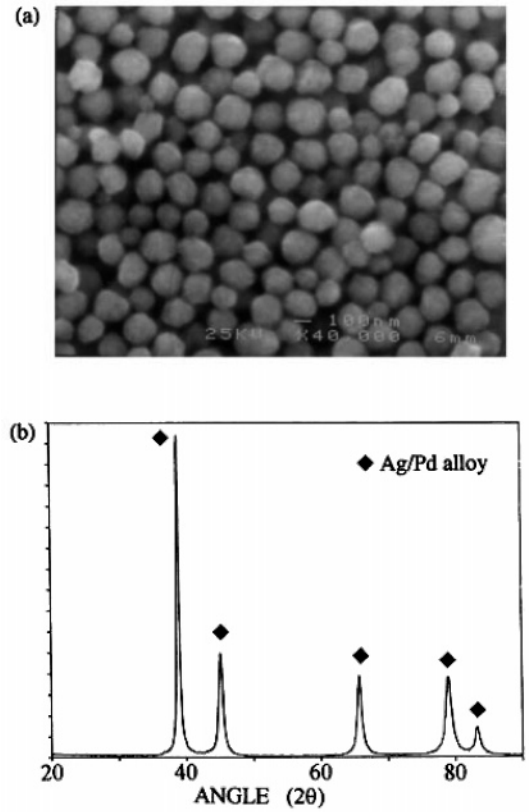

Figure 8. (a) SEM image of Pd−Ag alloy particles (wt ratio 70:30%) prepared by reducing a solution of mixed metal nitrates with ascorbic acid at 20 °C. (b) XRD pattern of the same particles showing the presence of a homogeneously mixed crystal lattice. (From ref 69. Reproduced by permission of The Royal Society of Chemistry on behalf of the Centre National de la Recherche Scientifique.)

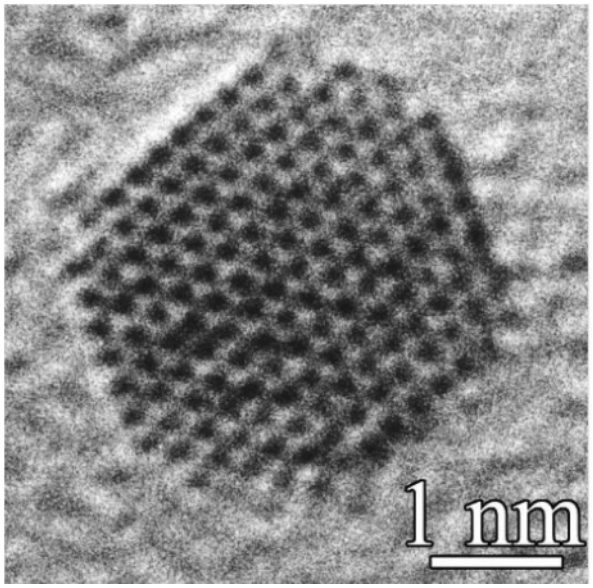

Figure 9. HREM image of a CuAu nanoparticle deposited on amorphous carbon. The nanoparticle has the structure of a truncated octahedron. (Reprinted with permission from ref 119. Copyright 2001 American Physical Society.)

the morphology of the nanoparticles (see Figure 9). Particle growth can also be studied using in situ TEM.

Scanning transmission electron microscopy (STEM) is a mode of operation of TEM in which the electron beam is scanned across the sample. This may be combined with the HAADF or "Z-contrast" imaging technique (as the HAADF image contrast is proportional to Z^{α}, where Z is the atomic number and α is in the range 1.5−2) to reveal the internal structure of the nanoparticle, based on the different electron scattering powers of different elements, so that chemical information can be obtained in tandem with structural information.[120] This method is particularly useful for studying bimetallic nanoparticles (e.g., Pd−Pt and Ag−Au) where the constituent elements have similar lattice spacings (so that alloyed and pure metallic regions cannot be distinguished by conventional TEM), but they have quite different atomic numbers. Langlois and colleagues used energy-filtered TEM to map out the elements in core−shell segregated nanoalloys, such as $Cu_{core}Ag_{shell}$.[121]

Scanning electron microscopy (SEM) is similar to STEM but the image is due to secondary electrons emitted by the sample surface following excitation by the primary electron beam. Although SEM images (see Figure 8a) have lower resolution than TEM, SEM is better for imaging bulk samples and has a greater depth of view, giving rise to better 3D images of the sample.

3.3.2. Scanning Probe Microscopy

Scanning probe microscopies constitute a group of techniques, including, for example, atomic force microscopy and scanning tunneling microscopy (STM), in which a surface is imaged at high (sometimes atomic) resolution by rastering an atomically sharp tip across the surface. Measurement of the strength of the interaction is used to map out the topography, electronic/magnetic structure, or chemistry of the surface.[113,122]

Atomic Force Microscopy (AFM). A fine tip is brought into close (but not touching) contact with the sample and senses the small (approximately 1 nN) repulsive force between the probe tip and the surface. The tip is rastered over the sample to measure the surface topography.

Scanning Tunneling Microscopy (STM). A fine tip is again brought extremely close to the surface, and a voltage is applied between the tip and the sample, which must be conducting, until a tunneling current flows, which is very sensitive to the distance between the tip and surface. In constant current mode, the STM tip is rastered across the surface and moved up or down to keep the current flow constant, thereby generating real-space, atomic resolution topographic images of the sample. In constant height mode, the tunneling current is measured with the tip maintained at a constant height, which can provide information on electronic structure as well as topography. Scanning tunneling spectroscopy is an off shoot of STM, which measures the local electronic structure (which depends on the atomic species and its environment) of a surface atom. Current vs voltage ($I-V$) curves (which are characteristic of the electronic structure at a specific location on the surface) are obtained by measuring the tunneling current as a function of the bias voltage.

3.4. X-ray Spectroscopy

High-energy X-ray radiation is particularly useful for studying metallic nanoparticles because the binding energies (and, hence, the spectral lines) of the atomic core electrons are very sensitive to the atomic number of the element, generally allowing metals which are adjacent in the periodic table to be distinguished.

3.4.1. X-ray Absorption Spectroscopy (XAS)

XAS (which comprises a number of related techniques) is very useful for probing the internal structures of metal nanoparticles and species adsorbed on them.[50,113] Its use has increased due to the availability of synchrotron radiation facilities around the world. Each element's X-ray absorption spectrum is unique and enables information to be obtained about the elements present in the nanoparticle and the local atomic environment and geometry, electron density, oxidation state, electronic configuration, site symmetry, coordination number, and interatomic distances. A recent review of the application of XAS to Pt-containing nanoalloys (with particular emphasis on electrocatalysts for fuel cell applications) has been presented by Russell and Rose.[50]

Extended X-ray Absorption Fine Structure (EXAFS). A monochromatic X-ray beam is directed at the sample. The photon energy of the X-rays is gradually increased so that it traverses one of the absorption edges of the elements contained within the sample. Below the absorption edge the photons cannot excite the electrons of the relevant atomic level, and thus, absorption is low. However, when the photon energy is just sufficient to excite the electrons, a large increase in absorption occurs, which is known as the absorption edge. The resulting photoelectrons have low kinetic energies and can be backscattered by the atoms surrounding the emitting atom. The backscattering of the photoelectron affects whether the X-ray photon is absorbed in the first place. Hence, the probability of X-ray absorption depends on the photon energy (as the photoelectron energy depends on the photon energy). The net result is a series of oscillations on the high photon energy side of the absorption edge. These oscillations can be used to determine the atomic number, distance, and coordination number of the atoms surrounding the element whose absorption edge is being examined. The necessity to scan the photon energy requires the use of synchrotron radiation in EXAFS experiments.

Near-edge X-ray Absorption Fine Structure (NEXAFS). It is generally applied to study chemisorbed molecules on surfaces. Information concerning the orientation of the molecule can be inferred from the polarization dependence. NEXAFS is sensitive to bond angles, whereas EXAFS is sensitive to the interatomic distances. NEXAFS spectra are frequently dominated by intramolecular resonances of π or σ symmetry. The energy, intensity, and polarization dependence of these resonances can be used to determine the orientation and intramolecular bond lengths of the molecule on the surface.

X-ray Absorption Near-Edge Structure (XANES). It uses radiation up to 40 eV from the X-ray absorption edge and can provide information about the vacant orbitals, electronic configuration, and site symmetry of the absorbing atom. The absolute position of the edge contains information about the oxidation state of the absorbing atom. In the near-edge region, multiple scattering events dominate. Theoretical multiple scattering calculations are compared with experimental XANES spectra in order to determine the geometrical arrangement of the atoms surrounding the absorbing atom.

3.4.2. X-ray Photoelectron Spectroscopy (XPS)

XPS is based on the photoelectric effect, whereby absorption of light by an atom, molecule, or solid/surface results in the ejection of electrons, provided that the photon energy is sufficient to overcome the binding energy of the electron. For XPS, Al Kα (1486.6 eV) or Mg Kα (1253.6 eV) photons are generally used.[113] Both valence and core electrons can be ejected by X-ray radiation. The core electron binding energies are characteristic of each element, and the peak areas can be used to determine the composition. As the peak shape and binding energy are sensitive to the oxidation and chemical state of the emitting atom, XPS can also provide chemical bonding information.[123−127] The XPS technique is highly surface specific due to the short range of the ejected photoelectrons.

Auger Electron Spectroscopy (AES). AES is a popular technique for determining the composition of the top few layers of a surface. It involves detection of secondary electrons which are ejected upon relaxation of a core hole, for example, a hole created in the XPS process.[113] AES is sensitive to chemical identity.

3.5. Energy-Disperse X-ray Microanalysis (EDX, EDS)

This analytical technique is often used in conjunction with SEM. An electron beam (typically 10−20 keV) strikes the surface of a conducting sample, causing X-rays to be emitted, whose energies depend on the material under examination. The X-rays are generated in a region about 2 μm in depth. By scanning the electron beam across the material, an image of each element in the sample can be obtained. EDX is a high-resolution (with approximately 1.5 nm lateral resolution) variant of electron microprobe analysis or X-ray microanalysis whereby information can be obtained on the chemical composition of individual nanoparticles.

3.6. Other Spectroscopic Techniques

Ultraviolet−Visible (UV−vis) Spectroscopy. As mentioned in section 1, the optical properties (in particular the surface plasmon resonance) are sensitive to the chemical composition and degree of ordering of bimetallic nanoparticles, especially of the noble metals.[53,54,112] Changes in UV−vis spectra can also be used to study the reduction of metal ions and their aggregation during the cluster formation process.[70]

Infrared (IR) Spectroscopy. IR (including Fourier transform IR (FT-IR)) spectroscopy is widely used to study the vibrational spectra of small molecules adsorbed on metallic clusters. For example, by making comparisons with pure metal clusters or surfaces, IR spectroscopy of small molecules (e.g., CO or RNC) adsorbed on bimetallic nanoparticles can be used as a probe of the surface composition and structure.[70,112]

Photolectron Spectroscopy. As well as XPS, electronic and dynamical properties of metal clusters can be investigated by photoelectron spectroscopy using lower energy radiation (from IR to UV). For example, intraband electronic transitions in small Hg clusters have been studied by time-resolved photoelectron imaging using IR radiation.[128]

Surface-Enhanced Raman Spectroscopy. The Raman scattering intensity of molecules is greatly enhanced (by as much as 5 orders of magnitude) when they are absorbed on certain metals.[112] The effect (which again probes vibrational structure) has been used to study the binding of adsorbates on metallic nanoparticles and the cluster formation process.[112]

Mössbauer Spectroscopy. A nucleus in a solid or cluster can sometimes emit and absorb γ-rays without recoil. Since the probability of such a recoil-free event depends on the energy of the γ-ray, the Mössbauer effect is restricted to certain isotopes with low-lying excited states. In Mössbauer

spectroscopy, the γ-ray energy is Doppler shifted by accelerating the source through a range of velocities, the spectrum being a plot of γ-ray intensity as a function of source velocity. At velocities corresponding to the resonant energy levels of the sample, some of the γ-rays are absorbed, resulting in a dip in the spectrum. These spectral features provide information about the chemical environment of the absorbing nuclei. Mössbauer-active isotopes which have been used (or could be used) in the study of bimetallic nanoparticles include ^{57}Fe, ^{57}Co, ^{191}Ir, and ^{197}Au.

Nuclear Magnetic Resonance (NMR). NMR spectroscopy probes the local magnetic environment of a nucleus with nonzero magnetic moment in terms of its chemical shift (which depends on the amount of diamagnetic and paramagnetic shielding or deshielding) and line splitting due to magnetic coupling to the nuclear spins of neighboring atoms. In the case of quadrupolar nuclei (with nuclear spin $I > 1/2$) the line shape and number of peaks can also give information on the symmetry of the atomic environment. Regarding mono- and bimetallic nanoparticles, NMR spectroscopy has been performed on metallic nuclei (e.g., ^{63}Cu, ^{103}Rh, ^{195}Pt, and ^{197}Au), where the chemical shift is dominated by the Knight shift, arising from the conduction electrons, thereby giving a measure of the metallic nature of the particle.[112] Cluster paramagnetism and ferromagnetism can also be probed by metal NMR. NMR has also been used to investigate the structures of adsorbed organic molecules (including passivating molecules and polymers), for which the most useful nuclei are ^{1}H, ^{13}C, and ^{31}P.[112]

Electrochemical NMR Spectroscopy (EC-NMR). EC-NMR was introduced in the late 1980s for the study of electrochemical surfaces, providing an electronic level description of electrochemical interfaces based on the local density of states at the Fermi level. ^{13}C and ^{195}Pt are particularly useful nuclei for investigating electrochemical interfaces and probing nanoparticle electrode surface modifications. In the field of nanoalloys, Wieckowski and co-workers used EC-NMR extensively to study nanoalloy particles in fuel cell electrodes[129] (see Figure 10 and section 5).

3.7. Magnetic Measurements

The properties of magnetic nanoparticles have been recently reviewed by Bansmann et al.[130] There have been many studies of the magnetism of free transition-metal clusters in molecular beams, dating back to the experiments of de Heer and colleagues,[131] who used Stern−Gerlach-type deflection experiments, coupled with time-of-flight mass spectrometry to show that Ni, Fe, and Co clusters are ferromagnetic (with higher magnetic moments per atom than in the bulk), and those of Cox, Bloomfield, and co-workers,[132,133] who showed that small Rh clusters are also ferromagnetic (unlike bulk Rh which is paramagnetic). Knickelbein has also shown that Mn clusters in the range Mn_5−Mn_{99} can exhibit ferromagnetic or ferrimagnetic coupling.[134,135] Stern−Gerlach deflection experiments have also been carried out for nanoalloy Bi−Co[136] and Bi−Mn[137] clusters. De Heer and co-workers have also performed molecular beam studies of the magnetism of Co−Mn and Co−Au clusters with up to a few tens of atoms.[138]

The magnetic properties of larger, surface-supported mono- and bimetallic clusters have also been measured using techniques such as SQUID magnetometry (to obtain magnetization curves as a function of field strength)[139] and magnetic force microscopy.[140]

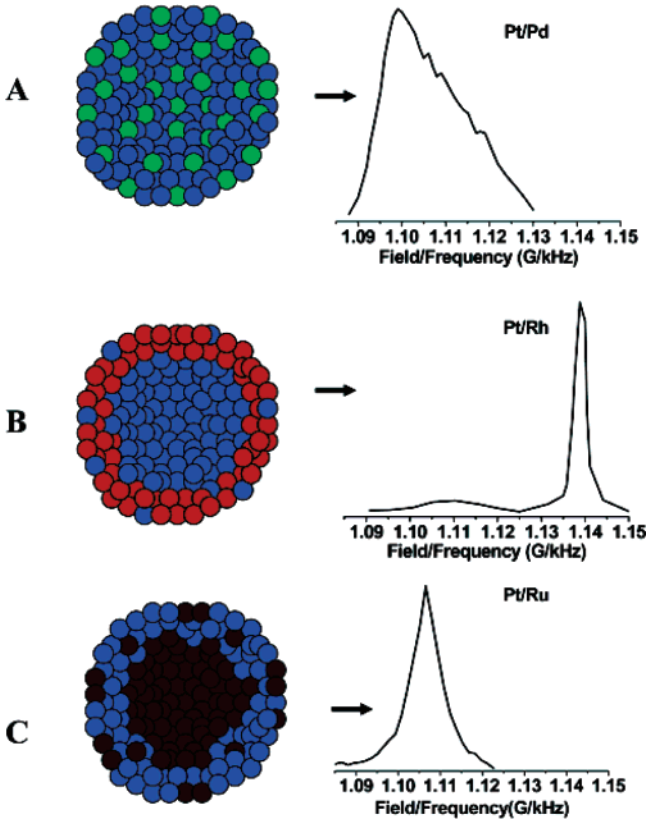

Figure 10. Schematic representation of three different Pt−alloy nanoparticle systems with their corresponding ^{195}Pt NMR spectra: (A) Pt−Pd, (B) Pt−Rh, and (C) Pt−Ru. Pt, Pd, Rh, and Ru atoms are shown in blue, green, red, and black, respectively. (Reprinted with permission from ref 129. Copyright 2003 American Chemical Society.)

3.8. Ion Spectroscopy/Scattering (IS)

IS techniques involve accelerating ions onto a sample and detecting the energies and distribution of scattered ions. Ion energies are as follows: 1−10 keV for low-energy IS (LEIS), 20−200 keV for medium-energy IS, and 200−2000 keV for high-energy IS. The higher the incident ion energy, the smaller the target atoms appear, though the yields are smaller, so low energies are best for surface-specific information.[113] The energy and angle of the scattered ions are analyzed simultaneously, allowing measurement of atomic mass (and hence composition), depth (down to 1 atomic layer is possible), and surface structure. Depending on the incident ion energy, ion scattering may be accompanied by surface etching. Following the time evolution of the surface composition therefore allows depth profiling of the composition of bimetallic nanoparticles.[141,142]

3.9. Electrochemistry

A variety of electrochemical techniques have been applied to nanoalloys, ranging from CV to scanning electrochemical microscopy. These measurements are particularly important for nanoparticles employed as electrode materials in electrocatalytic fuel cells. Russell and Rose reviewed research involving in situ XAS measurements in electrochemical cells, whereby the variation of particle size, coordination number, and other structural parameters can be investigated as a

function of the electrode potential.[50] Compared with UHV and electron-based spectroscopic techniques, electrochemical techniques for surface measurement allow direct investigation of the surfaces of real catalysts under ambient conditions, thereby bridging the so-called "pressure" and "materials" gap between surface science and heterogeneous catalysis.[143] Attard et al. reported the combination of CV (used as a measure of local structure) and STM to characterize the surface morphology of Pt particles (by comparison with bulk Pt surfaces) as well as the bimetallic surfaces formed by Bi adsorption on Pt nanoparticles.[143]

4. Theoretical Framework and Computational Methods for Studying Nanoalloys

From a theoretical point of view, the study of both equilibrium and dynamical properties of nanoalloys is extremely interesting and challenging.

Let us consider an A_mB_n cluster with $m + n = N$. Within the Born−Oppenheimer approximation, one starts from the determination of the cluster configurational energy as a function of atomic coordinates, namely, of the potential energy surface (PES) $E(r_1^A,...,r_m^A,r_1^B,...,r_n^B)$. Once E is known, the most stable cluster configuration corresponds to the lowest minimum of the PES, usually denoted as the global minimum. The solution to the problem of finding the global minimum can be (tentatively) achieved by global optimization methods. Finite temperature equilibrium properties, on the other hand, require the sampling of all significant portions of the PES in order to make averages over different configurations using appropriate statistical weights. Finally, the study of intermixing and growth kinetics also requires reliable modeling of nanoalloy dynamics. Several theoretical tools are now available to deal with these problems, which are however extremely complex.

For example, finding the most stable cluster structures for given cluster size and composition is a very difficult task. As we shall see in the following, a thorough exploration of the PES by means of ab initio methods is presently not feasible even for clusters containing a few tens of atoms. On the other hand, it is very difficult to simply guess the most stable structures on the basis of some chemical or physical intuition since these structure are often highly nontrivial. To overcome this problem, one may employ simpler interaction models (such as those given by atom−atom potentials) as a first step in the study. These models are less computationally intensive, thus allowing a much more complete sampling of their PES. In this way, large databases of possible cluster structures, containing clusters of different structural families, can be constructed. The structures in the databases can be the starting point for further ab initio calculations.[26,144] Atom−atom potentials must be used with care since their accuracy is strongly system dependent. In several cases, there is evidence that these potentials are valuable tools (see the discussion below). However, one must bear in mind that these potentials may give an oversimplified description of alloy nanoclusters, so that important structural families may be missed in the construction of the databases. The problem of developing efficient computational methods for finding the best nanoalloy structures is still open and constitutes a lively and rapidly changing research field.[145]

In the following, we first sketch models and methods for determining the PES. Then we deal with the global optimization problem and methods for studying finite-temperature equilibrium properties and dynamical behavior of nanoalloys. Finally, we introduce quantities which are useful for analyzing geometric structure, mixing pattern, energetic stability, and propensity to mixing of alloy nanoclusters.

4.1. Modeling the PES of Nanoalloys

Several methods and models have been employed to study the PES of nanoalloys. This study is indeed an extremely difficult task because the PES of alloy nanoclusters containing a few tens of atoms is of enormous complexity

Methods based on density functional theory (DFT),[146] when adequately tested (see, for example, ref 147) can be of sufficiently high accuracy, affording the possibility of treating a wide variety of systems and sizes, up to a few hundred atoms for symmetric structures. These methods have been applied to several nanoalloy systems (see, for example, refs 148−154). The main disadvantage of DFT calculations is that they are time consuming, so that it is usually possible to explore only a limited part of the PES. In fact, full DFT-based global optimization (see below) is still too cumbersome for nanoalloys. This means that DFT calculations are limited to the comparison of a few selected structures without any guarantee that these structures are indeed among the most stable ones. This is a serious drawback because, as discussed above, the variety of structures in nanoalloys is much richer than in single-element clusters. For this reason, it is very important to complement the time-consuming DFT methods with more approximate models, which are able to preselect the most promising structures. These more approximate methods comprise jellium-model calculations[155] and semiempirical potential calculations (e.g., EAM,[156,157] and SMATB potentials, the latter including Gupta/Rosato−Guillopé−Legrand and Sutton−Chen potentials[158−161]). The latter potentials have become popular in recent years, being among the simplest approaches to deal quantitatively with nanoalloy systems of transition and noble metals. It should be noted that, as a consequence of electron delocalization, metallic interactions inherently possess many-body nature. This implies that pairwise additive potentials are inadequate for nanoalloys.

Within the SMATB approach,[159−162] the configurational energy of a cluster is a function of the interatomic distances r_{kl} and is written as the sum of atomic energies

$$E = \sum_{k=1}^{N} \sum_{i=A,B} d_k^i E_{k,i} \tag{5}$$

where d_k^i is an occupation variable whose value is 1 if atom k is of species i and 0 otherwise. The atomic energy $E_{k,i}$ of an atom k ($k = 1,...,N$) of species i ($i = A, B$) includes a band-energy term $E_{k,i}^{band}$ and a repulsive term $E_{k,i}^{rep}$

$$E_{k,i} = E_{k,i}^{band} + E_{k,i}^{rep} \tag{6}$$

$E_{k,i}^{band}$ and $E_{k,i}^{rep}$ are given by

$$E_{k,i}^{band} = -\left\{\sum_{l\neq k}^{N} \sum_{j=A,B} d_l^j \xi_{ij}^2 \exp\left[-2q_{ij}\left(\frac{r_{kl}}{r_{ij}^0} - 1\right)\right]\right\}^{1/2}$$

$$E_{k,i}^{\mathrm{rep}} = \sum_{l\neq k}^{N} \sum_{j=A,B} d_l^j A_{ij} \exp\left[-p_{ij}\left(\frac{r_{kl}}{r_{ij}^0} - 1\right)\right] \qquad (7)$$

where r_{kl} is the distance between the kth and the lth atoms The parameters (A_{ij}, ξ_{ij}, p_{ij}, q_{ij}) are usually fitted to experimental properties of bulk metals and alloys[159−162] or to bulk properties and those of the diatomic molecules of the corresponding elements.[157,162] r_{AA}^0 and r_{BB}^0 are the nearest-neighbor distances of pure bulk elements. r_{AB}^0 is often taken as the average of the pure distances, namely, $r_{AB}^0 = (r_{AA}^0 + r_{BB}^0)/2$, but it can also be taken as the experimental nearest-neighbor A−B distance in some specific ordered bulk alloy, as in ref 161. This potential takes into account size-mismatch effects, and the interactions display a bond-order/bond-length correlation, with shorter and stronger bonds for low-coordination atoms. This effect is crucial in stabilizing polyicosahedral structures in several nanoalloy systems.[24]

Semiempirical potential modeling has advantages and drawbacks. It allows full global optimization up to rather large sizes (see below) and also MD simulations on long time scales. The main problem is the accuracy of the semiempirical potentials, which has to be checked system by system. These potentials may give an oversimplified description of nanoalloy clusters because they may miss important physical effects.

For example, charge-transfer effects, which are relevant for several nanoalloy systems, are not included in these potentials. Charge-transfer effects are important when the atoms have significant differences in electronegativity. Recently, Zhang and Fournier[163] added the electrostatic contribution to the energy to a scheme resembling SMATB or EAM potentials. They attributed screened Coulomb charges to the atoms, which were determined self-consistently within the electronegativity equalization method. They applied their method to Cu−Ag, Ag−Au, and Cu−Au icosahedral clusters of 55 atoms, finding that the electrostatic contribution enhances AB ordering at the cluster surfaces for Ag−Au and Cu−Au clusters.

We note also that specific quantum effects, related, for example, to electronic shell closure, are not modeled within the approaches described above but require fully quantum calculations. An example of the interplay of geometric and electronic shell-closure effects is given in ref 26.

Finally, we remark that the validity of the semiempirical approach has been successfully tested for several systems by means of comparison with experimental data and DFT calculations. In the case of Ni−Al clusters of sizes 12, 13, and 14, the structures found within the SMATB model are completely consistent with the results of experimental measurements of N_2 uptake by these clusters as a function of their composition (see section 5.5.1). In the case of Cu−Ag, Ni−Ag, and Cu−Au clusters of sizes 34, 38, and 40, the SMATB results agreed well with those of DFT calculations (see sections 5.1.1 and 5.3.2).

Following a well-established tradition in the field of statistical mechanics of bulk and surface alloys, nanoalloys have also been studied by means of lattice models. Within this framework, one defines an effective Hamiltonian depending on the occupation number of sites on a predefined lattice. Usually, only pair interactions between nearest-neighbor atoms are taken into account. The parameters of the Hamiltonian are usually fitted to experimental quantities.

The advantage of these models is that they are much easier and faster to handle from a computational point of view than off-lattice models, so that large systems can be treated in a large variety of conditions. A satisfactory sampling of the configuration space can easily be achieved. There are two main drawbacks. First, the a priori choice of a lattice is a severe limitation, much more severe than in bulk (or surface) systems. In fact, this limitation is even more severe in nanoalloys than in pure clusters, since nanoalloys are likely to form structures which are different from those of the best-known structural motifs, such as icosahedra, decahedra, and fcc clusters. Second, even when the choice of a given lattice is appropriate, atomic coordinates cannot be relaxed. Relaxation effects are generally important, especially when dealing with systems characterized by a large size mismatch between the atomic species.

A popular lattice model is the tight-binding Ising model,[164] which has been successful in predicting the properties of surface alloys. In this model, an effective Hamiltonian H^{eff} (which models the part of the energy depending on the chemical configuration of the system) is written as

$$H^{\mathrm{eff}} = \sum_k d_k^* \left(\Delta h^{\mathrm{eff}} - \sum_{l\neq k} V_{kl}\right) + \sum_{k,l\neq k} d_k^* d_l^* V_{kl} \qquad (8)$$

where $d_k^* = 1$ or 0 if site n is occupied by an atom of species A or B, the local field Δh^{eff} is the difference in excess energies at site k of the pure species A and B, and V_{kl} is the alloy effective pair interaction, $V_{kl} = (V_{AA} + V_{BB} - 2V_{AB})/2$. The parameters of the model are usually fitted to bulk properties.

Another widely used approach is the bond-order model, which was developed by Strohl and King[165] for pure elements and extended to alloy systems by Zhu and DePristo.[166] Within this model, the total energy of a cluster is written as the sum of atomic contributions. The energy of an atom of species i ($E_{k,i}$) depends on the number of neighbors of species i and j, denoted by Z_i,Z_j, with $Z = Z_i + Z_j$

$$E_{k,i} = \epsilon_i^Z + Z_j \Delta E_{ij}^Z + \frac{Z_j(Z_j-1)}{2}\lambda_{i,ij}^Z \qquad (9)$$

The parameters of the model are ϵ_A^Z, ϵ_B^Z, ΔE_{AB}^Z, ΔE_{BA}^Z, $\lambda_{A,AB}^Z$, and $\lambda_{B,BA}^Z$. The last four parameters are known as mixing parameters and usually fitted to bulk mixing energies.

4.1.1. Structural Optimization of Nanoalloys

Once an energetic model has been defined, searching the PES to find the lowest energy structure (the global minimum, GM) for a given size and composition can be a formidable task. In fact, global optimization is much more difficult for nanoalloys than for pure clusters of the same size. This is due to the inequivalence of homotops, which dramatically increases the number of different minima in the PES. As mentioned in section 1, an N-atom cluster A_mB_n has a number of inequivalent homotops of the order of $N!/(m!n!)$.

The most commonly employed global-optimization strategies are either based on genetic algorithms (see ref 167 for a recent review) or the basin hopping algorithm[168] and its variants. Genetic and basin-hopping algorithms are of comparable efficiency, and both are superior to simulated annealing. Both genetic and basin-hopping algorithms compare clusters after local minimization on the PES. In genetic algorithms, selection is made within an evolutionary proce-

dure with a tunable selective pressure. In basin hopping, a simple Metropolis Monte Carlo (MC) walk on the locally minimized PES is performed, and the tunable parameter is the temperature.

In all algorithms, rules for generating new cluster configurations from the present ones are necessary. Besides the usual moves that are employed for single-component clusters,[167,168] exchange moves between atoms of different species may be very effective in nanoalloys, since these moves allow the exploration of inequivalent homotops.

Global optimization is presently very cumbersome within a full DFT approach. There are examples in the literature concerning pure metal clusters up to a few tens of atoms.[169] Due to the higher complexity of their PES, the limiting size for nanoalloys should be even lower. To our knowledge, there are no examples in the literature yet.

A more feasible strategy is to perform global optimization using a more approximate model, which helps in selecting a set of promising structures. In fact, within semiempirical potential models, global optimization is much more feasible. For example, pure Lennard−Jones clusters of several hundred atoms have been optimized.[170] Presently, binary metallic clusters have been optimized up to size of ∼150 atoms[171] within the SMATB model. The most promising structures obtained in the optimization of the semiempirical model are then locally reoptimized by DFT methods.[24,26,144,152,153,172,173] Often, due to the limited accuracy of semiempirical potentials, DFT reoptimization may significantly change the energetic ordering of clusters belonging to different structural motifs (see, for example, ref 26). For this reason, selection of the most promising structure for reoptimization is better accomplished by algorithms which are able to explore different funnels of the PES, in order to possibly single out all significant motifs. To this purpose, algorithms which search the configuration space with the help of order parameters may be very useful.[174]

In our experience, there is no general rule for preferring a specific global optimization algorithm in all cases since the efficiency of the algorithms is system dependent. A good strategy is to perform optimization runs by different algorithms and use different order parameters. Moreover, a combination of unseeded searches (which start from random atomic positions) and seeded searches (which may start, for example, from structures found at nearby sizes and/or compositions) is usually fruitful. For example, system comparison and composition comparison are often useful.[175−177]

System comparison is performed as follows. Once putative global minima have been identified for two clusters X_nY_m and X_nZ_m, we build up two artificial clusters. These clusters are constructed by replacing all the Y atoms of the X_nY_m cluster with Z atoms and vice versa. These new clusters are then subjected to local minimization and compared to the old putative global minima, which are replaced if the new clusters have a lower energy.

Composition comparison starts from the putative global minima of three adjacent compositions, $X_{n-1}Y_{m+1}$, X_nY_m, and $X_{n+1}Y_{m-1}$. Then, the following test is made on the X_nY_m putative global minimum. The $X_{n-1}Y_{m+1}$ is taken, and all Y atoms are substituted one by one by X atoms, obtaining $m + 1$ clusters of composition X_nY_m, which are locally minimized. This is repeated, replacing each X atom of $X_{n+1}Y_{m-1}$ with a Y atom. All these new clusters are compared to the old putative X_nY_m global minimum.

The philosophy behind these approaches and variants, such as varying the heteronuclear parameters of the SMATB potential within the range defined by the values for the pure metals,[178] is to use the empirical potential as a tool for exploring the diversity of the PES. In this spirit, even more than focusing on the accuracy and predictive capabilities of the empirical potential, it is often fruitful to use two different potentials able to bracket the experimental behavior (tendency toward open vs compact configurations, etc.).

4.1.2. Thermodynamics, Diffusion, and Growth Kinetics

Thermodynamic properties and kinetic phenomena are challenging topics for a theoretical treatment, the former because of the complexity of the energy landscape of nanoalloys and the latter because of the long time scales involved.

For clusters composed of tens of thousands of atoms, or more, classical thermodynamic approaches can be useful. Recently, there have been several efforts to develop a thermodynamic theory of nanoalloy "phase diagrams" and melting.[179−185] These approaches extend the use of macroscopic thermodynamic quantities to nanosized systems and are therefore unsuitable when the precise structure of the alloy nanocluster is important. For example, transitions between structural motifs and size- (or structure-) dependent segregation phenomena are not included in these treatments. In section 7, we shall discuss in more detail some of these approaches, which have been successfully applied to the interpretation of the experimental data on size-dependent melting in Sn−Bi and Pb−Bi clusters.[179,183]

When dealing with smaller clusters (containing a few thousand atoms at most), microscopic approaches are feasible and more appropriate. In this size range, nanoalloys are studied mostly by simulation methods, while analytical or semianalytical treatments are less common. An example of a semianalytical treatment is the study of segregation profiles by mean-field Bragg−Williams calculations[187] or FCEM[188,189] on lattice models. These methods rely on the expansion of the partition function in terms of the atomic concentrations (see section 9 for an application of the FCEM).

In most cases, equilibrium properties of nanoalloys are usually calculated either by MC[190] or MD[191] methods.[14,16,17,24,186,192−194] There are few examples of ab initio treatments. In the case of alkali-metal nanoalloys, DFT-based MD simulations have been used to study melting.[150,151,195] In fact, alkali metals can be treated within a simplified DFT model, an approach allowing the accumulation of sufficient statistics even for clusters of 55 atoms. In the case of transition-metal nanoalloys, where DFT approaches are much more time-consuming, melting has mostly been studied by MD simulations based on semiempirical potentials [14,16,17,24,196−199] (see Figures 11and 12). Clusters containing even thousands of atoms are tractable in this way. In all MD applications, special attention must be paid to obtain a sufficient statistical sampling. This is especially true for the more time-consuming ab initio approaches.

MD simulations have also been employed to study the vibrational properties of nanoalloys, in analogy with previous studies on pure nanoclusters.[200] By Fourier transforming the velocity autocorrelation function of the different atomic species in Pt−Ag and Pt−Au clusters deposited on graphite substrates, Calvo and Balbuena[201] were able to extract the partial phonon density of states (DOS) of Ag, Pt, and Au atoms. They concluded that the measurement of partial DOS

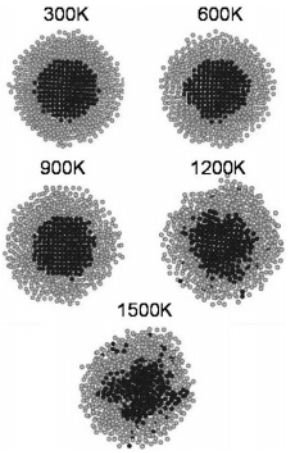

Figure 11. Snapshots from classical MD simulations of the melting of AgCo clusters. Black and light gray spheres correspond to Co and Ag atoms, respectively. (Reprinted with permission from ref 186. Copyright 2005 American Physical Society.)

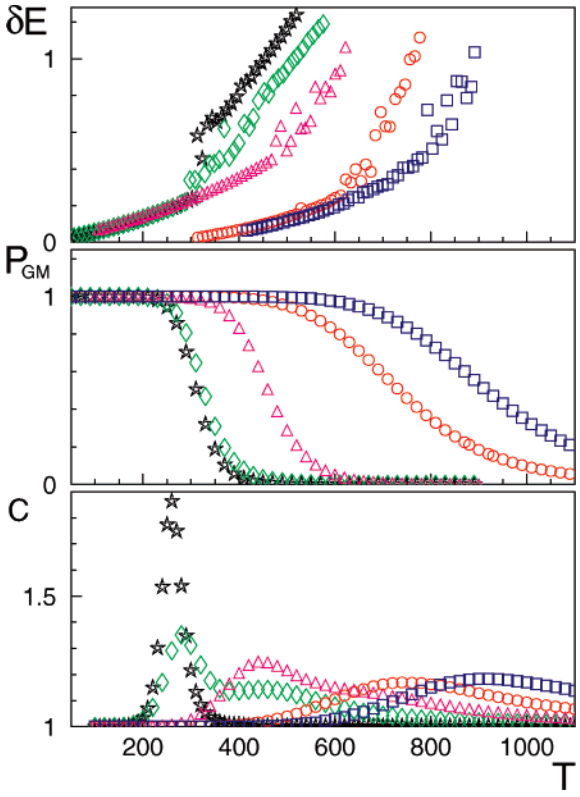

Figure 12. Melting of pure Ag, Cu, and Ni clusters and core−shell Cu−Ag and Ni−Ag polyicosahedra: (top) MD caloric curves δE (in eV) vs temperature T (in K), where $\delta E = E - E_{GM} - 3(N - 1)k_BT$, i.e., the total cluster energy minus the global minimum energy E_{GM} minus the harmonic contribution $3(N - 1)k_BT$; (middle) probability p_{GM} of occupying the global minimum; (bottom) vibrational specific heat c per degree of freedom (in units of the Boltzmann constant k_B). p_{GM} and c are calculated in the harmonic superposition approximation (see eq 10). Stars, diamonds, and triangles refer to pure Ag_{38}, Cu_{38}, and Ni_{38} clusters; circles and squares refer to the $Ag_{27}Cu_7$ and $Ag_{27}Ni_7$ core−shell polyicosahedra, which melt at considerably higher temperature than the pure clusters. (Reprinted with permission from ref 24. Copyright 2004 American Physical Society.)

could be used to extract information on the chemical ordering of experimentally produced nanoalloys.

MC simulations can be performed in different statistical ensembles. In canonical MC simulations, size, composition, and temperature T of the cluster are kept fixed. MC moves consist of either the displacement of a selected atom or the exchange of two atoms of different species (see, for example, ref 202). According to the Metropolis scheme, for each attempted move, the energy difference ΔE between the final and the initial configuration is computed. The move is accepted with probability $\min[\exp\{-\Delta E/(k_BT)\},1]$, where k_B is the Boltzmann constant.

It can also be useful to allow the composition of a cluster to vary. This is accomplished in the semi-grand canonical ensemble;[203] see refs 204 and 205 for an application to nanoalloys. In semi-grand canonical MC simulations, the chemical potentials $\mu_{A,B}$ are defined and the difference $\Delta\mu = \mu_A - \mu_B$ is kept fixed. Besides displacement and exchange moves, a third kind of move is allowed in which the chemical identity of a single randomly selected atom is changed. For this move, the quantity $\Delta E - \Delta\mu$ is calculated and the move accepted with probability $\min[\exp\{-(\Delta E - \Delta\mu)/(k_BT)\}, 1]$.

Melting and structural transformations of nanoalloys have also been studied within the harmonic superposition approximation.[5,24] Within this approach, a huge set of local minima is collected, and each minimum is weighted by its harmonic entropy.[206] The free energy F is evaluated from $F = -k_BT \ln Z$, where the partition function Z is given by

$$Z = \nu\left(\frac{Mk_B^2T^2}{\hbar^4}\right)^{3/2} \sum_s \bar{I}_s e^{-\beta E s^0} \prod_{i=1}^{3N-6}\left(\frac{k_BT}{\hbar\omega_{s,i}}\right) \qquad (10)$$

where M is the mass of the cluster and $\bar{I}_s$ and E_s^0 are the average moment of inertia and the energy of the structure (local minimum) s. $\omega_{s,i}$ are the $3N - 6$ normal-mode frequencies of minimum s, and ν is the volume of the box in which the cluster is enclosed. The results of the harmonic superposition approximation are in good agreement with those of MD simulations of the melting of highly symmetric magic number nanoalloys[24] (see Figure 12), though there are indications that the harmonic approximation is not always accurate.

Intermixing and growth phenomena have been studied both by kinetic MC[207,208] and MD simulations,[20,209] both based on semiempirical energetic modeling. These techniques are able to reach time scales of experimental interest for clusters of hundreds of atoms. This work will be discussed further in section 8.

4.2. Analysis of Geometric Structures and Mixing Patterns of Nanoalloys

As sketched in the Introduction, nanoalloys can be characterized by their structure and mixing pattern.

Geometric structures in nanoalloys can be either crystalline or noncrystalline, by analogy with pure clusters.[2,4,5] The common neighbor analysis[210] is a useful tool to discriminate different geometric structures. In this approach, a signature is assigned to each pair of nearest-neighbor atoms. This signature consists of three integers (r, s, t): r is the number of common nearest neighbors of the pair, s is the number of nearest-neighbor bonds among these common neighbors, and t is the length of the longest chain which can be formed with these s bonds. Local fivefold symmetries are singled out by (5, 5, 5) signatures, whereas bulk fcc pairs present (4, 2, 1) signatures. While the calculation of this signature for pure clusters is straightforward, some problems may arise when dealing with binary systems in which there is a

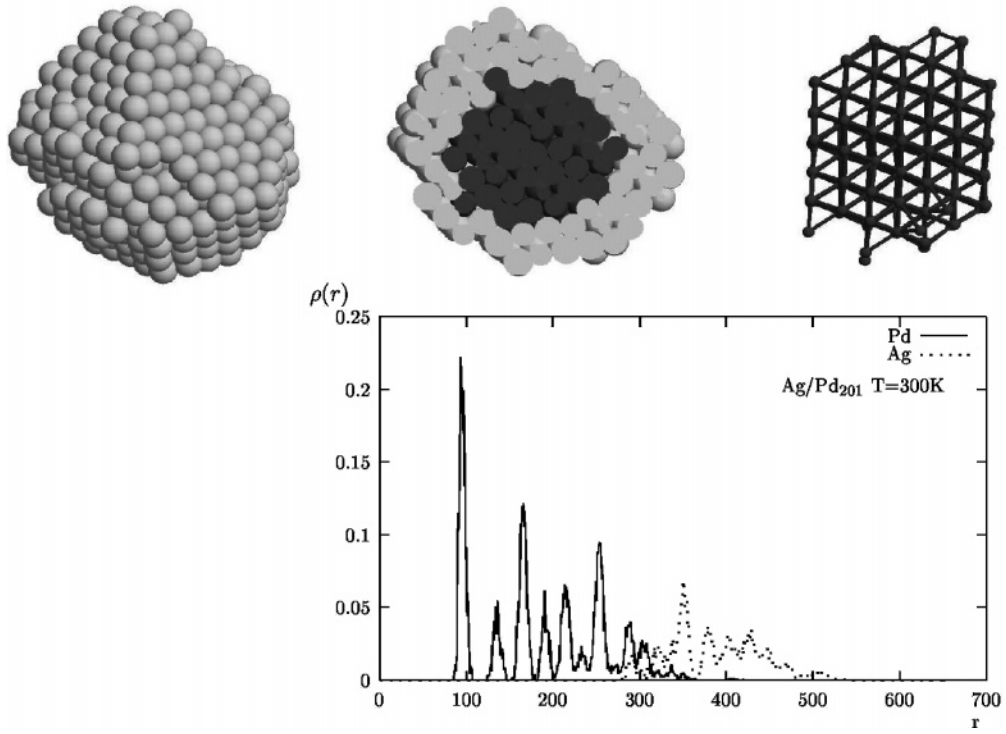

Figure 13. Cluster structure and radial distribution function from a MD growth simulation. In the top row, the same cluster is shown in three different ways: surface, cross section, and ball and stick representation of the Pd core. This core−shell structure is obtained by depositing 404 Ag atoms on a truncated octahedral Pd core, at $T = 500$ K and deposition flux of one atom each 2.1 ns. ρ is given in arbitrary units and r in Å. (Reprinted with permission from ref 209. Copyright 2002 American Physical Society.)

considerable size mismatch between different atoms. In this case, determination of the cutoff distance for first neighbors may require some care.

Chemical ordering in nanoalloys can be described by a number of parameters. When some specific ordered alloys is searched for, long-range order parameters defined as in the bulk cases can be useful. Local order may be measured by the correlation functions of AA, AB, and BB pairs. On the other hand, an overall measure of the degree of mixing can be obtained by counting the total numbers of AA, AB, and BB nearest-neighbor bonds.[211]

A quantity which can help in determining the mixing pattern in nanoalloys is the radial distribution function of the different atomic species. If $n_{A,B}(r)$ are the numbers of atoms of species A or B in a shell at a distance between r and $r + \Delta r$ of the center of the cluster, the radial densities $\rho_{A,B}$ are defined by

$$\rho_{A,B} = \frac{n_{A,B}(r)}{4\pi r^2 \Delta r} \tag{11}$$

The radial distribution function, which is most useful in the case of quasi-spherical clusters, can discriminate between clusters with radially mixed and radially segregated (like core−shell, as in Figure 13 or multishell) patterns. However, in the case of radially mixed clusters, eq 11 is not a good overall measure of mixing as it does not reveal whether the two components are mixed or segregated within a given shell (see, for example, the structure at left in Figure 1b). For geometric structures which are naturally separated into concentric shells (even though not exactly spherical shells) like icosahedra, cuboctahedra, or Ino decahedra, the concentrations of A and B elements are usually given as functions of the shell number instead of the distance from the cluster center.

For small clusters, another useful index of the degree of intermixing is the quantity ΔN_{mixed}, applied to compare the degree of intermixing in the global minima of clusters of same size and different compositions in ref 212. To calculate ΔN_{mixed}, the number of mixed nearest-neighbor bonds of the global-minimum structure (N_{mixed}) is calculated. Then a Monte Carlo search is performed by allowing exchange moves between atoms of different species, keeping the geometric structure fixed. This is done to search for the mixing pattern presenting the maximum number of nearest-neighbor mixed bonds within the geometric structure of the global minimum. If this maximum number is N^*_{mixed}, then ΔN_{mixed} is given by

$$\Delta N_{mixed} = N^*_{mixed} - N_{mixed} \tag{12}$$

Highly intermixed global minima present small values of ΔN_{mixed}, while surface-segregated global minima have large ΔN_{mixed} (see Figure 14).

4.3. Energetic Stability Indexes and Mixing Energy of Nanoalloys

As mentioned in the Introduction, nanoalloys may display both magic sizes and magic compositions. In order to single out possible magic compositions at a given size, stability indexes can be introduced as follows.

Let $E(A_mB_n)$ be the configurational energy of a given cluster A_mB_n of size $N = m + n$. $E(A_mB_n)$ is the energy difference between the specific cluster configuration A_mB_n (referring to some specified local minimum on its PES) and

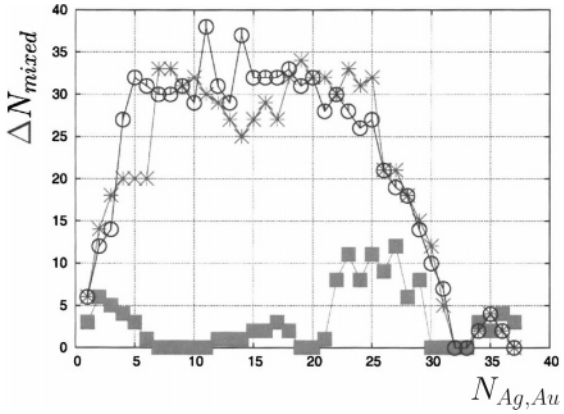

Figure 14. ΔN_{mixed} for Ni−Ag (circles), Cu−Ag (stars), and Cu−Au (squares) clusters of 38 atoms at varying composition. $N_{Ag,Au}$ is the number of Ag or Au atoms in the cluster. The results are obtained within the potential model of eq 7.[24] Ni−Ag and Cu−Ag clusters present large values of ΔN_{mixed}, indicating a low degree of intermixing in their global minima (which are in fact core−shell structures). On the contrary, Cu−Au clusters show small ΔN_{mixed}, corresponding to mixed global minima. (Reprinted with permission from ref 212. Copyright 2005 American Institute of Physics.)

separated atoms (mA + nB) at large distances and therefore is a negative quantity.

The excess energy E_{exc} of a A_mB_n is defined as follows[24]

$$E_{exc}(A_mB_n) = E(A_mB_n) - m\epsilon_b^A - n\epsilon_b^B \qquad (13)$$

where $\epsilon_b^{A,B}$ are the bulk energies of A and B atoms. E_{exc} represents the excess energy of the cluster A_mB_n with respect to m A atoms and n B atoms in the bulk solid. Its definition recalls the definition of surface energy (even though in clusters there may be positive volume contributions to the excess energy due to strain[5]), and therefore, one could expect that (for pure clusters) E_{exc} approximately scales as the number of surface atoms (i.e., as $N^{2/3}$ for large clusters). For this reason, the quantity $\Delta = E_{exc}/N^{2/3}$ is often calculated.[213] In nanoalloys, mixing may also give volume contributions (either negative or positive) to the excess energy. Low values of E_{exc} as a function of composition (for fixed size) indicate the most stable clusters. An example of the behavior of E_{exc} for Cu−Ag and Ni−Ag clusters of fixed size and varying composition is given in Figure 15. There, energies of putative global minima were used as $E(A_mB_n)$.

However, since metals with larger cohesive energy tend to give pure clusters with higher excess energy, E_{exc} may be a somewhat biased index. For this reason, it may be preferable to use E^*_{exc}, defined as follows

$$E^*_{exc}(A_mB_n) = E(A_mB_n) - m\frac{E(A_N)}{N} - n\frac{E(B_N)}{N} \qquad (14)$$

i.e., subtracting from the energy of the binary cluster the appropriate fraction of the configurational energy of pure reference clusters of the same size instead of the bulk cohesive energy. In this way, E^*_{exc} is unbiased, being zero for pure clusters. A negative value of E^*_{exc} indicates in general that mixing is favorable. In principle, there are many choices for the pure reference clusters to be used in the definition of E^*_{exc}. One possibility is to choose global minimum structures for the pure clusters, as in the case of the Cu−Ag and Ni−Ag clusters of Figure 15. There, also the energies of the A_mB_n clusters were related to global

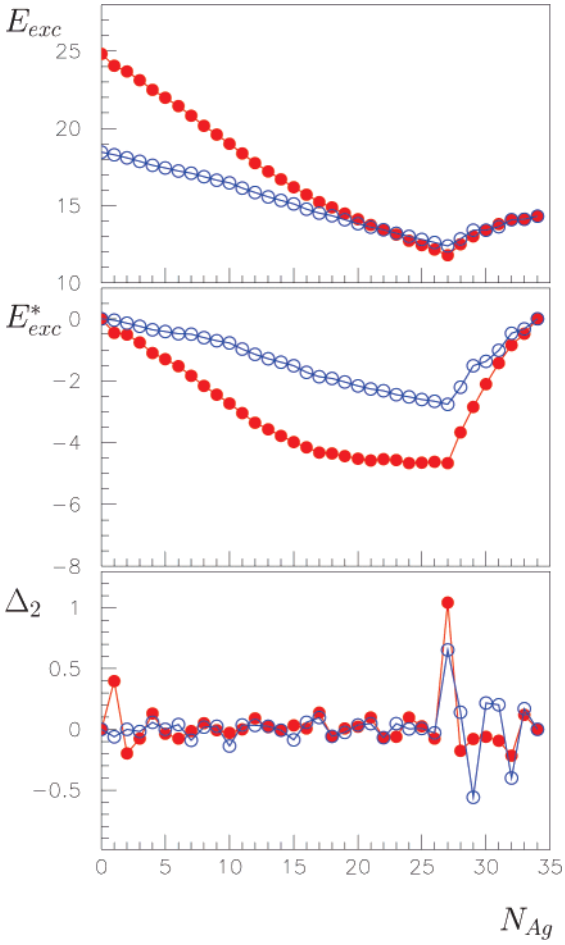

Figure 15. E_{exc}, E^*_{exc}, and Δ_2 for Ni−Ag (full circles) and Cu−Ag (open circles) clusters of 34 atoms as a function of composition (N_{Ag} is the number of Ag atoms in the cluster) after global optimization of the clusters within the potential model of eq 7.[24] All energies are in eV. The minimum of E_{exc} and E^*_{exc} and the maximum of Δ_2 single out a composition of special stability, corresponding to the perfect core−shell polyicosahedra $Ag_{27}Ni_7$ and $Ag_{27}Cu_7$ (see sections 5.1 and 5.3).

minimum structures. Within this choice, E^*_{exc} compares the best A_mB_n clusters with the best A_N and B_N clusters without any restriction on their structure.

The quantities defined so far compare two-element clusters to pure reference systems. On the other hand, an index comparing the stability of binary clusters of nearby compositions may be useful. This index is the second difference in the energy Δ_2, which is defined by analogy to the corresponding quantity for pure clusters. For pure clusters, Δ_2 usually compares sizes differing by one atom. In nanoalloys Δ_2 can be defined for fixed size and variable composition

$$\Delta_2(A_mB_n) = E(A_{m+1}B_{n-1}) + E(A_{m-1}B_{n+1}) - 2E(A_mB_n) \qquad (15)$$

Clusters with high relative stability correspond to peaks in Δ_2. An example of the behavior of Δ_2 for Ni−Ag and Cu−Ag clusters is given in Figure 15, where global minimum structures are compared.

Evaluation of E_{exc}, E^*_{exc}, and Δ_2 only requires calculation of total configurational energies of binary clusters and reference systems. These quantities can be calculated within semiempirical potential models (both two-body and many-body) within DFT and other ab initio schemes.

An important characteristic of two-component systems is the propensity of the constituent elements to mix or segregate. To characterize this propensity, one needs a quantitative measure. This is given by the mixing energy E_{mix} as introduced by Jellinek and Krissinel.[14,15] At variance with indexes based on counting nearest-neighbor bonds, E_{mix} is applicable to systems described by either pairwise-additive or many-body potentials, which may be short or long range. E_{mix} for a cluster A_mB_n in a given configuration is given by

$$E_{mix} = E(A_mB_n) - [E(A_m/A_mA_n) + E(B_n/B_mB_n)] \quad (16)$$

where $E(A_m/A_mA_n)$ is the energy of the A_m subcluster in the A_mA_n cluster and $E(B_n/B_mB_n)$ is the energy of the B_n subcluster in the B_mB_n cluster. In eq 16 the one-component A_mA_n and B_mB_n clusters have the same configuration as A_mB_n, and the configurations of the A_m and B_n subclusters are the same in A_mB_n, A_mA_n, and B_mB_n. Since

$$E(A_mB_n) = E(A_m/A_mB_n) + E(B_n/A_mB_n) \quad (17)$$

where $E(A_m/A_mB_n)$ and $E(B_n/A_mB_n)$ are the energies of the A_m and B_n subclusters in the A_mB_n cluster, the mixing energy can be expressed as

$$E_{mix} = [E(A_m/A_mB_n) - E(A_m/A_mA_n)] + [E(B_n/A_mB_n) - E(B_n/B_mB_n)] \quad (18)$$

E_{mix} is, therefore, the total change in energy experienced by the A_m and B_n subclusters (or, ultimately, their individual atoms) when they are removed from the one-component A_mA_n and B_mB_n clusters, respectively, and brought together to form the A_mB_n cluster. For eqs 16−18 to be meaningful, the energy of a part of a cluster (subcluster) has to be well defined. Of course, this condition is satisfied if the energy of each atom in a cluster is well defined, which is indeed the case not only for the pairwise-additive but also all the many-body potentials introduced in the literature. It is clear that for pairwise-additive potentials that extend only to the first neighbors the definition of E_{mix} becomes equivalent (proportional) to the number of bonds between first-neighbor atoms of unlike type. The (global) mixing coefficient M can be defined as the percentage of the mixing energy in the total configurational energy

$$M = \frac{E_{mix}}{E} \cdot 100\% \quad (19)$$

The mixing coefficient plays a central role in introducing hierarchical order in the very large manifolds of possible structural forms of alloy (more generally, mixed) clusters. As discussed in refs 14 and 15 these manifolds can be subdivided into classes of structures defined by four fixed descriptors: the cluster size, its isomeric form, its composition, and the type of its central (or most coordinated) atom. Within each such class, the energy ordering of the homotops is governed, strictly or globally, by the mixing coefficient. This is illustrated in Figure 16 for four classes of Ni_6Al_7. Two of these correspond to the (nearly ideal) icosahedral (ico) isomer and the other two to an isomer obtained by placing a surface atom of the ico over one of its faces. For each isomer, one of the classes contains the homotops with Ni in the center and the other with Al in the center. In the two classes corresponding to the ico isomer, the gaps between the energies of the neighboring homotops are relatively large,

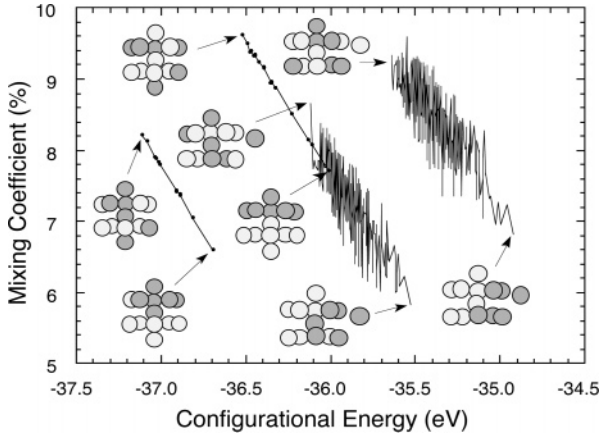

Figure 16. Functional relationship between the mixing coefficient, eq 19, and the equilibrium configurational energy of the homotops of four structural classes corresponding to the first two geometrical isomers of Ni_6Al_7[14,15] (see the text for details). Ni is represented by dark spheres; Al is depicted by light spheres. The clusters shown are the homotopic structures of the highest and lowest configurational energy in each class. (Reprinted from ref 14, Copyright 1999, with kind permission of Springer Science and Business Media.)

and the energy ordering of these homotops is defined strictly by the mixing coefficient; the dependence is essentially linear. The two classes corresponding to the other isomer also exhibit a nearly linear dependence of the homotop energies on the mixing coefficient, but this dependence holds in a global sense. The local "violations" in the ordering of the neighboring homotops (oscillations in the corresponding graphs of Figure 16) are caused by the structural relaxations of these homotops; although small, these relaxations are accompanied by energy changes that are comparable to or larger than the small energy gaps between the unrelaxed neighboring homotops.

5. Structural, Optical, and Magnetic Properties of Nanoalloys

Here we will consider specific examples of bimetallic nanoalloys from across the periodic table. As there are on the order of 80 metallic elements, in principle there are over 3000 possible binary combinations! However, we will limit most of our discussion to nanoalloys formed between the 24 transition-metal elements (the 3d (Ti−Cu), 4d (Zr−Ag), and 5d (Hf−Au) elements), giving rise to 276 possible binary combinations. However, most of the interest and research has tended to concentrate on nanoalloys of the later transition metals (of groups 8−11) and, in particular, those formed between the group 10 metals (Ni, Pd, Pt), between the group 11 metals (Cu, Ag and Au), and the nine group 10−group 11 combinations.

The elemental properties of the atomic radius, bulk cohesive energy (ϵ_{coh}), average surface energy (E_{surf}), and electronegativity for the group 10 and 11 elements are listed in Table 1.

5.1. Nanoalloys of Group 11 (Cu, Ag, Au)

The coinage metals (copper, silver, and gold) can occur naturally as the free metal (though Cu and Ag are also often found as compounds), but they invariably have trace amounts of other noble metals incorporated into the lattice. In the solid state Au mixes with both Cu (making ordered phases) and Ag (making solid solutions), while Cu and Ag present

Table 1. Atomic Radii, Cohesive Energy (ϵ_{coh}), Average Surface Energy (E_{surf}), and Pauling Electronegativity of the Elements Studied[a]

	Ni	Pd	Pt	Cu	Ag	Au
atomic radius [Å]	1.245	1.375	1.385	1.28	1.445	1.44
ϵ_{coh} [eV]	−4.44	−3.89	−5.84	−3.49	−2.95	−3.81
E_{surf} [meVÅ^{-2}]	149	131	159	113.9	78.0	96.8
electronegativity	1.8	2.2	2.2	1.9	1.9	2.4

[a] Surface energies are taken from refs 214 and 215 and 177. Copyright 1977, 1978, and 2005 American Institute of Physics.)

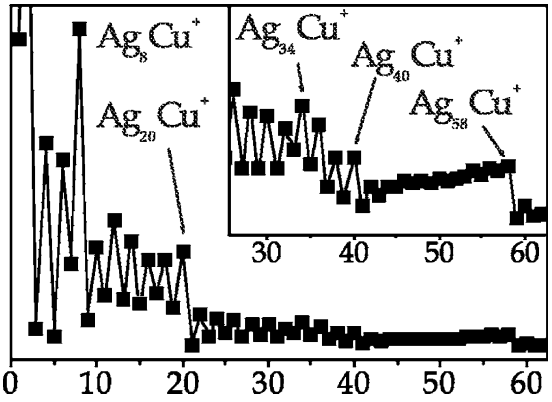

Figure 17. Mass spectra of $Ag_nCu_1^+$. (Reprinted from ref 217, Copyright 2005, with kind permission of Springer Science and Business Media.)

a wide miscibility gap.[216] In the solid state, the pure metals and their alloys have structures based on fcc packing.

5.1.1. Cu–Ag

To date, Cu−Ag clusters have not been extensively studied in experiments. $Ag_{core}Cu_{shell}$ clusters have been generated by radiolysis of solutions containing copper and silver sulfate. This configuration is consistent with the more noble nature of Ag compared with Cu.[95,218] On the other hand, bare Cu−Ag clusters deposited on inert substrates adopt the Cu_{core}-Ag_{shell} arrangement, as expected from the segregation properties of Ag with respect to Cu. In fact, the sequential deposition of Cu and Ag on an amorphous carbon surface[121] produced clusters with Ag on the surface and Cu inside. Finally, the abundances of small free Ag clusters with a single Cu impurity have been determined.[217] The mass spectra of cationic clusters $Ag_nCu_1^+$ have revealed peaks at $n = 8$, 20, 34, 40, and 58 (see Figure 17), in good agreement with the predictions of jellium-model calculations.

Theoretical Studies. Global optimization studies within the Gupta potential model have been performed at sizes 34 and 38 for all compositions.[24,177] These studies have shown that the most stable structures (the ones with lowest Δ and highest Δ_2, see Figure 15) are core−shell polyicosahedra with a Cu core embedded in an Ag shell. For example, at size 34, the most stable cluster is $Ag_{27}Cu_7$, which is the cluster with the largest Cu core without any Cu atom on the surface, as shown in Figure 18. Polyicosahedra are found for many compositions besides those corresponding to the core−shell structures, but the most stable are encountered for compositions allowing formation of perfect core−shell structures. DFT calculations have shown that Cu−Ag clusters of size 34 present large HOMO−LUMO gaps (of about 0.8 eV), indicating electronic shell closure.[24,152] The results of the optimization at sizes 40 and 45 indicate a natural pathway

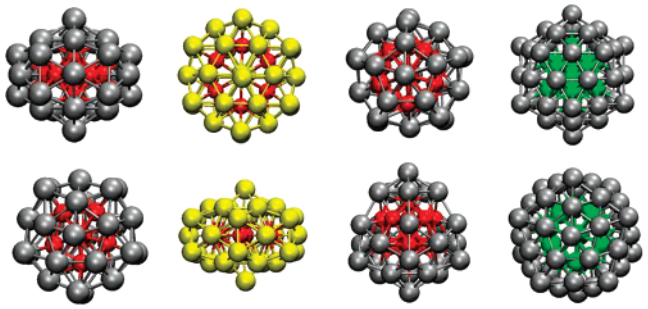

Figure 18. Examples of the four most stable core−shell polyicosahedra. Each cluster is shown from two different perspectives. (From left to right) Fivefold pancake of size 34, capped sixfold pancake of size 40, capped fivefold pancake of size 40, and anti-Mackay icosahedron of size 45. Courtesy of Giulia Rossi.

to formation of the anti-Mackay icosahedron, a polyicosahedron made of 12 elementary icosahedra.[26]

The special stability of core−shell polyicosahedra has been confirmed by DFT calculations[24,152] and originates from the interplay of size mismatch, bond-order−bond length correlation, and the tendency to surface segregation of Ag. In fact, polyicosahedra are compact structures with a high number of nearest-neighbor bonds. In pure-metal polyicosahedra, these bonds are strained: surface bonds are expanded, and internal bonds are compressed. However, the bond order−bond length correlation would require the opposite, namely, that internal bonds are longer than surface bonds. For this reason, pure Ag or Ni polyicosahedra are not favorable at these sizes. However, if we substitute the internal atoms of an Ag polyicosahedron with atoms of smaller size (Cu is smaller than Ag by 12%), surface bonds can contract and internal bonds can be shorter than surface bonds because they are connecting smaller atoms. Thus, strain is greatly reduced, and the structure is stabilized by Ag segregating to the surface. Similar behavior (i.e., segregation of the larger atom to the cluster surface) is found for Ni−Ag and Ni−Au clusters in which the size mismatch is even larger (14%). These classical geometric arguments can be reinforced by specific quantum effects in those clusters which have closed electronic shells.[152] A very nice example of the interplay of geometric and electronic effects has been found by Barcaro et al.[26] at size 40, which is a magic jellium size. Here, depending on composition, the global optimization within the SMATB model singles out three structural families (capped decahedra, capped sixfold pancakes, and capped fivefold pancakes, see Figure 18). The cluster with the lowest excess energy is a perfect core−shell capped fivefold pancake at composition $Ag_{27}Cu_{13}$. However, the DFT reoptimization shows that only those clusters belonging to the family of the capped fivefold pancake are able to close the electronic shells and become the lowest in energy at almost all compositions. The DFT calculations confirm the special stability of $Ag_{27}Cu_{13}$, as predicted by the SMATB model. The SMATB model predicted also a much closer competition between fivefold and sixfold pancakes for Cu−Au at size 40 due to strain relaxation problems in fivefold pancakes. Also, this prediction has been confirmed at the DFT level.[26]

The tendency to surface segregation of Ag has also been confirmed by Jiang et al.,[219] who studied small $Cu_{n-1}Ag$ clusters for $2 \leq n \leq 8$ by DFT methods, finding that the Ag atoms tend to occupy peripheral positions.

Larger Cu−Ag clusters have been studied semianalytically within the tight-binding Ising model on a lattice.[220,221] Segregation isotherms have been determined for cuboctahedral and icosahedral lattices. It has been found that the surface segregation of Ag is strongly enhanced in icosahedral clusters because the expanded intrashell distances in icosahedra favor segregation of species having larger atomic radius.

The growth of larger Cu−Ag clusters has been studied by simulations, as shown later in section 8.3.

5.1.2. Cu–Au

There are three common ordered stoichiometric bulk Cu−Au phases: Cu_3Au and $CuAu_3$ (fcc, $L1_2$ structure) and CuAu (tetragonal, with local fcc packing, $L1_0$ structure).[216] In addition to extensive research on bulk alloy Cu−Au phases, in recent years there have been a large number of experimental and theoretical studies of Cu−Au nanoalloys.

In the early 1990s, Yasuda, Mori, and co-workers used in situ TEM to study the dissolution of copper atoms in nanometer-sized gold clusters by evaporating Cu atoms onto the surface of host Au nanoclusters supported on an amorphous carbon film.[222−224] They found that rapid mixing is observed at room temperature (or even below). This phenomenon will be discussed in section 8. Yasuda and Mori subsequently performed TEM measurements of stoichiometric $(Cu_3Au)_M$ clusters, which were prepared by dual-source electron beam vaporization.[225] They observed that, for larger cluster sizes (9 and 20 nm), annealing results in ordering of the initially generated solid solutions, giving the $L1_2$ structure of bulk Cu_3Au.[225] For smaller clusters (4 nm), however, the solid solution is the most stable phase. The local packing in the Cu−Au clusters was found to be fcc-like, as in the bulk alloy phases.

Stoichiometric Cu−Au nanoalloys were generated by Pauwels, Lievens, and co-workers by laser vaporization of bulk alloy CuAu, Cu_3Au, and $CuAu_3$ targets with the Cu−Au clusters deposited on amorphous carbon and MgO substrates.[119] They carried out electron diffraction and HREM measurements of the 1−4.5 nm-sized Cu−Au clusters and found that the chemical composition of the clusters matches that of the target material, with lattice spacings consistent with those of the bulk alloys. In the case of cluster deposition on amorphous carbon, a number of cluster morphologies were observed, such as cuboctahedra, decahedra (with 5-fold symmetry), and more spherical geometries with no clear morphology, often exhibiting twinning. For clusters deposited on MgO, however, only truncated octahedral morphologies were observed. The electron diffraction and HREM experiments indicate that the stoichiometric $(CuAu)_M$, $(Cu_3Au)_M$, and $(CuAu_3)_M$ clusters all have fcc structures, i.e., the Cu and Au atoms are chemically disordered, forming a solid solution, both on amorphous carbon and MgO substrates. These findings are consistent with the earlier results of Yasuda and Mori for the smaller Cu−Au particles[225] and recent results of Pal et al.[226]

Using a dual-laser vaporization source, which allows generation of Cu−Au clusters of varying compositions, Lievens and co-workers also studied predominantly gold clusters with only one or two atoms of copper present as dopants.[227] Mass spectra showed that magic number (stable) clusters occur at $N = 8$, 18, 20, and 34 atoms, as expected on the basis of the jellium model for small monovalent metals.[4,8] As for pure elemental Cu and Au clusters, an even−odd alternation of stability was observed for the calculated second differences in the binding energy. Their results were interpreted in terms of addition of one or two Cu atoms leading to no change in the geometry of the cluster, with the electronic structure being sufficiently similar for the same (jellium) electronic shell closings (and hence magic numbers) to be observed. On the other hand, for chemically very distinct dopant atoms (e.g., Al, Y, and In), the electronic structure of the gold cluster is altered, leading to different geometries and different electronic shell closures.[227] This work has recently been extended to include Au clusters with one or more 3d transition-metal atom (V, Fe, Mn, Cr, Fe, Co, Zn) dopants.[228] The intense peak observed in the mass spectrum for Au_5^{M+} has been attributed (with the aid of jellium and ab initio MO calculations) to 2D planar structures which are stabilized by the single dopant atom. This approach has subsequently been applied to other doped binary systems.[217]

Recently, Schaak and co-workers developed a novel, multistep "metallurgy in a beaker" procedure for the low-temperature solution synthesis of bimetallic nanoparticles (both ordered intermetallics and alloys) and solid-state materials.[229,230] It has been shown, for example, that Cu−Au nanoparticle aggregates can be used as precursors to synthesize atomically ordered nanocrystals of the intermetallics CuAu, Cu_3Au, and $CuAu_3$.[229,230] In Schaak's experiments, a mixture of PVP-stabilized Cu and Au nanoparticles is formed by the aqueous borohydride reduction of copper acetate followed by reduction of stoichiometric amounts of $HAuCl_4$. Upon aging for several hours, Cu−Au nanoparticle aggregates form. TEM measurements show that the Cu and Au remain segregated at this stage but that there is Cu−Au surface contact. This has been confirmed by EDX, XRD, and electron diffraction measurements,[229] which also reveal that while the Au nanoparticles are crystalline, the Cu particles appear to be amorphous.

The Cu−Au aggregates are then collected as a powder by centrifugation. Heating the dried powder at 50−500 °C for 2−12 h, under flowing argon, followed by annealing at 200−300 °C leads to stoichiometric, atomically ordered (as confirmed by XRD) nanocrystals of CuAu, Cu_3Au, and $CuAu_3$ as well as an ordered CuAu−II superlattice phase.[230] Detailed temperature-dependent studies have shown that for Cu:Au = 1:1 diffusion of Cu into Au occurs at temperatures below 175 °C, initially forming the solid solution Cu_xAu_{1-x}, with nucleation of ordered CuAu starting at 200 °C. For Cu:Au = 3:1, again Cu diffusion is followed by CuAu nucleation at 200 °C, with ordered Cu_3Au nucleation commencing (following further Cu diffusion) at 300 °C.[229] For both the CuAu and Cu_3Au nanocrystals, further heating to 400 °C leads to an order−disorder transition, yielding solid solutions, which is consistent with phase transitions in bulk Cu−Au systems.[231]

Schaak and colleagues have also shown that the CuAu and Cu_3Au nanocrystals can be redispersed as colloidal atomically ordered nanoparticles by sonication in ethanol.[229] Visible absorption spectra have been obtained for the precursor particles and at various stages of the processing in order to monitor the degree of mixing. Schaak stated that use of precursor nanoparticles, which are composed of zerovalent metals, modulated at the nanoscale, means that solid−solid diffusion is not rate limiting, so low reaction temperatures can be adopted. The avoidance of high-temperature annealing prevents sintering, so that relatively

small nanocrystals can be redispersed into solution for high-volume catalytic and other applications.[229] The methodology has been extended to other binary systems to prepare the intermetallic compounds $FePt_3$, CoPt, CuPt, and Cu_3Pt and the alloys Ag−Pt, Au−Pd, and Ni−Pt, either as discrete colloidal nanoparticles or as bulk solids or thin films.[230] In some cases, the solids produced in this way have improved properties compared with those synthesized by conventional means; for example, films of CuAu have been generated with resistivities 1−2 orders of magnitude higher than in bulk CuAu; $FePt_3$ has been shown to be a room-temperature ferromagnet with a coercivity (8000 Oe at 10 K) which compares favorably with other Fe−Pt nanomaterials.[230]

There is considerable interest in the process of selective dealloying of bulk alloys and nanoalloys for formation of nanoporous metals for catalytic or optoelectronic applications.[232] In selective corrosion, the most electrochemically active metal is preferentially dissolved away, leaving a nanoporous structure which is predominantly composed of the more noble metal.[233] Mattei et al. have shown that chemical selective dealloying of Cu−Au nanoparticles (generated by ion implantation in silica) by thermal annealing in air, as expected, extracts the more electrochemically active Cu, initially as Cu_2O.[234] Prolonged annealing results in the extraction of all the Cu, forming the thermodynamically most stable oxide CuO. In contrast, irradiation by Ne^+ ions of energy 190 keV leads to preferential loss of Au atoms (perhaps due to a lower vacancy formation energy for Au than Cu), resulting in nanoporous Cu particles surrounded by small "satellite" Au clusters.[234] This may also be aided by the tendency for Au to segregate to the surface and Cu to the core of medium-large clusters.[25,177,197,235−237] Similar results (i.e., selective removal of Au) have been observed in the ion bombardment of Ag−Au nanoalloys.[234]

Theoretical Studies. López and collaborators concluded, based on MD simulations (using a many-body Gupta-type potential) of the melting transitions of 13- and 14-atom Cu, Au, and Cu−Au clusters, that the bimetallic clusters resemble copper clusters more closely than gold ones, dynamically as well as structurally.[238] Gold clusters, for example, only exhibit a single stage of melting, whereas pure copper and alloy clusters display two stages.

Pauwels, Lievens et al. perfomed Monte Carlo (MC) simulations on free $(Cu_3Au)_M$ clusters[119] using a potential based on the second moment tight binding approximation.[239] The structures studied were isolated truncated octahedral clusters with 456 and 786 atoms and a "spherical" cluster of 959 atoms. The MC simulations predict that these clusters are not ordered (i.e., they do not have the $L1_2$ structure of ordered Cu_3Au throughout) but not completely homogeneous. In fact, the core is slightly deficient in Au and does exhibit $L1_2$ ordering, while the mantle is a Au-rich solid solution. (The terms "Au rich" and "Au deficient" being relative to a homogeneous Cu_3Au distribution.) The core is predicted to be fully ordered at 300 K, undergoing a second-order order−disorder transition at around 600 K.[119] These authors also found that substrate-induced strain (due to cluster−substrate lattice mismatch) can lead to destruction of the core order. Lievens and co-workers presented a detailed discussion of possible reasons why their MC simulations disagree with the experimental results (both their own and those of Yasuda and Mori[225]), where there appears to be no evidence for core ordering and segregation of excess Au to the mantle.[119] It was pointed out that experimentally the Cu−Au clusters are not generated in thermodynamic equilibrium, being cooled rapidly by the He carrier gas, which may lead to formation of metastable solid solutions. The process of cluster deposition, even at relatively low impact energies, may lead to cluster rearrangement, and structural/ordering changes may be induced by interactions with the substrate (especially in the case of MgO). The sizes of the clusters are also relevant in that the MC simulations are generally performed on quite small clusters (with diameters of up to 3 or 4 nm), and many of the experiments have dealt with larger clusters (with diameters of upward of 4 nm). Finally, application of a potential energy function, which was parametrized by fitting experimental properties of the bulk elements and alloys, to study finite alloy particles is questioned.[119]

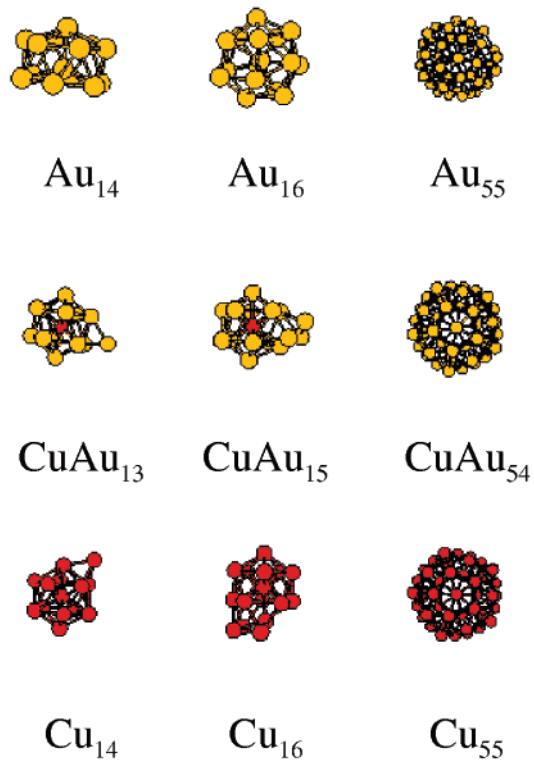

Figure 19. Examples of changes in structure induced by doping of a single copper atom into a gold cluster: (top row) Au_N, (middle row) $CuAu_{N-1}$, (bottom row) Cu_N (dark atoms, Cu; light atoms, Au). (Reprinted with permission from ref 25. Copyright 2002 American Institute of Physics.)

Using the Gupta many-body potential, as implemented by Cleri and Rosato,[161] combined with a GA search method,[167] Johnston and co-workers made a study of stoichiometric nanoalloys with the compositions of the common bulk Cu−Au alloy phases: $(Cu_3Au)_M$, $(CuAu)_M$, and $(CuAu_3)_M$, comparing them with pure Cu and Au clusters.[25] Pure copper clusters were found to adopt regular, symmetrical structures based on icosahedral packing, while gold clusters showed a greater tendency toward amorphous structures, as found previously by Garzón et al.[240] As shown in Figure 19, in many cases (e.g., for 14, 16, and 55 atoms) replacement of a single Au atom by Cu was found to change the GM structure to that of the pure Cu cluster, in agreement with the study by López et al.[238] For the stoichiometric nanoalloys, the lowest energy structures found were generally based on icosahedral packing. The $(CuAu)_M$ and $(CuAu_3)_M$ clusters tend to have layered arrangements of Cu and Au atoms, whereas the Cu and Au atoms are noticeably more mixed in the $(Cu_3Au)_M$ clusters. When layered structures are formed

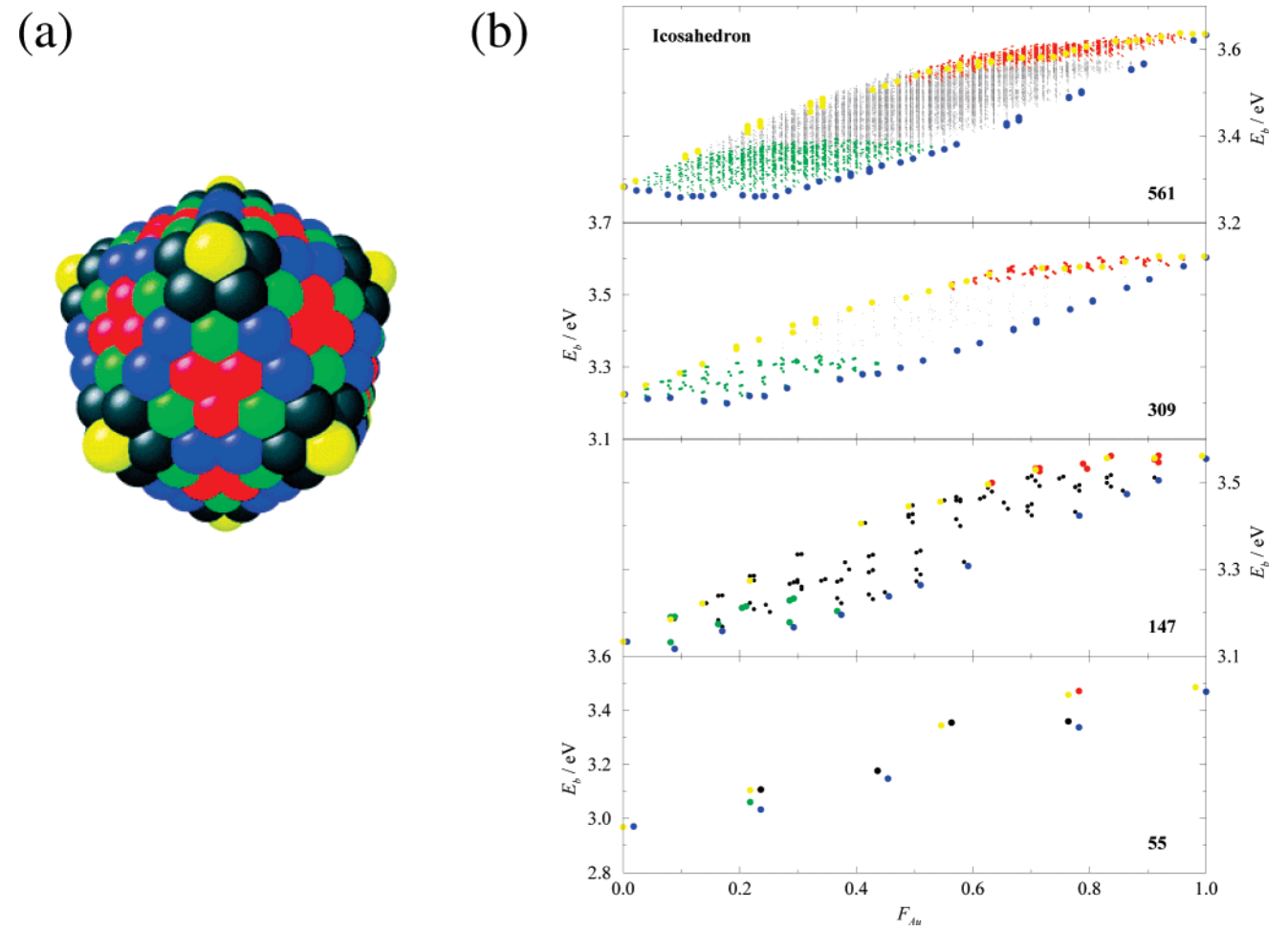

Figure 20. (a) Subshells (sets of symmetry-equivalent atoms, indicated by different colors) in the outer shell of a 5-shell (561-atom) icosahedral cluster. (b) Plot of binding energy (E_b) vs the fraction of gold atoms (F_{Au}) for icosahedral Cu−Au clusters with 55, 147, 309, and 561 atoms. Key: red = Au at surface; green = Cu at surface; blue = Cu surface and Au core; yellow = Au surface and Cu core. (From ref 236. Reproduced by permission of The Royal Society of Chemistry.)

the surfaces of the clusters are comprised of mainly gold atoms with most of the copper atoms being in bulk-like positions. In the icosahedron-based structures, the central atom is generally a copper atom. The predicted tendency to Au surface segregation, which is in agreement with MD simulations on Cu−Au nanoalloys (using the Sutton−Chen many-body potential[158]) by Rodríguez-López et al.[197,237] is understandable in terms of the lower surface energy of Au compared with Cu and the smaller size of the Cu atoms. However, the greater cohesive energy of Au compared with Cu opposes this segregation as it should favor Au in the core.

Wilson and Johnston subsequently carried out energy calculations on 1−5-shell icosahedral and cuboctahedral Cu−Au nanoalloys (i.e., with up to 561 atoms) of varying composition within the constraints that the atoms in each subshell (where a subshell is defined as a set of symmetry-equivalent atoms, as shown in Figure 20a) were either all Cu or all Au, with the interatomic interactions again modeled by the Gupta many-body potential.[236] It was found that for each composition the lowest energy homotops tend to have predominantly Au atoms on the surface and Cu atoms in the core (see Figure 20b). Again, this was explained in terms of the lower surface energy of Au compared to Cu. More detailed considerations of mixing and segregation were obtained by taking into account the relative strength of Cu−Cu, Cu−Au, and Au−Au bonding interactions and, in the case of icosahedral clusters, the relief of bulk strain that is possible upon substituting the smaller Cu atoms for Au in the compressed core.

Johnston and co-workers subsequently reported detailed studies of Cu−Au clusters of varying compositions and nuclearities.[19,117,241] In a detailed study of 34-atom Cu−Au clusters, disordered structures were observed for Cu-rich compositions, where the driving force appears to be maximization of Cu−Au bonds, which overcomes the normal tendency for Au atoms to segregate to the surface.[177] A number of polyicosahedral geometries were also observed, particularly for Au-rich compositions, including Cu_4Au_{30} (incomplete 6-fold pancake) and the perfect core−shell clusters Cu_6Au_{28} and Cu_7Au_{27} (5-fold pancake). For 38-atom clusters, truncated octahedra dominate for Cu-rich compositions (Au_{38} also has this geometry), polyicosahedral 6-fold pancakes for Au-rich compositions, and a number of decahedral and disordered structures.[177,241] These results are in general agreement with a recent detailed study by Hsu and Lai, who used a hybrid GA-basin-hopping search algorithm, with the same Gupta potential as Johnston and co-workers, to study 38-atom Cu−Au nanoalloys.[242]

Fernández et al. recently performed DFT calculations on $(CuAu)_N$ clusters, with $N = 5-22$, by reminimizing geometries generated as low-energy isomers by a GA search employing a Gupta potential.[153] Although the exact ordering of the homotops was not exactly the same for the DFT and

Gupta potential calculations, the general stability of icosahedral structures was confirmed.

5.1.3. Ag–Au

In the bulk, silver and gold form solid solutions for all compositions, i.e., there are no ordered phases. All of the alloys have fcc structures (cubic close packing), as for the pure Ag and Au solids. The mixing of Ag and Au in the bulk is weakly exothermic, and there is believed to be very little surface segregation in bulk Ag−Au alloys.

There have been many experimental studies of Ag−Au bimetallic particles, dating back to the 1960s.[54,61,62,74,95,243−263] Most of the experimental interest has centered on the optical properties of Ag−Au nanoalloys; for example, how the shape and frequency of the plasmon resonance of Ag−Au clusters varies with composition and the degree of segregation or mixing.[54] In this regard, Wilcoxon and Provencio postulated that composition- and segregation-dependent fine tuning of the color of Ag−Au nanoalloys could lead to their use as taggant materials (metal inks) with potential applications in anti-counterfeiting measures.[62] In addition to these optical applications, there is also interest in improving the selectivity of Ag nanoparticle catalysts for alkene epoxidation by alloying with Au.[264,265]

Core−shell ($Ag_{core}Au_{shell}$ and $Au_{core}Ag_{shell}$) particles can be generated by chemical or electrochemical deposition of one metal onto a preformed cluster of the other.[61,62,260,266] Optical measurements on these core−shell clusters have shown that the surface plasmons of the bimetallic particles are broad and complex. On the other hand, intermixed Ag−Au clusters (generated, for example, by laser vaporization of rods made of Ag−Au alloys or by co-reduction of a mixed solution of Ag and Au salts) show a single plasmon resonance, as for the pure metals. For intermixed clusters of fixed size, experiment and theory agree that the plasmon frequency varies smoothly with composition between that of the pure Ag and pure Au clusters: frequency increasing with increasing Ag content.[54,57,74,244,249,251,267,268] (The strong nonlinear evolution of the plasmon frequency of Ag−Au particles with Ag content observed by Teo et al.[245] has been attributed to either differences in degree of mixing−segregation or in the stacking structure.[74]) Alloyed Ag−Au clusters also exhibit increasing plasmon frequency with decreasing size, with the rate of increase of frequency being intermediate between that of pure Au (large) and pure Ag (small) clusters.[74,251,267] In fact, the UV−vis spectrum is generally used to distinguish between core−shell and intermixed Ag−Au clusters.[62] Even though a cluster is "intermixed", there may still be some degree of surface segregation. It should also be noted that this method of distinguishing between intermixed and segregated Ag−Au nanoparticles cannot be applied to small nanoparticles (below 2 nm diameter) because they exhibit no plasmon resonance.

In 1998, Han et al. reported formation of 4 nm-diameter dodecanethiol-derivatized Ag−Au nanoalloys by reduction of a solution containing a mixture of Ag and Au salts.[248] A single plasmon resonance was observed, and the plasmon frequency was found to vary linearly with Ag/Au composition, which is generally indicative of homogeneous mixing. However, surface-sensitive probes (XPS and FT-IR spectroscopy) indicated that the surfaces of the particles were actually enriched in Ag. More recently, Srnová-Sloufová et al. found a degree of segregation of Ag to the surface of Ag−Au particles,[259] though Santra et al. (on the basis of their experiments involving deposition of Au onto Ag particles preformed on a TiO_2 (110) surface) postulate formation of intermixed particles.[258] Hodak et al. have shown that kinetically stable $Ag_{core}Au_{shell}$ and $Au_{core}Ag_{shell}$ particles can be converted into intermixed particles by laser irradiation.[61] Chen and Yeh also showed that bimetallic Ag−Au nanoparticles can be generated by laser irradiation of mixtures of colloidal Ag and Au particles.[252]

Both $Ag_{core}Au_{shell}$ and $Au_{core}Ag_{shell}$ core−shell structures (with diameters of up to around 7 nm) have been studied by Wilcoxon and Provencio.[62] The core−shell particles are generated by metal hydride reduction of Ag− or Au− organometallic complexes in a stirred solution of thiol-passivated "seed" nanocrystals of the other metal. With the aid of size-exclusion chromatography and TEM, it was shown that deposition occurs in a uniform manner, only on the seed nanocrystals, thereby preserving the monodispersity of the parent sample. In $Au_{core}Ag_{shell}$, increasing the thickness of the Ag shell leads to an increase in the plasmon frequency, with the peak becoming narrower and more symmetrical, as for pure Ag nanoparticles. Hubenthal et al. investigated the optical properties of intermixed Ag−Au and $Au_{core}Ag_{shell}$ particles, finding that annealing of the core−shell particles leads to mixing and allows the surface plasmon frequency to be tuned between 2.2 and 2.6 eV.[269]

Recently, Benten et al.[270] studied the optical properties of Ag−Au nanoparticles grown on alumina substrates. In their experiment, the STM tip injects electrons into selected clusters to excite Mie plasmons. Photons emitted due to the radiative decay of the plasmons are analyzed according to their wavelength. From the position of the peaks information about the chemical ordering in the nanoparticles is inferred. Benten et al. performed three different kinds of deposition on the alumina substrate: co-deposition of Ag and Au to form intermixed particles, deposition of pure Au followed by pure Ag to form $Au_{core}Ag_{shell}$ particles, and deposition of Ag followed by Au to form $Ag_{core}Au_{shell}$ particles. In the case of intermixed particles, the photoemission spectra showed a single peak, whose position shifted from the resonance wavelength of pure Au to that of pure Ag at increasing Ag fraction (Figure 21a). In the case of core−shell particles, two peaks were detected (Figure 21b), which were attributed to the separate plasmon resonances of the metals in the core and in the shell. From the separation between the two peaks, Benten et al. inferred a higher degree of interdiffusion in the case of $Ag_{core}Au_{shell}$ particles, in agreement with the stronger tendency of Au to incorporate into Ag compared to the reverse (as confirmed by several theoretical studies, see below).

Experimentally, it has proved challenging to obtain detailed internal structural information for bimetallic Ag−Au nanoparticles. Due to the small difference in the lattice constants of Ag and Au, direct lattice imaging using high-resolution electron microscopy is not very informative. For particles of 10 nm diameter and above, chemically sensitive diffraction contrast can be used to determine the elemental separation inside the bimetallic particles by making use of the difference in the extinction distances in Ag and Au metals.[61,250] For small nanoparticles with sizes below 5 nm, conventional TEM has also failed because of difficulties in distinguishing the chemical contrast from strain contrast.[62] Li and co-workers recently exploited the HAADF-STEM imaging technique to reveal successfully the internal structure

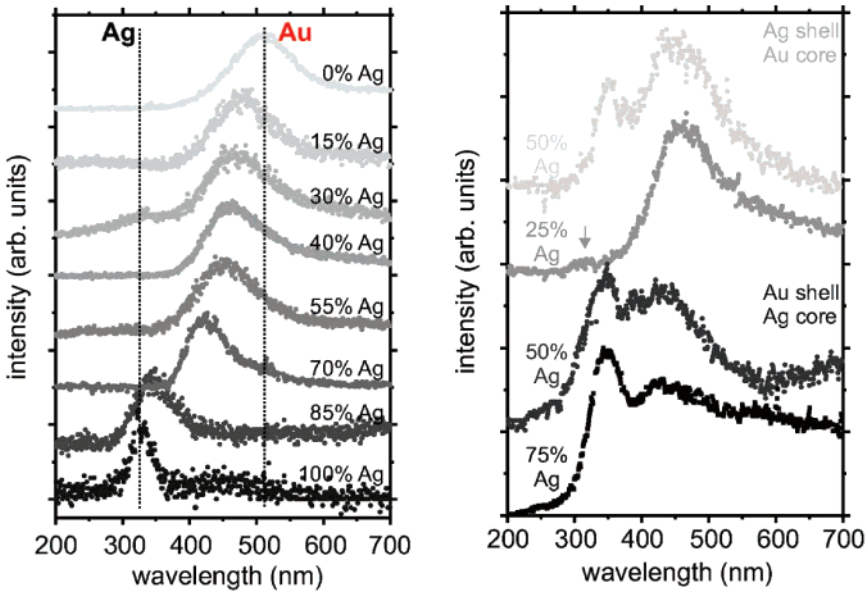

Figure 21. Photon emission spectra of Au−Ag nanoparticles grown on alumina substrates. (Left) Intermixed clusters of different compositions. (Right) $Au_{core}Ag_{shell}$ (upper two curves) and $Ag_{core}Au_{shell}$ (lower two curves). The Ag content is specified in the figures. (Reprinted with permission from ref 270. Copyright 2005 American Physical Society.)

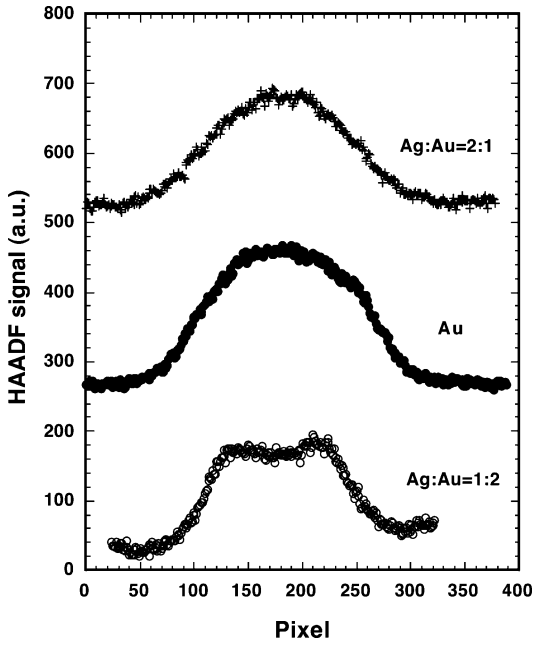

Figure 22. Comparison of HAADF-STEM Z-contrast line profiles for 4 nm pure Au and (postulated) $Ag_{core}Au_{shell}$ nanoparticles with Ag/Au compositions of 1:2 and 2:1. The *x* scale is in pixels, with 73 pixels corresponding to 4 nm, and the curves have been shifted vertically for clarity. For an Ag/Au ratio of 1:2 the experimental intensity contrast is consistent with a $Ag_{core}Au_{shell}$ structure, but for an Ag/Au ratio of 2:1 the maximum in intensity at the center is not consistent with the expected $Ag_{core}Au_{shell}$ structure, perhaps indicating intermixing or even inverted core−shell structure. (Reprinted with permission from ref 262. Copyright 2005 American Institute of Physics.)

of 4 nm bimetallic Ag−Au nanoparticles[261−263] (see Figure 22). This technique utilizes the large difference in atomic number of Ag (47) and Au (79) to probe the composition modulation within the particles. With the aid of simple geometric simulations, the internal core−shell structure of small Ag−Au nanoparticles has been unambiguously revealed. Li's results also confirm not only the existence but also the long-term stability of the nanosized $Ag_{core}Au_{shell}$ particles when the overcoated Au shell is thick. However, when the Au shell is thin, the Au atoms initially deposited in the outer shell appear to be unstable with respect to replacement by Ag[261−263] (see Figure 22).

Belloni and co-workers used γ-ray radiolysis to generate core−shell Ag−Au nanoparticles.[95] Mixed solutions of $KAuCl_4$ and Ag_2SO_4 irradiated in the presence of PVA at a dose rate of 3.8 kGy h^{-1} generate Au-rich $Au_{core}Ag_{shell}$ particles (as indicated by X-ray microanalysis), which is consistent with Au being the more noble metal. On increasing the dose rate, the plasmon edge moves from 520 (as for pure Au clusters) to 440 nm (pure Ag clusters have their plasmon around 400 nm), indicating a thickening Ag shell.[95] The same group has shown that in the presence of cyanide ions the inverse ($Ag_{core}Au_{shell}$) core−shell particles are formed, showing that Au is less noble than Ag in the presence of CN^-.[271] The plasmon edge thus starts off close to that of pure Ag clusters and is red shifted with increasing dosage (i.e., increasing Au reduction and deposition). At high γ-ray dose rates (35 kGy h^{-1}), the shape of the plasmon spectrum does not change with dose (though the intensity increases). Similar results are obtained with electron beam radiation at dose rates of 7.9×10^3 kGy h^{-1}. At these higher reduction rates, the Ag−Au particles are intermixed and the plasmon resonance is now centered (at 480 nm) between the limits of the pure Ag and Au clusters.[97] In certain cases, ordered Au_3Ag superlattice peaks have also been observed by single-particle X-ray diffraction.[97]

It should also be noted that, as far back as 1964, Morriss and Collins reported the preparation of onion-like Au−Ag−Au hydrosols (with an average diameter of 40 nm) by sequential deposition of the metals.[243] TEM images of the colloid show alternating dark−bright−dark bands, corresponding to the Au−Ag−Au ordering.

Another class of nanoalloys—termed "colloidal nanoalloys"—have been synthesized by Kiely et al., who generated separate solutions of C_{10}-thiol-stabilized Ag and Au nanoparticles in toluene and subsequently mixed and evaporated them onto a carbon-coated copper mesh.[272] For approximately equal concentrations of Ag and Au particles of similar size (4−5

nm), random alloy $(Ag_N)(Au_M)$ structures form. For Au:Ag ratios > 10:1, ordered superlattice structures were observed. TEM and EDX measurements showed an ordered AB_2-type phase (analogous to the AlB_2 structure) consisting of 8 nm Au particles (type A) and 5 nm Ag particles (type B). This has been described as an ordered colloidal alloy, where the alloying is of the colloidal particles and hence on the mesoscale not at the atomic scale. It has been noted that the ordered phase may be stabilized by electrostatic or polarization effects via electron-transfer tunneling from the Ag particles to the Au particles (the work functions of bulk Ag and Au are 4.5 and 5.2 eV, respectively[273]), which are only separated by a 1.5 nm thick dielectric layer (the C_{10}−thiol ligands).[272]

Theoretical Studies. Considering thermodynamic contributions to Ag−Au cluster stability, first, the M−M bond lengths in elemental Ag (2.90 Å) and Au (2.88 Å) are very similar, so there will be no strain-induced driving force toward segregation. However, the surface energy of Ag (78 meV $Å^{-2}$) is less than that of Au (97 meV $Å^{-2}$), which favors surface enrichment by Ag. The cohesive energy of Au (3.81 eV/atom) is greater than that of Ag (2.95 eV/atom). This coupled with the weak exothermic enthalpies of formation of the bulk Ag−Au alloys indicates that the metal−metal bond strengths are in the order Au−Au > Ag−Au > Ag−Ag, favoring core enrichment of Au. These simple considerations are in agreement with the results of calculations by Johnston, Ferrando, and co-workers.

From Gupta potential calculations,[212,274] Ag−Au clusters have been found to present $Au_{core}Ag_{shell}$ segregation. Recent DFT studies by Zhao and Zheng,[275] who considered Au_m-Ag_n with $2 \leq m + n \leq 8$, however, indicate that in very small clusters Au atoms have a tendency to occupy peripheral sites. Similar findings have been reported by Chen and Johnston based on DFT calculations on Ag_3Au_{10} clusters.[58] Thirty-four-atom Ag−Au clusters present a considerable number of disordered structures. For Au-rich and intermediate compositions, these are either distorted fcc or defect decahedra. From $Ag_{30}Au_4$ to $Ag_{23}Au_{11}$ there is a series of polyicosahedral structures, including defect "6-fold pancakes". For 38-atom Ag−Au clusters, complete 6-fold pancakes are identified in the range from $Ag_{33}Au_5$ to Ag_{26}-Au_{12}—the clusters with 6 and 12 Au atoms are predicted to have full D_{6h} symmetry.[212,274] For most other compositions, truncated octahedral (fcc) clusters are predicted. Examples of lowest energy (at the Gupta level) 38-atom Ag−Au clusters, for varying compositions, are shown in Figure 23.[212]

As Au is more electronegative than Ag (Pauling electronegativities are 2.4 (Au) and 1.9 (Ag)), there should be some degree of electron transfer from Ag to the Au atoms. The ionic contribution to the Au−Ag bonding will favor Au−Ag mixing as this increases the number of favorable $Ag(\delta+)$−$Au(\delta-)$ interactions. It should be noted, however, that bulk Ag−Au alloys are solid solutions (randomly mixed, not ordered) for all compositions, which would seem to militate against charge transfer being a dominant factor in the bulk. The contribution of heteropolar (ionic) bonding in Au−Ag alloy clusters has been studied (for small clusters, with up to 20 atoms) by Bonaćić-Koutecký and co-workers, using DFT calculations, who predicted that there should indeed be some degree of electron transfer from Ag to Au atoms.[149,276]

Zhang and Fournier recently modeled 55-atom icosahedral Ag−Au clusters (as well as Cu−Ag and Cu−Au clusters) using a pairwise-additive Morse potential coupled with an ionic term.[163] In the case of Ag−Au and Cu−Au clusters, where there is a significant difference in atomic electronegativities, a 1% increase in cohesive energy was observed on including the ionic term, with the stabilizing effect of charge transfer being greatest near 50/50 compositions. For the Ag−Au clusters, although the surfaces were predicted to be Ag rich (in agreement with previous studies[212,274]), the ionic contribution was observed to drive some of the Au atoms to the surface as it favors surface Ag−Au mixing.[163]

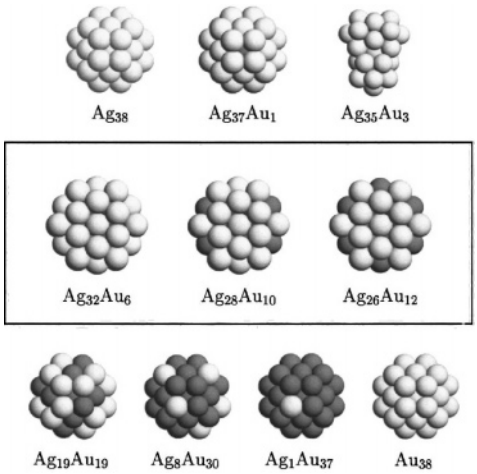

Figure 23. Snapshots from the 38-atom Ag−Au sequence. Light and dark gray spheres correspond to Ag and Au atoms, respectively. In the first row, the first two global minima of the sequence are truncated octahedral structures, while a core−shell disordered structure is located at $Ag_{35}Au_3$. In the box, the cluster $Ag_{32}Au_6$ is the perfect sixfold pancake, and this perfect structure is the best up to $Ag_{26}Au_{12}$. Thereafter, all the global minimum structures are truncated octahedra, with silver atoms preferentially occupying vertex or edge positions. (Reprinted with permission from ref 212. Copyright 2005 American Institute of Physics.)

5.1.4. Cu–Ag–Au

Radiolytic reduction of a solution containing $[AuCl_4]^-$, Ag^+, and Cu^{2+} leads to deposition of first Au, then Ag, then Cu (following the decreasing order of reduction potentials), leading to a trimetallic onion-like layered $Au_{core}Ag_{shell}Cu_{shell}$ nanoparticle. As the γ-ray dose is increased, the plasmon resonance shows that first all Au particles form (λ_{max} (Au) = 520 nm), then the plasmon edge blue shifts as Ag is deposited (λ_{max} (Ag) = 400 nm), and finally it red shifts again as Cu is deposited in the outer layer (λ_{max} (Cu) = 570 nm).[95]

5.2. Nanoalloys of Group 10 (Ni, Pd, Pt)

The bulk metals Ni, Pd, and Pt and their alloys all display fcc packing, with the alloys forming solid solutions at high temperatures and (apart from Pd−Pt) ordered phases (depending on composition) at low temperatures.[216]

5.2.1. Ni–Pd

In contrast to Ni−Pt (see discussion below), Pd is found to segregate to all surfaces in bulk disordered Ni−Pd alloys.[277,278] This is consistent with the higher cohesive energy of Ni and the lower surface energy of Pd. In Ni−Pd nanoalloy particles, these factors, together with the smaller size of Ni, compared with Pd, should favor formation of $Ni_{core}Pd_{shell}$ nanoparticles. However, in the presence of CO

(despite the fact that Pd−CO bonding is stronger than Ni−CO[279]), the opposite segregation is observed; thus, $[Ni_{16}Pd_{16}(CO)_{40}]^{4-}$ and $[Ni_{26}Pd_{20}(CO)_{54}]^{6-}$ have interstitial Pd atoms and predominantly surface Ni atoms.[280] Also, since Pd is more noble than Ni, co-reduction of a solution of Ni(II) and Pd(II) salts is likely to lead to $Pd_{core}Ni_{shell}$ segregation, which is not useful for catalytic applications, where surface Pd is generally required.[281]

Manago et al. reported the generation of Pd-coated Ni particles by electroless plating of Pd ions onto preformed Ni particles.[282] They were subsequently investigated under an H_2 atmosphere using in situ magnetometry and XRD. These particles were found to consist of a ferromagnetic Ni core surrounded by ferromagnetic and paramagnetic Pd. As the deposition was carried out at low temperature, no measurable Ni−Pd mixing was detected. At room temperature, the magnetization in the hydrogen atmosphere showed a steep saturation and a small decrease in the residual magnetization, indicating that the interface magnetic anisotropy was reduced by hydrogenation.[282]

In 1998, Nunomura et al. reported the synthesis of Ni−Pd nanoparticles by refluxing an isopropanol solution of PVP-coated Pd nanoparticles (2.5 nm diameter) with $Ni(OAc)_2$.[283] A range of compositions were generated (as measured by chemical analysis and EDX) from pure Pd to 99 atom % Ni, with sizes up to 4 nm for 0−50 atom % Ni and up to 150 nm for 99 atom % Ni. XPS measurements seem to indicate that the particles are intermixed rather than core−shell in nature, while magnetization measurements reveal that they are superparamagnetic (apart from the very Ni-rich particles, which are ferromagnetic, as for pure Ni clusters).[283]

Raja et al. recently reported formation of 3 nm Ni−Pd colloidal nanoparticles prepared by the polyol reduction pathway[285]—a method previously used by Miyake and co-workers to produce $Pd_{core}Ni_{shell}$ particles.[286] It is not yet know if the particles generated by Raja et al. have core−shell or intermixed structures. Hyeon and co-workers used thermal decomposition of Ni and Pd complexes of the surfactant trioctylphosphine to generate Ni−Pd nanoparticles with various compositions.[281] Combining HRTEM, XRD, and EDX data the particles generated in this way have been characterized as having a $Ni_{core}Pd_{shell}$ configuration, which has been attributed to the lower thermal stability of the Ni−trioctylphosphine complex.

Henry and co-workers reported the generation of 5−7 nm $Ni_{core}Pd_{shell}$ nanoparticles by deposition of Pd (formed by thermal decomposition and H_2 reduction of $Pd(OAc)_2$) on preformed MgO-supported Ni particles (formed by reductive decomposition of Ni(OAc)2).[284] The supported particles were characterized by EDS, XPS, HRTEM, and energy-filtered TEM (which allows the Ni core and Pd shell to be clearly distinguished). An HRTEM image of a $Ni_{core}Pd_{shell}$ nanoparticle is shown in Figure 24. XPS indicated partial oxidation of Ni in the nanoparticles.

Theoretical Studies. Calculations on $Ni_{101}Pd_{100}$ clusters by Zhu and DePristo[287] have predicted that for Ni−Pd clusters, where there is a relatively large size mismatch (10%), a small difference in surface energy and a small exothermic energy of mixing (for Pd compositions of 40% or higher: the mixing is endothermic for <40% Pd[277]), 16 of the Pd atoms lie in bulk positions and there is some bulk and surface Ni−Pd mixing, though the surface is Pd rich. Recent simulations of Ni−Pd clusters using a Gupta potential, coupled with a GA search routine, confirmed the tendency of Pd to segregate to the surface.[288]

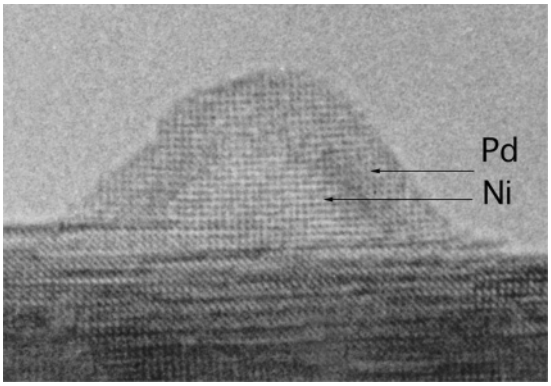

Figure 24. HRTEM image of a supported $Ni_{core}Pd_{shell}$ cluster. (Reprinted with permission from ref 284. Copyright 2005 American Chemical Society.)

A recent theoretical investigation of the magnetic properties of Ni−Pd clusters assumed a $Ni_{core}Pd_{shell}$ configuration for cuboctahedral particles with up to 561 atoms and for variable Ni/Pd compositions.[289] Empirical and ab initio calculations agree that Ni−Pd hybridization leads to an enhancement of the magnetic moments of the Ni atoms, above that of the bulk, as well as (for Ni-rich clusters) a nonzero Pd magnetic moment of $0.2\mu_b$.[289] Comparisons were made with the experimental results of Nunomura et al. for intermixed Ni−Pd particles.[283] Wang et al. also carried out simulations of $Ni_{core}Pd_{shell}$ clusters.[290]

5.2.2. Ni–Pt

Bulk Ni−Pt alloys form fcc solid solutions for all compositions above 950 K. At lower temperatures, depending on composition, a number of ordered phases with fcc local packing are observed: Ni_3Pt and $NiPt_3$ ($L1_2$); NiPt ($L1_0$).[216]

Ni−Pt nanoalloys have been made by radiolytic as well as by other methods.[95,230] Ross and co-workers[291] have shown that Ni−Pt and Co−Pt nanoparticles (of various compositions, with sizes of 2.5−5 nm and truncated octahedral morphologies) exhibit significant surface Pt enrichment, as observed (using LEIS) for polycrystalline Ni−Pt and Co−Pt alloys.

There has been a detailed study of Ni−Pt−carbonyl clusters by Longoni and co-workers.[36,37,292] Examples of Ni−Pt−CO clusters include the following: $[Ni_{38}Pt_6(CO)_{48}H_{6-n}]^{n-}$, where a Pt_6 octahedron is encapsulated within a Ni_{38} octahedron;[292] $[Ni_{24}Pt_{14}(CO)_{44}]^{4-}$ (see Figure 3), where the overall truncated octahedral geometry again consists of a Pt_6 octahedral core surrounded by Ni atoms, but where eight additional Pt atoms cap the faces of the octahedron, occupying the centers of the (111) faces of the $Ni_{24}Pt_8$ truncated octahedron;[37] and $[Ni_{36}Pt_4(CO)_{45}]^{6-}$ and $[Ni_{37}Pt_4(CO)_{46}]^{6-}$, both of which contain tetrahedral Pt_4 cores.[36] These clusters all have Pt cores surrounded by Ni atoms, with the CO molecules mainly bound to the surface Ni atoms. This is consistent with simple ideas (given above) based on cohesive and surface energies but is in contrast to the experimental and simulation results for bare Ni−Pt nanoparticles. The binding energy of CO to Pt is actually greater than Ni−CO binding (e.g., the heats of adsorption of CO on the (111) single-crystal surfaces of Ni and Pt are 111 and 146 kJ mol^{-1}, respectively[279]), so the reversed $Pt_{core}Ni_{shell}$ segregation observed in these Ni−Pt−carbonyl clusters cannot simply

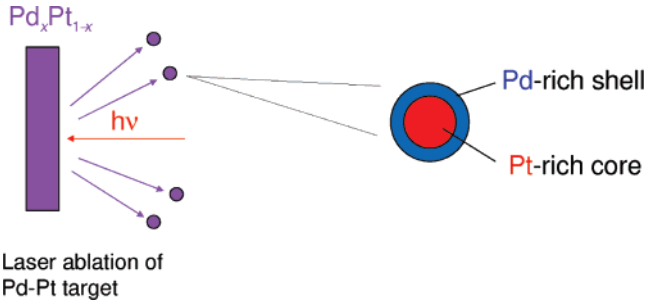

Figure 25. Schematic representation of the formation of Pt_{core}-Pd_{shell} particles by laser ablation of Pd−Pt alloy rods.

be explained in terms of M−CO bond strengths. More theoretical work is therefore required in order to achieve a better understanding of the segregation properties of Ni−Pt and Ni−Pt−CO nanoparticles.

Theoretical Studies. Wang et al. recently carried out MC simulations (based on the MEAM model) of Ni−Pt nanoparticles for two compositions ($Ni_{0.5}Pt_{0.5}$ and $Ni_{0.25}Pt_{0.75}$) and a variety of shapes, for particles with 560−4631 atoms (D = 2.5−5 nm).[293] Some degree of surface segregation of Pt is observed in these calculations with the extent depending on cluster size, composition, and temperature. At 600 K, for example, cuboctahedral particles of composition $Ni_{0.5}Pt_{0.5}$, with more than 2000 atoms, are predicted to undergo an order−disorder transition, resulting in a core−shell structure with a Pt-rich shell surrounding a Pt-deficient core. Segregation in NiPt nanoclusters was also predicted in an earlier tight binding study by Treglia and Ducastelle.[294]

Comparison of the cohesive and surface energies of Ni and Pt (see Table 1) shows that the higher cohesive energy of Pt coupled with the lower surface energy of Ni should actually favor Ni segregation to the surface, contrary to the findings of the experimental work and simulations discussed above.[291,293] It is interesting to note that in bulk disordered fcc Ni−Pt alloys (over a range of compositions), Pt segregates to the (111) and (100) surfaces while Ni segregates to the (110) surface, the latter being accompanied by Ni−Pt−Ni layering.[278,295]

5.2.3. Pd–Pt

Pd−Pt nanoparticles have been extensively studied, primarily because of their importance in catalysis (see section 6). The pure elements and bulk alloy phases exhibit face-centered cubic (fcc) packing of atoms and cubic symmetry ($L1_2$).[216] Bulk Pd−Pt alloys are continuous solid solutions, i.e., structures in which the atoms are randomly mixed, for all compositions.[296] This is consistent with the relatively low enthalpy of formation of $Pd_{0.5}Pt_{0.5}$: −4 kJ mol^{-1}.[296] However, calculations by Rousset et al. indicate that the (100) and (111) surfaces of Pd−Pt alloys show strong surface segregation of Pd.[277] The surface segregation of Pd (especially to more open faces) has been confirmed by a combined voltammetric and LEED/AES study of the (100) and (110) surfaces of bulk Pd−Pt alloys by Watson and Attard.[297]

Renouprez, Rousset, and colleagues performed extensive experimental studies of the structures, compositions, and catalytic activity of Pd−Pt particles generated by the Nd:YAG laser vaporization of rods of bulk Pd−Pt alloys of various compositions (see Figure 25).[141,142] The particles were deposited on either amorphous carbon (for electron microscopy and EDX studies), Suprasil disks (for EXAFS measurements), or high surface area γ-alumina powder for catalytic measurements.

The TEM measurements of Rousset and Renouprez showed that the Pd−Pt particles (which typically have diameters in the range 1−5 nm) mainly have cuboctahedral structures, with fcc packing, as in the bulk alloy phases. EDX measurements showed that the overall compositions of the particles are very similar to those of the alloys used as the laser vaporization target. EXAFS measurements indicated that the Pd−Pt particles are intermixed but that there are more Pt−Pt interactions than expected for a Pd−Pt solid solution. This suggests that a degree of segregation has occurred relative to the bulk alloys. LEIS experiments have shown that the surfaces of these Pd−Pt particles are enriched in Pd, relative to a homogeneous distribution of Pt and Pd atoms, with the relative surface Pd enhancement being largest for low Pd concentrations and larger particles, so that they may be regarded as $Pt_{core}Pd_{shell}$ particles (see Figure 25). It was also found that in the course of the LEIS experiment ion etching occurs with Pd atoms being etched preferentially (the Pd LEIS signal is reduced). This is consistent with there being proportionally more Pd atoms on the surface of the clusters to start with.[141,142]

The results of Renouprez and Rousset are consistent with the work of Fiermans et al., who studied Pd−Pt particles supported on β-zeolites (as hydrocracking catalysts).[298] The particles (with a Pd:Pt ratio of 1:3) were prepared by impregnation of tetraamine metal complexes on H-β-zeolites or cation exchange on NH_4-β-zeolites followed by calcination and reduction at 400 °C. Pd segregation to the surface of the nanoparticles was shown by XPS and Ar^+ sputtering by monitoring the change in intensities of the Pd(3d) and Pt(4d) lines as a function of etching by Ar^+.[298]

In the 1990s, Toshima and co-workers reported the synthesis of Pd−Pt colloids (1.5−5.5 nm) with controllable $Pt_{core}Pd_{shell}$ structure for catalytic applications[299−301] (see section 6). The core−shell segregation was confirmed by EXAFS measurements. The Toshima group has also reported the synthesis of PVP-stabilized inverted ($Pd_{core}Pt_{shell}$) core−shell nanoalloys by preforming the Pd nanoparticles and reducing Pt onto them using sacrificial hydrogen, which was adsorbed onto the Pd.[302] XPS was used to confirm that both metals are in their zerovalent metallic state. FT-IR spectra of CO adsorbed to the Pd−Pt nanoparticles (the so-called "IR-CO method") show an intense CO stretching band at 2068 cm^{-1} and a weak broad band at 1892 cm^{-1}. These peaks are characteristic of CO bound in terminal (2062 cm^{-1}, strong) and bridging sites (1860 cm^{-1}, broad and weak) on the surface of Pt clusters (in contrast to CO adsorption on Pd clusters, which have a weak terminal CO band at 2052 cm^{-1} and a strong bridging CO band at 1941 cm^{-1}). This finding is consistent with the Pd core being completely covered by the Pt shell.[302] However, NMR studies of PVP-protected $Pd_{0.2}Pt_{0.8}$ and $Pd_{0.8}Pt_{0.2}$ nanoparticles of average diameter 2.4 nm show a broad ^{195}Pt resonance, which is consistent with a homogeneous Pd−Pt nanoalloy with bulk-like and surface-like Pt atoms (see Figure 10A).[129,303]

$Pt_{core}Pd_{shell}$ particles (5 nm diameter) have also been generated electrochemically by Reetz and co-workers by electrolyzing preformed Pt colloidal particles (3.8 nm), stabilized by tetraoctylammonium bromide, in a solution of tetraoctylammonium bromide in tetrahydrofuran with Pd as the sacrificial anode.[89] The core−shell nature of the particles was confirmed by EXAFS measurements.

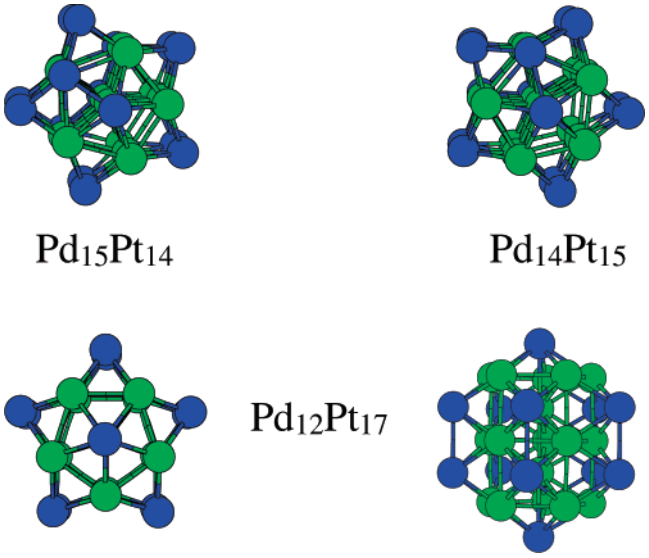

Figure 26. Twenty-nine-atom star-shaped capped decahedral clusters predicted to be the lowest energy structures (from Gupta potential calculations) for $Pd_{15}Pt_{14}Pd_{14}Pt_{15}$ (from ref 305) and 5-fold-symmetric $Pd_{12}Pt_{17}$ (from ref 306). Blue (dark gray) and green (light gray) spheres correspond to Pd and Pt atoms, respectively. (From refs 305 and 306. Reproduced by permission of The Royal Society of Chemistry.)

Considering CO-coated Pd−Pt clusters, in 1997 Bemis and Dahl reported the synthesis and X-ray crystal structure of $H_{12}Pd_{28}(PtPMe_3)(PtPPh_3)_{12}(CO)_{27}$, which consists of a 4-layer hcp $Pd_{28}Pt$ core which is capped by 12 $Pt-PPh_3$ fragments.[304] ^1H NMR spectroscopy and deuterium-exchange experiments have shown that the cluster contains hydride anions within the Pd_5Pt octahedral interstices, thereby possibly serving as a model of the hydrogen storage in Pd metal. The fact that Pt rather than Pd atoms occupy the lowest coordination surface sites may be due to the stronger bonding of Pt to the terminal PPh_3 ligands.

Theoretical Studies. Massen et al. performed global optimization studies of Pd, Pt, and Pd−Pt clusters using a genetic algorithm and describing interatomic interactions by the Gupta many-body potential.[305] The Gupta potential parameters for Pd−Pt interactions were obtained by averaging those for Pd−Pd and Pt−Pt interactions. It was found that the predicted lowest energy structures for stoichiometric $(PdPt)_M$ nanoalloys generally had different geometries than the corresponding pure Pt or Pd clusters with a reduced tendency to display icosahedral packing and a larger number of capped decahedral structures, such as the star-shaped 29-atom clusters $Pd_{15}Pt_{14}$, $Pd_{14}Pt_{15}$, and $Pd_{12}Pt_{17}$ (see Figure 26).[305,306] Compared with Pd, there was also an increase in the number of disordered structures for the Pd−Pt clusters. Shell-like atomic segregation is favored for these Pd−Pt clusters with the surface becoming richer in Pd and the core becoming richer in Pt. This segregation, which is consistent with experimental studies on Pt−Pd particles, has been explained in terms of the lower surface energy of Pd and the greater cohesive energy of Pt. For nonstoichiometric Pt−Pd clusters, the calculated global minimum has been shown to depend strongly on the composition with the doping of even a single Pt atom into a Pd cluster (or vice versa) being sufficient to change the geometrical structure of the cluster.[305] It was also shown that varying the Pd−Pt interaction parameters of the Gupta potential can have very significant effects on the geometrical structures (including the degree of geometrical order or disorder) and the tendency toward ordering or segregation (of the Pt and Pd atoms) of Pt−Pd clusters.

The above work was extended by Lloyd et al., who analyzed the dependence of cluster binding energy on coordination for a selection of cluster sizes (including icosahedral and cuboctahedral shell clusters with up to 147 atoms) and compositions.[306] In this study it was shown that the most stable isomers (geometrical isomers and homotops) generally have the greatest number of Pt−Pt bonds (or Pt−Pd bonds if there are few Pt atoms). It was also found to be important to consider all of the atoms in the cluster since the preferred site for a particular atom (corresponding to the site giving the highest partial binding energy for that atom) may not give the most stable cluster (highest average binding energy, E_b) if the other atoms are destabilized in that isomer. $Pt_{core}Pd_{shell}$ segregation, which was manifest in the correlation between average binding energies and distribution-dependent structural order parameters, such as the average radius $\langle R_{Pt}\rangle$ and the radius of gyration $\langle R_{Pt}\rangle^{gyr}$ of the Pt subset of atoms, is consistent with the experimental studies of Renouprez and Rousset.[141,142] Similar results have recently been obtained by Cheng et al., using the same Gupta potential parameters in a MC simulation study of icosahedral and decahedral Pd−Pt nanoalloys with 55 atoms.[307]

A study of 34- and 38-atom Pd−Pt nanoalloys (again using the Gupta potential) has recently been carried out by Rossi et al.[212] Many of the 34-atom clusters (as for the pure Pd_{34} and Pt_{34} clusters) were predicted to adopt incomplete decahedral geometries, especially in the Pt-rich regime. For Pd-rich and intermediate compositions, however, polyicosahedral structures are often found, for example, $Pd_{30}Pt_4$ and $Pd_{29}Pt_5$, which are fragments of the 38-atom "pancake structure" and $Pd_{24}Pt_{10}$, which has a tetrahedral $Pt_{core}Pd_{shell}$ arrangement. For the 38-atom clusters, the truncated octahedral (fcc) geometry dominates with other structures including incomplete 2-shell icosahedra (for 30−34 Pd atoms), incomplete decahedron ($Pd_{13}Pt_{25}$), and a disordered structure ($Pd_{35}Pt_3$). A subsequent detailed analysis using the Gupta potential confirmed the composition dependence of the preferred structural motif for 34-atom Pd−Pt clusters, though at the DFT level a single motif (based on a double tetrahedral core) was found to be the most stable over a wide composition range.[144]

Fernández et al. recently studied $(PdPt)_N$ clusters, with $N = 5-22$, by carrying out DFT reminimizations of low-energy isomers generated by a GA search employing a Gupta potential.[153] Although the exact ordering of the homotops was not exactly the same for the DFT and Gupta potential calculations, $Pt_{core}Pd_{shell}$ segregation was confirmed. Similar findings have also been reported by Paz-Borbón et al.[144]

5.3. Group 10–Group 11 Nanoalloys

Much attention has focused on nanoalloys formed between metals from group 10 (Ni, Pd, Pt) and group 11 (Cu, Ag, Au) since the alloying of the catalytically active group 10 metal with the less active (or even inactive) group 11 metal can dramatically alter the surface structure, composition, and reactivity of the catalyst.[308]

5.3.1. Ni–Cu

The phase diagram for bulk Ni−Cu consists of solid solutions with fcc structures with a miscibility gap below 630 K.[231,309] This has been attributed[310] to the small lattice

size mismatch between Cu and Ni (a_0 (Cu) = 3.62 Å; a_0 (Ni) = 3.54 Å[311]) and the small positive enthalpies of solution of Cu in Ni and Ni in Cu.[312]

In contrast to the results for Ni−Au nanoalloys (vide infra), it has been found that a small amount (1%) of Cu in a Ni particle leads to increased carbon formation in the steam reforming of hydrocarbons, while larger amounts of Cu (10%) lead to reduced carbon formation, relative to pure Ni particles.[313] It is known that Cu segregates to the surface of Ni−Cu nanoparticles at low temperatures, driven by the lower surface energy of Cu compared with Ni.[287,310,314] Recent DFT calculations on small Cu clusters ($N \leq 5$) with single Ni-atom impurities confirm that the most stable homotops maximize the coordination of the Ni atom.[315] For larger clusters, in contrast to Ni−Au, because there is a small size mismatch between Cu and Ni, surface-segregated Cu atoms preferentially occupy flat terrace sites,[314] so (at low concentrations) they do not block the edge and kink Ni sites responsible for carbon formation.[316]

Nanocrystalline Ni−Cu has been produced by high-temperature routes using laser ablation of cold-pressed Ni/Cu powder targets,[317] mechanical alloying,[318] and ion implantation in silica.[319] Recently, however, Damle and Sastry reported a low-temperature synthetic pathway for producing Cu−Ni nanoalloys.[320] Their technique begins with impregnation of a fatty acid (stearic acid) film (which has been thermally evaporated onto a support) with Cu^{2+} ions, which are subsequently reduced by hydrazine to form Cu particles embedded in the fatty acid matrix. The next stage involves reducing Ni^{2+} ions to form Ni nanoparticles, which are also embedded in the fatty acid matrix. Thermal treatment of the nanocomposite film leads to Ni−Cu alloying at 100 °C. The Cu−Ni particles are quite large, with an average size of 35 nm estimated from TEM images. XRD measurements are consistent with fcc structure and a lattice parameter intermediate between those of Cu and Ni. Application of Vegard's law, based on the lattice parameters, gives the composition $Ni_{0.5}Cu_{0.5}$. The low-temperature (100 °C) alloying has been attributed to the high surface free energy of the Cu and Ni particles, leading to low-temperature surface melting and appreciable Ni/Cu diffusion. The stearic acid matrix (which may be molten at the annealing temperature, thereby increasing metal diffusion rates) may also play a direct role in lowering the annealing temperature. Ultimately, perhaps by carrying out in situ reduction of two metals which have been simultaneously incorporated into the fatty acid film it may be possible to carry out room-temperature alloying.[320]

5.3.2. Ni–Ag

In the bulk, Ni and Ag are known to be immiscible for all compositions.[231] Annealing studies of Ni−Ag films also show clustering of Ni atoms to form Ni nanoparticles embedded in a Ag matrix with similar results being observed for chemically similar Co−Ag films.[321]

Portales et al. used LFRS to study the quadrupolar vibrational mode of Ni−Ag nanoparticles embedded in alumina.[322] TEM measurements indicate an average particle size of approximately 3 nm. The observation of a LFRS signal confirms resonance with the silver conduction electrons contributing to the surface dipolar plasmon. Detailed analysis of the LFRS spectrum confirms core−shell (Ni_{core}-Ag_{shell}) segregation and weak bonding between the Ni core and the Ag shell.[322] The segregation is driven by the lower surface energy of Ag (approximately one-half that of Ni) and the large size mismatch (the atomic radii of Ni and Ag are 1.25 and 1.45 Å, respectively).

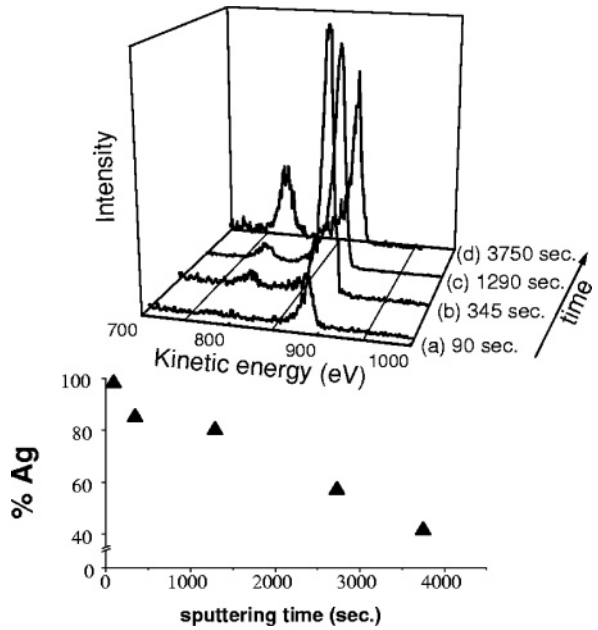

Figure 27. (Top) Evolution of the whole LEIS spectrum versus sputtering time for $Ni_{0.5}Ag_{0.5}$ clusters. (Bottom) Evolution of the silver concentration versus sputtering time. (Reprinted with permission from ref 60. Copyright 2003 American Physical Society.)

In 2003 Gaudry et al. used LEIS of $Ni_{0.5}Ag_{0.5}$ nanoparticles to show that initially the surface is 95−100% Ag, confirming the Ag surface segregation[60] (see Figure 27). As time proceeds, the surface Ag atoms are preferentially sputtered, so the measured silver concentration decreases with time. The optical absorption spectrum of the Ni−Ag particles is found to be intermediate between those of pure Ag and pure Ni clusters with the Ag surface plasmon being broadened and blue shifted relative to pure Ag clusters (see Figure 4) due to mixing of the silver conduction electron plasmon with the excitations of the Ni sp−d-hybridized bands.[60,267] Co−Ag clusters were found to give similar spectra to Ni−Ag.[60]

Theoretical Studies. Recent simulation results[24,177] confirmed the clear tendency of Ni−Ag to form core−shell structures by analogy with the case of Cu−Ag. In these studies, global optimization has been performed for Ni−Ag clusters of size 34 and 38 for all possible compositions with the bonding described by the many-body Gupta potential. At fixed size and for variable composition, perfect core−shell structures (all Ag atoms on the cluster surface, no Ni atoms on the surface) turned out to be the most stable structures, in qualitative agreement with the experimental finding,[60] which indicates a strong preference for this chemical ordering. The perfect core−shell structures presented the lowest excess energy and highest peaks in Δ_2 (see Figures 15 and 18). The driving forces leading to formation of these clusters are the same as in Cu−Ag, for which the same kind of structures are found.

5.3.3. Ni–Au

The bulk binary phase diagram for Ni−Au has a large miscibility gap, leading to no alloy formation at low temperatures.[231] Experimental and theoretical studies, however, indicate that surface alloying is energetically favorable when Au atoms are deposited on Ni(110) and Ni(111) surfaces.[9,323]

Molenbroek et al. reported the generation of supported Ni−Au nanoparticles (with Ni/Au ratios ranging from 18 to 215) by impregnating reduced monometallic Ni clusters, supported on SiO_2 and $MgAl_2O_4$, with an aqueous solution of $Au(NH_3)_4(NO_3)_3$.[316] Powder XRD measurements indicate that the as-prepared particles contain NiO, but this is reduced to Ni metal after heating to over 800 K in hydrogen. TEM images of the SiO_2-supported particles show Ni-rich particles with sizes ranging from 2.5 to 6 nm and a smaller number of larger (10−20 nm) clusters composed mostly of Au. Those particles supported on $MgAl_2O_4$ show a wider size range (3−15 nm). EXAFS measurements indicate the presence of Ni in the nearest-neighbor shell of Au, consistent with formation of a Ni−Au surface alloy, as predicted by MC simulations. Au segregation to the surface of small Ni clusters has also been observed in a combined study using XPS, LEIS, TEM, and MC simulations for $Ni_{0.5}Au_{0.5}$ nanoalloys.[324] This surface segregation of Au is driven by the significantly lower surface energy of Au and the lower cohesive energy, compared with Ni (see Table 1).[60]

Interestingly, the Ni−Au carbonyl cluster $[Ni_{32}Au_6(CO)_{48}]^{6-}$ contains an octahedral Au_6 core embedded in a Ni_{32} truncated octahedron,[325] representing the opposite segregation to that predicted on the basis of cohesive and surface energies. In this case, segregation of Ni to the surface is probably driven by the stronger Ni−CO binding.[36] As Longoni and colleagues pointed out,[36] adsorbate-induced segregation has previously been observed in bulk alloys, where stronger binding of an adsorbate to the metal with the highest cohesive energy causes segregation of that metal to the surface—the opposite of what is observed in vacuo.[326,327]

Gaudry et al. reported optical absorption measurements for Ni−Au nanoparticles (generated by laser vaporization of alloy rods) embedded in alumina.[60] On the basis of the relative surface energies and previous LEIS studies,[324] it is believed that these are core−shell ($Ni_{core}Au_{shell}$) nanoparticles, though no clear Au plasmon was observed.[60]

5.3.4. Cu–Pd

Cu−Pd nanoalloys have been widely studied over the past two decades with much of the interest being due to their catalytic importance (see section 6).

Bulk Cu−Pd alloys form continuous solid solutions with fcc structures at high temperatures for all compositions. However, complex ordering behavior is observed below 900 K.[312] There are three common ordered phases: CuPd (bcc, *B*2), Cu_3Pd (fcc, $L1_2$), and Cu_4Pd (tetragonal).[216] The enthalpies of formation of the solid solutions and ordered phases are negative and quite large (for example, the enthalpy of formation of the CuPd solid solution is approximately −13 kJ mol^{-1} [328]). While earlier experimental studies indicated that Pd segregates to the surface of Cu−Pd alloy thin films,[329] by combining AES, LEIS, and theoretical calculations, Rousset et al. have shown that the (111) surface of Cu−Pd alloys has a surface composition which is close to that of the bulk while the top layer of the (100) surface is Cu rich.[277]

In 1995, Nosova et al. performed a combined XPS, IR absorption, and catalytic study on Cu−Pd nanoparticles (with a mean particle size of 3−4 nm) formed by the reduction of the bimetallic complex $CuPd(OAc)_4$ which had been chemisorbed onto dehydrated γ-alumina.[330] These studies showed that the surface of the Cu−Pd particles was Cu rich, though the degree of segregation was observed to be surface dependent. Fernández-Garcia et al. used XANES and IR spectroscopy to study Cu−Pd nanoalloys, formed by the reduction of Cu and Pd nitrates impregnated into KL-zeolite, and found substitutionally disordered Cu−Pd alloys.[331] Renouprez and co-workers, using a combination of XRD and LEIS on silica-supported Cu−Pd particles, confirmed that the surface concentration of Cu is greater than in the bulk.[116]

Molenbroek et al. grew Cu−Pd particles on silica and alumina substrates using atomic layer epitaxy, a modification of chemical vapor deposition in which Cu and Pd complexes are either sequentially deposited and their ligands oxidized off (on SiO_2) or Cu and Pd nitrates are coadsorbed onto Al_2O_3, followed by calcination in Ar at 673 K.[11] From TEM and EXAFS measurements, the Cu−Pd particles were found to have diameters ranging from 2 to 6 nm with the co-impregnation of Cu and Pd into alumina yielding larger particles and a broader size distribution. The EXAFS measurements (at the Cu and Pd K edges) indicated alloying on both substrates, though there was evidence for Cu-rich surfaces for the particles generated on alumina and random mixing for the particles supported on silica. These results were found to be consistent with simple modeling studies of Cu−Pd alloying.

Zhu, DePristo, and co-workers generated Cu−Pd nanoalloys of varying compositions, prepared in colloidal suspension (protected by PVP), by reducing Pd acetate and Cu acetate monohydrate in 2-ethoxyethanol at 90 °C.[332] Particle sizes (as determined from TEM and X-ray scattering) were found to be in the range 6−10 nm. At the composition $Cu_{0.5}Pd_{0.5}$, Zhu et al. found no evidence for the ordered bcc (*B*2) superstructure observed as the low-temperature bulk alloy at around this composition or of any of the other known Cu−Pd crystalline phases,[312] though other TEM and HREM studies have indicated perfectly ordered bcc *B*2 structures when thermodynamic equilibrium is attained.[333−335]

Henry and co-workers used TEM and EDX to study the nucleation and growth kinetics of Cu−Pd particles deposited on the (100) surface of NaCl by co-condensation of Cu and Pd atoms under UHV.[336,337] Because of the much weaker interaction of the Cu atoms with the NaCl surface, the nucleation of pure Pd clusters is favored initially, despite the fact that an 8 times greater flux of Cu atoms was used. Particles can grow by diffusion and capture (efficient for Pd which interacts more strongly with the surface) and by direct impingement on the growing cluster (more efficient for Cu). As the particles grow, therefore, relatively more Cu is incorporated (now the higher flux of Cu atoms is significant). The particles grown at 553 K were found to have the fcc structure of the disordered bulk alloy. Upon annealing at 638 K, however, the particles transform to the ordered bcc *B*2 structure.[336]

As an example of the importance of surface chemistry for colloidal bimetallic particles, reversible surface enrichment by Pd has been observed for colloidal Cu−Pd particles on exposure to CO.[84] This enrichment is driven by the greater strength of the Pd−CO bond, as compared with Cu−CO (for example, the enthalpies of adsorption of CO on the (111) surfaces of bulk Cu and Pd are 50 and 142 kJ mol^{-1}, respectively.[279]).

In a recent study, Mattei et al. used a combination of TEM, HRTEM, EDS, and EXAFS to investigate the dynamics and compositional and structural evolution (as a function of time) of Pd−Cu nanoparticles as they are heated in various atmospheres.[86] Both Pd and Cu diffusion is observed, though the diffusion is believed to be triggered by the Cu atoms.

Annealing in reducing atmospheres (heating to 900 °C in H_2/N_2) leads to Pd migration to the surface and aggregation of larger particles (average diameter ≈ 9.8 nm). By contrast, annealing in oxidizing atmospheres (heating to 900 °C in air) leads to preferential oxidation of Cu and formation of a partial CuO shell around a Pd core. This is in contrast to the oxidation of silica-implanted Cu−Au nanoclusters, where a Au-rich core is surrounded by a partial shell of Cu_2O.[234] The difference between the Cu−Pd and Cu−Au systems has been attributed to the following factors.[86]

(i) Cu−Pd mixing is more exothermic (enthalpy of formation of solid solution = -13 ± 1 kJ mol^{-1}) than Cu−Au (enthalpy of formation = -5.3 ± 0.5 kJ mol^{-1}),[328] making Cu−Pd more stable to oxidation—it should be noted that the enthalpies of formation of CuO and Cu_2O are similar (approximately -160 kJ mol^{-1}).

(ii) The lattice mismatch between Cu_2O and the Cu−Pd alloy is large (over 9%) when compared with that between Cu_2O and the Cu−Au alloy (4%), so Cu_2O is not stabilized by templating by the underlying cubic Cu−Pd nanoalloy.

In another recent study, Rodríguez-López et al. performed HRTEM measurements and MD simulations (based on the Sutton−Chen model[158]) on PVP-stabilized Pd−Au and Cu−Au nanoalloys ($D = 1.5-3$ nm).[197] They identified a number of imperfect decahedral nanoparticles and observed structure stabilization by surface reconstructions. It has been proposed that the (100) facetting in the decahedral particles, as observed by HRTEM and in the MD simulations, may be important in catalysis by bimetallic catalysts such as Pd−Au, Cu−Au, and Pd−Pt.[197]

Theoretical Studies. Simple energetic arguments indicate that, for Cu−Pd nanoalloys, the lower surface energy of Cu favors surface segregation but the negative mixing energy favors subsurface Pd and Cu−Pd mixing on the (111) facets.[332]

MD simulations by Zhu et al., based on the bond order simulation (BOS) model[287] and MD/MC-corrected effective medium theory,[338] for truncated octahedral fcc structures indicate Cu−Pd mixing but with surface-dependent Cu segregation.[332] Thus, while the (100) facets are preferentially occupied by Cu, there is mixing on the close-packed (111) facets, which agrees with the findings of Rousset et al. for bulk Cu−Pd alloys.[277] Where the surface is Cu rich, the subsurface layer is found to be Pd rich.

The EAM model was used by Montejano-Carrizales et al. to study Cu−Pd and Cu−Ni clusters.[310] The complex segregation effects observed for Cu−Pd nanoalloys were attributed to the interplay between the tendency for Pd surface segregation (though this disagrees with the studies mentioned above) and formation of ordered bulk phases at low temperatures below a critical temperature T_c. More recently, a second-moment Gupta-like potential has been used by Mottet et al. in MC and MD simulations of Cu−Pd nanoalloys ranging in size from a few hundred to a few thousand atoms[202] (see Figure 28). The relative stabilities of fcc, bcc, and icosahedral morphologies were found to depend critically on the competition or synergy between surface-dependent segregation and bulk ordering effects, which in turn depends on the size and composition of the nanoparticles.[202]

Recently, Rubinovich and co-workers[339] studied 923-atom Cu−Pd cuboctahedra within the FCEM method within a tight-binding energetic model. At low temperatures, they found competitive multisite segregation. Starting from the pure Pd cluster and increasing the Cu content, they found

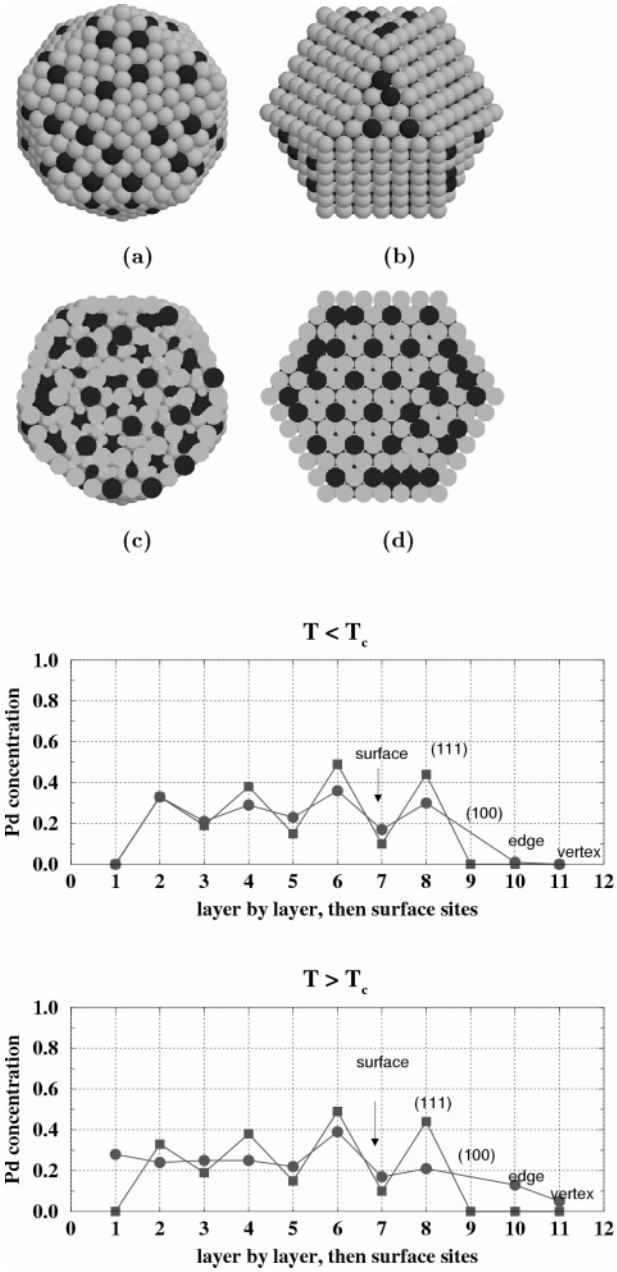

Figure 28. Snapshots of the $Pd_{74}Cu_{235}$ cluster from a simulation within the second-moment Gupta-like potential at $0.06T_c$. Pd and Cu atoms are represented in dark and light gray, respectively: (a) relaxed icosahedron and (b) cuboctahedron. (c and d) Cross sections of the same clusters are presented. The two graphs show (at $0.06T_c$ and $2.5T_c$) the concentration profiles of the two clusters as concentric shells from the center to the surface of the clusters and for the different sites on the surface. Squares refer to the cuboctahedron and circles to the icosahedron. (Reprinted with permission from ref 202. Copyright 2002 American Physical Society.)

that Cu atoms begin to occupy the vertices of the cluster and then the surface shell up to 24% Cu concentration, forming however a mixed-order surface with Pd atoms. Above that concentration, a $L1_2$-like ordered phase is formed in the cluster core. The perfect ordered phase, with $L1_2$ core and mixed surface order, is reached at the magic composition $Cu_{318}Pd_{605}$.

5.3.5. Cu–Pt

Compared with the wealth of research on Cu−Pd, Cu−Pt nanoalloys have received relatively little attention. The first

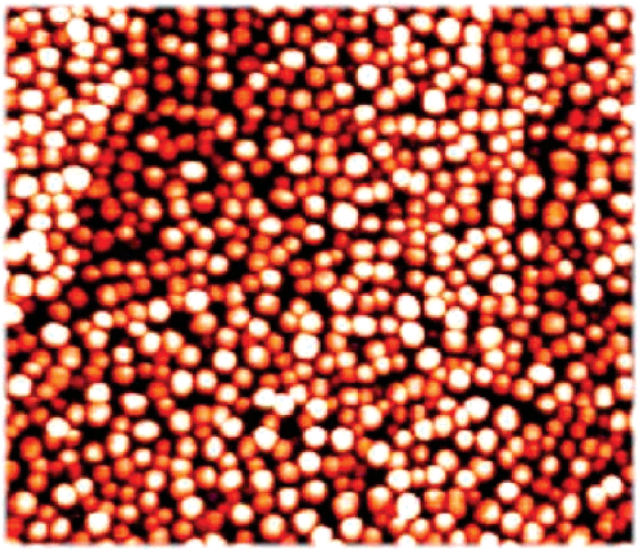

Figure 29. Room-temperature STM images of Pd−Ag nanoparticles obtained by vapor deposition on thin alumina films. (Reprinted from ref 343, Copyright 2006, with permission from Elsevier.)

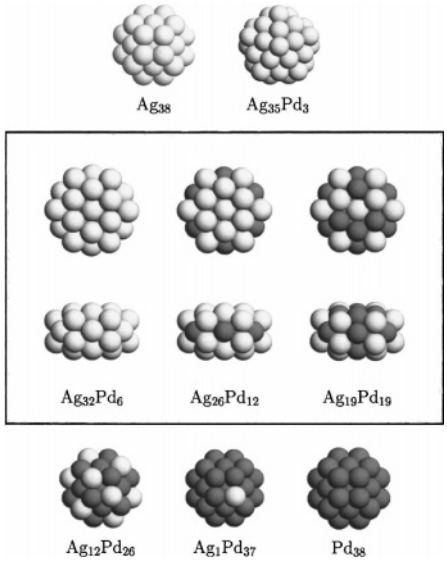

Figure 30. Global minimum structures of Pd−Ag clusters of size 38 within the Gupta potential model. Ag and Pd atoms correspond to light and dark spheres, respectively. Within this model, intermediate compositions prefer the sixfold pancake structure (clusters in the box), while for Pd-rich clusters the fcc truncated octahedron is lower in energy. (Reprinted with permission from ref 212. Copyright 2005 American Institute of Physics.)

synthesis of colloidal Cu−Pt particles was reported by Toshima and Wang in 1994, who applied them to catalytic hydrogenation in solution.[340] More recently, it has been suggested that Cu−Pt alloys may be efficient catalysts for NO_x reduction.[341]

In a recent study, Eichhorn and colleagues prepared Cu_{core}-Pt_{shell} and $Pt_{core}Cu_{shell}$ core−shell nanoparticles (by successive polyol reductions) as well as intermixed particles (by refluxing Pt and Cu salts in glycol in the presence of PVP).[342] TEM, XRD, and EDX were used to characterize the particles. The $Cu_{core}Pt_{shell}$ particles (mean diameter 8.8 nm) were found to have approximately equal concentrations of Cu and Pt, as were the $Pt_{core}Cu_{shell}$ particles, though they were generally larger (mean diameter 18.3 nm), due to the larger starting Pt nanoparticles forming the cores. From XRD, the as-prepared $Pt_{core}Cu_{shell}$ particles were found to have an fcc Pt core with a $Pt_{0.2}Cu_{0.8}$ shell (i.e., not pure Cu). Annealing at 370 °C for 5 h leads to an intermixed CuPt particle. By contrast, the $Cu_{core}Pt_{shell}$ particles have fcc Cu cores and fcc Pt shells. In this case, however, annealing at 370 °C for 5 h generates a Cu-rich Cu−Pt core and a pure Pt shell rather than the CuPt alloy. This difference has been attributed to the greater kinetic stability (controlled by atomic diffusion) of $Cu_{core}Pt_{shell}$ core−shell particles.[342] Interestingly, the same authors postulated that the intermixed CuPt particles formed by annealing $Pt_{core}Cu_{shell}$ nanoparticles may actually be hollow. XPS and Ar plasma etching experiments confirmed the core−shell and composition information described above.[342]

5.3.6. Pd–Ag

Chemical reduction of mixed solutions of Ag and Pd salts leads to formation of surface-segregated core−shell particles for Pd−Ag, though these metals are fully miscible in the bulk phase, forming no ordered phases.[344] Pd−Ag nanoparticles have also been generated by radiolysis[94,98] and microwave-induced reduction.[345] $Ag_{core}Pd_{shell}$ nanoparticles have been produced by underpotential deposition of Ag adatoms onto Pd.[247] Pd−Ag nanoparticles have also been generated by vapor deposition onto thin alumina films[343] (see Figure 29). These particles were identified as being intermixed but with some silver segregation at the surface.

Theoretical Studies. Small Pd−Ag nanoparticles have been studied by global optimization methods within the Gupta potential model.[212] At size 38, a competition between fcc (truncated octahedral) structures and polyicosahedral structures (based on the sixfold pancake structure, see Figure 30) has been found depending on composition. As the Pd content increases, fcc structures become more and more favorable. As for the chemical ordering, a tendency to form a high number of mixed Pd−Ag bonds has been identified together with the propensity of Ag atoms to occupy surface sites, in qualitative agreement with the tendency observed in the experimental studies reported in ref 343.

5.3.7. Pd–Au

Pd−Au nanoalloys have been widely studied, primarily because of their importance in catalysis (see section 6).

In the 1990s, Schmid and co-workers prepared colloidal $Au_{core}Pd_{shell}$ and $Pd_{core}Au_{shell}$ clusters by the seed-germ process, wherein a gold (or palladium) cluster without passivating ligands undergoes a second reduction step in the presence of salts of the other metal.[12,346] The outer metal shell is then passivated by coordination of an appropriate sheath of ligands.

Lee et al. used XRD, EXAFS, and XANES to study the temperature-dependent mixing of Pd and Au atoms in Pd−Au particles in the range 300−573 K.[347] Starting from the core−shell segregated cluster $Au_{core}Pd_{shell}$ (generated by the seed-germ process), Pd−Au intermixing takes place until, at the highest temperatures, a homogeneous random substitutional alloy with approximate stoichiometry Au_5Pd is produced. $Au_{core}Pd_{shell}$ particles have also been generated by sonochemical reduction of solutions of Pd and Au salts.[348] In the latter case, ^{197}Au Mössbauer measurements showed the presence of a pure Au core and a thin alloy region between the Au and Pd shells.[348]

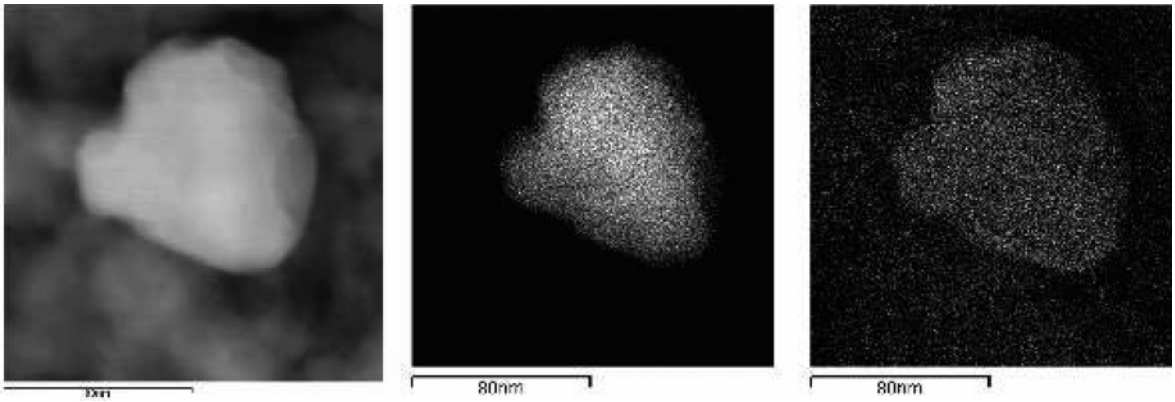

Figure 31. (Left) STEM-ADF image of a calcined Pd−Au particle on TiO_2. (Middle and right) STEM-XEDS signal from Au and Pd only, respectively. The Pd signal seems to originate from a larger area, indicating Pd enrichment at the surface. (Reprinted from ref 352, Copyright 2005, with permission from Elsevier.)

Recently, Wong and co-workers reported the synthesis of $Au_{core}Pd_{shell}$ nanoparticles by reducing a solution of Pd salts in the presence of a preformed Au sol.[349] Simple calculations showed that Au−Pd particles with 1.9, 3.8, 5.7, and 11.4 wt % Pd have 1/3, 2/3, 2, and 3 Pd layers, respectively. The Au sol was noted to be ruby red with a characteristic plasmon peak at around 520 nm, while for more than a monolayer coverage of Pd, the sols have a gray-violet tint. For all but the lowest Pd loadings, XPS measurements revealed the Pd/Au surface ratio to be higher than that of the bulk of the nanoparticle, proving that there is surface segregation of Pd.

Liu et al. also recently reported the colloidal synthesis of PVP-stabilized Au−Pd nanoalloys ($D = 1-7$ nm) with compositions Pd:Au = 1:1, 5:1, and 1:5.[350] HREM studies (including HAADF measurements) showed the coexistence of decahedral and octahedral particles and a mixture of $Pd_{core}Au_{shell}$, $Au_{core}Pd_{shell}$, and intermixed Pd−Au particles.[350] Shiraishi et al. also reported the synthesis of $Pd_{core}Au_{shell}$ nanoparticles, though these have been said to be difficult to prepare.[351]

An elegant and thorough investigation of the formation, structure, and catalytic properties of Pd−Au nanoparticles deposited on a TiO_2 substrate by the calcination of coprecipitated Au and Pd has been reported by Hutchings and co-workers.[352,353] The particles were examined using AAS, XPS, XRD, ADF-STEM, and STEM-XEDS as well as being investigated for their catalytic activity (see section 6). Coprecipitation of Pd and Au was found to lead to formation of Pd, Au, and Pd−Au nanoparticles. ADF-STEM measurements of the Pd−Au nanoparticles showed a bimodal size distribution with a small number lying in the size range 1−8 nm but with most being much larger (40−70 nm). Similar distributions were found for uncalcined and calcined particles. STEM-XEDS mapping confirmed the mixed Pd−Au nature of the particles, as evidenced by the spatial coincidence of the Pd and Au X-ray maps.[352,353]

For an uncalcined sample with 2.5 wt % Au, 2.5 wt % Pd on TiO_2, XPS showed clear Au(4d) and Pd(3d) peaks.[352,353] After heat treatment at 200 °C, the Au(4d) peaks were dramatically decreased in intensity. After calcination in air at 400 °C followed by reduction in H_2 at 500 °C, the Au($4d_{3/2}$) peak could no longer be detected. Detailed analysis of the XPS peaks indicated a surface Pd:Au ratio (for the uncalcined nanoparticles) of 1:2.9 by weight, i.e., a Pd:Au atomic ratio of approximately 1:1.6, while AAS showed the overall Pd:Au ratio to be 1:1. After calcination at 200 °C, however, XPS showed a significant surface enrichment by Pd, with a Pd:Au ratio of 5.1:1 by weight (an atomic ratio of almost 10:1), which is consistent with a core−shell segregated $Au_{core}Pd_{shell}$ conformation, with the outer shell actually being PdO prior to hydrogen reduction. The $Au_{core}Pd_{shell}$ nature of these particles is confirmed by the STEM-XEDS maps (see Figure 31), which show that the Pd X-ray signal originates from a larger area of the particle than the Au signal.[352,353] Subsequent reduction of the calcined nanoparticles by H_2 was found not to change the surface composition. The results of Hutchings and co-workers for PdAu nanoparticles are consistent with Hilaire et al., who found that heating bulk PdAu alloys in O_2 above 300 °C leads to surface Pd enrichment with the surface consisting of PdO, the process being driven by the exothermic formation of PdO, as compared with the endothermic enthalpy of formation of Au_2O_3.[354]

It should be noted that the $Au_{core}Pd_{shell}$ particles prepared by Hutchings and co-workers are stable to heating to at least 500 °C,[352] though Nakagawa et al. reported mixing of $Au_{core}Pd_{shell}$ particles (in porous silica) when heated to 300 °C.[355] While calcination is expected to stabilize $Au_{core}Pd_{shell}$ (or rather $Au_{core}(PdO)_{shell}$) structured due to the greater thermal stability of PdO compared with Au_2O_3, which helps to draw the Pd atoms out to the surface, the segregation properties of Pd−Au nanoparticles appear to be far from simple. Interestingly, Kan et al. reported that $Au_{core}Pd_{shell}$ segregation was observed when Au was deposited on preformed Pd particles.[102]

Theoretical Studies. Liu et al. reported the results of MD simulations (using an analytical EAM model) for 262-atom decahedral and 861-atom cuboctahedral clusters with stoichiometries Pd:Au = 1:1, 5:1, and 1:5, as for their experimental work (described above).[350] Their calculations indicated that $Pd_{core}Au_{shell}$ clusters have the lowest (most negative) enthalpy of formation with random solutions having smaller (though still negative) enthalpies of formation. It was also observed that the structural incoherence (incommensuracy) due to the lattice mismatch between Au and Pd is important in determining the type of segregation in Au−Pd nanoalloys. Thus, the destabilizing effect of the lattice mismatch is maximized for the $Au_{core}Pd_{shell}$ configuration, while it is minimized for the $Pd_{core}Au_{shell}$ configuration due to shrinking of the outer Au shell.[350] The $Pd_{core}Au_{shell}$ arrangement is also favored by the lower surface energy of Au and the higher cohesive energy of Pd and is consistent with LEIS measurements which have shown Au enrichment of the (100) and (111) surfaces of bulk Pd−Au alloys.[277]

Although the inverse $Au_{core}Pd_{shell}$ configuration can be generated as the kinetic product at low temperatures (see references cited above and refs 356 and 357), the MD simulations predict that above 500 K $Au_{core}Pd_{shell}$ clusters should undergo a transition corresponding to a core−shell reversal to $Pd_{core}Au_{shell}$. This prediction, which is consistent with results for Cu−Au nanoalloys,[358] awaits experimental verification.

5.3.8. Pt–Ag

Generation of Pt−Ag nanoparticles by radiolysis has been reported by two groups.[97,99] The earlier study by Treguer et al.[97] yielded nearly spherical particles, whereas in the later study Pt−Ag nanowires with high aspect ratios (with lengths up to 3.5 μm and diameters of 3−20 nm) were generated.[99] SAED studies show that the nanowires are polycrystalline with the grains having fcc packing. EXAFS analysis at the Pt L3 edge (11.564 keV) show that although the Pt atoms are disordered, there is little Pt−Ag mixing (the Pt lattice spacing is similar to that in the bulk, in contrast to what would be expected for intermixed particles).[99] The more noble metal (Ag) is believed to be reduced first, forming a seed core, with Pt depositing as a shell on the surface, to generate $Ag_{core}Pt_{shell}$ grains which then assemble into wires, probably aided by the fact that the micelles (PVA in water) can form cylindrical topologies. Formation of nanowires, rather than spherical particles, is dependent on the source of Pt (H_2PtCl_6 yields nanowires, but K_2PtCl_6 yields spheres[97]) and Ag (Ag_2SO_4 yields wires but $AgNO_3$ yields spheres). Similarly, nanowires are only formed for Ag mole concentrations of 20−80%.[99] Pt−Ag nanoparticles have also been prepared by microwave heating of a solution of Pt and Ag salts in the presence of PVP.[345]

5.3.9. Pt–Au

It is known that Pt and Au form a continuous solid solution at high temperatures, though at low temperatures phase segregation occurs.[216]

^{197}Au Mössbauer spectroscopy reveals that both the surface atoms and the inner atoms of surface-passivated Au_{55} clusters are influenced by the ligands and that the central atom charge densities are not the same as those in the bulk metal. By contrast, in Pt_{309} clusters (in which ^{197}Au nuclei are produced by neutron activation) Schmid, de Jongh, and co-workers have shown that the inner shell atoms have the same charge density as in the bulk metal.[359]

In 2001, Lou et al. reported the synthesis of decanethiolate-capped Pt−Au nanoparticles by reduction of a 1:5 Pt:Au ratio of K_2PtCl_6 and $HAuCl_4$[360] (1:1 Pt−Au particles have also been reported[361]). TEM measurements revealed an average metal core size of 2.5 ± 0.4 nm. These clusters have been investigated for their catalytic properties, as discussed in section 6. Recently, Ascencio and co-workers reported the production (by chemical reduction) of 1−5 nm PVP-stabilized Pt−Au nanoparticles.[362]

Au−Pt and Ag−Pt clusters adsorbed onto transparent immogolite fibers have been studied by Liz-Marzán et al.[363] The bimetallic clusters were formed by simultaneous reduction of two metallic salts. Optical properties indicate kinetically controlled core−shell structures, with the most easily reduced (noblest) metal (Ag or Au) nucleating first to form the core, which acts as a nucleation site for formation of a shell of the other metal, yielding $(Ag/Au)_{core}Pt_{shell}$ structures. Surface energies, which are lower for Ag and Au than for Pt, mean that the thermodynamic product should have the reverse $Pt_{core}(Ag/Au)_{shell}$ structure.

Belloni and co-workers used γ-ray radiolysis to generate both $Au_{core}Pt_{shell}$ and $Pt_{core}Au_{shell}$ bilayered nanoparticles.[95] The $Au_{core}Pt_{shell}$ arrangement is consistent with the fact that Au is more noble (easier to reduce) than Pt, making this the kinetic product, though surface and cohesive energy would favor the reverse configuration. In fact, the inverse (Pt_{core}-Au_{shell}) ordering can be produced by a two-step reduction, depositing Au onto preformed Pt clusters), or by a one-step reduction of a solution containing $[Au(CN)_2]^-$ (with a very low redox potential) and $[PtCl_4]^{2-}$ in the presence of PVA.[95] It was not possible to generate intermixed Pt−Au particles radiolytically, perhaps because the dose rate was not sufficiently high to overcome rapid interion electron transfer.

Henglein reported the synthesis of both $Au_{core}Pt_{shell}$ and $Pt_{core}Au_{shell}$ clusters: $Au_{core}Pt_{shell}$ by hydrogen reduction of Pt salts onto preformed Au particles and $Pt_{core}Au_{shell}$ by radiolysis of gold salts onto Pt particles.[364] The optical absorption spectra of both types of core−shell particles were measured. For the $Pt_{core}Au_{shell}$ clusters, a surface plasmon peak (absent for pure Pt clusters) is evident, moving to longer wavelengths and becoming more intense with greater Au deposition onto the Pt core. For the $Au_{core}Pt_{shell}$ clusters, the reverse is observed: the Au plasmon grows successively weaker and shifts to shorter wavelengths as more Pt is deposited onto the Au core. The $Au_{core}Pt_{shell}$ particles were also found to catalyze the reduction of Ag^+ ions, leading to onion-like trimetallic Au−Pt−Ag clusters.[364] Femtosecond laser experiments have subsequently revealed that the Pt_{core}-Au_{shell} nanoparticles have very large electron−phonon coupling constants, giving rise to electron−phonon coupling times ($T_{e-ph} \approx 200$ fs) which are roughly one-third of those for pure Au particles ($T_{e-ph} \approx 650$ fs).[365] This change is observed even for low Pt concentrations because Pt has a much larger density of electronic states near the Fermi level compared with Au.

Finally, Cao et al.[366] produced $Au_{core}Pt_{shell}$ nanoparticle assemblies by Pt deposition onto self-assembled Au colloids.

Theoretical Studies. Ge and colleagues recently reported a DFT study of the structures and energetics of Pt−Au clusters with up to 13 atoms for various compositions.[367] Their calculations indicate some segregation of Au and Pt in these small clusters, although some intermixed particles do have negative enthalpies of formation, unlike the bulk alloy at low temperatures. For $PtAu_{12}$ the lowest energy isomer has icosahedral symmetry, with the Pt atom occupying the center of the icosahedron, while for $Pt_{12}Au$ the lowest energy homotop has C_{5v} symmetry, with the Au atom occupying a surface vertex site. These results are consistent with the higher cohesive energy and surface energy of Pt compared with Au. DFT calculations also indicate that CO binds strongly to both the Pt and Au atoms (and more strongly than to bulk Pt−Au alloys), with the strongest binding being to Pt atoms which are adjacent to Au.[367] This may help to explain the activity of Pt−Au nanoalloys for the electrocatalytic oxidation of CO.[368]

5.4. Other Transition-Metal–Transition-Metal Bimetallic Nanoalloys

Some of the research that has been carried out on the synthesis and structural characterization of bimetallic transition-metal nanoalloys, other than those described in the

previous section, is presented here. Examples can also be found under catalytic applications in section 6.

5.4.1. Fe–Co

Sudfeld et al. reported the synthesis of Fe−Co nanoalloys formed by the pyrolysis of a mixture of $Fe(CO)_5$ and $Co_2(CO)_8$ in dichlorobenzene solution.[369] Fe−Co intermixed particles were found to form chains of particles (in contrast to pure Co, which forms 2D arrays of 100 nm diameter domains separated by 50 nm). The mean particle diameter was measured by TEM to be approximately 4.9 nm (the mean diameter for pure Co particles = 6.2 ± 1.31 nm). EDX measurements revealed the composition of the nanoparticles to be approximately $Fe_{0.70}Co_{0.30}$.

Zubris et al. recently reported the synthesis of Fe−Co nanoalloys, again by co-decomposition of $Fe(CO)_5$ and $Co_2(CO)_8$ with the particles being stabilized by polystyrene.[370] By a careful study of the mechanism and kinetics of the decomposition of the organometallic precursors, these investigators have been able to control the co-decomposition process and thus control the microstructure and morphology of the resulting nanoalloys, ranging from crystalline Co_{core}-Fe_{shell} particles (of average size 14.2 ± 2.9 nm) to noncrystalline more-mixed particles (average size 21.7 ± 7.4 nm).[370]

5.4.2. Fe–Ni

In 2000, Parks et al. reported the investigation of the isomeric structures of small (up to 53 atoms) Ni-rich Fe−Ni clusters in a molecular beam by investigating their uptake of N_2,[371] using the technique they previously employed for pure Ni clusters.[372,373] Reduced N_2 adsorption is observed for Fe−Ni nanoalloys if the Fe atoms are on the surface of the cluster, compared with pure Ni clusters, which is consistent with the low adsorption of N_2 on pure Fe clusters. In general, however, the most stable isomers (in the range where pure Ni clusters are icosahedral or polyicosahedral) are found to be those with Fe atoms in the core, leading to unchanged N_2 uptake, compared with the pure Ni cluster. Metastable isomers with surface Fe atoms are also detected, though they are observed to convert to the more stable (core Fe) isomers on millisecond timescales. Unlike other nuclearities, for Ni_{26}, replacing a single Ni atom by Fe leads to a clear change in geometry and a different N_2 uptake.

Recent DFT studies by Sahoo et al.[374] of the chemical ordering of icosahedral Fe−Ni clusters of size 13 and 55 confirmed that Fe atoms preferentially occupy core sites, while Ni atoms are scattered to maximize Fe−Ni bonds and then segregate to the surface.

5.4.3. Co–Ni

In a recent article, Brayner and co-workers reported the templated growth of Co−Ni nanoalloys (as well as Co and Ni particles) in polysaccharidic alginate biopolymers by the co-reduction of Co^{2+} and Ni^{2+} salts under flowing H_2 with the reaction proceeding via formation of gelled capsules.[104] After reduction at 350 °C, XRD and TEM measurements show that the Co−Ni−alginates yield Co−Ni fcc solid solution nanoalloys (rather than the ordered cubic CoNi phase) with particle sizes of approximately 10 nm. SQUID measurements show that, as for the pure Co and Ni particles, the Co−Ni particles are ferromagnetic at 2 K. The authors report that extension of this templating synthesis approach to Fe, Ru, and Au clusters is under investigation.[104]

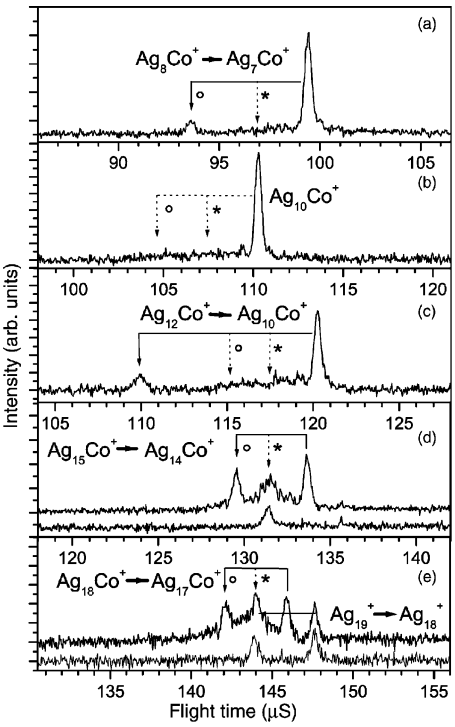

Figure 32. Delayed fragmentation of Ag_8Co^+ (a), $Ag_{10}Co^+$ (b), $Ag_{12}Co^+$ (c), $Ag_{15}Co^+$ (d), and $Ag_{18}Co^+$ (e). The main fragmentation channel is given by a solid arrow and labeled. The expected position of the mass peaks after loss of silver and cobalt monomers are marked by o and *, respectively. The bottom curves in panels d and e are signals recorded without cobalt in the cluster beam and give the fragmentation paths of Ag_{n+1}^+. (Reprinted from ref 380, Copyright 2006, with permission from Elsevier.)

5.4.4. Co–Cu

Co−Cu nanoalloys have attracted interest due to the GMR effect observed for Co clusters embedded in Cu matrices, where the average magnetization per Co atom is significantly lower (0.25−1.3 μ_b) than for thin Co films.[375]

Theoretical calculations have been carried out by Wang and co-workers using a GA search method coupled with a Gupta potential on Co−Cu clusters with up to 147 atoms.[172,172,376,377] For most of the sizes and compositions studied, icosahedral cluster geometries were observed. Surface segregation of Cu was also observed, which is favored by the lower surface energy and cohesive energy of Cu, compared with Co. On the basis of DFT calculations, it was predicted that coating a Co cluster with two layers of Cu should lead to the Co core becoming nonmagnetic.[377]

5.4.5. Fe–Ag

It is known that Fe and Ag are mutually insoluble, both in the liquid and in the solid state, though Fe−Ag solid solutions can be prepared by ion implantation or sputtering and thermal evaporation. Andrews and O'Brien reported the preparation of Fe−Ag nanoparticles by pulsed supersonic expansion of pressed powder mixtures of Ag and Fe.[13] Gram-scale quantities of Fe−Ag particles (D < 10 nm) were formed by direct combination of metal atoms in a rotating cryostat. There is no evidence for segregation in small Fe−Ag clusters, despite the fact that the noble-metal Ag has weaker intermetallic bond strengths and lower surface energy than Fe. It should be noted, however, that the presence of surface-coordinated CO ligands has been shown to favor segregation of Fe to the surface in small organometallic

clusters such as $[Ag_6Fe_3(CO)_{12}(PPh_2)_3CH]^-$.[33] Stronger Fe−CO bonding also leads to Fe occupying the surface capping sites in $[Fe_6Pd_6(CO)_{24}H]^{3-}$.[378]

DFT calculations on bare Fe−M and CO−Fe−M clusters (M = Cu, Ag, Au) have shown that (as for most bulk alloys) there is negligible intermetallic electron transfer in the absence of the CO ligands but that the electron-withdrawing effect of CO helps to drive electron transfer from the more electronegative M atom to the Fe.[379]

5.4.6. Co–Ag and Co–Pd

Recently, Janssens et al.[380] performed a combined experimental−theoretical study of Co−Ag clusters for sizes up to 50 atoms. The clusters were produced by laser evaporation and inert gas condensation. The mass spectra of silver-rich clusters showed clear quantum-size effects, which were absent on the cobalt-rich side. Photofragmentation experiments revealed that the detachment of neutral Ag atoms is the favorable channel (see Figure 32). This finding agreed with the MC simulations based on the embedded atom energetic model. These simulations showed that Ag atoms tend to occupy surface sites. Studies of larger clusters within the same model confirmed this tendency[186,381] (see also section 7).

Recent DFT studies by Ferrando et al.[152] confirmed that Ag atoms tend to occupy surface sites. Optimizing polyicosahedral structures of sizes 34 and 28, Ferrando et al. found that the clusters with the lowest excess energy have intermediate compositions. This is at variance with the results for Cu−Ag and Ni−Ag clusters, systems that present the same size mismatch as Co−Ag and the same tendency to surface segregation of Ag. In fact, in Cu−Ag and Ni−Ag the clusters with lowest excess energy were perfect core−shell structures formed at Ag-rich compositions. This peculiar behavior of Co−Ag was attributed to specific quantum effects, i.e., to the interaction of the magnetic moments of the buried Co atoms in core−shell structures. This interaction opposes the energy gain due to cluster shrinking and strain relaxation.

Carlsson et al.[382] produced Co−Pd nanoparticles on Al_2O_3 thin films by sequential deposition of the metals. They found that Pd shells easily form on preexisting Co clusters, while much more Co was required to coat preformed Pd particles because Co nucleated between Pd particles as well as on top of them.

5.4.7. Co–Rh and Ni–Rh

Ferromagnetism has been predicted for small Rh clusters (with fewer than 50 atoms) and detected experimentally by Stern−Gerlach-type cluster molecular beam deflection,[132,133] the spin polarization arising as a finite size effect. Inclusion of paramagnetic ions (such as Co and Ni) in Rh clusters is also expected to give rise to interesting spin polarization effects.[383]

Casenove, Respaud, and co-workers synthesized PVP-stabilized Co−Rh nanoalloys via the co-decomposition of organometallic precursors.[384,385] It was found that alloying with Co led to successive loss of the fcc ordering of the Rh particles. For particles under 2 nm, HRTEM, EXAFS, and wide-angle X-ray scattering measurements show that Co-rich clusters have noncrystalline polytetrahedral packing while Rh-rich particles have defective fcc structures (though they become more regular at increased temperatures).[385] Larger particles (4−6 nm), however, show a greater stability of bulk-like structures (hcp for Co-rich and fcc for Rh-rich compositions).

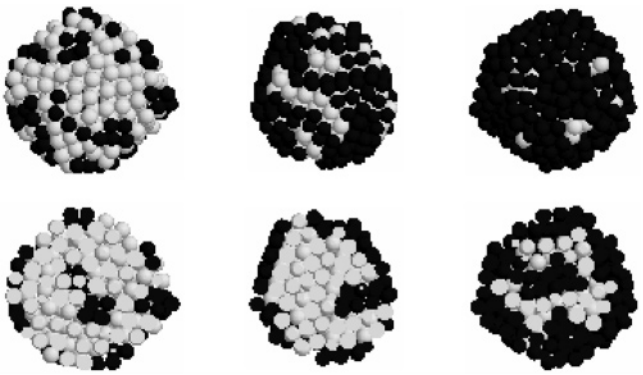

Figure 33. CoRh clusters after simulated annealing at 1600 K. Co and Rh atoms are represented in dark and light gray, respectively: (top row) Clusters surfaces and (bottom row) cross section of the same clusters. From left to right, the proportion of Co is 25%, 50%, and 75%, respectively. (Reprinted from ref 21, Copyright 2006, with kind permission of Springer Science and Business Media.)

EXAFS measurements on Rh-rich Co−Rh nanoparticles indicate a segregated stucture, with Co occupying the surface sites, though the analysis was more ambiguous for other compositions.[385] Recent MD and MC simulations (using a Gupta-like many-body potential) obtained a good agreement with the experiments concerning the composition-dependent nearest-neighbor distance. These simulations confirm the surface segregation of Co, though the innermost core sites are predicted to be occupied by Co atoms for Co-rich compositions,[21] leading to a three-shell structure (see Figure 33).

Due to the lower surface energy of Co, migration of Co to the surface is to be expected for Rh-rich compositions, while the greater size of Rh favors surface migration of Rh for Co-rich compositions.[385] This is consistent with measurements by Ellison et al. on the bulk alloys, which found surface migration of the (minority) solute metal.[386] As Fromen et al. noted,[385] there should be no strong enthalpic drive toward ordered mixing, as evidenced by the fact that, in the bulk, Co and Rh form solid solutions at all compositions.

Magnetic measurements on these Co−Rh nanoparticles have shown a strong enhancement (by up to two times) of the magnetization compared with the bulk alloys. This has been attributed to a combination of size reduction and coupling with a magnetic 3d element (Co), leading to an enhanced induced electronic spin polarization of the 4d (Rh) atoms, while retaining the magnetism due to the Co atoms.[384] Similar effects have been predicted by Sondón and Guevara for Ni−Rh nanoparticles, based on MD atomistic modeling and simulation of magnetism using a Hubbard-like Hamiltonian.[387] Icosahedral-like structures are predicted for these nanoparticles with (as for the Co−Rh particles) Rh atoms tending to occupy core sites. In a more recent study, Sondon et al.[388] optimized the structure of Ni−Rh clusters of size 55 and varying composition within an improved SMATB model and calculated their magnetic properties by solving self-consistently a tight-binding Hamiltonian in the unrestricted Hartree−Fock approximation. Their structural optimization confirmed the preference for icosahedral structures at all compositions. A magnetic moment was found in pure icosahedral Ni but not in pure Rh. However, introduction of

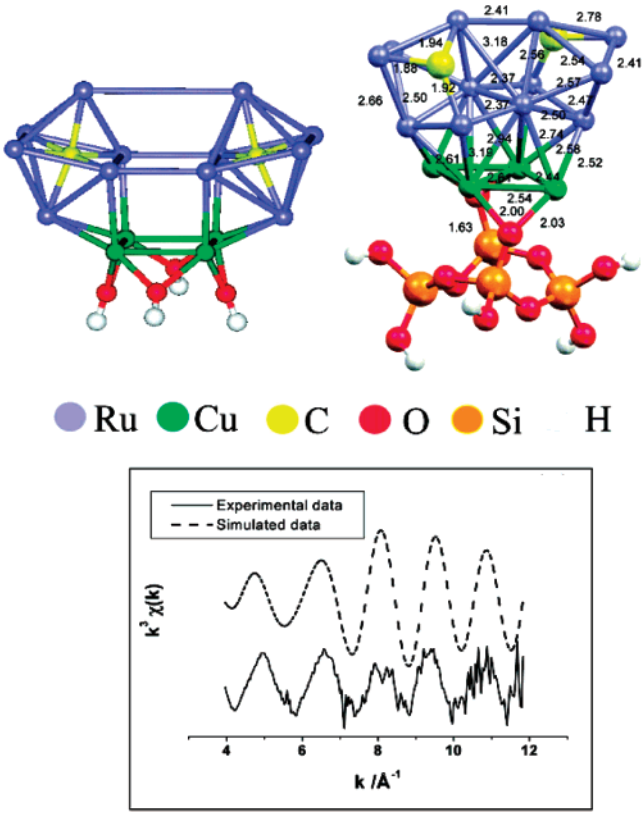

Figure 34. (Top left) Model of $Ru_{12}Cu_4C_2$ from force field calculations.[391] (Top right) The same after DFT relaxation.[391] (Lower panel) Comparison of the Cu K-edge EXAFS data with the spectrum calculated taking the structural details from the DFT calculations. (Top panel: Reprinted with permission from ref 41. Copyright 2003 American Chemical Society. Lower panel: Reprinted from ref 391, Copyright 2001, with permission from Elsevier.)

a few Rh impurities in a Ni cluster enhanced its magnetic moment. For intermediate compositions, Sondon et al. found isomers which lie very close in energy but present very different magnetic properties.

Considering Ni−Rh carbonyl clusters, $[Rh_5Ni_6(CO)_{12}H_x]^{3-}$ consists of a Rh_5 core capped by six Ni atoms.[389] This segregation is driven by the higher enthalpy of sublimation (i.e., cohesive energy) of Rh.[390]

5.4.8. Cu–Ru

Ru and Cu are virtually immiscible in the bulk, but nanoparticles exhibit selective inhibition of hydrogenolysis, similar to that observed by the completely miscible Cu−Ni system. This affords the possibility of generating new catalysts with structural and bonding properties that are not a simple combination of the constituent elements.[316]

Thomas, Johnson, and co-workers generated Cu−Ru catalysts ($Ru_{12}C_2Cu_4$) anchored to porous silica by the thermal decomposition of the organometallic precursor $[Ru_{12}C_2(CO)_{32}Cu_4C_{12}]^{2-}$.[41] Theoretical models of the catalyst[391] and experimental and simulated EXAFS data[41] are shown in Figure 34.

5.4.9. Fe–Pt and Co–Pt

Fe−Pt and Co−Pt alloys (and nanoalloys) are candidates for ultrahigh-density magnetic recording media due to their high magnetic anisotropy with associated high magnetic susceptibility and coercivity. Thus, intermixed Fe−Pt and

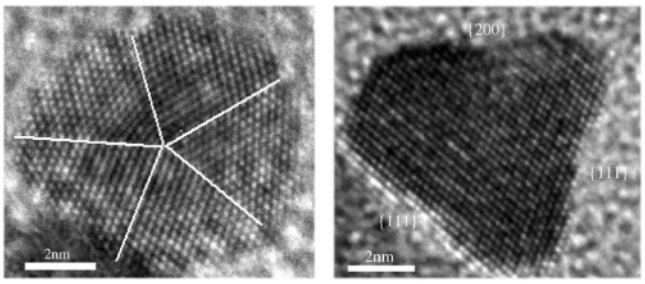

Figure 35. HRTEM images of Marks-decahedral (left) and truncated tetrahedral (right) Fe−Pt nanoparicles. (Reprinted from ref 396, Copyright 2006, with permission from Elsevier.)

Co−Pt particles exhibit ferromagnetic-like behavior, which can be contrasted to pure Co or Fe clusters which are strongly fluctuating superparamagnets.[392,393] Co−Pt also exhibits good chemical stability toward corrosion.[394]

In 2001, Park and Cheon reported the synthesis of "solid solution" (intermixed) and core−shell-type Co−Pt nanoalloys with diameters below 10 nm.[394] The Co−Pt particles were formed by redox transmetalation reactions without the need for additional reductants. Reaction of $Co_2(CO)_8$ with $Pt(hfac)_2$ (where hfac = hexafluoroacetylacetonate) led to solid−solution-type alloys, e.g., $(CoPt_3)_N$, while reaction of preformed Co nanoparticles with $Pt(hfac)_2$ led to $Co_{core}Pt_{shell}$ nanoalloys. Both reactions result in fairly monodispersed nanoparticles (σ < 10%), with compositions which can be tuned by altering the ratio of reactants. Structural properties of both types of particles were investigated by TEM, UV−vis, IR, EDX, and XRD measurements.

For the solid−solution nanoalloys, SQUID measurements of the blocking temperatures (T_B) and coercivities (H_c) gave the following values: for $CoPt_3$, T_B = 20 K and H_c = 6900 Oe at 5 K; for CoPt, T_B = 15 K and H_c = 5300 Oe at 5 K. These values are higher than those for pure cobalt clusters of similar sizes because of the increased anisotropy associated with alloy formation. The solid−solution nanoalloys are superparamagnetic at 300 K. Magnetic studies of the Co_{core}-Pt_{shell} particles, however, reveal that the magnetic properties are similar to those of pure Co clusters with the same size as the Co core (e.g., T_B = 15 K, H_c = 330 Oe at 5 K), so the Pt shell does not significantly affect the magnetism of the Co core.[394]

More recently, Park, and co-workers have shown (using TEM and EXAFS) that Co−Pt nanoparticles generated by the redox transmetalation reaction have average diameters of 6.4 nm with fcc packing and $Co_{core}Pt_{shell}$ structures.[395] (EDS measurements indicate a composition of $Co_{0.45}Pt_{0.55}$.) They used EXAFS and XANES to follow the thermally induced (annealing at 700 °C for 12 h) dynamic phase transition of the $Co_{core}Pt_{shell}$ particles to face-centered tetragonal (fct) solid solution intermixed CoPt particles. While the core−shell clusters are superparamagnets, the intermixed particles are found to be ferromagnetic at room temperature, which may lead to applications in ultrahigh-density memory devices or biomedical magnetic sensors.[395]

Evans and co-workers used microwave heating for the stoichiometrically controlled synthesis of Fe−Pd and Fe−Pt nanoparticles from $Na_2Fe(CO)_4$ and $M(acac)_2$ (M = Pd, Pt) in the presence of various surfactants.[139,397] In the Fe−Pt case, this has proved to be an efficient method for the rapid production of small (2 nm) monodispersed intermixed fcc Fe−Pt particles. Subsequent heating at relatively low temperature (364 °C) leads to formation of the ordered phase,

which is of interest for magnetic applications.[139,397] This method compares favorably with previous approaches involving thermal decomposition of $Fe(CO)_5$ and reduction of $Pt(acac)_2$, where the fcc−fct transition could only be accomplished at higher temperatures (over 500 °C), where significant particle agglomeration is observed (work cited in ref 397). Evans and co-workers have also shown that microwave reduction at high pressures yields a mixture of fcc and fct particles.

Stappert et al.[398] produced free Fe−Pt by gas-phase condensation, finding a size-dependent structural transition from multiply twinned (of 5.9 nm diameter) to fcc structures (of 7.6 nm diameter). Recently, Tan et al.[396] produced Fe−Pt nanoparticles by condensation of sputtered atoms, confirming a size-dependent structural change, however without a clear-cut transition to fcc particles at large sizes. In fact, they found icosahedra for sizes of 4 nm and a mixture of different shapes in the size range 5−15 nm (see Marks-decahedral and truncated tetrahedral particles in Figure 35) and attributed their findings to possible kinetic trapping phenomena during the growth of the nanoparticles.

In a recent communication, Petridis and co-workers reported the synthesis and characterization of CoPt nanopolypods by thermolytic reduction of $Pt(acac)_2$ and $Co(OAc)_2$ in a high boiling solvent (which also acts as a capping agent).[399] Nanopolypods are aggregates (of approximately 50 nm dimensions) of CoPt nanorods (average diameter 5 nm; average length 20 nm) with CoPt nanorods having first been synthesized in ionic liquids by Wang and Yang.[293] Selected area electron diffraction and XRD measurements show that the nanopolypods have an fcc structure, average composition $Co_{0.4}Pt_{0.6}$, and Pt enrichment in the center (with a core composition of $Co_{0.3}Pt_{0.7}$ and a $Co_{0.48}Pt_{0.52}$ shell).[399] In agreement with the work of Park et al.,[395] annealing at 700 °C in a reducing atmosphere leads to formation of quite highly ordered fct Co−Pt alloys. All of the phases observed are ferromagnetic. The authors report that new nanostructures of Fe−Pt and Ni−Pt nanoalloys have also been generated in this way.[399]

Theoretical Studies. Fortunelli and Velasco used extended Hückel theory to study Fe−Pt nanoclusters with icosahedral, cuboctahedral, and truncated octahedral geometries in the range of 13−309 atoms.[400] Exothermic mixing was found to occur, though with the Fe atoms segregating to the core of the Fe−Pt nanoparticles, with crystal-like (cuboctahedral and truncated octahedral) packing being preferred over icosahedral.

Müller and Albe[194] studied, by rigid-lattice MC simulations, the order−disorder transition in truncated octahedral nanoparticles for compositions around 50 atom % Fe, at which the $L1_0$ ordered phase is formed in the bulk. The energetics of the system was described by a pair-interaction Hamiltonian, including first- and second-neighbor interactions, whose intensity was fitted to experimental data on bulk and surface properties of the macroscopic alloy. In the case of nanoclusters (see Figure 36), Müller and Albe found a practically perfect $L1_0$ phase at the ideal composition 50 atom % Fe. For small deviations around this composition, they found that excess Pt atoms tend to segregate to facets and edges, while excess Fe atoms tend to alloy in the bulk and in the facets. A significant decrease of the ordering temperature with decreasing size was found (see Figure 37). This effect has been confirmed recently by the MC simulations of Yang et al.,[401] who found that the disordering mechanism at high temperature is surface induced.

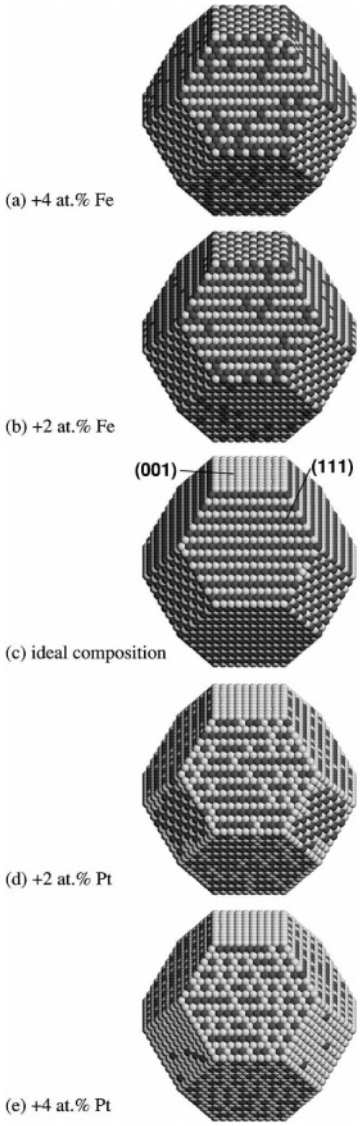

Figure 36. Snapshots from MC simulations of FePt truncated octahedral nanoparticles at compositions close to 50 atom % Fe. Fe and Pt atoms are in dark and light gray, respectively. (Reprinted with permission from ref 194. Copyright 2005 American Physical Society.)

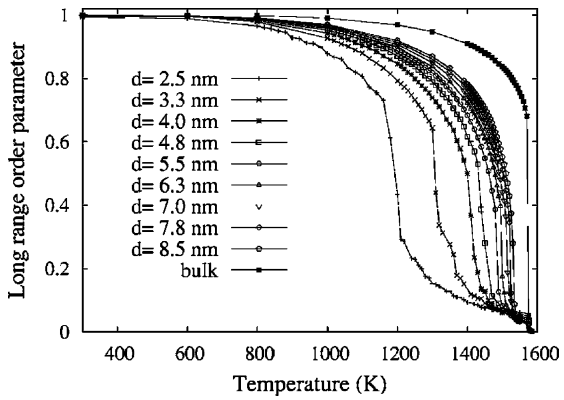

Figure 37. Dependence of ordering on temperature for truncated octahedral Fe−Pt particles of different sizes, at 50 atom % Fe composition. The results for the bulk alloy are also shown. (Reprinted with permission from ref 194. Copyright 2005 American Physical Society.)

Wang and co-workers used a GA coupled with a Gupta potential to study Co−Pt clusters with 13 atoms and 38 atoms.[172,173] In both cases, surface segregation of Pt is predicted, with introduction of Pt atoms leading to a dramatic reduction in the magnetic moments of the Co atoms.[172,173] For the 38-atom clusters $Co_{38-n}Pt_n$, truncated octahedral geometries are predicted for the pure Co and Pt clusters and for $n = 1$, 2, and 34−37, with all other compositions giving rise to defective icosahedral structures.[173] In a related study, Kaszkur and Mierzwa used Sutton−Chen potentials[158] in MC and MD simulations of segregation in Co−Pd clusters.[402] In agreement with XRD studies on silica-supported Co−Pd catalysts (for neopentane conversion),[403] Kaszkur and Mierzwa found that Pd segregates to the surface of Co−Pd nanoparticles.[402]

5.4.10. Fe–Au and Co–Au

In 1999, Koga and co-workers described the preparation of Fe−Au nanoalloys, in the gas phase, by thermal vaporization (at 1623 K into a stream of He) of an Au−Fe alloy ingot, followed by deposition on an amorphous carbon film.[404] Starting with an Au−20%-Fe alloy ingot, Au−Fe particles with diameters (measured by HREM) ranging from 2 to 10 nm were generated with approximate composition (measured by EDX) of $Au_{0.89}Fe_{0.11}$ (i.e., 11 atom % Fe). The reduced percentage of Fe in the particles, as compared with the ingot source, was attributed to the lower volatility of Fe.[404] The HREM measurements showed that the Au−Fe particles were icosahedral, and this icosahedral morphology was found to be retained in most particles, even after annealing at 723 K for 1 h in vacuo. This is in contrast with the bulk Au−11%-Fe alloy, which is known to phase segregate into Au and α-Fe at 710 K.[231] The authors postulate that in addition to possible electronic effects, stabilization of icosahedral Au particles well beyond the normal size range (typically a few nanometers) by incorporation of 11 atom % Fe may be due to the relief of bulk strain energy caused by the smaller Fe atoms (R(Fe) ≈ 86% R(Au)) occupying the relatively compressed core sites in the icosahedra.[404]

Paulus et al. (also in 1999) reported studies of the magnetic properties of Au-coated Fe and Co clusters.[405] These M_{core}-Au_{shell} particles (with diameters up to around 5 nm) were prepared chemically by reduction of Fe or Co salts by tetraalkylammonium hydrotriorganoborates followed by treatment with $AuCl_3$, which is reduced to Au metal, with some of the Co atoms of the seed particle being oxidized and removed as $CoCl_2$. In the Co−Au case, Au coating was found to significantly reduce the magnetic anisotropy of the Co particles to a value close to that of bulk Co. However, for the Fe−Au particles the magnetic anisotropy remained higher than the bulk Fe value. On the basis of Mössbauer experiments and comparison with bulk Fe−Au alloys, Paulus et al. suggested that the Fe−Au particles are not core−shell particles but rather that mixing has taken place (albeit inhomogeneous mixing).[405]

As pure Fe nanoparticles are unstable to oxidation in air, coating with a noble metal (e.g., gold) offers the possibility of stabilizing the Fe particles to oxidation while retaining the magnetic properties that make them of interest for applications in high-density memory devices. To this end, Zhou et al. reported formation of Fe−Au nanoparticles via a two-stage growth process using inverse micelles.[406] TEM and HREM measurements showed that the resulting particles have $Fe_{core}Au_{shell}$ structures with a 6 nm diameter Fe core and a 1−2 nm thick Au shell. EDS measurements found no oxygen peaks, indicating that the Au coating protects the Fe from oxidation. The magnetic moments of the particles were found to be similar to bulk Fe. The Fe−Au nanoparticles were also successfully assembled in a magnetic field into 1D "nanobands", some of which are over 10 μm in length.[406]

5.4.11. (Ru, Rh, Re)–Pt

Shapley, Nuzzo, and co-workers generated Ru−Pt nanoparticles (supported on a carbon substrate) by temperature-programmed decomposition under hydrogen of a mixed-metal carbonyl precursor, $Ru_5PtC(CO)_{16}$, which was dispersed on carbon black from tetrahydrofuran solution.[407] The resulting nanoalloys were investigated using a combination of EXAFS, EDX, XANES, TEM, and electron microdiffraction. Narrow distributions of particle widths were obtained with average diameters of 1.5 nm and the composition sharply peaked at that of the precursor cluster: Pt:Ru ≈ 1:5. The particles were found to adopt fcc packing (in contrast to bulk Ru_5Pt which is hcp). At low temperatures (473 K), the Ru−Pt particles (with average diameter 0.9 nm) are initially disordered, with Pt enrichment of the core. This may occur due to kinetic growth, with the more noble Pt nucleating first and the Ru forming a shell around it. The Pt core may be responsible for the fcc packing due to epitaxial growth. Similar results have been observed for Re−Pt nanoparticle growth on Si, where Re is reduced at a higher temperature than Pt and a Re shell grows epitaxially on the Pt core to form fcc particles.[408]

At higher temperatures (673 K), the reverse core−shell structure is observed, which is presumably the thermodynamic product, with Pt atoms lying on the surface and a preference for Pt−Pt over Ru−Pt bonds at the interface. $Ru_{core}Pt_{shell}$ segregation has also been inferred by Wieckowski and co-workers on the basis of ^{195}Pt NMR spectroscopy[129] of $Ru_{0.5}Pt_{0.5}$ particles of average diameter 2−3 nm. For these particles, the single, rather narrow ^{195}Pt resonance (see Figure 10C) is clearly shifted from that of bulk Pt.

Recent DFT calculations[409] have considered the $Ru_{31}Pt_6$ cluster adsorbed on carbon, showing segregation of Pt atoms to the cluster top layer within a truncated cuboctahedral structure. The stronger binding of Ru to the substrate was found to be an important driving force to cause Pt segregation.

Recent IR studies of CO adsorbed on 2−4 nm Ru−Pt nanoparticles (formed by the co-reduction of Pt and Ru salts), however, seem to indicate that the particles are intermixed, while smaller (1 nm) particles are believed to phase segregate.[410] A discussion of further studies of Ru−Pt nanoparticles for fuel cell applications is presented in section 6.

The structure of $[Pt_4Rh_{18}(CO)_{35}]^{4-}$, which has a central Pt_4 core, can be rationalized in terms of the stronger M−M bonds of the third-row transition metal (Pt),[411] compared with the second-row metal (Rh). $Pt_{core}Rh_{shell}$ segregation has been inferred from ^{195}Pt NMR spectroscopy of $Rh_{0.2}Pt_{0.8}$ particles, following calcination in air and reduction in hydrogen.[412] The single sharp ^{195}Pt resonance (see Figure 10B) occurs at the position expected for bulk Pt.[129,412] For particles with CO adsorbed on the surface, ^{195}Pt−^{13}C spin−echo double-resonance (SEDOR) experiments confirmed the core−shell segregation.[412]

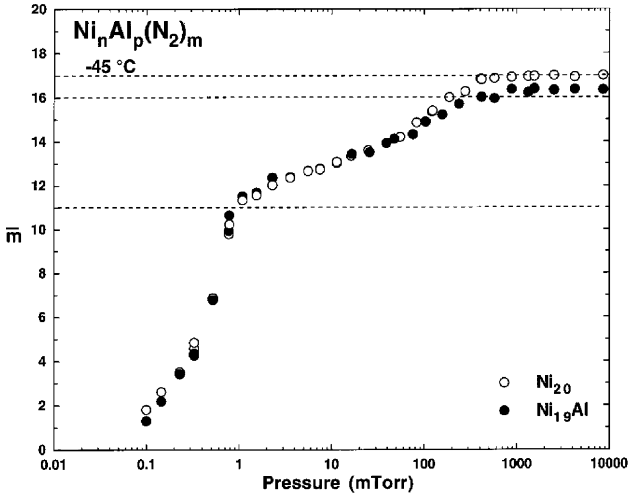

Figure 38. N_2 uptake plots for Ni_{20} and Ni_{19} Al at a flow-tube reactor temperature of −45 °C as a function of N_2 pressure. Horizontal dashed lines are drawn at significant values to guide the eye. (Reprinted with permission from ref 417. Copyright 2002 American Institute of Physics.)

5.4.12. (V,Nb,W)–Au

Synthesis of the bimetallic cluster WAu_{12} was reported in 2002 by Li et al.[413] The existence and stability of this molecule had actually been predicted earlier the same year by Pyykkö and Runeberg[414] on the basis of it having a closed jellium-shell 18-electron configuration. More recent DFT calculations confirmed the stability of this molecule.[415] The isoelectronic anions $[MAu_{12}]^-$ (M = V, Nb) have also been characterized by photoelectron spectroscopy and studied by DFT calculations.[416]

5.5. Transition-Metal–Main-Group-Metal Nanoalloys

5.5.1. Ni–Al

Ni, Al, and most bulk Ni−Al alloys exhibit fcc packing. There are a number of ordered stoichiometric Ni−Al phases: Ni_3Al (fcc, Cu_3Au-type $L1_2$ structure), NiAl (bcc, *B*2 structure, with the Ni and Al atoms adopting a CsCl-type arrangement), and $NiAl_3$ (orthorhombic, DO_{11} structure).[216] Two more complex ordered phases are also known: Ni_2Al_3 and Ni_5Al_3.[418] Mixing in Ni−Al alloys is known to be strongly exothermic ($\Delta_f H = -37.6 \pm 4.2$kJ/mol(atoms) for Ni_3Al[312]).

Massicot et al. produced subnanometer Ni−Al particles by reduction, using NaH, of $Ni(OAc)_2$ and $Al(OAc)_3$.[419] The resulting nanoparticles were found to exhibit high catalytic activity for the reductive dehalogenation of aliphatic and aromatic halides and polychlorinated arenes.

Parks, Riley, and co-workers at Argonne National Laboratory carried out N_2-uptake experiments on Ni_N and $Ni_{N-1}Al$ clusters ($N \leq 20$) in the gas phase, using a flow-tube reactor.[417,420,421] As an example of this work, Figure 38 shows how for Ni_{20} they found saturation at $Ni_{20}(N_2)_{17}$, with no intermediate saturation plateau. These results were rationalized on the basis of Ni_{20} having a waist-capped double-icosahedral (WDI) geometry.[417,420] For $Ni_{19}Al$, they found a similar N_2-uptake plot (as a function of N_2 pressure) as for Ni_{20} but with a final saturation average number of N_2 molecules between 16 and 17 (see Figure 38). A detailed analysis of the uptake results led to the conclusion that Ni_{19}-Al also has a WDI structure, with the Al atom occupying one of the three symmetry-inequivalent positions in the waist five-ring (but not the waist-capping position), as shown in Figure 39.[417] The same group also considered the adsorption of N_2 on Ni_nAl_p clusters with $n + p = 11$, 12, and 13 (see Figure 40). The experimental data about the binding of N_2 to the clusters were completely consistent with the adsorption properties derived from the cluster structures, which were found within the Gupta potential model of eq 7.[421]

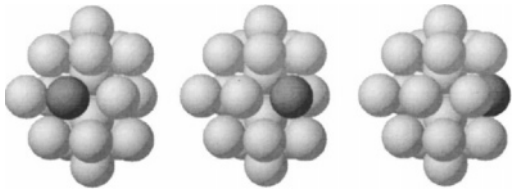

Figure 39. Three possible configurations for $Ni_{19}Al$, having the Al atom (dark sphere) in the waist of a waist-capped double-icosahedral cluster. (Reprinted with permission from ref 417. Copyright 2002 American Institute of Physics.)

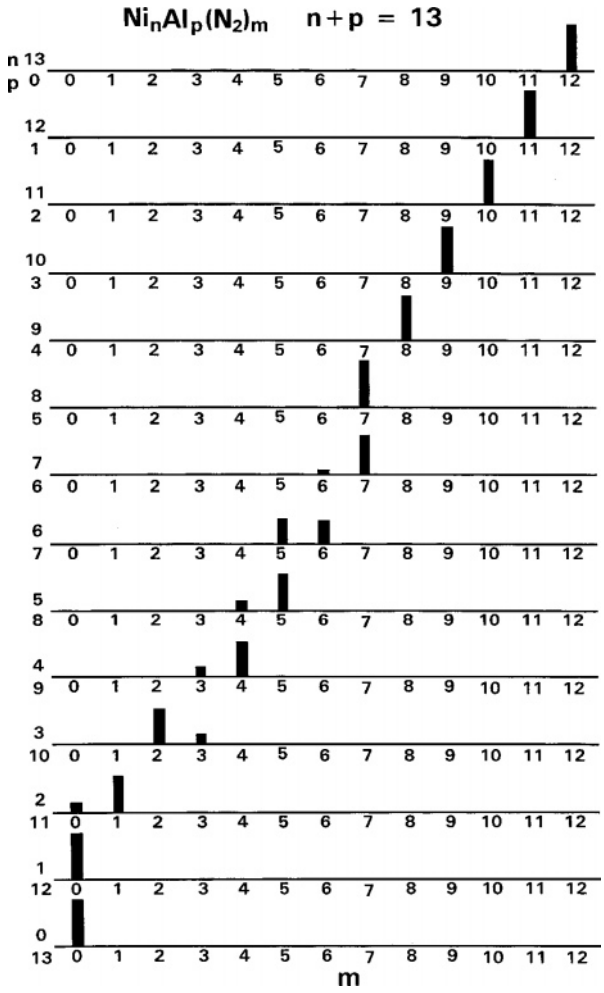

Figure 40. Intensities of the N_2 adsorption channels as a function of composition for Ni−Al clusters of 13 atoms. (Reprinted with permission from ref 421. Copyright 2002 American Institute of Physics.)

Theoretical Studies. Ni−Al clusters have been the subject of many theoretical studies, notably the Gupta potential simulations of Jellinek and co-workers[14−18,421] and Johnston and co-workers[241,422,423] and the EAM and DFT calculations of Gallego and co-workers.[424,425] Ni−Al nanoparticles have become useful models for investigating those factors which

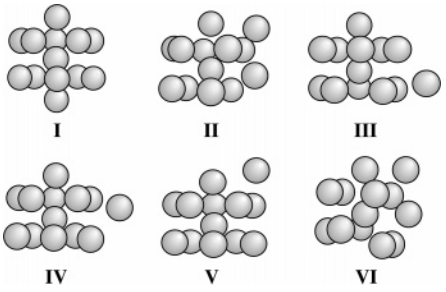

Figure 41. Six lowest energy isomers of Al_{13} obtained using the Gupta potential. Their energies are as follows: (I) −33.812, (II) −33.085, (III) −33.066, (IV) −33.060, (V) −33.037, and (VI) −33.013 eV. (Reprinted from ref 14, Copyright 1999, with kind permission of Springer Science and Business Media.)

are responsible for determining the atomic ordering or segregation in alloy nanoclusters.

As discussed in section 4.3, Jellinek and Krissinel developed a general definition of mixing energy and mixing coefficient and introduced a partitioning of the manifolds of structural forms of alloy clusters into hierarchical classes, such that within each class the energy ordering of its homotops is governed by the mixing coefficient.[14,15] They used their analysis to characterize the energy spectra of structural forms of 12-, 13-, and 14-atom Ni−Al alloy clusters.[14,15,421] In particular, they obtained all the possible homotops for all the possible compositions for a finite number of isomeric forms that represent low-energy structures of the pure Al_{12}, Al_{13}, and Al_{14}. Figure 41 shows the first six lowest energy isomers of Al_{13} that were used as initial geometrical templates for the alloy 13-mers. All six either correspond to or are based on icosahedral packing.

The distributions of the optimized configurational energies of the homotops obtained for the first four (of the six considered) isomeric forms of the Ni_6Al_7 cluster are shown in Figure 42. For an alloy cluster of a given size and composition, the energy ordering of its isomers is defined by the energies of their corresponding most stable homotops. As is clear from the figure, the composition affects the energy ordering of the different isomeric forms. The homotop energy spectra of the three higher energy isomers of Ni_6Al_7 are quite similar. They overlap only a little with the homotop energy spectrum of the most stable icosahedral isomer. For each isomeric form, the part of the spectrum that represents the class of homotops with Ni in the center is shifted quite a bit toward lower energies as compared to the part of the spectrum that corresponds to homotops with Al in the center. Some of these features (e.g., the similarity of the homotop energy spectra of the higher energy isomers) are robust in that they persist for all compositions of the Ni−Al 13-mer. Others (e.g., the patterns of the homotop energy spectra of the individual classes or the gap between the homotop energy spectrum of the icosahedral isomer, on one hand, and the homotop energy spectra of the higher energy isomers, on the other hand) change systematically with the cluster composition (for details see refs 14, 15, and 421).

An illustration of such systematic changes is given in Figure 43, which shows the structures and configurational energies of the most stable homotops in the two classes corresponding to every possible composition of the Ni−Al 13-mer. One notices that the energy gap between these homotops decreases as the number of Ni atoms in the cluster increases. The configurational energy of both homotops decreases as the cluster composition gets closer to 50%/50%. This stabilization is caused by maximization of the mixing energy.[14,15,421] One also notices that the most stable homotop in both classes (and, consequently, the most stable isomer) corresponding to all compositions has an icosahedral packing (but not icosahedral symmetry). With the single exception of $Ni_{12}Al_1$, for all compositions the homotop with Ni in the center has lower energy than the one with Al in the center. An important detail to notice, though, is that the icosahedral homotops of $Ni_{12}Al_1$ with Ni and Al in the center have, as defined by the Gupta potential,[14,15,421] very close energies. Taking into account the finite accuracy of this potential, these two homotops are best characterized as having comparable energies and stability.

The most stable structures of the Ni−Al 13-mer shown in Figure 43 as well as those predicted by Jellinek and Krisssinel for the different compositions of the Ni−Al 12-mer and 14-mer[421] are completely consistent with the results of experimental measurements of N_2 uptake by these clusters as a function of their composition performed by Parks, Riley, and co-workers[421] (see Figure 40). The idea underlying these experiments is that N_2 binds to Ni but not to Al, and therefore, saturation uptake levels of N_2 indicate the number of surface Ni atoms in Ni−Al alloy clusters. Theoretical analysis of the composition-dependent patterns of the configurational energies of different isomeric and homotopic forms of the clusters also provided an explanation of the measured multiple saturation uptake channels and their intensities (see ref 421 for details).

Rey et al. performed MD simulations (using EAM) to predict the ground-state configurations of Ni−Al clusters with 13, 19, and 55 atoms for all compositions.[424] In all three cases they found icosahedral structures for all compositions, with a tendency for Al segregation to the surface, though it was found that Ni−Al ordering (which is favored by the strong Ni−Al bonding interactions) and Al surface segregation (favored by the lower surface energy of Al) can coexist.[424] This is similar to the behavior discussed above for Cu−Pd nanoalloys. DFT calculations by Calleja et al. on icosahedrically packed $Ni_{12}Al_1$[425] confirmed the close energetic proximity of the homotops with Al and Ni in the center, with the latter case presenting a slightly lower energy.

Johnston and co-workers reported a detailed study of the structures and relative stabilities of Ni and Al clusters and Ni−Al nanoalloys, with up to 55 atoms, modeled by the many-body Gupta potential.[241,422] For the pure Al and Ni clusters, the lowest energy structures were predicted to be identical for most nuclearities, but different structures were found for clusters with 15−18 atoms—the Al clusters having nonicosahedral structures. For these nuclearities it was observed that replacement of a single atom in a pure Al or Ni cluster by a dopant atom (i.e., an atom of the other type) is often sufficient to change the cluster geometry. The lowest energy structures of Ni−Al clusters were found to be both size and composition dependent. The lowest energy isomers of nanoalloys with the approximate composition Ni_3Al were generally found to have structures based on icosahedral packing, though truncated octahedral (fcc packing) and decahedral motifs were also observed[422] (see Figure 44). In agreement with previous studies, the atom ordering in the mixed Ni−Al clusters was found to depend on maximization of the number of Ni−Al interactions, minimization of the cluster surface energy, and atom size effects.[422] A tendency for Ni−Al mixing was observed (consistent with the strong exothermic mixing in the alloys), although some segregation

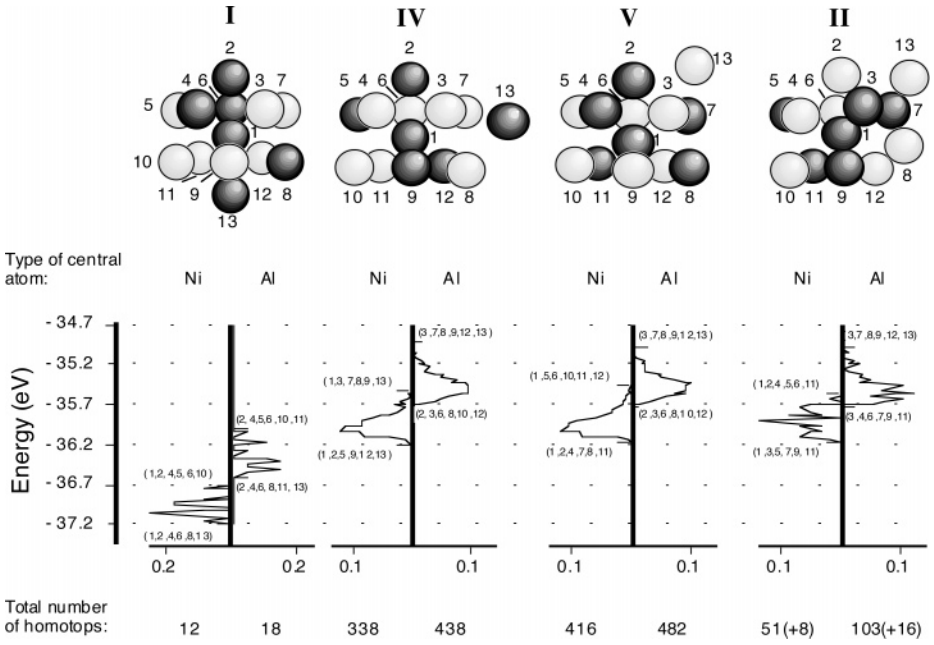

Figure 42. First four isomers of Ni_6Al_7 (with their atomic sites labeled by numbers) and the (normalized) distributions of the energies of their homotops (see refs 14 and 15). Each isomer is represented by its lowest energy homotop (the darker spheres depict Ni, the lighter ones Al; the Roman numerals establish correlation with the "parent" isomers of Figure 41). For each isomer, the distributions of the homotop energies are separated into two classes defined by the type of the central atom. The distributions (histograms) are obtained with a box size of 0.03 eV. The homotops of the highest and lowest energy in each class are indicated by labels in parentheses. The numbers forming a label represent the isomeric sites occupied by Ni atoms in the corresponding homotop. The numbers in parentheses with a "+" indicate the number of additional stationary homotopic structures, which correspond to saddles, rather than minima, of the potential energy surface. These were not included in the distributions. (Reprinted from ref 14, Copyright 1999, with kind permission of Springer Science and Business Media.)

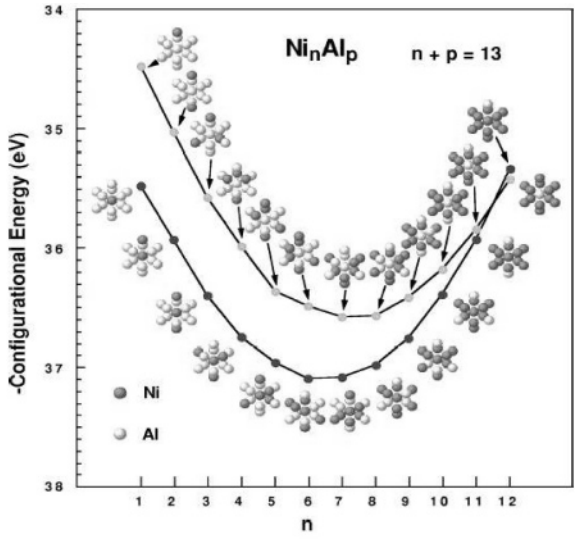

Figure 43. Computed configurational energies and the corresponding lowest energy structures of 13-atom Ni−Al clusters with a fixed type of central atom, plotted as a function of the number of Ni atoms. The upper curve and structures are for clusters with a central Al atom and the lower for clusters with a central Ni atom. (Reprinted with permission from ref 421. Copyright 2002 American Institute of Physics.)

of Al atoms to the surface was noted (due to the lower Al surface energy and larger size of the Al atoms).

In a recent study, Johnston and colleagues performed energy minimizations of 2- and 3-shell cuboctahedral Ni−Al nanoalloy clusters of varying composition with the interatomic interactions again modeled by the Gupta many-body potential.[423] It was found that the peak in binding energy vs fraction of Ni atoms moves toward the composition

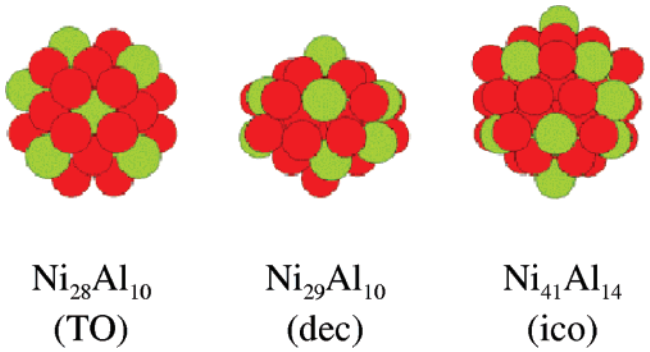

Figure 44. Examples of truncated octahedral (TO), decahedral (dec), and icosahedral (ico) clusters found as lowest energy isomers (using the Gupta potential) for clusters of approximate composition "Ni_3Al".[422] Dark and light gray spheres correspond to Ni and Al atoms, respectively.

of the most stable alloy (Ni_3Al) on increasing the size of the clusters and that the relative stabilities can be explained in terms of the degree of Ni−Al mixing and the nature of the surface atoms. These results are consistent with atomistic simulations by Polak and Rubinovich using the statistical mechanical FCEM.[436] They studied the interplay of ordering and Al surface segregation for cuboctahedral Ni−Al clusters with 13−923 atoms (1−6 shells), predicting that the order−disorder temperature rises from 1030 K for $Ni_{36}Al_{19}$ to 1450 K for $Ni_{205}Al_{104}$ (with a predicted value of 1580 K for bulk Ni_3Al).

Moskovkin and Hou used MD simulations to model the diffusion properties of nanostructured materials assembled from Ni_3Al clusters.[427] The Ni_3Al clusters themselves were obtained from MC simulations, generating (at 700 K and below) clusters with numbers of atoms ranging from hundreds to thousands (with a mean particle size of around

7000 atoms), comprising a stoichiometric $L1_2$ Ni_3Al core, surrounded by an Al-rich shell. Previous studies by Zhurkin and Hou of Ni−Al clusters with up to 10 000 atoms indicated that due to surface segregation of Al, the metastable (*B*2) martensitic phase found in bulk Ni−Al systems is suppressed in free clusters.[204] However, it was also observed that the degree of Al surface segregation decreases with increasing cluster size.

5.5.2. Cu–Zn

Cu nanoparticles are used in the heterogeneous catalysis of methanol synthesis. As the support for such catalysts is often ZnO, there is considerable interest in the interface between the Cu and ZnO and the oxidation state of the Cu in the catalyst. This has led to research into the structures of Cu−Zn and Cu−ZnO particles.

Fischer and co-workers generated Cu−Zn "nanobrass" colloidal nanoparticles by thermolysis of $[Cu(OCH(Me)CH_2NMe_2)_2]$ and Et_2Zn in hexadecylamine.[428] EDX measurements revealed Cu−Zn particles with Cu:Zn compositions of 95:5, 70:30, and 35:65 (starting from precursor Cu:Zn ratios of 90:10, 50:50, and 30:70, respectively). TEM measurements show that the $Cu_{0.95}Zn_{0.65}$ particles have diameters ranging from 5 to 10 nm, while $Cu_{0.7}Zn_{0.3}$ and $Cu_{0.35}Zn_{0.65}$ have mean diameters of around 10 nm. The particles are pseudo-spherical, being more faceted for the higher Zn compositions. UV−vis spectroscopy showed that the Cu surface plasmon resonance (at 558 nm) is observed (and unshifted) for $Cu_{0.95}Zn_{0.05}$, red shifted (to 564 nm) for $Cu_{0.7}Zn_{0.3}$, and disappears for the Zn-rich $Cu_{0.35}Zn_{0.65}$ particles. SAED measurements indicate that even the lowest concentration of Zn (5%) was sufficient to stabilize the Cu with respect to oxidation. Results for $Cu_{0.7}Zn_{0.3}$ indicate a Cu core surrounded by a Cu−Zn alloy shell (probably $CuZn_2$). For the $Cu_{0.35}Zn_{0.65}$ sample, however, SAED measurements indicate that the particles may have regions corresponding to the alloy phases Cu_5Zn_8 and $CuZn_2$ and the α- and γ-phases of CuZn (brass), possibly along with some crystalline Cu.

More recently, the Fischer group reported the synthesis of red-violet Cu−Zn nanoalloys by the co-hydrogenolysis of mesitylene solutions of $CpCu(PMe_3)$ and Cp*Zn in the presence of the surfactant PPO.[429] (This route has also been used to synthesize Cu−Al colloids.[430]) Using a combination of TEM, EDX, SAED, EXAFS, powder XRD, and UV−vis spectroscopy, α- and β-CuZn colloidal particles have been identified. For these brass particles, preferential oxidation of the Zn atoms occurs, leading to core−shell particles with a shell of ZnO surrounding a Zn-depleted Cu−Zn alloy core.[429]

5.5.3. (Cu,Ag,Au)–Main-Group Element

Boyen et al. recently created $Au_{core}In_{shell}$ nanoalloys, based on Au nanoparticles which are deposited on the surface of silica-coated Si.[431] Larger Au cores (up to 3 nm) are prepared by an inverse micelle route (where the stabilizing organic diblock copolymer matrix is subsequently removed by an oxygen plasma, generating Au−oxide particles which are then reduced by a hydrogen plasma). An ensemble of smaller monodisperse Au cores ($D = 1.4$ nm) were generated by taking triphenylphosphine-stabilized Au_{55} clusters and removing the ligands by O plasma etching followed by H plasma reduction of the oxide. Finally, the $Au_{core}In_{shell}$ particles are prepared by evaporation of In atoms onto the bare Au cores. All of the Au particles (except Au_{55}) show a shift of the Au 4f peaks (measured by XPS) to higher binding energy (by 0.9 eV, independent of size) on addition of In. This shift is consistent with formation of $AuIn_2$ intermetallic particles for all sizes, with no unreacted Au left, except for the Au_{55} clusters. This work is promising for future applications in nanoscience, for example, the a posteriori manipulation and tailoring of metallic nanoparticles by subsequent alloying. The stability of Au_{55}, which may be due to its possessing a closed (presumably cuboctahedral) geometrical shell, also opens up the possibility of using it as a chemically inert building block for nanoscale device fabrication.[431]

Core−shell Ag−Cd, Ag−Pb, Ag−In, and Au−Sb nanoalloys have been produced chemically by Henglein et al.[78,432,433] The noble metal (Ag,Au) acts as an antenna for the main-group metal. For small deposits of the main-group metal, a blue shift and damping of the core Ag/Au plasmon resonance is observed, whereas the resonance (if any) of the shell metal dominates for greater shell thickness. For Au−Sb there was found to be competition between mixing and segregation.

Small clusters of Cu, Ag, and Au with Na as well as Cs_x-Au and Na_xAu clusters have also been studied experimentally and theoretically.[434,435]

According to calculations by Kumar and Kawazoe, $CuAl_{12}$ has perfect icosahedral symmetry and may be described as a "P super atom", having (a half-filled jellium 2P shell, with three unpaired electrons.[436] The theory of other transition-metal−main-group heteroatomic clusters has been discussed in a recent review by Kumar.[154]

6. Catalysis by Nanoalloys

Because catalytic reactions occur on the surface of nanoparticles, a significant proportion of the atoms are effectively wasted in the catalytic process. This is particularly important for expensive catalyst metals such as Pd and Pt.[281] In order to cut costs, there is, therefore, considerable interest in synthesizing $A_{core}B_{shell}$ nanocatalysts, where A is a relatively inexpensive metal (e.g., Co, Ni, Cu), which is (generally) less catalytically active, and B is a more expensive, more catalytically active metal (typically Pd or Pt). In certain cases, however, formation of core−shell or intermixed particles may also result in synergistic effects upon the catalytic properties of one or both of the component metals.

6.1. Ni–Pd

Hyeon and co-workers have shown that $Ni_{core}Pd_{shell}$ nanoparticles have much better catalytic activity (for a fixed amount of Pd metal) than pure Pd particles for Sonogashira coupling reactions.[281] Raja et al. have also shown that Ni−Pd particles deposited on mesoporous silica are effective catalysts for the hydrogenation of a range of nitro-substituted aromatics under mild conditions.[285] Recently, Rothenberg and co-workers produced $Ni_{core}Pd_{shell}$ nanoparticles by electrochemical formation of Ni particles followed by chemical reduction of Pd onto the surface of these Ni seeds.[437] The Ni−Pd particles were found to be efficient catalysts for Hiyama cross coupling of phenyltrimethoxysilane and haloaryls, being more active (per Pd atom) than monometallic Pd clusters and binary Ni−Pd particles[437] (see Figure 45).

In contrast to the above findings, Henry and co-workers observed that the catalytic activity of MgO-supported Ni_{core}-Pd_{shell} nanoparticles, for CO oxidation, is similar to that of

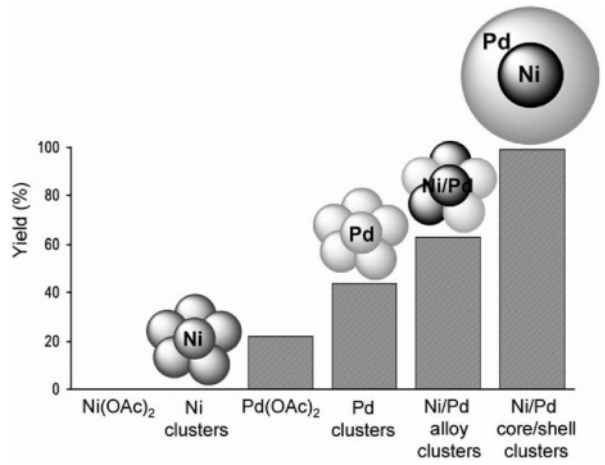

Figure 45. Comparison of the catalytic activity for six different systems in the Hiyama cross-coupling of iodotoluene and trimethoxyphenylsilane: $Ni(OAc)_2$, Ni clusters, $Pd(OAc)_2$, NiPd alloy clusters, and $Ni_{core}Pd_{shell}$ clusters. (From ref 437. Reproduced by permission of the PCCP Owner Societies.)

pure Pd particles.[284] The absence of enhanced catalytic activity (relative to pure Pd) observed in this work and in studies of catalytic hydrogenation of butadiene on binary Ni−Pd nanoparticles[438] is also in contrast to the catalytic enhancement observed for bulk NiPd alloys and thin layers of Pd deposited on Ni(110)) and may be due to edge formation in the particles relieving the strain in the outer Pd layer.[284]

6.2. Ni–Pt

Ni−Pt nanoparticles are of interest as electrocatalysts for oxygen reduction in low-temperature polymer electrolyte fuel cells. As Ross and co-workers have shown, depending upon the method of surface preparation, carbon-supported Ni−Pt nanoparticles (3−4 nm) may even have enhanced activity over pure Pt catalysts for oxygen reduction.[439] As mentioned in section 5, MEAM simulations of Ni−Pt nanoalloys have predicted a core−shell structure with a Pt-rich shell surrounding a Pt-deficient core.[293] As Wang et al. stated, this opens the way for an economical design of Ni−Pt electrocatalysts wherein the expensive, catalytically active Pt segregates to the surface of the cheaper, inactive Ni.[293]

6.3. Pd–Pt

Platinum and palladium are of interest because they are widely used as catalysts (often as finely divided metal particles, in elemental or alloy form) in a number of important reactions, involving hydrogenation. They are used, for example, in catalytic converters in automobiles for the reduction of exhaust gases. A review of the effects of co-metals in catalysis by Pd-based alloys has been presented by Coq and Figueras.[440] Due to their importance in catalysis, Pd−Pt nanoalloys have also been widely studied.

An important catalytic application of Pt and Pd is in the reduction (by hydrogenation) of aromatic hydrocarbons in fuel. This process, however, suffers from the problem of catalyst poisoning by H_2S, formed from sulfur-containing impurities in the fuel. Pt is particularly susceptible to sulfur poisoning, which has been attributed to H_2S-induced agglomeration of the Pt particles.[441] It has been claimed that Pd−Pt alloy particles are more catalytically active for aromatic hydrocarbon hydrogenation and more resistant to sulfur-poisoning than either of the pure metals (i.e., there is said to be synergism),[442] though Renouprez, Rousset, and co-workers challenged these conclusions, stating that the most important interaction is likely to be that between the metallic particle and the alumina or silica support.[141,142]

Rousset and Renouprez investigated the catalytic activity of Pd−Pt nanoalloys (as compared with pure Pd and Pt particles) for the hydrogenation of tetralin (1,2,3,4-tetrahydronapthalene) in the presence of H_2S.[141,142] They found that while Pt is more active than Pd at low sulfur concentrations, Pd is slightly more active at high pressures of H_2S, though no evidence was found for synergism, as the thioresistance and activity of the Pd−Pt nanoalloys always lie between those of the pure metals, taking into account the measured surface compositions of the nanoalloys. This contradicts previous studies by Yasuda and co-workers[443] and Fujikawa et al.,[444] who found maximum sulfur resistance for 80 atom % Pd and 70 wt % Pd, respectively. Rousset and Renouprez suggested that these discrepancies may be due to the different substrates (zeolites and $Al_2O_3-SiO_2$) used in these previous studies or the fact that (for example) the Yasuda studies were carried out in the liquid phase while those of Rousset and Renouprez were carried out in the gas phase. In the case of the nanoalloy $Pd_{0.65}Pt_{0.35}$ on alumina, the reactivity and thioresistance was found to be very similar to pure Pd, in good agreement with the postulated segregation of Pd to the surface[141,142] (LEIS measurements indicate a surface Pd concentration of approximately 87 atom % for nanoalloys with overall composition $Pd_{0.65}Pt_{0.35}$). On the other hand, the $Pd_{0.17}Pt_{0.83}/Al_2O_3$ sample exhibited reactivity and thioresistance which are the average of those for the pure metals, which is consistent with a measured surface composition of 40 atom % Pd:60 atom % Pt.

It has been shown that "normal" core−shell Pd−Pt nanoparticles ($Pt_{core}Pd_{shell}$) with a Pd:Pt ratio of 4:1 exhibit much higher catalytic activity for olefin hydrogenation than pure Pd nanoparticles, with monometallic Pt clusters having the lowest activity.[299,300] Investigation of the catalytic activity, for the hydrogenation of acrylate under mild conditions, of "inverted" ($Pd_{core}Pt_{shell}$) core−shell nanoalloys revealed that for greater than 50 mol % Pt the activity is less than predicted by interpolating between the limits of pure Pt (low activity) and Pd (high activity) clusters.[302] This is consistent with there being fewer surface Pd atoms (than predicted for a random alloy) at higher Pt concentrations. For less than 50 mol % Pt, however, the catalytic activity is greater than the interpolation value, which has been attributed to an electronic effect of the Pt atoms on the remaining Pd surface atoms. In fact, the normalized catalytic activity (taking into account the number of surface Pd atoms) is fairly constant from 30 to 80 mol % Pd and higher (per surface Pd atom) than for pure Pd nanoparticles[302]

Bazin et al. confirmed (in a study of hydro-dearomatization catalysis by $Pt_{core}Pd_{shell}$ nanoparticles) that the optimum Pd/Pt ratio is size-dependent and must be adjusted in order to maintain a Pt core surrounded by a complete Pd shell.[445]

6.4. Ni–Au

In a study of Ni−Au nanoalloys by Molenbroek et al., on-line mass spectrometry and thermogravimetric analyses were used to study the catalytic steam reforming of *n*-butane.[316] It was found that Ni−Au nanoalloy catalysts are active for steam reforming and more resistant than pure Ni particles toward carbon formation on the catalyst, which leads

to catalyst deactivation. The resistance to carbon formation has been attributed to blocking of the high reactivity exposed edge and kink sites on the surface of the particle by the larger Au atoms, as predicted by MC simulations.[316]

6.5. Cu–Pd

Cu−Pd nanoalloys are of interest for improving the selectivity of a number of catalytic processes, such as isomerization and aromatization, CO oxidation and CO hydrogenation.[11] It has been shown, for example, that Cu−Pd nanoalloys have greatly enhanced selectivity (compared with pure Pd clusters) for partial hydrogenation of dienes[446] and that the temperature range in which a high turnover rate can be maintained for CO oxidation is extended by Cu−Pd alloying.[447]

6.6. Cu–Pt

Core−shell and intermixed Cu−Pt nanoparticles (supported on γ-Al_2O_3) were investigated by Eichhorn and colleagues with regard to their catalytic activity for NO reduction.[342] Compared with pure Pt nanoparticles, intermixed Cu−Pt particles exhibited higher selectivity for N_2 formation but reduced overall activity. $Cu_{core}Pt_{shell}$ particles (which are stable under operating conditions of 275−400 °C), however, combine the high activity of Pt with even higher selectivity than intermixed CuPt, while $Pt_{core}Cu_{shell}$ particles showed very little NO reduction.[342] The authors postulated that the enhanced performance of $Cu_{core}Pt_{shell}$ catalysts may be due to near surface alloy (NSA) effects, where subsurface metal and alloy layers affect the binding of adsorbates and, hence, the reaction rate and selectivity.[448]

6.7. Pd–Au

In recent years, Pd−Au nanoparticles have been widely studied for a number of different catalytic applications. Schmid and colleagues investigated the catalytic activity of $Au_{core}Pd_{shell}$ and $Pd_{core}Au_{shell}$ clusters (supported on TiO_2) for the hydrogenation of hex-2-yne to *cis*-hex-2-ene.[12] The presence of the Au core was found to lead to a dramatic increase in catalytic activity compared with pure Pd clusters with the influence of the (fixed size) core decreasing with increased thickness of the Pd shell. The unique catalytic behavior of Pd−Au clusters (compared with pure Pd or Au clusters) arises because their electronic structures are quite distinct from those of the pure metals (due to their differing atomic electron configurations and electronegativities).

Lee et al. found that at 300 K $Au_{core}Pd_{shell}$ particles are efficient catalysts for acetylene cyclotrimerization (to yield benzene) and for related reactions.[347] However, substantial changes in catalytic selectivity (for production of benzene vs *n*-hexane) were observed in the narrow temperature range 300−400 K (before significant Pd−Au mixing has occurred) which has been attributed to a small number of surface Au atoms breaking up certain Pd surface features which are critical in the cyclohexane hydrogenolysis step.[347] Remita et al. also reported the use of Pd−Au and Pd−Ag clusters for the selective hydrogenation of buta-1,3-diene, where the clusters were generated by γ-irradiation of metal-ion solutions.[94]

Bönnemann et al. generated intermixed Pd−Au particles (as evidenced by ^{197}Au Mössbauer spectroscopy and XRD) by the co-reduction of Pd and Au salts, showing that (after embedding in a silica matrix via a sol−gel procedure) they exhibit a high selectivity (>95%) for the catalytic hydrogenation of 3-hexyn-1-ol to *cis*-3-hexen-1-ol.[51,449]

Wong and co-workers used $Au_{core}Pd_{shell}$ particles as catalysts for the hydrodechlorination of trichloroethene in water at room temperature under a hydrogen atmosphere.[349] This is a process of great environmental importance as trichloroethene is one of the most common organic groundwater pollutants and highly toxic. Wang and Zhang also studied the use of Pd-coated Fe nanoparticles for the same process.[90] In Wong's study, the Pd−Au nanoparticles were found to be more active than pure Pd clusters, Pd black, or Pd/Al_2O_3 powders, while pure Au nanoparticles are inactive. The greatest enhancement of catalytic activity was observed for a submonolayer coverage of Pd on the Au particles. The catalytic enhancement may be due to Au promotion of Pd activity (via electronic or geometric effects) or direct involvement of the exposed Au surface.

Schaak et al. recently reported that PVP-stabilized $AuPd_4$ alloy nanoparticles exhibit improved selectivity (compared with conventional Pd/SiO_2-supported catalysts) for the catalytic formation of H_2O_2 from O_2 and H_2.[230] Hutchings and co-workers also investigated the use of alumina- and titania-supported Pd−Au nanoalloys for the low-temperature synthesis of hydrogen peroxide.[352,450] Titania-supported Pd−Au catalysts were found to be significantly better than pure Pd or Au nanoparticles. Although uncalcined particles gave higher yields of H_2O_2, these catalysts were less stable, being susceptible to leaching of Au and Pd atoms.[352] Catalysis of CO and alcohol reduction has also been studied by this group.[353]

Rothenberg, Eiser and co-workers reported the growth of Pd, Au, and Pd−Au nanoparticles inside polyelectrolyte shells or microcapsules.[451] The authors state that such microencapsulated clusters show promise as catalysts for the Sonagashira cross-coupling reaction with the cell-like encapsulation giving advantages such as the ability to recover the catalyst from the reaction mixture, thereby yielding both economical and environmental benefits.[451]

In a related study, Goodman and colleagues recently described the synthesis of vinyl acetate by acetoxylation of ethylene using Pd−Au nanoalloy particles supported on high surface area SiO_2[452] and bulk Pd−Au catalysts.[453] TEM-EDS measurements indicate surface Au enrichment in the Pd−Au particles with the enhanced reactivity of the Pd−Au nanoalloys being attributed to the enhanced capacity of the Pd−Au surface for oxygen.[452] This is consistent with the studies of bulk Pd−Au surfaces, where it is found that the reactivity is enhanced for low surface Pd concentrations, where the Pd atoms are isolated, thereby facilitating the coupling of ethylene with acetic acid while preventing formation of undesirable byproducts such as CO_2, CO, and carbon.[453]

6.8. Pt–Au

Using 1,9-nonanedithiol as a cross-linking agent, Pt−Au nanoparticles have been assembled on a glassy carbon electrode surface and used for the electrocatalytic oxidation of methanol with the reaction studied by cyclic voltammetry.[360] Previous studies showed that Pt−Au nanoparticles can also be used for the electrocatalytic oxidation of CO.[368] It is believed that CO oxidation takes place at surface Au sites, while methanol oxidation takes place at Pt.[360]

6.9. Co–Ni

There have been both experimental and theoretical studies on the design of efficient bimetallic nanoparticle catalysts for the growth of single-walled carbon nanotubes.[454,455] Aided by DFT calculations, the high efficiency of Co−Ni nanoparticles as catalysts has been attributed to a tradeoff between the efficiency with respect to initial nucleation (high for Co) and for subsequent growth (high for Ni).[455] Ni−Mo particles have been predicted to be even better catalysts than Co−Ni.[455]

6.10. Co–Pt

Xiong and Manthiram investigated the electrocatalytic activity of bulk Co−Pt alloys in alkaline electrolyte and PEMFCs.[456] The driving force behind this work is to reduce the costs of electrocatalysts by alloying Pt (generally the most efficient single-metal electrocatalyst in PEMFCs) with less expensive metals (e.g., Fe, Co, Ni or Cu). As well as reducing costs, alloying is sometimes accompanied by an improvement (over Pt) for oxygen reduction in both phosphoric acid fuel cells and PEMFCs. This work opens up the possibility of using discrete Co−Pt nanoalloys as electrocatalysts in membrane fuel cells. Ross and co-workers also investigated carbon-deposited Co−Pt nanoalloys for oxygen reduction in fuel cell applications.[439]

6.11. Ru–Pd

Ru_6Pd_6 nanocatalysts supported on mesoporous silica (for low-temperature single-step hydrogenation) have been prepared by Thomas, Johnson, and co-workers by gentle thermolysis of the organometallic precursor $[Ru_6Pd_6(CO)_{24}]^{2-}$.[41,457,458] A clear synergism was observed: the bimetallic particles were found to be more active, selective, and resistant to sulfur poisoning than the corresponding pure Pd or Ru particles.[41]

6.12. Ru–Pt

In Pt-electrode applications in fuel cells, alloying of Pt with other metals enhances the electro-oxidation currents at lower potentials and extends the catalyst lifetime. Ru−Pt nanoparticles, supported on carbon, have found widespread use for catalyzing a variety of fuel cell reactions,[46,459] such as methanol oxidation in so-called "direct methanol fuel cells",[460] as well as in the electrocatalyzed oxidation of methanol.[461] Os−Pt nanoparticles, however, were found to have low catalytic activity for methanol oxidation catalysis.[462] Ru also helps to remove CO, which otherwise poisons the Pt. Oxidation of CO proceeds via oxidation of the Ru atoms on the surface.[463] Alloyed Ru−Pt, Pt−Sn, and Ru−Pt−Sn particles (passivated by CO in solution) have been generated by high dose rate electron beam radiolysis.[95] The nanoparticles have subsequently been impregnated into carbon powder for production of composite fuel cell electrodes.

Considering the electrocatalytic oxidation of H_2 and H_2/CO mixtures, compared with Pt, pure polycrystalline Ru exhibits a much lower activity for H_2 oxidation but a much higher activity for CO oxidation. This is because the Ru−H_2O interaction is strong, leading to Ru−OH_{ad} formation at very low potential. While this species is an intermediate in the oxidation of CO to CO_2, it is not an intermediate for H_2 oxidation and, in fact, inhibits H_2 oxidation.[49] For H_2/CO mixtures, Ru−Pt bulk alloys are much more active than either Pt or Ru individually (as the Pt preferentially oxidizes H_2 while the Ru oxidizes the CO). Bulk Ru−Pt alloys exhibit very strong surface segregation of Pt presumably due to the lower enthalpy of sublimation of Pt compared with Ru and the endothermic mixing.[464] Unlike in the bulk case, however, Ru−Pt nanoparticles can be prepared with surface compositions which are close to the bulk stoichiometry (i.e., they do not show such large Pt surface enrichment), and the electrochemical properties of the 1:1 Pt−Ru nanoalloys resemble those of the 50% surface alloy rather than the Pt-enriched surface.[291]

Russell and co-workers used XAS to study Ru−Pt anode catalysts (on carbon) in situ in miniature proton-exchange membrane (PEM) fuel cells.[50,465] For Ru:Pt compositions of 1:1 (which have previously been shown to provide the most active surface for polycrystalline bulk Ru−Pt and supported alloys[466]), EXAFS measurements showed that the Pt was fully reduced by the hydrogen in the fuel, while the Ru was only fully reduced under conditions of good hydrogen flow and electrochemical contact.[50,465] The Russell group also used a combination of XRD, EXAFS, CV, and half-cell polarization studies to investigate the carbon-supported Ru−Pt nanoparticles (formed by hydrogen reduction of Cp_2Ru deposited on Pt/C) with nominal surface Ru:Pt compositions ranging from 1:4 to 1:1.[50,467] Following exposure to air, EXAFS shows that the Ru is present as an oxide, while XRD does not indicate any bulk Ru−Pt mixing. On reduction, the EXAFS measurements indicate formation of a surface Ru−Pt alloy. Electrochemical measurements suggest that Ru promotes CO oxidation (as in the bulk alloy), as evidenced by the decrease in peak potential and onset potential for CO oxidation. Finally, increasing the Ru content of the surface alloy resulted in an increased CO tolerance and CO oxidation activity.[50,467] The CO tolerance was found to be comparable with that of the commercially available RuPt alloy catalysts (though for different compositions).

Wieckowski, Oldfield, and co-workers used a combination of solid-state electrochemical NMR (EC-NMR), CV, and potentiostatic measurements to study Ru promotion of methanol electro-oxidation by Pt nanoparticle catalysts.[468] ^{13}C EC-NMR spectra show two sites of adsorption of ^{13}CO: on Pt sites and in Pt/Ru domains. The small Knight shifts and weak Korringa relaxation of CO on Pt/Ru indicate a significant decrease in the ligand- and metal-based local DOS at the Fermi energy. Because of the reduced LDOS at the Fermi energy, Ru doping leads to a weakening of the metal−CO bonding (by reducing the metal−CO (d-π*) back-donation), which results in a lower activation barrier to CO thermal diffusion in the Pt/Ru domains.[468] Subsequent ^{195}Pt and ^{13}C EC-NMR measurements of chemisorbed CO on commercially available Ru−Pt alloy nanoparticle catalysts confirm that Ru causes a depletion of the d-electron DOS, but there is also a degree of Pt surface enrichment of the Ru−Pt alloy.[129]

6.13. Rh–Pt

A clear synergistic effect has been observed in the catalytic hydrogenation of crotonic acid to butanoic acid by bimetallic $Pt_{0.2}Rh_{0.8}$ colloids. The most active catalysts have a concentration gradient with increasing Rh concentration toward the surface of the cluster.[31] Pt−Rh nanoparticles have also been used to catalyze the reduction of NO with Pt-rich clusters having higher catalytic activity and also being more active than pure Pt particles.[469]

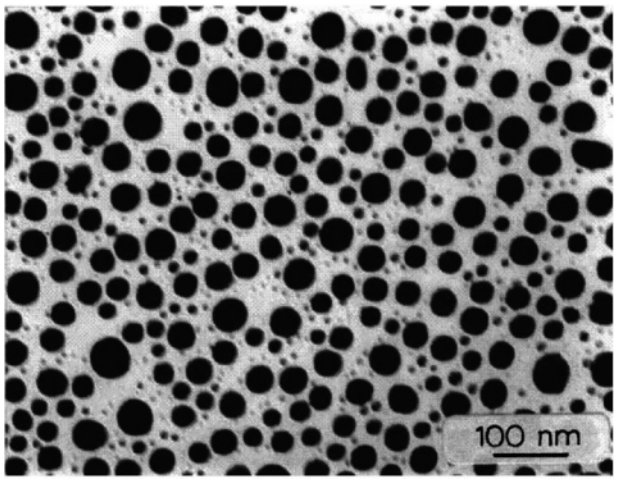

Figure 46. Bright-field TEM image of in-situ-deposited Bi−Pb alloy nanoparticles. The composition of the particles varies from 51 atom % Bi at $R \approx 4$ nm to 56 atom % Bi at $R \approx 25$ nm. (Reprinted with permission from ref 183. Copyright 2004 American Physical Society.)

6.14. Re–Ir

Shapley, Nuzzo, and co-workers generated Re−Ir nanoparticles by hydrogen reduction at 773 K of the bimetallic carbonyl precursor $[Re_7IrC(CO)_{23}]^{2-}$, which was impregnated into high surface area alumina.[38] Two different isomers of the precursor cluster and various different counter cations were studied. It was found that the catalytic activity (for ethane hydrogenolysis) at 500 K varied significantly (from 3 to 63 mmol(CH_4) mol(Re_7Ir)$^{-1}$ s^{-1}), depending on which isomer of the Re_7Ir cluster was used as the precursor and on the countercation. The more active catalysts were found to be hemispherical hcp particles of average diameter 1 nm with Ir at the core, while the less active catalysts were found to have 2D layered structures. Evolution of the final catalyst nanoparticle nanostructure was found to depend critically on the initial cluster fragmentation followed by preferential nucleation at Ir centers.

6.15. Mo–Pt

Bulk Mo−Pt alloys are even better electrocatalysts for oxidation of H_2/CO mixtures than the 50% Ru−Pt surface, perhaps because there is significantly less segregation of Pt to the surface than in other systems, which is driven by the more exothermic Mo−Pt mixing.[464] Mo−Pt nanoparticles have been studied experimentally for stoichiometries ranging from 1:1 to 1:5. The electrochemical behavior of these nanoparticles (as compared with the bulk alloys) suggests that the surface is enriched in Mo relative to the overall stoichiometry, which has been attributed to different equilibrium segregation in the Mo−Pt nanoparticles as compared with the bulk alloys.[470] MC simulations (within the MEAM model) have been performed on cuboctahedral Mo−Pt nanoparticles (2.5−5 nm) by Wang et al.[471] These simulations predict good Mo−Pt mixing with only weak surface segregation of Pt (with surface Pt enrichment of between 5 and 14 atom %, compared with the bulk). Pt segregation is predicted to occur mainly to facet sites with alternation of Pt and Mo atoms on the edges and vertices of the nanoparticles.[471]

7. Melting of Nanoalloys

The study of the dependence of melting processes of nanoalloys on size and composition has gained increasing attention in the past few years. Particularly noteworthy are the experimental studies (e.g., those on the main-group nanoalloy systems: Bi−Pb and Bi−Sn, discussed below[179,183]) which clearly show that the melting behavior depends strongly on composition.

From a theoretical point of view, melting of nanoalloys has been studied by classical thermodynamic methods,[180−185] while several systems have been studied by computer simulations, which are very well suited to analyze the melting process in detail. The simulations have shown that nanoalloys may undergo complex structural transformations before complete melting.[14,186,195,238] For example, with increasing temperature nanoalloys may fluctuate between homotops, keeping their overall geometric structure fixed. In the case of core−shell structures, the outer shell may change structure and then melt while the core keeps its low-temperature structure.[186,196] Perfect core−shell clusters can present an increased thermal stability, as demonstrated by simulations of transition- and alkali-metal clusters.[24,195] Demixing may occur with increasing temperature, leading to formation of core−shell structures starting from intermixed configurations, as seen in simulations of NiAl and CuAu clusters.[472,473] Melting temperatures of nanoalloys may depend strongly not only on size but also on composition, so that a single impurity in a pure cluster can have a considerable effect.

7.1. Melting of Bi–Pb Nanoalloys

Jesser et al.[183] studied the melting of Bi−Pb nanoalloys. The clusters, with radii R between 5 and 40 nm, were deposited on amorphous carbon and observed by transmission electron microscopy, as shown in Figure 46. At compositions of 51−56 atom % Bi (where Pb and Bi form an ϵ-phase in the bulk) and for particles with $R \geq 6$ nm, melting was observed to occur through different stages. At a specific temperature T_s reached during heating, a liquid external shell of finite thickness (on average 10% of R) was observed to appear suddenly, in coexistence with a solid core. On increasing the temperature further, the solid core gradually shrank down to about $0.7R$ and then disappeared suddenly at a temperature T_l, leaving a fully liquid cluster. Both T_s and T_l showed the same kind of behavior with R as the melting temperatures of pure clusters[5]

$$T_{s,l} = \alpha_{s,l} - \frac{\beta_{s,l}}{R} \tag{20}$$

However, T_l decreased faster than T_s with decreasing R, so that their difference $\Delta T_{s,l}$ became zero for small clusters at around 5 nm. For these clusters, melting occurred suddenly in a single stage without any temperature range in which liquid and solid phases could coexist.

Jesser et al. analyzed their results theoretically, developing a simple thermodynamic approach for determining the phase diagram of isolated nanoparticles.[179] They considered a spherical nanoparticle (of radius R) in contact with an infinite reservoir having a rigid, impermeable, and diathermal wall. Under these conditions, the Helmoltz free energy is a minimum at equilibrium. The low-temperature state of the particle is solid. When the temperature is raised, the particle may develop an outer liquid layer of thickness t covering a solid core of radius R_s (with $R_s + t = R$). The free energy F_0 of the initial, fully solid state is written as

$$F_0 = \sum_{i=A,B} \mu_{i0}^s N_i^s - P_0^s V_0^s + \gamma^s A_0^s \quad (21)$$

where the superscript s refers to the solid phase, μ is the chemical potential, P is the pressure, V is the particle volume, A is the surface area, and γ is the surface energy per unit area. On the other hand, for the core−shell particle one has

$$F_f = \sum_{i=A,B} \mu_i^l N_i^l - P^l V^l + \gamma^l A^l + \sum_{i=A,B} \mu_i^s N_i^s - P^s V^s + \gamma^{sl} A^s \quad (22)$$

where the superscript l refers to the liquid shell. The difference $\Delta F = F_f - F_0$ is plotted against the composition and liquid fraction for constant material parameters to search for minima corresponding to stable or metastable phases. To estimate the model parameters it is assumed that a regular solution model represents the bulk chemical potentials and that a linear relationship exists between interfacial energies and composition.

This kind of approach cannot model effects depending on the local environment of the atoms and does not take into account the possibility of solid-state structural transitions. However, the thermodynamic theory was able to give a qualitatively satisfactory description of the melting of Bi−Pb nanoparticles, correctly predicting both the three-stage melting of the larger particles and the single-stage abrupt melting of the smaller particles. Contrary to infinite systems, where an infinitesimal quantity of liquid can be in equilibrium with the solid, for nanoparticles there is a discontinuous transition from all solid to a finite amount of liquid coexisting with the solid. The same kind of abrupt transition was also found theoretically by Shirinyan and Gusak.[182]

Jesser et al.[179] also applied their model to Sn−Bi nanoalloys and successfully compared their calculations with their previous experimental results.[474] The model was applied to particles of 40 nm diameter and predicted a strong increase of the solubility of Sn in Bi compared to the bulk.

Due to its generality, this kind of modeling also predicts some features of melting in nanoalloys that should apply (qualitatively) to a wide class of systems. For example, the model predicts a decrease of both the solidus temperature (the temperature at which liquid−solid coexistence starts when heating the particle) and the liquidus temperature (the temperature at which the cluster becomes fully liquid) with decreasing size, a behavior observed in the BiPb experiment (see Figure 47). However, the decrease of the liquidus temperature is greater, so the solid−liquid coexistence temperature interval shrinks with decreasing particle size.

7.2. Depletion Effect

The finite size of nanoalloy particles may cause an even more drastic effect on melting, freezing, and first-order phase transitions in general.[475] This is known as the depletion effect and originates from the fact that a nanoparticle is not an infinite reservoir of atoms, so that there may be a critical size below which a given phase transition cannot occur. This can be understood in terms of mass conservation. Let us consider a phase transition to a new phase which nucleates by formation of a critical nucleus of radius r_{cr}. Let x_0 and x_n be the mole fractions of species B in the old and new phases, respectively. Let the number of atoms in the critical nucleus

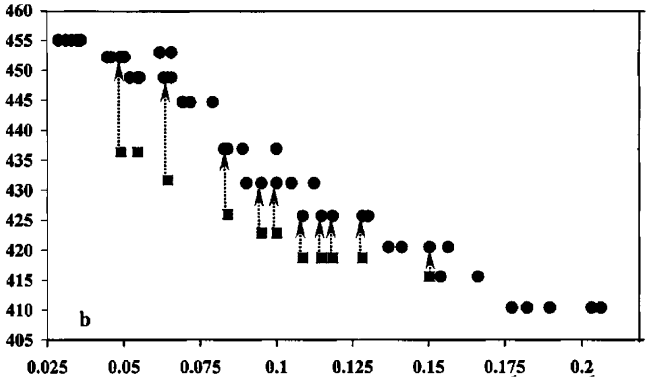

Figure 47. Dependence of solidus and liquidus temperatures for Bi−Pb nanoparticles. The composition of the particles varies from 51 atom % Bi at $R \approx 4$ nm to 56 atom % Bi at $R \approx 25$ nm. (Reprinted with permission from ref 183. Copyright 2004 American Physical Society.)

be N_{cr}. If $x_0 N < x_n N_{cr}$, the atoms of species B are not sufficient to sustain the critical nucleus. Therefore, there is a minimum cluster size N^* with a corresponding minimum cluster radius R^* given by

$$N^* = N_{cr} x_n / x_0$$

$$R^* = [(\rho_n x_n)/(\rho_0 x_0)]^{1/3} \quad (23)$$

where ρ_0 and ρ_n are the densities of the old and new phases, respectively. Even though this approach does not include the possible cluster-size dependence of the critical nucleus size, there is an indication that some transitions may be suppressed in nanoalloys.

7.3. Melting of Cu–Au and Ag–Au clusters

The melting of Cu−Au clusters with size $N = 13$ and 14 and varying composition was considered by Lopez et al.[238] in one of the first simulation studies of nanoalloys. Lopez et al. modeled Cu and Au by means of a Gupta potential and performed MD simulations. With the exception of pure Au clusters, all mixed global minima had icosahedral structures (perfect icosahedron for $N = 13$; icosahedron plus an atom above a triangular facet for $N = 14$). Their melting behavior was qualitatively the same as for pure Cu clusters. For size 13, the simulations showed a single-stage melting, whereas for size 14 melting was a two-stage process (with the exception of pure Au_{14}). The first melting stage (denoted as premelting) was due to diffusion of the external atom by substitutional exchanges with the atoms below. Yen et al.[476] simulated melting of clusters in the same size range, noting that clusters presenting "floating" surface atoms in their global-minimum configurations are more likely to undergo isomerization transitions involving permutational isomers.

Recently, the melting of larger Cu−Au clusters, in the size range 1−10 nm, has been studied by Delogu[473] at composition Cu_3Au in the framework of a SMATB approach, finding that the disordering process begins at the cluster surface and causes surface segregation of Au.

The thermodynamic properties of Ag_xAu_{7-x} for $x = 0$, 3, 4, and 7 have been investigated by Michaelian and Garzon[477] again within a Gupta potential model. Instead of performing MD simulations, they made an exhaustive search for local minima by means of a genetic algorithm, so that they were able to reconstruct the density of states as a function of the

energy. From the density of states, thermodynamic properties were extracted by calculating appropriate averages. For all compositions, the global minimum was a pentagonal bipyramid. By analogy with the 13-atom Cu−Au clusters, the melting of this compact global minimum occurred in a single stage.

Recently, the melting of 55-atom Ag−Au nanoalloys, modeled by the Gupta potential, has been investigated by Chen et al.[478] The melting temperature was found to decrease with increasing Au content despite the higher melting point of bulk Au compared with Ag. This has been attributed to stress-related destabilization of the icosahedral structure on incorporating Au atomd due to the short-ranged, sticky nature of interactions involving Au.[5,479]

7.4. Phase Changes and Their Dynamics in Small Ni–Al Clusters

Jellinek and Krissinel studied total energy-dependent structural transformations of small Ni−Al clusters by MD simulations, paying special attention to the dynamical aspects of these processes.[14,16−18]

The analyses of the dynamics were performed in terms of the following quantities.

(1) Caloric curve, i.e., time-averaged kinetic energy (per atom), or temperature, as a function of total energy (per atom).

(2) Relative root-mean-square (rms) bond length fluctuation δ

$$\delta = \frac{2}{N(N-1)} \sum_{i<j} \frac{(\langle r_{ij}^2 \rangle_t - \langle r_{ij} \rangle_t^2)^{1/2}}{\langle r_{ij} \rangle_t} \qquad (24)$$

as a function of total energy (per atom).

(3) Specific heat C (per atom)

$$C = \left[N - N\left(1 - \frac{2}{3N-6}\right) \langle E_k \rangle_t \langle E_k^{-1} \rangle_t \right]^{-1} \qquad (25)$$

as a function of total energy (per atom). In eq 25, E_k is the (internal) kinetic energy of the cluster and $\langle E_k \rangle_t$ stands for time averaging over the entire trajectory.

Jellinek and Krissinel noted that the specificity of the structural forms (isomeric and homotopic) and the peculiarities of their energy spectra, as defined by the stoichiometric composition, translate into composition-specific dynamical features of the two-element clusters. From constant energy MD simulations on Ni−Al 13-mers of varying compositions they found that, similarly to pure clusters, their bimetallic counterparts undergo a stage-wise solid-to-liquid-like transition as their energy is increased. The possible stages include surface structural transformations (both isomeric and homotopic), global structural changes that may involve any atom of the cluster, surface melting, and global or complete melting. The stages present in the melting-like transition of an alloy cluster depend on its size and composition.[14,16−18]

The graphs of the caloric curves, rms bond length fluctuations (δ), and specific heats per atom (C) for six compositions of the Ni−Al 13-mer are shown as functions of the total energy (per atom) in Figure 48.[14] For each composition, the graphs are generated using the corresponding lowest energy structure as its zero-temperature form (the temperature is defined as twice the time-averaged kinetic energy of the cluster per vibrational degree of freedom divided by the Boltzmann constant). $Ni_{12}Al$ melts in a manner similar to that observed for pure Ni_{13} and Al_{13}.[14,17] The δ graph clearly displays well-separated stages of surface and global structural changes, which correspond to the first and second, respectively, abrupt increases in the δ value which may be isomeric and homotopic in character. The barrier for exchanging the central atom with a surface atom in the icosahedral geometry is very high. Energetically, it is easier first to convert the icosahedral geometry into an isomer (or isomers) with an incomplete shell by moving a surface atom into the second layer. Surface structural transitions are the only ones experienced by the cluster over a finite range of extra energy. In the course of these transitions the central atom continues to occupy the same position. As the energy is increased further, the global structural changes get "switched on" as well and the central atom can escape to the surface. The barrier for such an escape is lower in isomers with an incomplete shell. At still higher energies the cluster samples a larger number of its isomeric and homotopic forms, the rate of transitions between these forms increases, and the cluster gradually attains its liquid-like state. The transition to this state is signified by the peak in the graph of the specific heat.

This stage-wise melting is also characteristic of other compositions (Figure 48). The only difference is that the number of the homotops available for sampling increases as the composition approaches 50/50%. The details of the transition, however, change in the limit of small number of Ni atoms. The graphs of the rms bond length fluctuation and the specific heat for $NiAl_{12}$ (and Ni_2Al_{11}, not shown) are different from those for the other compositions. There is only one abrupt increase in the δ value (a remnant of the second increase can be identified as a variation in the slope of the curve at higher energies), whereas the C graph displays two peaks. These features can be correlated with the patterns of the isomer and homotop energy spectra shown in Figure 49. For each geometrical isomer, the single homotop of $NiAl_{12}$ with Ni at the center is separated from those with Al at the center by a large energy gap. On the other hand, the homotops with Ni in the center that correspond to the three higher energy isomers have very close energies. They become accessible almost simultaneously and remain the only ones sampled over quite a broad range of extra energy. The effect of the extra energy is to increase the rate of the surface isomerizations that interconvert these homotops. Eventually the rate becomes so high that the cluster is best described as a liquid-like shell of 12 Al atoms surrounding the single Ni atom. This is the stage of surface melting. The signature of the transition to this stage is the first (lower energy) peak in the graph of the specific heat. As the energy of the cluster is increased further, global structural changes also become accessible (the central Ni atom can now escape to the surface) and a new peak begins to develop in the graph of the specific heat. The expected second abrupt increase in the rms bond length fluctuation associated with the onset of global structural transitions is masked by the large values of δ caused by surface melting. Eventually, the cluster attains the state of complete melting. The transition to this state is marked by the second (higher energy) peak in the graph of the specific heat. Similar arguments apply to the Ni_2Al_{11} cluster, which exhibits a similar (albeit less distinctly expressed) behavior.

The preceding analysis establishes a correlation between the dynamical features of the mixed clusters and the

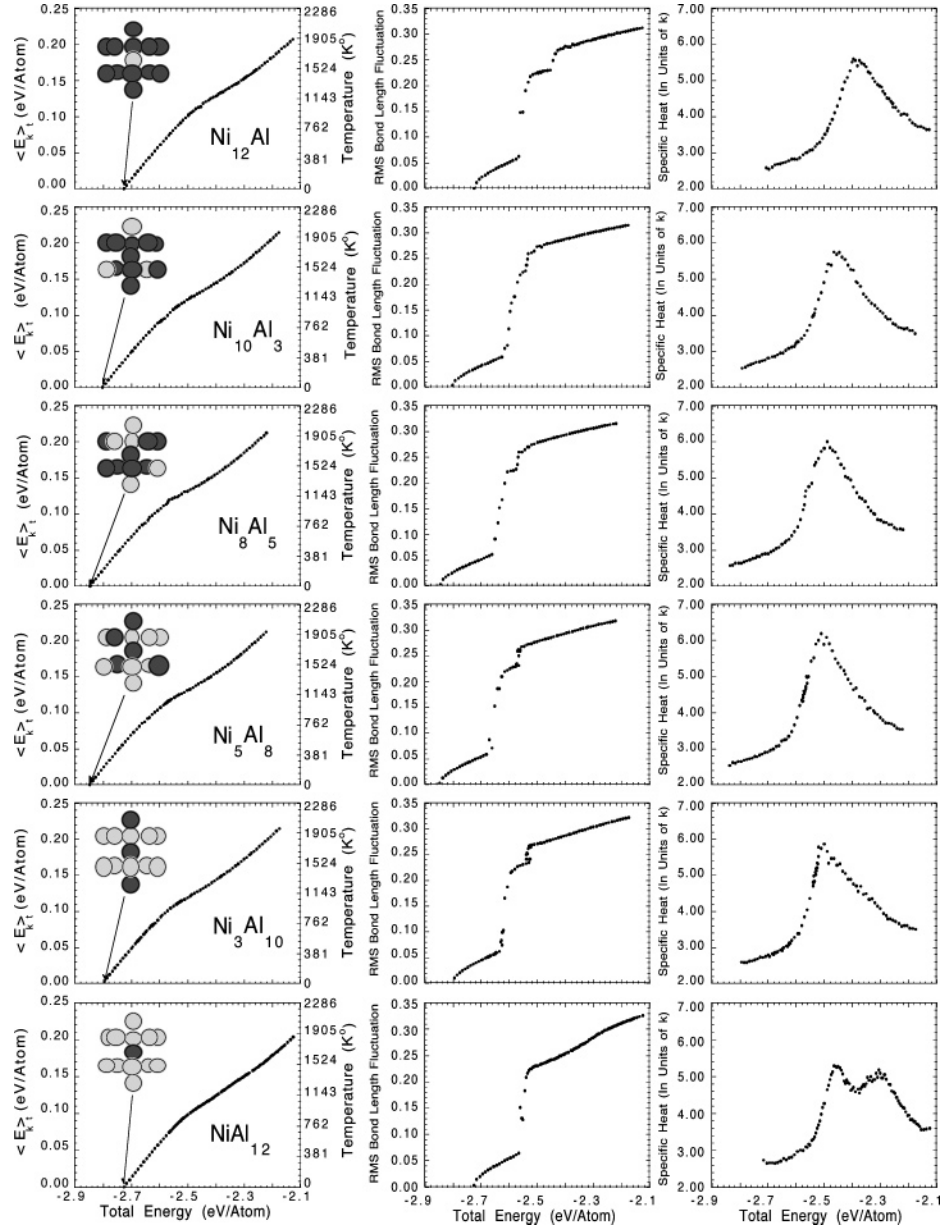

Figure 48. Caloric curves, rms bond length fluctuations, and specific heats per atom (in units of the Boltzmann constant, *k*) for 13-atom Ni−Al clusters with various compositions (dark spheres depict Ni, light spheres Al). The lowest energy homotop (shown) is used as the zero-temperature (initial) structure for each composition. (Reprinted from ref 14, Copyright 1999, with kind permission of Springer Science and Business Media.)

composition-specific energy spectra of their equilibrium structural forms. In general, however, the dynamics depend not only on the minima but also on the barriers of the potential energy surfaces. The fact that the discussed features of the dynamics can be rationalized in terms of the minima alone suggests that the distributions of the barriers of the corresponding potential energy surfaces follow the same trends as the distributions of their minima.

Table 2 lists the temperatures characterizing the onset of the different stages in the melting-like transition of the pure and mixed 13-atom Ni−Al clusters. The temperature T^s of surface structural changes corresponds to the lowest energy point in the part of the graphs showing the first abrupt increase in the δ values. The temperature T^g of global structural transitions is defined for all clusters, except $NiAl_{12}$ and Ni_2Al_{11}, by the lowest energy point in the part of the graphs showing the second abrupt increase in the δ values. For $NiAl_{12}$ and Ni_2Al_{11}, T^g is specified by the energy of the minimum between the two maxima in the corresponding graphs of the specific heat. The energies of the first and second maxima in these graphs define the temperatures of surface melting ($T_m^{(s)}$) and global (or complete) melting (T_m^g), respectively. For all the other compositions, T_m^g is specified by the energy of the single maximum in the corresponding graph of the specific heat. Inspection of the table shows that replacement of Al atoms in Al_{13} by Ni atoms, even if only one, has a stabilizing effect: the temperatures of all the individual stages increase.

It is particularly interesting that even the temperatures of surface melting in $NiAl_{12}$ and Ni_2Al_{11} are higher than the melting temperature of pure Al_{13}. An increase in the number of Ni atoms beyond one does not introduce new trends, at least not systematic ones. The overall calibration of the values in Table 2 can be established by noting that the melting temperatures of bulk Al and Ni are 933 and 1726 K, respectively.

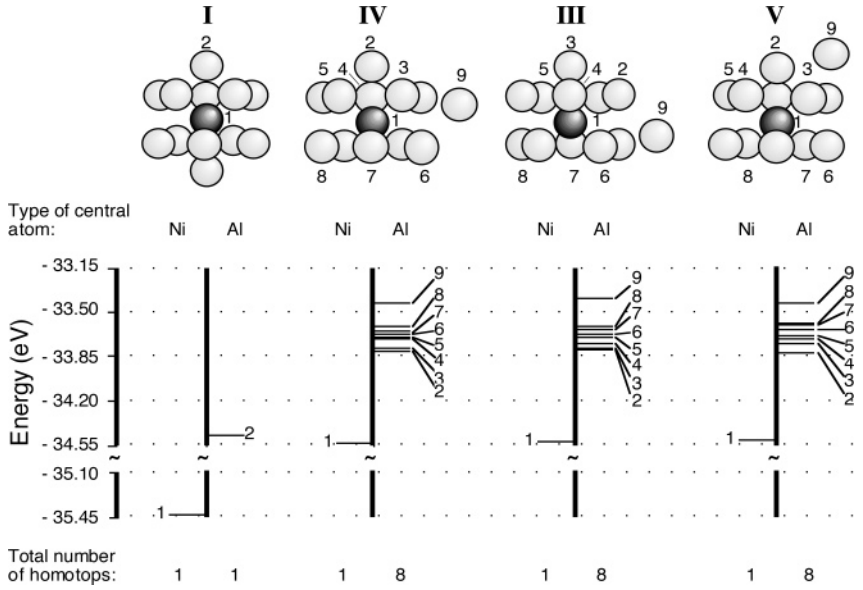

Figure 49. First four isomers of $NiAl_{12}$ (with their different atomic sites labeled by numbers) and the energies of their homotops separated into classes defined by the type of the central atom.[14,15] Each isomer is represented by its lowest energy homotop (the dark spheres depict Ni, the light ones Al; the Roman numerals establish correlation with the "parent" isomers of Figure 41). The numbers labeling the homotop energies represent the isomeric site occupied by the Ni atom in the corresponding homotop. (Reprinted from ref 14, Copyright 1999, with kind permission of Springer Science and Business Media.)

Table 2. Temperatures (in K) Associated with Different Stages in the Meltinglike Transition[a]

cluster	T^s	T^g	$T_m^{(s)/g}$
Al_{13}	570	715	850
$NiAl_{12}$	680	1180	(985)/1365
Ni_2Al_{11}	690	1220	(1070)/1315
Ni_3Al_{10}	680	1000	1085
Ni_4Al_9	705	1010	1145
Ni_5Al_8	710	1050	1180
Ni_6Al_7	790	1135	1200
Ni_7Al_6	735	1080	1200
Ni_8Al_5	785	1030	1220
Ni_9Al_4	780	1070	1220
$Ni_{10}Al_3$	750	1015	1200
$Ni_{11}Al_2$	775	1020	1215
$Ni_{12}Al$	680	1040	1200
Ni_{13}	810	1050	1190

[a] T^s and T^g are the temperatures of the onset of surface and global structural changes, respectively. $T_m^{(s)/g}$ are the temperatures of the onset of surface (only in $NiAl_{12}$ and Ni_2Al_{11}) and global melting. See text for details. Reprinted from ref 14, Copyright 1999, with kind permission of Springer Science and Business Media.)

7.5. Melting of Core–Shell Clusters

In some core−shell clusters the outer shell may melt at a significantly lower temperature than the core. This has been shown explicitly by computer simulations for several systems, including Cu−Ni,[196] Ag−Co,[186] and Pd−Pt.[199]

Huang and Balbuena[196] performed MD simulations of Cu−Ni clusters within a Sutton−Chen potential model. They considered clusters of 343 and 1000 atoms and different compositions for each size. As discussed in section 5, Cu tends to segregate to the surface of Cu−Ni clusters, so that the most favorable structures present a Ni core and a Cu outer shell. Due to the much higher melting temperature of Ni with respect to Cu, the outer shell melts at 400−500 K, while complete cluster melting (corresponding to the highest peak of the specific heat curve) occurs between 700 and 900 K. At temperatures somewhat below that of complete melting, some diffusion of Cu atoms inside the cluster was observed in the simulations.

Several melting stages have been observed in simulations of $Co_{core}Ag_{shell}$ clusters. Van Hoof and Hou[186] simulated this system by MC and molecular statics simulations within an embedded-atom potential model for the atomic interactions. As for the Cu−Ni clusters, the Ag shell melts at a lower temperature than the Co core. Before melting the surface shell may undergo a structural transformation from crystalline to amorphous when the initial cluster structure is fcc. The melting temperature of the Co core is fairly independent of the thickness of the Ag shell. The Co core melting starts at the interface with the Ag shell and proceeds toward the center of the cluster, so there may be a temperature range in which the core itself is partially liquid and partially solid.

Also, melting of Pd−Pt core−shell clusters occurs in two stages, as shown by the simulations of Sankaranarayanan et al.,[199] who found that surface melting of the external Pd shell is followed by homogeneous melting of the Pt core.

An enhanced thermal stability of perfect core−shell clusters and especially of high-symmetry core−shell polyicosahedra was found in the simulation of small-size Ni−Ag and Cu−Ag clusters by Rossi et al.[24] They performed both MD simulations and harmonic thermodynamic calculations (using eq 10), finding good agreement between the two approaches and showing that $Ag_{27}Cu_7$ and $Ag_{27}Ni_7$ melt at a much higher temperatures than pure clusters in the same size range.

Recently, Cheng et al.[480] simulated the melting of three-shell Cu−Au icosahedra ($Au_{43}Cu_{12}$, composed of a central Au atom, an intermediate Cu shell, and an Au surface shell). They found that the structure may undergo a transformation from three shell to core−shell after melting.

7.6. Single-Impurity Effect on Cluster Melting

The melting of icosahedral Ag clusters, doped by a single impurity atom, has recently been studied by Mottet et al.[198] by means of MD simulations within a Gupta-like potential model. Cu, Ni, Pd, and Au impurities were considered. In the case of Cu and Ni impurities the most favorable site is

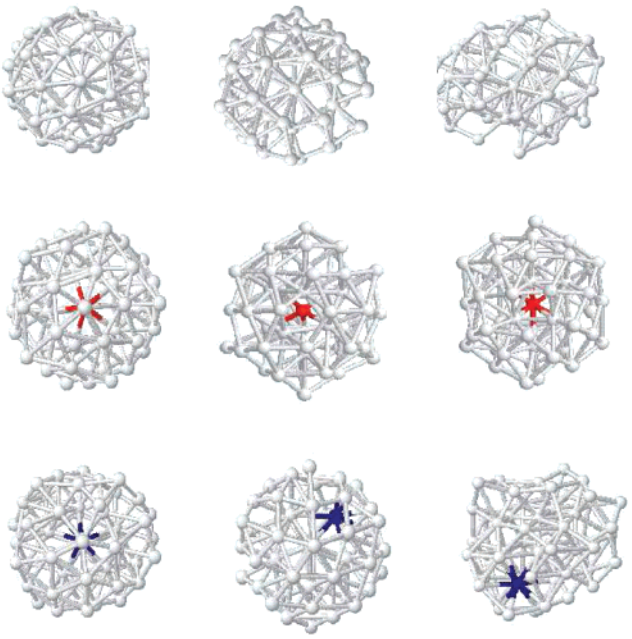

Figure 50. Snaphots from molecular-dynamics simulations of the melting of icosahedral Ag clusters with a single impurity: (top row) Pure silver cluster Ag_{55}, (middle row) $Ag_{54}Ni_1$, and (bottom row) $Ag_{54}Pd_1$. The cluster with Ni impurity is the only one which stays solid up to 600 K. (Reprinted with permission from ref 198. Copyright 2005 American Physical Society.)

at the cluster center. In fact, Cu and Ni atoms are considerably smaller than Ag atoms, so that an icosahedral cluster with these central impurities can contract and partially release the strain of the icosahedral structure. In fact (see, for example, ref 5) radial (intershell) interatomic distances in icosahedra are contracted with respect to the optimal value of the bulk crystal, while intrashell distances are expanded. A small central impurity can thus allow the cluster to relax toward a configuration with better interatomic distances, so that the resulting structure is of increased stability (even a central vacancy can increase the stability[481]). This can lead to an upward shift of the melting temperature (see Figure 50), even in clusters containing hundreds of atoms. For a Ni impurity, the upward shift is of 70, 50, 30, and 20 K for clusters of 55, 147, 309, and 561 atoms, respectively (see Figure 51). On the other hand, Pd or Au impurities present a much less significant size mismatch and do not prefer to be located at the central site. For these impurities, the shift of the melting temperature is negligible.

The enhanced stability of the clusters with Cu and Ni impurities can also be rationalized by inspection of the solution energy of the impurity ΔE_{imp}, which follows from eq 14 with $m = N - 1$ and $n = 1$. In this case ΔE_{imp} becomes

$$\Delta E_{imp} = E(Ag_{N-1}X_1) - \frac{N-1}{N}E(Ag_N) - \frac{1}{N}E(X_N) \qquad (26)$$

where X = Cu, Ni, Au, and Pd, $E(Ag_N)$ is the energy of the (icosahedral) global minimum of the pure Ag_N cluster, and $E(X_N)$ is the energy of the global minimum of the cluster X_N. Even though the solution energy of Cu and Ni impurities in bulk Ag is highly positive, the solution energy in icosahedra is clearly negative, more negative than for Au or Pd impurities whose solution energy is already negative in the bulk (see Figure 52). Moreover, the atomic stress on the central site is greatly reduced in the case of Ni and Cu

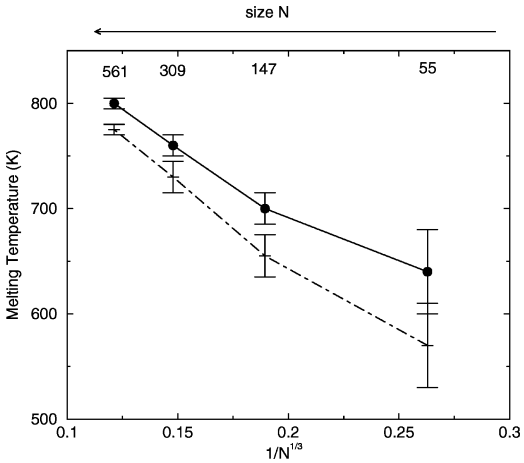

Figure 51. Melting temperatures of pure icosahedral Ag clusters (crosses) and icosahedral Ag clusters with a single central Ni impurity. The results were obtained by MD simulations. (Reprinted with permission from ref 198. Copyright 2005 American Physical Society.)

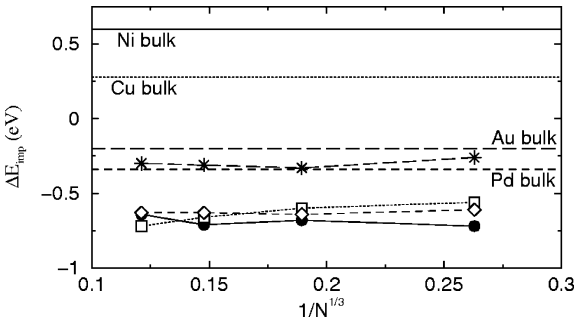

Figure 52. Single impurity energy ΔE_{imp}, as defined in eq 26, for a single central impurity in an icosahedral cluster. Solid circles, squares, diamonds, and asterisks refer to Ni, Cu, Pd, and Au impurities, respectively. The impurity solution energies in bulk Ag are also reported. (Reprinted with permission from ref 198. Copyright 2005 American Physical Society.)

impurities, while it is slightly increased for Au and Pd impurities.

The increase of the melting temperature for icosahedra with a single central impurity has recently been confirmed in the MD simulations (within the SMATB model potential) by Cheng et al.[480] for the case of $Au_{54}Cu_1$ compared to icosahedral Au_{55}. However, it should be noted that the icosahedron is not the lowest energy structure of Au_{55} within the SMATB model, so that the results of Cheng et al. single out a structural transformation whose temperature may depend on the time scale of the simulation.

7.7. Melting of Mixed Alkali-Metal Clusters

Melting of binary and ternary alkali-metal clusters has recently been studied by Aguado et al. in a series of papers.[150,151,195,482,483] Aguado et al. performed MD simulations within an orbital-free DFT approach. This approach gives good energetic accuracy, allowing at the same time rather long simulation times, which are necessary to accumulate a sufficient statistical sampling.

Contrary to what happens in Ag clusters, substituting the central atom of a 55-atom Na icosahedron with a Li impurity leads to a lowering of the melting temperature.[483] In fact, in icosahedral alkali-metal clusters, strain is much better accommodated than in transition-metal clusters, so the effect

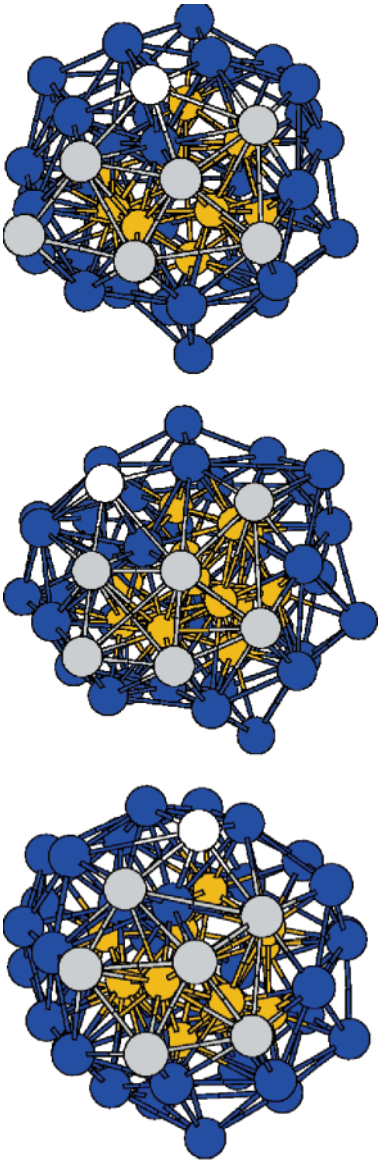

Figure 53. Three snapshots of $Li_{13}Na_{42}$, from a molecular-dynamics run at 118 K, showing the surface melting mechanism at that temperature. A group of six atoms forming a pentagonal pyramid on the cluster surface is represented by light-colored spheres. The white sphere represents a Na atom which substitutes for one of the Na atoms initially in the pentagonal pyramid. (Reprinted with permission from ref 151. Copyright 2005 American Physical Society.)

of a central impurity becomes much less important and may be overcome by other effects.

$Na_{13}Cs_{42}$ adopts a polyicosahedral structure,[151] with Cs atoms forming an external shell. This cluster exhibits premelting effects, which involve isomerization without significant atom diffusion. In $Li_{13}Na_{42}$, the lowest energy structure is amorphous, though with a high degree of polyicosahedral ordering. Na atoms form the external shell in this case. Premelting effects involve the partial melting of the cluster surface (see Figure 53). A rather surprising result for this amorphous-like cluster is the observation of a sharp peak in the specific heat curve, associated with a non-negligible latent heat. This is due to the fact that the cluster is not amorphous from the point of view of chemical ordering, and the melting transition involves substantial intermixing of Na and Li atoms. For both $Na_{13}Cs_{42}$ and $Li_{13}Na_{42}$, the melting temperatures are close to those of 55-atom clusters of the majority component.

In ref 195 Aguado and López compared the melting behavior of pure Cs_{55}, binary $Li_{42}Cs_{55}$, and ternary $Li_{13}Na_{32}Cs_{55}$. They found that the binary and ternary clusters adopt perfect core−shell arrangements with an external Cs shell and exhibit enhanced thermal stability compared to the pure Cs cluster. This enhanced stability was attributed to poor coupling between the vibrations of the core and shell atoms in the radial direction due to the difference in mass between the Cs and Li/Na atoms. In all three clusters, single-stage melting occurred without evident premelting effects. Melting was initiated by generation of floater Cs atoms: atoms which migrate from the surface to the subsurface layer.

8. Intermixing Kinetics, Freezing, Growth, and Coalescence of Nanoalloys

As discussed in section 5, it is often difficult to understand whether nanoalloys that are produced in a particular experiment represent equilibrium structures or not. Even though the mixing process can be much faster than in bulk systems (see section 8.1), we expect that the approach to equilibrium is slower in nanoalloys than in single-component clusters due to the higher complexity of the energy landscape of nanoalloys. Since kinetic trapping effects have been demonstrated in the case of several single-component clusters,[2,5,484−490] we expect that these effects would be even stronger for nanoalloys.

In the following, we consider examples of intermixing, freezing, growth, and coalescence kinetics.

8.1. Fast Intermixing Kinetics of Cu−Au Clusters

Yasuda, Mori, and co-workers used in situ TEM to study the dissolution of copper atoms in nanometer-sized gold clusters.[222−224] They found that, starting with 4 nm Au particles, rapid, spontaneous mixing is observed at room temperature (and even at 245 K) with Cu-atom diffusion coefficients ($D \geq 1.1 \times 10^{-19}$ m^2 s^{-1}) approximately 9 orders of magnitude greater than those measured in bulk crystalline Cu−Au alloys or for Cu dissolution in bulk Au ($D \geq 2.4 \times 10^{-28}$ m^2 s^{-1} at 300 K[491]). Under these conditions, solid solutions form, while at lower temperatures (215 and 165 K) a two-phase structure results, consisting of a Au core surrounded by a Cu−Au solid solution.[222−224] Independent of composition, solid solutions were found at temperatures well below the bulk order−disorder temperature (e.g., T_c = 663 K for bulk Cu_3Au[492]). For larger (10 nm) Au particles, however, Cu dissolution only occurs near the surface of the cluster and for even larger (30 nm) particles no dissolution occurs. The rapid mixing, which is driven by the negative heat of solution of Cu in Au, has been modeled by Shimizu and co-workers[207] using simple Morse-like pair potentials. Shimizu confirmed that the negative heat of solution is one driving force toward complete mixing and that mixing occurs in the solid phase (i.e., the cluster core is not molten), though the low-temperature surface melting of the particles is important in the rapid mixing process.

Yasuda et al. also studied the deposition of Au atoms on preformed Cu clusters (4 nm diameter).[493] Again, they found rapid mixing and estimated a diffusion constant of approximately 2×10^{-19} m^2 s^{-1}, which is on the order of 10^{19} times faster than gold atom diffusivity in bulk copper!

Rapid, spontaneous mixing has also been observed for many other binary nanocluster systems, e.g., Au−Ni, Au−

Zn, Au−Al, Au−Sn, and In−Sb.[222−224,494,495] Yasuda and Mori also investigated the dissolution of Au atoms into amorphous Sb clusters from Au clusters deposited onto a film containing preformed a-Sb clusters.[496] Alloying occurs at relatively low temperatures (onset at around 200 K), with an activation barrier of approximately 0.5 eV. At first, amorphous Au−Sb nanoparticles form, until the gold concentration reaches the stoichiometric composition of $AuSb_2$, when the amorphous clusters crystallize into ordered $AuSb_2$ nanocrystals.[496] Shimizu and colleagues also investigated rapid mixing in binary 4d metal nanoalloys (e.g., Ru−Mo, Mo−Nb, and Mo−Zr)[208] using Pettifor's SMATB-type model potential.[497] Again, rapid mixing is predicted for those systems (e.g., Ru−Mo) where the heat of solution is negative, though the results are composition dependent. For alloy systems exhibiting small positive heats of formation (e.g., Mo−Nb and Mo−Zr), atomic convection can lead to some of the dopant atoms diffusing into the core. Lee and Mori also reported that the solubility of Sn in 12 nm Pb particles at room temperature is almost 10 times higher than in bulk lead.[498]

Shibata et al. used EXAFS to study size-dependent mixing in $Au_{core}Ag_{shell}$ nanoparticles (generated radiolytically in solution) with Au core diameters of 2.5−20 nm and variable Ag shell thickness.[257] In the smaller nanoparticles, spontaneous interdiffusion was found to occur at the core−shell boundary. The rate of mixing was found to be size dependent, being greater for smaller particles, and this was attributed to the presence of vacancy defects at the core−shell boundary, rather than simply to the lowering of the particle's melting point with decreasing size.[257] It is interesting to note that the measured diffusion coefficients for Ag−Au mixing (e.g., $D \approx 10^{-24}$ m^2 s^{-1} for a 2.5 nm Au core coated in a shell of three Ag layers) are significantly smaller than for Cu−Au and the other systems studied by Mori and coworkers.[222−224,494,495] According to Shibata et al., this reduced diffusion rate may be due to the close size match between Ag and Au, the similar Ag−Ag, Au−Au, and Ag−Au bonding energies, and the fact that these measurements were performed in solution rather than on a support (which may give rise to support-induced strain and enhanced diffusion).[257]

8.2. Freezing of Ni–Al and Au–Pd Clusters

Chushak and Bartell[499] studied the freezing of Ni−Al liquid droplets by MD simulations within an EAM energetic model. Starting from an initial well-ordered configuration, they heated up the clusters to a temperature well above melting and then cooled down at a fast rate (2.5 10^3 K/ns) to low temperatures. They considered both Al-rich and Ni-rich compositions. For Al-rich compositions, segregation of Al to the cluster surface hindered the development of ordered structures after freezing, thus leading to formation of amorphous structures (see Figure 54). On the contrary, in the Ni-rich case, structurally ordered clusters were obtained (icosahedra, decahedra, and twinned fcc structures), but due to the fast cooling rate, it was not possible to obtain good chemical ordering.

Recently, Liu et al.[500] studied the heating and freezing of Au−Pd clusters by MD simulations within the EAM model. Their heating simulations showed that the $Pd_{core}Au_{shell}$ chemical arrangement is the most stable one and can be reached from structures with different initial chemical ordering while heating up. In their freezing simulations, Liu et al. employed a rather slow cooling rate (0.5 K/ns) and found that the final structures were always characterized by gold surface segregation but presented different shapes depending on the temperature at which freezing was initiated. For high starting temperatures, nanorod shapes were obtained (either fcc or icosahedral), while for lower starting temperatures compact fcc shapes were obtained. The nanorod shapes were demonstrated to be less stable than core−shell decahedra.

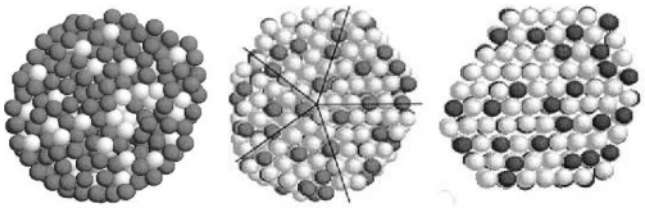

Figure 54. Ni−Al clusters obtained after freezing of liquid droplets by MD simulations. Ni and Al atoms are represented by light and dark gray spheres, respectively. (Left) Amorphous cluster obtained at composition 75 atom % Al. (Middle and right) Decahedral and twinned fcc clusters obtained at composition 25 atom % Al. (Reprinted with permission from ref 499. Copyright 2003 American Chemical Society.

8.3. Growth of Core–Shell and Three-Shell Cu–Ag, Ni–Ag, and Pd–Ag Clusters

The formation process of nanoalloys by addition of single atoms has been studied by MD simulations within the Gupta potential model for a series of binary systems (Cu−Ag, Ni−Ag, Pd−Ag).[20,209] The simulations were started from a seed consisting of a pure cluster of metal A of given size and structure. Atoms of metal B are then deposited one by one onto this seed. Both the cases of direct deposition (where metal B has a tendency to surface segregation with respect to A) and inverse deposition (where metal B has the tendency to incorporate inside A) have been treated.

In the case of direct deposition,[209] the initial core was either a Cu or a Pd cluster of size close to 200 atoms. Both icosahedral and fcc seeds were considered, and Ag atoms were deposited at different temperatures and deposition fluxes. The simulations showed the possibility of growing well-defined (although strained) Ag shells of monatomic thickness over a wide range of temperatures and fluxes. In the case of a fcc Cu seed, the external Ag shell induced a significant rearrangement of the Cu core in order to reduce the strain.

Inverse deposition was simulated starting from either icosahedral or fcc Ag cores and depositing Cu, Ni, and Pd atoms onto them.[20] Depending on the seed structure and temperature, either stable core−shell structures or metastable three-shell onion-like structures were formed. The three-shell onion-like structure, consisting of an external Ag shell of monatomic thickness, an intermediate Cu, Ni, or Pd shell, and an internal Ag core, was obtained in the case of inverse deposition above fcc clusters (see Figure 55). On the contrary, deposition on icosahedral Ag clusters was followed by fast incorporation of the deposited atoms and formation of a central (Cu or Ni) core in the cases of Cu and Ni. Pd deposition onto icosahedral Ag cores led to a structural transformation of the cluster into a decahedral particle. Formation of three-shell onion-like clusters was rationalized by noting that single Cu, Ni, or Pd impurities inside fcc Ag clusters preferentially occupy subsurface sites, where they can achieve a better strain relaxation. In fact, single impurities

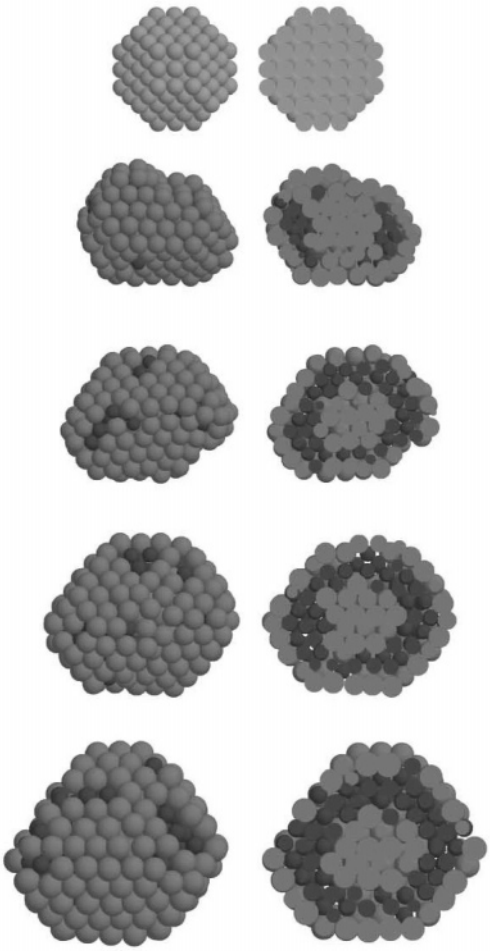

Figure 55. Growth of three shell Cu−Ag nanoparticles by inverse deposition. Snapshots from the same growth simulation at different sizes are given. Ag and Cu atoms are shown in light and dark gray, respectively. In the left column the cluster surface is shown, while in the right column a cross section of the same clusters is presented to show the multishell arrangement. (Reprinted with permission from ref 20. Copyright 2003 American Physical Society.)

present a lower energy in subsurface sites, as shown in Figure 56. Therefore, the first deposited atoms stop in the subsurface layer, where they trigger formation of an intermediate metastable shell. In the case of icosahedral Ag clusters, the most favorable site for a single impurity is that at the center of the cluster (especially for Cu and Ni), and this triggers formation of simple core−shell structures. The preferential subsurface position for single impurities and small aggregates has also been found in equilibrium MC simulations of Ag−Co clusters[193] and in tight-binding calculations for Fe impurities in Pd clusters.[501]

8.4. Coalescence of Nanoalloys

A possible way of producing binary clusters is by the collision and subsequent coalescence of single-component particles. This possibility has been investigated so far only by simulations,[502,503] which have, however, indicated a promising methodology for experimental applications.

Mariscal et al.[502] investigated the collision of three different pairs of clusters (Au−Pt, Au−Pd, and Cu−Ag) by means of MD simulations. The metals were modeled by EAM potentials. Depending on the system (and also on the kinetic energy of the clusters before collision), structures with different kinds of chemical ordering were obtained. As a

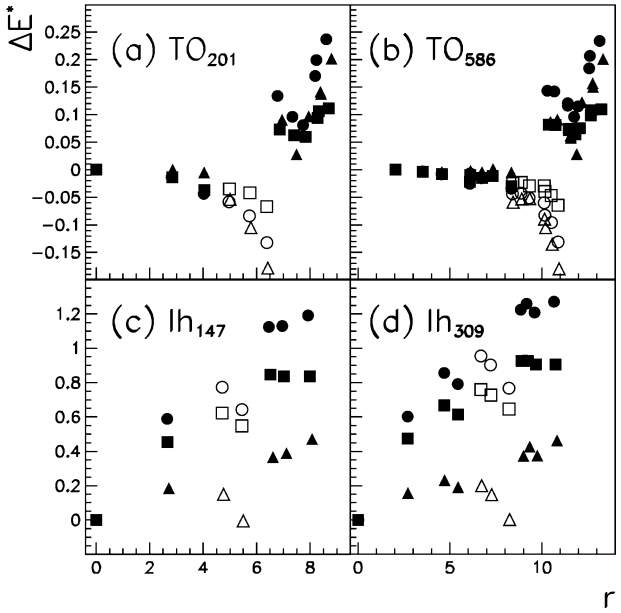

Figure 56. Impurity energies ΔE^* (in eV) in inequivalent sites for four different clusters: (a) truncated octahedron of 201 atoms; (b) truncated octahedron of 586 atoms; (c) icosahedron of 147 atoms; (d) icosahedron of 309 atoms. r is the distance of the impurity from the geometric center of the cluster. Circles, squares, and triangles refer to Ni, Cu, and Pd impurities, respectively. Open symbols refer to subsurface sites and full symbols to all other sites. In truncated octahedral clusters, the subsurface sites are clearly the most favorable for single impurities. In icosahedral clusters, the central site is favorable for Ni and Cu impurities, whereas Pd impurities are favorably placed also in subsurface sites. (Reprinted with permission from ref 20. Copyright 2003 American Physical Society.)

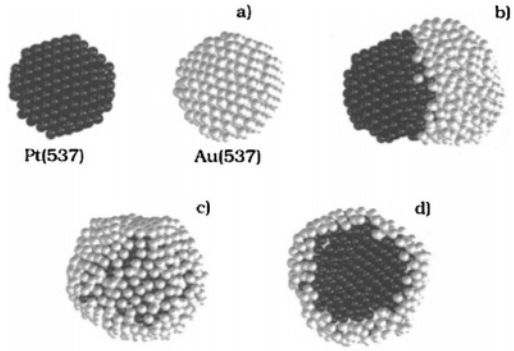

Figure 57. Snapshots from a molecular-dynamics simulation of the coalescence of a Pt cluster with an Au cluster. A $Pt_{core}Au_{shell}$ structure is formed. (Reprinted with permission from ref 502. Copyright 2005 American Institute of Physics.)

general trend, Au−Pt collisions produced ($Pt_{core}Au_{shell}$) core−shell structures, Au−Pd collisions produced intermixed clusters, and Cu−Ag collisions produced three-shell onion-like clusters like those found in the growth simulations of Baletto et al.,[20] shown in Figure 55. The different behavior of Au−Pt and Au−Pd was attributed mainly to the fact that Pt is much more cohesive than Au and Pd, so that it has a clear tendency to remain in the core of the resultant cluster. In fact, when Au and Pt clusters collide, the Au cluster quickly becomes concave after contact and incorporates the Pt cluster, which preserves its initial structure (Figure 57). In the case of Au−Pd, the very small difference in cohesive energy of the two metals and their negative bulk mixing energy combine to drive formation of intermixed structures.

Kim et al.[503] studied the coalescence of 16-atom Pd and 135-atom Ag clusters, finding that Pd penetrates into Ag but stops in subsurface positions to form a metastable structure.

9. Ternary Alloy Nanoclusters

In the field of ternary nanoalloys, the few systems which have been reported in the literature have mostly been studied from the point of view of theory or simulation. In section 7 we already reviewed the simulation results for the melting of ternary alkali-metal clusters. Here we concentrate on the segregation properties of Ni−Cu−Pd clusters, studied recently by Rubinovich and Polak.[188,189] This system was chosen because it may display interesting magnetic properties (Ni should accumulate in the core) and interesting catalytic properties (which should be tunable by changing the surface proportions of Cu and Pd).

Rubinovich and Polak considered a discrete lattice cub-octahedral model of 309 sites, describing the energetics within the bond-order model (see section 4.1). The choice of this simplified lattice model was necessary to cope with the difficulty of the problem, since the number of possible configurations of a ternary nanocluster is incredibly large. Moreover, the thermodynamics of the system was treated within FCEM,[504] previously developed for bulk surface alloys. The FCEM approach is site specific and more accurate than the simple mean-field Bragg−Williams approach since it takes into account short-range correlations between pairs of atoms, and it can be solved in a semianalytical way, so that it is much less expensive than computer simulations.

The FCEM approach allows ensembles of clusters of given average composition to be treated but allows composition fluctuations between clusters in the ensemble. In this way, FCEM can determine the mixing tendency at two different levels: the intercluster level (whether it is more favorable to form multicomponent clusters or separate into a collection of single-element clusters) and the intracluster level (whether the elements segregate within each individual cluster).

Rubinovich and Polak found that the Ni−Cu−Pd system always has a tendency to form multicomponent clusters, without separation into Ni-rich and Cu-rich clusters. This is another indication of the enhanced tendency to mixing in nanoalloys with respect to bulk systems: in fact, Ni and Cu tend to separate in bulk alloys. As expected, Ni atoms accumulate in the core. At fixed Pd concentration, if the concentration of Cu is increased at the expense of Ni, Cu atoms begin to replace Pd atoms at the cluster surface, beginning at the vertices and then occupying the edges and facets (see Figure 58).

Rubinovich and Polak also applied the FCEM approach to the Rh−Ni−Cu system.[189] They considered a 55-atom icosahedron and determined the mixing free energy as a function of composition. The mixing free energy revealed an absolute maximum corresponding to a ternary "magic number" cluster of composition $Rh_{13}Ni_{30}Cu_{12}$, with Rh atoms forming an inner icosahedral core and Ni atoms occupying the edges and Cu atoms the vertices of the surface shell.

Recently, Rubinovich et al.[339] applied the FCEM method with tight-binding energetics to 923-atom Rh−Cu−Pd cub-octahedra, finding clusters with mixed surface order and a pure Rh core at low temperatures.

In a rare example of an experimental study of ternary nanoalloys, Thiel and co-workers reported formation of trimetallic clusters by laser vaporization and gas aggregation of icosahedral Al−Pd−Mn quasicrystals.[505] Mass spectra showed trimetallic cluster compositions consistent with that of the starting material, while multiphoton ionization/fragmentation was found to primarily induce loss of Al and Mn, leading to Pd-rich (average 60 atom % Pd) Al−Pd clusters.

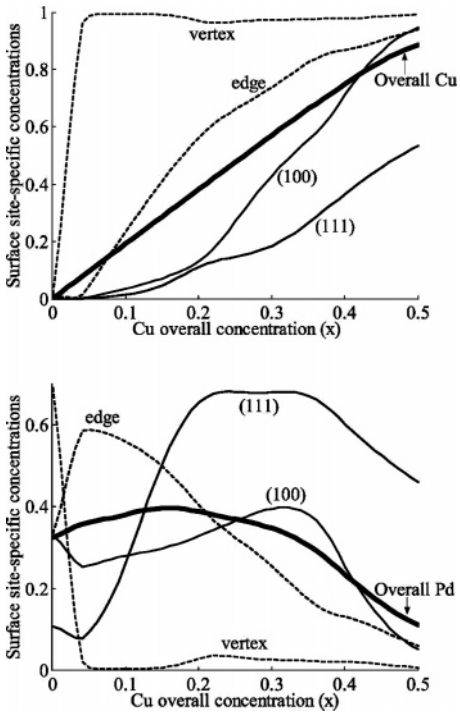

Figure 58. Sequential multisite segregation of Cu (top) and Pd (bottom), as computed by FCEM for a $Ni_{1-x-0.25}Cu_xPd_{0.25}$ 309-atom cluster. (Reprinted with permission from ref 188. Copyright 2004 American Physical Society.)

10. Conclusions and Future Outlook

The material reviewed here clearly shows that the experimental and theoretical study of nanoalloys is a research field which is growing rapidly along many fronts, ranging from theory and simulation via synthesis, analysis, and property measurement to applications in catalysis, materials science, optics, electronics, and magnetics. We have tried to present an up-to-date overview of the rich field of nanoalloys. However, the subject is vast, and several hundred papers are published each year. Therefore, it is impossible to take into account all contributions to the field, and we apologize if some significant contributions have been overlooked.

In the future, we are confident that there will be significant improvements in the ability to control experimentally the size, composition, and chemical ordering of bi- and multimetallic nanoalloys by careful control of reaction conditions, choice of precursor materials, and combining physical, chemical, and even biological generation methods. The sensitivity and resolution of characterization methods (e.g., spectroscopy, microscopy, and diffraction) are also likely to improve, which will enable detailed information to be obtained as to the geometric and electronic structures and the chemical ordering of individual nanoalloys, both for free and supported particles. Supraorganization of alloy nanoclusters into regular superstructures is likely to be obtained for several systems.

Advances in experimental techniques will be combined with a better theoretical understanding of structure−property relationships, aided by the ability to perform high-level

quantum mechanical calculations on larger systems (up to the sorts of sizes that are currently attracting experimental interest) and explore and map larger regions of configuration, composition, and chemical ordering (homotop) space. So far, most theoretical studies have considered free nanoalloys in the gas phase. However, in many experiments and for most potential applications, nanoalloys are either adsorbed on substrates or passivated by ligands. Therefore, there is often a gap between theory/modeling and experiment, a gap that theorists should try to close. Improvements and developments in theory and modeling will, of course, be facilitated by increasing computer speed as well as improved search algorithms. As well as rationalizing existing experimental results, more reliable theoretical calculations will also guide experimentalists toward likely systems, sizes, and compositions to investigate for specific desired properties, thereby screening out most of the myriad of possible combinations; so we predict the development of "nanoalloy-informatics".

Improvements in experimental and theoretical capabilities will enable more detailed studies of the effect of cluster size and composition on all properties of nanoalloys, e.g., structural (geometrical and homotopic), electronic, magnetic, optical, thermal, and chemical (including catalytic). As well as static properties, measurement and calculation of atomic dynamics and electrodynamics will be increasingly important. These developments should enable the many open questions described above to be answered and apparent anomalies and contradictory experimental results to be understood.

On the technological side, advances in fine tuning of nanoalloy properties by controlled doping will facilitate a wide range of applications and make nanoalloy-based nanodevices a reality. Experimental and theoretical studies will also be extended to tailored 1D, 2D, and 3D nanoarchitectures constructed from nanoalloy building blocks. The future will also see an expansion of the field to tri- and multimetallic nanoalloys as well as heterogeneous particles, such as alloy−oxide composites and functionalized hybrid bionanoalloy particles for medical applications. Increasingly complex systems are becoming amenable to computational as well as experimental study, so we expect detailed studies of the important processes in catalysis by nanoalloys, e.g., nanoalloy catalysts in fuel cell applications, to become feasible. In fact, nanoalloys are likely to find many more technological applications in the coming years, and the exciting field of nanoalloys will grow at an ever-increasing rate.[506]

11. List of Abbreviations

AAS	atomic absorption spectroscopy
AES	Auger electron spectroscopy
AFM	atomic force microscopy
CV	cyclic voltammetry
DFT	density functional theory
DOS	density of states
EAM	embedded atom method
EC-NMR	electrochemical nuclear magnetic resonance
EDX/EDS	energy-dispersive X-ray spectroscopy
EXAFS	extended X-ray absorption fine structure
FCEM	free-energy concentration expansion method
FT-IR	Fourier transform infrared
GA	genetic algorithm
GMR	giant magnetoresistance
HAADF	high-angle annular dark field
HOMO	highest occupied molecular orbital
HREM	high-resolution electron microscopy
HRTEM	high-resolution transmission electron microscopy
IS	ion spectroscopy/ion scattering
LEED	low-energy electron diffraction
LEIS	low-energy ion spectroscopy/ion scattering
LFRS	low-frequency Raman scattering
LUMO	lowest unoccupied molecular orbital
MC	Monte Carlo
MD	molecular dynamics
MEAM	modified embedded atom method
NEXAFS	near-edge X-ray absorption fine structure
NMR	nuclear magnetic resonance
PEMFC	proton exchange membrane fuel cell
PES	potential energy surface
PVA	polyvinyl alcohol
PVP	polyvinylpyrrolidone
SAED	selected area electron diffraction
SEM	scanning electron microscopy
SMATB	second-moment approximation to tight binding
SQUID	superconducting quantum interference device
STEM	scanning transmission electron microscopy
STM	scanning tunneling microscopy
TEM	transmission electron microscopy
UHV	ultrahigh vacuum
XANES	X-ray absorption near-edge structure
XAS	X-ray absorption spectroscopy
XEDS	X-ray energy-dispersive spectroscopy
XPS	X-ray photoelectron spectroscopy
XRD	X-ray diffraction

12. Acknowledgments

The authors are grateful to Drs. Sarah Horswell and Ziyou Li (University of Birmingham), Alessandro Fortunelli and Giovanni Barcaro (IPCF/CNR, Pisa), and Giulia Rossi (University of Genova) for helpful comments and suggestions. R.F. acknowledges financial support from the Italian CNR for the project "(Supra-)Self-Assemblies of Transition Metal Nanoclusters" within the framework of the ESF EUROCORES SONS and by European Community Sixth Framework Programme for the project "Growth and Supra-Organization of Transition and Noble Metal Nanoclusters" (Contract n. NMP4-CT-2004-001594). J.J. was supported by the Office of Basic Energy Sciences, Division of Chemical Sciences, Geosciences, and Biosciences, U.S. Department of Energy, under contract number DE-AC-02-06CH11357. R.L.J. acknowledges financial support from EPSRC and The Leverhulme Trust.

13. References

(1) *Clusters of Atoms and Molecules*; Haberland, H., Ed.; Springer: Berlin, 1994; Vols. I and II.
(2) *Large Clusters of Atoms and Molecules*; Martin, T. P., Ed.; Kluwer: Dordrecht, 1996.
(3) *Theory of Atomic and Molecular Clusters*; Jellinek, J., Ed.; Springer: Berlin, 1999.
(4) Johnston, R. L. *Atomic and Molecular Clusters*; Taylor and Francis: London, 2002.
(5) Baletto, F.; Ferrando, R. *Rev. Mod. Phys.* **2005**, *77*, 371.
(6) Jortner, J. *Z. Phys. D* **1992**, *24*, 247.
(7) Johnston, R. L. *Philos. Trans. R. Soc. London A* **1998**, *356*, 211.
(8) De Heer, W. A. *Rev. Mod. Phys.* **1993**, *65*, 611.
(9) Ruban, A. V.; Skriver, H. L.; Norskov, J. K. *Phys. Rev. B* **1999**, *59*, 15990.
(10) Bozzolo, G.; Ferrante, J.; Noebe, R. D.; Good, B.; Honecy, F. S.; Abel, P. *Comput. Mater. Sci.* **1999**, *15*, 169.
(11) Molenbroek, A. M.; Haukka, S.; Clausen, B. S. *J. Phys. Chem. B* **1998**, *102*, 10680.
(12) Schmid, G. In *Metal Clusters in Chemistry*; Braunstein, P., Oro, L. A., Raithby, P. R., Eds.; Wiley-VCH: Weinheim, 1999; Vol. 3, p 1325.

(13) Andrews, M. P.; O'Brien, S. C. *J. Phys. Chem.* **1992**, *96*, 8233.
(14) Jellinek, J.; Krissinel, E. B. In *Theory of Atomic and Molecular Clusters*; Jellinek, J., Ed.; Springer: Berlin, 1999; p 277 and references therein.
(15) Jellinek, J.; Krissinel, E. B. *Chem. Phys. Lett.* **1996**, *258*, 283.
(16) Krissinel, E. B.; Jellinek, J. *Chem. Phys. Lett.* **1997**, *272*, 301.
(17) Krissinel, E. B.; Jellinek, J. *Int. J. Quant. Chem.* **1997**, *62*, 185.
(18) Jellinek, J.; Krissinel, E. B. In *Nanostructured Materials: Clusters, Composites, and Thin Films*; Shalaev, V. M., Moskovits, M., Eds.; ACS Symposium Series; American Chemical Society: Washington, DC, 1997; pp 239−254.
(19) Lordeiro, R. A.; Guimarães, F. F.; Belchior, J. C.; Johnston, R. L. *Int. J. Quantum Chem.* **2003**, *95*, 112.
(20) Baletto, F.; Mottet, C.; Ferrando, R. *Phys. Rev. Lett.* **2003**, *90*, 135504.
(21) Fromen, M. C.; Morillo, J.; Casanove, M. J.; Lecante, P. *Europhys. Lett.* **2006**, *73*, 885.
(22) Cheng, D.-J.; Wang, W.-C.; Huang, S.-P. *J. Phys. Chem. B* **2006**, *11*, 16193.
(23) Ferrer, D.; Torres-Castro, A.; Gao, X.; Sepulveda-Guzman, S.; Ortiz-Mendez, U.; Jose-Yacaman, M. *Nano Lett.* **2007**, *7*, 1701.
(24) Rossi, G.; Rapallo, A.; Mottet, C.; Fortunelli, A.;Baletto, F.; Ferrando, R. *Phys. Rev. Lett.* **2004**, *93*, 105503.
(25) Darby, S.; Mortimer-Jones, T. V.; Johnston, R. L.; Roberts, C. *J. Chem. Phys.* **2002**, *116*, 1536.
(26) Barcaro, G.; Fortunelli, A.; Rossi, G.; Nita, F.; Ferrando, R. *J. Phys. Chem. B* **2006**, *110*, 23197.
(27) Rajesh, C.; Majumder, C. *Chem. Phys. Lett.* **2006**, *430*, 101.
(28) Faraday, M. *Philos. Trans. R. Soc. London* **1857**, *147*, 145.
(29) *Clusters and Colloids: From Theory to Applications*; Schmid, G., Ed.; VCH: Weinheim, 1994.
(30) Broglia, R. A. *Contemp. Phys.* **1994**, *35*, 95.
(31) Bönnemann, H.; Richards, R. M. *Eur. J. Inorg. Chem.* **2001**, 2455.
(32) *Transition Metal Clusters*; Johnson, B. F. G., Ed.; Wiley: New York, 1980.
(33) Mingos, D. M. P.; Wales, D. J. *Introduction to Cluster Chemistry*; Prentice Hall: Englewood Cliffs, NJ, 1990.
(34) *Metal Clusters in Chemistry*; Braunstein, P., Oro, L. A., Raithby, P. R., Eds.; Wiley-VCH: Weinheim, 1999; Vols. 1−3.
(35) Dyson, P. J.; McIndoe, J. S. *Transition Metal Carbonyl Chemistry*; Gordon & Breach: Amsterdam, 2000.
(36) Demartin, F.; Fabrizi de Biani, F.; Femoni, C.; Iapalucci, M. C.; Longoni, G.; Macchi, P.; Zanello, P. *J. Cluster Sci.* **2001**, *12*, 61.
(37) Femoni, C.; Iapalucci, M. C.; Longoni, G.; Svensson, P. H. *Chem. Commun.* **2001**, 1776.
(38) Nashner, M. S.; Somerville, D. M.; Lane, P. D.; Adler, D. L.; Shapley, J. R.; Nuzzo, R. G. *J. Am. Chem. Soc.* **1996**, *118*, 12964.
(39) Braunstein P.; Rosé, J. In *Metal Clusters in Chemistry*; Braunstein, P., Oro, L. A., Raithby, P. R., Eds.; Wiley-VCH: Weinheim, 1999; Vol. 2, p 616.
(40) Ichikawa, M. In *Metal Clusters in Chemistry*; Braunstein, P., Oro, L. A., Raithby, P. R., Eds.; Wiley-VCH: Weinheim, 1999; Vol. 3, p 1273.
(41) Thomas, J. M.; Johnson, B. F. G.; Raja, R.; Sankar, G.; Midgley, P. *Acc. Chem. Res.* **2003**, *36*, 20.
(42) Sinfelt, J. H. *J. Catal.* **1973**, *29*, 308.
(43) Sinfelt, J. H. *Bimetallic Catalysts: Discoveries, Concepts and Applications*; Wiley: New York, 1983.
(44) Sachtler, J. W. A.; Biberian, J. P.; Somorjai, G. A. *Surf. Sci.* **1981**, *110*, 43.
(45) Schmid, G.; Lehnert, A.; Malm, J. O.; Bovin, J.-O. *Angew. Chem., Int. Ed. Engl.* **1991**, *30*, 874.
(46) Burda, C.; Chen, X.-B.; Narayanan, R.; El-Sayed, M. A. *Chem. Rev.* **2005**, *105*, 1025.
(47) Kunz, H. R.; Gruver, G. A. *J. Electrochem. Soc.* **1975**, *122*, 1279.
(48) Stonehart, P. *J. Appl. Electrochem.* **1992**, *22*, 995.
(49) Markovic, N. M.; Radmilovic, V.; Ross, P. N., Jr. In *Catalysis and Electrocatalysis at Nanoparticle Surfaces*; Wieckowski, A., Savinova, E. R., Vayenas, C. G., Eds.; Marcel Dekker: New York, 2003; Chapter 9, p 911.
(50) Russell, A. E.; Rose, A. *Chem. Rev.* **2004**, *104*, 4613.
(51) Bonnemann, H.; Brijoux, W. In *Metal Clusters in Chemistry*; Braunstein, P., Oro, L. A., Raithby, P. R., Eds.; Wiley-VCH: Weinheim, 1999; Vol. 2, p 913.
(52) Mie, G. *Ann. Phys. (Leipzig)* **1908**, *330*, 377.
(53) Kreibig, U.; Quinten, M. In *Clusters of Atoms and Molecules*; Haberland, H., Ed.; Springer-Verlag: Berlin, 1994; Vol. II, p 321.
(54) Kreibig, U.; Vollmer, M. *Optical Properties of Metal Clusters*; Springer-Verlag: Berlin, 1995.
(55) Aden, A. L.; Kerker, M. *J. Appl. Phys.* **1951**, *22*, 1242.
(56) Kelly, K. L.; Coronado, E.; Zhao, L. L.; Schatz, G. C. *J. Phys. Chem. B* **2003**, *107*, 668.
(57) Bruzzone, S.; Arrighini, G. P.; Guidotti, C. *Mater. Sci. Eng. C* **2003**, *23*, 965.
(58) Chen, F. Y.; Johnston, R. L. *Appl. Phys. Lett.* **2007**, *90*, 153123.
(59) Idrobo, J. C.; Ogut, S.; Jellinek, J. *Phys. Rev. B* **2005**, *72*, 085445.
(60) Gaudry, M.; Cottancin, E.; Pellarin, M.; Lermé, J.; Arnaud, L.; Huntzinger, J. R.; Vialle, J.-L.; Broyer, M.; Rousset, J. L.; Treilleux, M.; Mélinon, P. *Phys. Rev. B* **2003**, *67*, 155409.
(61) Hodak, J. H.; Henglein, A.; Giersig, M.; Hartland, G. V. *J. Phys. Chem. B* **2000**, *104*, 11708.
(62) Wilcoxon, J. P.; Provencio, P. P. *J. Am Chem. Soc.* **2004**, *126*, 6402.
(63) Sumiyama, K.; Suzuki, K.; Makhlouf, S. S.; Wakoh, K.; Kamiyama, T.; Yamamuro, S.; Konno, T. J.; Xu, Y. F.; Hihara, T. *J. Non-Cryst. Solids* **1995**, *192/193*, 539.
(64) Alivisatos, P. *Nat. Biotechnol.* **2004**, *22*, 47.
(65) Rosi, N. L.; Mirkin, C. A. *Chem. Rev.* **2005**, *105*, 1547.
(66) Cao, Y. W.; Jin, R. C.; Mirkin, C. A. *J. Am. Chem. Soc.* **2001**, *123*, 7961.
(67) Nam, J.-M.; Stoeva, S. I.; Mirkin, C. A. *J. Am. Chem. Soc.* **2004**, *126*, 5932.
(68) Schmid, G. *Nanoparticles: From Theory to Application*; Wiley-VCH: Weinheim, 2003.
(69) Goia, D. V.; Matijevic, E. *New J. Chem.* **1998**, *22*, 1203.
(70) Toshima, N.; Yonezawa, T. *New J. Chem.* **1998**, *22*, 1179.
(71) Milani, P.; Iannotta, I. *Cluster Beam Synthesis of Nanostructured Materials*; Springer: Berlin, 1999.
(72) Binns, C. *Surf. Sci. Rep.* **2001**, *44*, 1.
(73) Whetten, R. L.; Schriver, K. E. In *Gas Phase Inorganic Chemistry*; Russell, D. H., Ed.; Plenum: New York, 1989.
(74) Cottancin, E.; Lermé, J.; Gaudry, M.; Pellarin, M.; Vialle, J.-L.; Broyer, M.; Prével, B.; Treilleux, M.; Mélinon, P. *Phys. Rev. B* **2000**, *62*, 5179.
(75) Turkevich, J.; Stevenson, P. C.; Hiller, J. *Discuss. Faraday Soc.* **1951**, *11*, 55.
(76) Binder, W. H. *Angew. Chem., Int. Ed. Engl.* **2005**, *44*, 5172.
(77) Rao, C. N. R.; Kulkarni, G. U.; Thomas, P. J.; Edwards, P. P. *Chem. Soc. Rev.* **2000**, *29*, 27.
(78) Henglein, A.; Giersig, M. *J. Phys. Chem.* **1994**, *98*, 6931.
(79) Ul Haq, I.; Matijevic, E.; Akhtar, K. *Chem. Mater.* **1997**, *9*, 2659.
(80) Ul Haq, I.; Matijevic, E. *Prog. Colloid Polym. Sci.* **1998**, *109*, 185.
(81) Watzky, M. A.; Finke, R. G. *Chem. Mater.* **1997**, *9*, 3083.
(82) Torigoe, K.; Esumi, K. *Langmuir* **1993**, *9*, 1664.
(83) Esumi, K.; Tano, T.; Torigoe, K.; Meguro, K. *Chem. Mater.* **1990**, *2*, 564.
(84) Bradley, J. S.; Via, G. H.; Bonneviot, L.; Hill, E. W. *Chem. Mater.* **1996**, *8*, 1895.
(85) Harikumar, K. R.; Ghosh, S.; Rao, C. N. R. *J. Phys. Chem. A* **1997**, *101*, 536.
(86) Mattei, G.; Maurizio, C.; Mazzoldi, P.; D'Acapito, F.; Battaglin, G.; Cattaruzza, E.; de Julián Fernández, C.; Sada, C. *Phys. Rev. B* **2005**, *71*, 195418.
(87) Reetz, M. T.; Helbig, W.; Quaiser, S. A. In *Active Metals*; Fürstner, A., Ed.; VCH: Weinheim, 1996; p 279.
(88) Reetz, M. T.; Helbig, W.; Quaiser, S. A. *Chem. Mater.* **1995**, *7*, 2227.
(89) Kolb, U.; Quaiser, S. A.; Winter, M.; Reetz, M. T. *Chem. Mater.* **1996**, *8*, 1889.
(90) Wang, C. B.; Zhang, W. X. *Environ. Sci. Technol.* **1997**, *31*, 2154.
(91) Cheng, Y.; Schiffrin, D. J. *J. Chem. Soc., Faraday Trans.* **1996**, *92*, 3865.
(92) Platt, M.; Dryfe, R. A. W.; Roberts, E. P. L. *Chem. Commun.* **2002**, 2324.
(93) Platt, M.; Dryfe, R. A. W. *Phys. Chem. Chem. Phys.* **2005**, *7*, 1807.
(94) Remita, S.; Mostafavi, M.; Delcourt, M. O. *Radiat. Phys. Chem.* **1996**, *47*, 275.
(95) Belloni, J.; Mostafavi, M.; Remita, H.; Marignier, J.-L.; Delcourt, M.-O. *New J. Chem.* **1998**, *22*, 1239.
(96) Belloni, J.; Mostafavi, M. In *Metal Clusters in Chemistry*; Braunstein, P., Oro, L. A., Raithby, P. R., Eds.; Wiley-VCH: Weinheim, 1999; Vol. 2, p 1213.
(97) Treguer, M.; de Cointet, C.; Remita, H.; Khatouri, M.; Mostafavi, M.; Amblard, J.; Belloni, J.; de Keyzer, R. *J. Phys. Chem. B* **1998**, *102*, 4310.
(98) Doudna, C. M.; Bertino, M. F.; Tokuhiro, A. T. *Langmuir* **2002**, *18*, 2434.
(99) Doudna, C. M.; Bertino, M. F.; Blum, F. D.; Tokuhiro, A. T.; Lahiri-Dey, D.; Chattopadhay, S.; Terry, J. *J. Phys. Chem. B* **2003**, *107*, 2966.
(100) Amblard, J.; Belloni, J.; Platzer, O. *J. Chim. Phys. PCB* **1991**, *88*, 835.
(101) Mizukoshi, Y.; Fujimoto, T.; Nagata, Y.; Oshima, R.; Maeda, Y. *J. Phys. Chem. B* **2000**, *104*, 6028.
(102) Kan, C. X.; Cai, W. P.; Li, C. C.; Zhang, L. D.; Hofmeister, H. *J. Phys. D Appl. Phys.* **2003**, *36*, 1609.

(103) Mann, S. *Biomineralization: Principles and Concepts in Bioinorganic Materials Chemistry*; Oxford University Press: Oxford, 2001.
(104) Brayner, R.; Coradin, T.; Fievet-Vincent, F.; Livage, J.; Fievet, F. *New J. Chem.* **2005**, *29*, 681.
(105) Mann, S. *Biomimetic Materials Chemistry*; VCH: New York, 1996.
(106) Mertig, M.; Wahl. R.; Lehmann, M.; Simon, P.; Pompe, W. *Eur. Phys. J. D* **2001**, *16*, 317.
(107) Srivastava, S.; Samanta, B.; Arumugam, P.; Han, G.; Rotello, V. M. *J. Mater. Chem.* **2007**, *17*, 52.
(108) Lloyd, J. R.; Lovley, D. R. *Curr. Opin. Biotechnol.* **2001**, *12*, 248.
(109) Macaskie, L. E.; Baxter-Plant, V. S.; Creamer, N. J.; Humphries, A. C.; Mikheenko, I. P.; Mikheenko, P. M.; Penfold, D. W.; Yong, P. *Biochem. Soc. Trans.* **2005**, *33*, 76.
(110) Mabbett, A. N.; Macaskie, L. E. *J. Chem. Technol. Biotechnol.* **2002**, *77*, 1169.
(111) Liu, H. B.; Canizal, G.; Schabes-Retchkiman, P. S.; Ascencio, J. A. *J. Phys. Chem. B* **2006**, *110*, 12333.
(112) Bradley, J. S. In *Clusters and Colloids: From Theory to Applications*; Schmid, G., Ed.; VCH: Weinheim, 1994; p 459.
(113) *113*. United Kingdom Surface Analysis Forum URL: http://www.uksaf.org/.
(114) Brack, M. *Rev. Mod. Phys.* **1993**, *65*, 677.
(115) Martin, T. P. *Phys. Rep.* **1996**, *273*, 199.
(116) Renouprez, A. J.; Lebas, K.; Bergeret, G.; Rousset, J. L.; Delichere, P. *Stud. Surf. Sci. Catal.* **1996**, *101*, 1105.
(117) Hall, B. D.; Hyslop, M.; Wurl, A.; Brown, S. A. In *Fundamentals of Gas-phase Nachnology*; Kish, L., Granqvist, C. G., Marlow, W., Siegel, R. W., Eds.; Kluwer: Dordrecht, 2001; p 1.
(118) Maier-Borst, M.; Cameron, D. B.; Rokni, M.; Parks, J. H. *Phys. Rev. A* **1999**, *59*, R3162.
(119) Pauwels, B.; Van Tendeloo, G.; Zhurkin, E.; Hou, M.; Verschoren, G.; Theil Kuhn, L.; Bouwen, W.; Lievens, P. *Phys. Rev. B* **2001**, *63*, 165406.
(120) Voyles, P. M.; Muller, D. A.; Grazul, J. L.; Citrin, P. H.; Gossmann, H.-J. L. *Nature* **2002**, *416*, 826.
(121) Cazayous, M.; Langlois, C.; Oikawa, T.; Ricolleau, C.; Sacuto, A. *Phys. Rev. B* **2006**, *73*, 113402.
(122) Samorì, P. *J. Mater. Chem.* **2004**, *14*, 1353.
(123) Menezes, W. J. C.; Knickelbein, M. B. *Chem. Phys. Lett.* **1991**, *183*, 357.
(124) Nonose, S.; Sone, Y.; Kaya, K. *Z. Phys. D* **1991**, *19*, 357.
(125) Hoshino, K.; Naganuma, T.; Watanabe, K.; Konishi, Y.; Nakajima, A.; Kaya, K. *Chem. Phys. Lett.* **1995**, *239*, 369.
(126) Koyasu, K.; Mitsui, M.; Nakajima, A.; Kaya, K. *Chem. Phys. Lett.* **2002**, *358*, 224.
(127) Koretsky, G. M.; Kerns, K. P.; Nieman, G. C.; Knickelbein, M. B.; Riley, S. J. *J. Phys. Chem. A* **1999**, *103*, 1997.
(128) Bragg, A. E.; Verlet, J. R. R.; Kammrath, A.; Cheshnovsky, O.; Neumark, D. M. *J. Chem. Phys.* **2005**, *122*, 054314.
(129) Babu, P. K.; Kim, H. S.; Oldfield, E.; Wieckowski, A. *J. Phys. Chem. B* **2003**, *107*, 7595.
(130) Bansmann, J.; Baker, S. H.; Binns, C.; Blackman, J. A.; Bucher, J.-P; Dorantes-Davila J; Dupuis, V.; Favre, L.; Kechrakos, D; Kleibert, A.; Meiwes-Broer, K.-H.; Pastor, G. M.; Perez, A.; Toulemonde, O.; Trohidou, K. N.; Tuaillon, J.; Xie, Y. *Surf. Sci. Rep.* **2005**, *56* 189.
(131) Billas, I. M. L.; Chatelain, A.; de Heer, W. A. *Science* **1994**, *265*, 1682.
(132) Cox, A. J.; Louderback, J. G.; Bloomfield, L. A. *Phys. Rev. Lett.* **1993**, *71*, 923.
(133) Cox, A. J.; Louderback, J. G.; Apsel, S. E.; Bloomfield, L. A. *Phys. Rev. B* **1994**, *49*, 12295.
(134) Knickelbein, M. B. *Phys. Rev. Lett.* **2001**, *86*, 5255.
(135) Knickelbein, M. B. *Phys. Rev. B* **2004**, *70*, 014424.
(136) Hihara, T.; Pokrant, S.; Becker, J. A. *Chem. Phys. Lett.* **1998**, *294*, 357.
(137) Yin, S.-G.; Xu, X.-S.; Moro, R.; de Heer, W. A. *Phys. Rev. B* **2005**, *72*, 174410.
(138) Yin, S.-G.; Xu, X.-S.; Liang, A.; de Heer, W. A. *Magnetism of Alloy Clusters in a Molecular Beam*; 2006, URL: electra.physics.gatech.edu/alloy.html.
(139) Nguyen, H. L.; Howard, L. E. M.; Giblin, S. R.; Tanner, B. K.; Terry, I.; Hughes, A. K.; Ross, I. M.; Serres, A.; Bürckstümmer, H.; Evans, J. S. O. *J. Mater. Chem.* **2005**, *15*, 5136.
(140) Sul, Y. C.; Liu, W.; Yue, L. P.; Li, X. Z.; Zhou, J.; Skomski, R.; Sellmyer, D. J. *J. Appl. Phys.* **2005** *97*, 10J304.
(141) Renouprez, A. J.; Rousset, J. L.; Cadrot, A. M.; Soldo, Y.; Stievano, L. *J. Alloys Compd.* **2001**, *328*, 50.
(142) Rousset, J. L.; Stievano, L.; Cadete Santos Aires, F. J.; Geantet, C.; Renouprez, A. J.; Pellarin, M. *J. Catal.* **2001**, *202*, 163.
(143) Attard, G. A.; Ahmadi, A.; Jenkins, D. J.; Hazzazi, O. A.; Wells. P. B.; Griffin, K. G.; Johnston, P.; Gillies, J. E. *Chem. Phys. Chem.* **2003**, *4*, 123.
(144) Paz-Borbón, L. O.; Johnston, R. L.; Barcaro, G.; Fortunelli, A. *J. Phys. Chem. C* **2007**, *111*, 2936.
(145) Ferrando, R.; Fortunelli, A.; Johnston, R. L. *Phys. Chem. Chem. Phys.*, **2008**, *10*, 640.
(146) Hohenberg, P.; Kohn, W. *Phys. Rev.* **1964**, *136*, B864.
(147) Wang, L.-L.; Johnson, D. D. *J. Phys. Chem. B* **2005**, *109*, 23113.
(148) Derosa, P. A.; Seminario, J. M.; Balbuena, P. B. *J. Phys. Chem. A* **2001**, *105*, 7917.
(149) Bonaćić-Koutecký, V.; Burda, J.; Mitric, R.; Ge, M.; Zampella, G.; Fantucci, P. *J. Chem. Phys.* **2002**, *117*, 3120.
(150) Aguado, A.; López, J. M. *J. Chem. Theory Comput.* **2005**, *1*, 299.
(151) Aguado, A.; López, J. M. *Phys. Rev. B* **2005**, *71*, 075415.
(152) Ferrando, R.; Fortunelli, A.; Rossi, G. *Phys. Rev. B* **2005**, *72*, 085449.
(153) Fernández, E. M.; Balbás, L. C.; Pérez, L. A.; Michaelian, K.; Garzón, I. L. *Int. J. Mod. Phys. B* **2005**, *19*, 2339.
(154) Kumar, V. *Comput. Mater. Sci.* **2006**, *36*, 1.
(155) Janssens, E.; Neukermans, S.; Lievens, P. *Curr. Opin. Solid State Mater. Sci.* **2004**, *8*, 185.
(156) Daw, M. S.; Baskes, M. I. *Phys. Rev. B* **1984**, *29*, 6443.
(157) Voter, A. F. *Los Alamos Unclassified Technical Report LA-UR 93*, **1999**, 3901.
(158) Sutton, A. P.; Chen, J. *Philos. Mag. Lett.* **1990**, *61*, 139.
(159) Gupta, R. P. *Phys. Rev. B* **1981**, *23*, 6265.
(160) Rosato, V.; Guillopé, M.; Legrand, B. *Philos. Mag. A* **1989**, *59*, 321.
(161) Cleri, F.; Rosato, V. *Phys. Rev. B* **1993**, *48*, 22.
(162) López, M. J.; Jellinek, J. *J. Chem. Phys.* **1999**, *110*, 8899.
(163) Zhang, M.; Fournier, R. *J. Mol. Struct. (Theochem*) **2006**, *762*, 49.
(164) Treglia, G.; Legrand, B.; Ducastelle, F. *Europhys. Lett.* **1988**, *7*, 575.
(165) Strohl, J. K.; King, T. S. *J. Catal.* **1989**, *118*, 53.
(166) Zhu, L.; DePristo, A. E. *J. Catal.* **1997**, *167*, 400.
(167) Johnston, R. L. *Dalton Trans.* **2003**, 4193.
(168) Wales, D. J.; Doye, J. P. K. *J. Phys. Chem. A* **1997**, *101*, 5111.
(169) Apra, E.; Ferrando, R.; Fortunelli, A. *Phys. Rev. B* **2006**, *73*, 205414.
(170) See the Cambridge Cluster Database, http://www-wales.ch.cam.ac.uk/CCD.htm.
(171) Doye, J. P. K.; Ferrando, R. Manuscript in preparation.
(172) Lu, Q. L.; Zhu, L. Z.; Ma, L.; Wang, G. H. *Chem. Phys. Lett.* **2005**, *407*, 176.
(173) Lu, Q. L.; Zhu, L. Z.; Ma, L.; Wang, G. H. *Phys. Lett. A* **2006**, *350*, 258.
(174) Rossi, G.; Ferrando, R. *Chem. Phys. Lett.* **2006**, *423*, 17.
(175) Doye, J. P. K.; Meyer, L. *Phys. Rev. Lett.* **2005**, *95*, 063401.
(176) Calvo, F.; Yurtsever, E. *Phys. Rev. B* **2004**, *70*, 045423.
(177) Rapallo, A.; Rossi, G.; Ferrando, R.; Fortunelli, A.; Curley, B. C.; Lloyd, L. D.; Tarbuck, G. M.; Johnston, R. L. *J. Chem. Phys.* **2005**, *122*, 194308.
(178) Gupta, A.; Paz-Borbón, L. O.; Johnston R. L. Unpublished work.
(179) Jesser, W. A.; Shiflet, G. J.; Allen, G. L.; Crawford, J. L. *Mater. Res. Innovations* **1999**, *2*, 211.
(180) Vallée, R.; Wautelet, M.; Dauchot, J. P.; Hecq, M. *Nanotechnology* **2001**, *12*, 68.
(181) Liang, L. H.; Liu, D.; Jiang, Q. *Nanotechnology* **2003**, *14*, 438.
(182) Shirinyan, A. S.; Gusak, A. M. *Philos. Mag.* **2004**, *84*, 579.
(183) Jesser, W. A.; Shneck, R. Z.; Gile, W. W. *Phys. Rev. B* **2004**, *69*, 144121.
(184) Shirinyan, A. S.; Pasichnyy, M. O. *Nanotechnology* **2005**, *16*, 1724.
(185) Shirinyan, A.; Wautelet, M.; Belogorodsky, Y. *J. Phys.: Condens. Matter* **2006**, *18*, 2537.
(186) Van Hoof, T.; Hou, M. *Phys. Rev. B* **2005**, *72*, 115434.
(187) Montejano-Carrizales, J. M.; Moran-Lopez, J. L. *Surf. Sci.* **1990**, *239*, 169.
(188) Rubinovich, L.; Polak, M. *Phys. Rev. B* **2004**, *69*, 155405.
(189) Polak, M.; Rubinovich, L. *Phys. Rev. B* **2005**, *71*, 125426.
(190) Newman, M. E. J.; Barkema, G. T. *Monte Carlo Methods in Statistical Physics*; Clarendon Press: Oxford, 1999.
(191) Frenkel, D.; Smit, B. *Understanding molecular simulation*; Academic Press: San Diego, 1996.
(192) Mainardi, D. S.; Balbuena, P. B. *Langmuir* **2001**, *17*, 2047.
(193) Van Hoof, T.; Hou, M. *Eur. Phys. J. D* **2004**, *29*, 33.
(194) Müller, M.; Albe, K. *Phys. Rev. B* **2005**, *72*, 094203.
(195) Aguado, A.; López, J. M. *Phys. Rev. B* **2005**, *72*, 205420.
(196) Huang, S. P.; Balbuena, P. B. *J. Phys. Chem. B* **2002**, *106*, 7225.
(197) Rodríguez-López, J. L.; Montejano-Carrizales, J. M.; Pal, U.; Sánchez-Ramírez, J. F.; Troiani, H. E.; García, D.; Miki-Yoshida, M.; José-Yacamán, M. *Phys. Rev. Lett.* **2004**, *92*, 196102.
(198) Mottet, C.; Rossi, G.; Baletto, F.; Ferrando, R. *Phys. Rev. Lett.* **2005**, *95*, 035501.
(199) Sankaranarayanan, S. K. R. S; Bhethanabotla, V. R.; Joseph, B. *Phys. Rev. B* **2005**, *71*, 195415.
(200) Kara, A.; Rahman, T. S. *Phys. Rev. Lett.* **1998**, *81*, 1453.
(201) Calvo, S. R.; Balbuena, P. B. *Surf. Sci.* **2005**, *581*, 213.

(202) Mottet, C.; Treglia, G.; Legrand, B. *Phys. Rev. B* **2002**, *66*, 045413.
(203) Foiles, S. M. *Phys. Rev. B* **1985**, *32*, 7685.
(204) Zhurkin, E. E.; Hou, M. *J. Phys. Condens. Matter* **2000**, *12*, 6735.
(205) Hou, M.; Kharlamov, V. S.; Zhurkin, E. E. *Phys. Rev. B* **2002**, *66*, 195408.
(206) Doye, J. P. K.; Calvo, F. *Phys. Rev. Lett.* **2001**, *86*, 3570.
(207) Shimizu, Y.; Ikeda, K. S.; Sawada, S. *Phys. Rev. B* **2001**, *64*, 075412.
(208) Sawada, S.; Shimizu, Y.; Ikeda, K. S. *Phys. Rev. B* **2003**, *67*, 024204.
(209) Baletto, F.; Mottet, C.; Ferrando, R. *Phys. Rev. B* **2002**, *66*, 155420.
(210) Faken, D.; Jónsson, H. *Comput. Mater. Sci.* **1994**, *2*, 279.
(211) López, G. E.; Freeman, D. L. *J. Chem. Phys.* **1993**, *98*, 1428.
(212) Rossi, G.; Ferrando, R.; Rapallo, A.; Fortunelli, A.; Curley, B. C.; Lloyd, L. D.; Johnston, R. L. *J. Chem. Phys.* **2005**, *122*, 194309.
(213) Cleveland, C. L; Landman, U. *J. Chem. Phys.* **1991**, *94*, 7376.
(214) Tyson, W. R.; Miller, W. A. *Surf. Sci.* **1977**, *62*, 267.
(215) Miedama, A. R. *Z. Metallkd.* **1978**, *69*, 287.
(216) *The Crystal Chemistry and Physics of Metals and Alloys*; Pearson, W. B., Ed.; Wiley: New York, 1972.
(217) Janssens, E.; Neukermans, S.; Wang, X.; Veldeman, N.; Silverans, R. E.; Lievens, P. *Eur. Phys. J. D* **2005**, *34*, 23.
(218) Henglein, A.; Tausch-Tremel, R. *J. Colloid Interface Sci.* **1981**, *80*, 84.
(219) Jiang, Z.-Y.; Lee, K.-H.; Li, S.-T.; Chu, S.-Y. *Phys. Rev. B* **2006**, *73*, 235423.
(220) Lequien, F.; Creuze, J.; Berthier, F.; Legrand, B. *J. Chem. Phys.* **2006**, *125*, 094707.
(221) Moreno, V.; Creuze, J.; Berthier, F.; Mottet, C.; Tréglia, G.; Legrand, B. *Surf. Sci.* **2006**, *600*, 5011.
(222) Mori, H.; Komatsu, M.; Takeda, K.; Fujita, H. *Philos. Mag. Lett.* **1991**, *63*, 173.
(223) Yasuda, H.; Mori, H.; Komatsu, M.; Takeda, K.; Fujita, H. *J. Electron Microsc.* **1992**, *41*, 267.
(224) Yasuda, H.; Mori, H. *Z. Phys. D* **1994**, *31*, 131.
(225) Yasuda, H.; Mori, H. *Z. Phys. D* **1996**, *37*, 181.
(226) Pal, U.; Ramirez, J. F. S.; Liu, H. B.; Medina, A.; Ascencio, J. A. *Appl. Phys. A* **2004**, *79*, 79.
(227) Bouwen, W.; Vanhoutte, F.; Despa, F.; Bouckaert, S.; Neukermans, S.; Theil Kuhn, L.; Weidele, H.; Lievens, P.; Silverans, R. E. *Chem. Phys. Lett.* **1999**, *314*, 227.
(228) Janssens, E.; Tanaka, H.; Neukermans, S.; Silverans, R. E.; Lievens, P. *New J. Phys.* **2003**, *5*, 46.
(229) Sra, A. K.; Schaak, R. E. *J. Am. Chem. Soc.* **2004**, *126*, 6667.
(230) Schaak, R. E.; Sra, A. K.; Leonard, B. M.; Cable, R. E.; Bauer, J. C.; Han, Y.-F.; Means, J.; Teizer, W.; Vasquez, Y.; Funck, E. S. *J. Am. Chem. Soc.* **2005**, *127*, 3506.
(231) Massalki, T. B.; Okamoto, H.; Subramanian, P. R. *Binary Alloy Phase Diagrams*, 2nd ed.; ASM International: Metals Park, OH, 1990.
(232) Ji, C.-X.; Searson, P. C. *J. Phys. Chem. B* **2003**, *107*, 4494.
(233) Erlebacher, J.; Aziz, M. J.; Karma, A.; Dimitrov, N.; Sieradzki, K. *Nature* **2001**, *410*, 450.
(234) Mattei, G.; De Marchi, G.; Maurizio, C.; Mazzoldi, P.; Sada, C.; Bello, V.; Battaglin, G. *Phys. Rev. Lett.* **2003**, *90*, 085502.
(235) Foiles, S. M.; Baskes, M. I.; Daw, M. S. *Phys. Rev. B* **1986**, *33*, 7983.
(236) Wilson, N. T.; Johnston, R. L. *J. Mater. Chem.* **2002**, *12*, 2913.
(237) Rodríguez-López, J. L.; Montejano-Carrizales, J. M.; José-Yacamán, M. *Appl. Surf. Sci.* **2003**, *219*, 56.
(238) López, M. J.; Marcos, P. A.; Alonso, J. A. *J. Chem. Phys.* **1996**, *104*, 1056.
(239) Ackland, G. J.; Vitek, V. *Phys. Rev. B* **1990**, *41*, 10324.
(240) Garzón, I. L.; Michaelian, K.; Beltrán, M. R.; Posada-Amarillas, A.; Ordejón, P.; Artacho, E.; Sánchez-Portal, D.; Soler, J. M. *Phys. Rev. Lett.* **1998**, *81*, 1600.
(241) Tarbuck, G. M.; Curley, B. C.; Lloyd, L. D.; Johnston, R. L. Manuscript in preparation.
(242) Hsu, P. J.; Lai, S. K. *J. Chem. Phys.* **2006**, *124*, 044711.
(243) Morriss, R. H.; Collins, L. F. *J. Chem. Phys.* **1964**, *41*, 3357.
(244) Papavassiliou, G. C. *J. Phys. F* **1976**, *6*, L103.
(245) Teo, B. K.; Keating, K.; Kao, Y. H. *J. Am. Chem. Soc.* **1987**, *109*, 3494.
(246) Sinzig, J.; Radtke, U.; Quinten, M.; Kreibig, U. *Z. Phys. D* **1993**, *26*, 242.
(247) Mulvaney, P. *Langmuir* **1996**, *12*, 788.
(248) Han, S.-W.; Kim, Y.; Kim, K. *J. Colloid Interface Sci.* **1998**, *208*, 272.
(249) Link, S.; Wang, Z. L.; El-Sayed, M. A. *J. Phys. Chem. B* **1999**, *103*, 3529.
(250) Srnová-Sloufová, I.; Lednický, F.; Gemperle, A.; Gemperlová, J. *Langmuir* **2000**, *16*, 9928.
(251) Gaudry, M.; Lermé, J.; Cottancin, E.; Pellarin, M.; Vialle, J.-L.; Broyer, M.; Prével, B.; Treilleux, M.; Mélinon, P. *Phys. Rev. B* **2001**, *64*, 085407.
(252) Chen, Y.-H.; Yeh, C.-S. *Chem. Commun.* **2001**, 371.
(253) Lee, I.; Han, S.-W.; Kim, K. *Chem. Commun.* **2001**, 1782.
(254) Mallik, K.; Mandal, M.; Pradhan, N.; Pal, T. *Nano Lett.* **2001**, *1*, 319.
(255) Portales, H.; Saviot, L.; Duval, E.; Gaudry, M.; Cottancin, E.; Lermé, J.; Pellarin, M.; Broyer, M.; Prevel, B.; Treilleux, M. *Eur. Phys. J. D* **2001**, *16*, 197.
(256) Mallin, M. P.; Murphy, C. J. *Nano Lett.* **2002**, *2*, 1235.
(257) Shibata, T.; Bunker, B. A.; Zhang, Z.-Y.; Meisel, M.; Vademan, C. F.; Gezelter, J. D. *J. Am. Chem. Soc.* **2002**, *124*, 11989.
(258) Santra, A. K.; Yang, F.; Goodman, D. W. *Surf. Sci.* **2004**, *548*, 324.
(259) Srnová-Sloufová, I.; Vlckova, B.; Bastl, Z.; Hasslett, T. L. *Langmuir* **2004**, *20*, 3407.
(260) Zhu, J.; Wang, Y.-C; Huang, L.-Q; Lu, Y.-M. *Phys. Lett. A* **2004**, *323*, 455.
(261) Li, Z. Y.; Yuan, J.; Chen, Y.; Palmer, R. E.; Wilcoxon, J. P. in *Microscopy and Microanalysis*; Anderson, I. M., Price, R., Hall, E., Clark, E., McKernan, S., Eds.; Proceedings of Microscopy and Microanalysis; Cambridge University Press: Cambridge, 2004; Vol. 10, Suppl. 2, p 346.
(262) Li, Z. Y.; Yuan, J.; Chen, Y.; Palmer, R. E.; Wilcoxon, J. P. *Appl. Phys. Lett.* **2005**, *87*, 243103.
(263) Li, Z. Y.; Yuan, J.; Chen, Y.; Palmer, R. E.; Wilcoxon, J. P. *Adv. Mater.* **2005**, *17*, 2885.
(264) Toreis, N.; Verykios, X. E.; Khalid, S. M.; Bunker, G. B. *Surf. Sci.* **1988**, *197*, 415.
(265) Kondarides, D. I.; Verykios, X. E. *J. Catal.* **1996**, *158*, 363.
(266) Sanedrin, R. G.; Georganopoulou, D. G.; Park, S.; Mirkin, C. A. *Adv. Mater.* **2005**, *17*, 1027.
(267) Gaudry, M.; Lermé, J.; Cottancin, E.; Pellarin, M.; Prével, B.; Treilleux, M.; Mélinon, P.; Rousset, J. L.; Broyer, M. *Eur. Phys. J. D* **2001**, *16*, 201.
(268) Zhu, J. *Physica E* **2005**, *27* 296.
(269) Hubenthal, F.; Ziegler, T.; Hendrich, C.; Alschinger, M.; Träger, F. *Eur. Phys. J. D* **2005**, *34*, 165.
(270) Benten, W.; Nilius, N.; Ernst, N.; Freund, H.-J. *Phys. Rev. B* **2005**, *72*, 045403.
(271) De Cointet, C.; Mostafavi, M.; Khatouri, J.; Belloni, J. *J. Phys. Chem. B* **1997**, *101*, 3512.
(272) Kiely, C. J.; Fink, J.; Zheng, J. G.; Brust, M.; Bethell, D.; Schiffrin, D. J. *Adv. Mater.* **2000**, *12*, 640.
(273) *CRC Handbook of Chemistry and Physics*, 64th ed.; CRC Press: Boca Raton, FL, 1984; p E-76.
(274) Curley, B. C.; Johnston, R. L.; Rossi, G.; Ferrando, R. *Eur. Phys. J. D* **2007**, *43*, 53.
(275) Zhao, G. F.; Zeng, Z. *J. Chem. Phys.* **2006**, *125*, 014303.
(276) Mitrić, R.; Burgel, C.; Burda, J.; Bonaćić-Koutecký, V.; Fantucci, P. *Eur. Phys. J. D* **2003**, *24*, 41.
(277) Rousset, J. L.; Bertolini, J. C.; Miegge, P. *Phys. Rev. B* **1996**, *53*, 4947.
(278) Pourovskii, L. V.; Ruban, A. V.; Abrikosov, I. A.; Vekilov, Y. Kh.; Johansson, B. *Phys. Rev. B* **2001**, *64*, 035421.
(279) Connor, J. A. In *Transition Metal Clusters*; Johnson, B. F. G., Ed.; Wiley: New York, 1980.
(280) Femoni, C.; Iapalucci, M. C.; Longoni, G.; Svensson, P. H.; Wolowska, J. *Angew. Chem., Int. Ed.* **2000**, *39*, 1635.
(281) Son, S. U.; Jang, Y.; Park, J.; Na, H. B.; Park, H. M.; Yun, H. J.; Lee, J.; Hyeon, T. *J. Am. Chem. Soc.* **2004**, *126*, 5026.
(282) Manago, T.; Otani, Y.; Miyajima, H.; Akiba, E. *J. Appl. Phys.* **1996**, *79*, 5126.
(283) Nunomura, N.; Hori, H.; Teranishi, T.; Miyake, M.; Yamada, S. *Phys. Lett. A* **1998**, *249* 524.
(284) Sao-Joao, S.; Giorgio, S.; Penisson, J. M.; Chapon, C.; Bourgeois, S.; Henry, C. *J. Phys. Chem. B* **2005**, *109*, 342.
(285) Raja, R.; Golovko, V. B.; Thomas, J. M.; Berenguer-Murcia, A.; Zhou, W.-Z.; Xie, S.-H.; Johnson, B. F. G. *Chem. Commun.* **2005**, 2026.
(286) Teranishi, T.; Miyake, M. *Chem. Mater.* **1999**, *11*, 3414.
(287) Zhu, L.; DePristo, A. E. *J. Chem. Phys.* **1995**, *102*, 5342.
(288) Oppong, G.; Curley, B. C.; Johnston, R. L. Unpublished work.
(289) Guevara, J.; Llois, A. M.; Aguilera-Granja, F.; Montejano-Carrizales, J. M. *Physica B* **2004**, *354*, 300.
(290) Wang, Q.; Sun, Q.; Yu, J. Z.; Hashi, Y.; Kawazoe, Y. *Phys. Lett. A* **2000**, *267*, 394.
(291) Ross, P. N., Jr. In *Electrocatalysis*; Lipowski, J., Ross, P. N., Jr., Eds.; Wiley-VCH: New York, 1998; Chapter 2, p 43.
(292) Ceriotti, A.; Demartin, F.; Longoni, G.; Manassero, M.; Marchionna, M.; Piva, G.; Sansoni, M. *Angew. Chem., Int. Ed. Engl.* **1985**, *24*, 697.

(293) Wang, G.-F.; Van Hove, M. A.; Ross, P. N.; Baskes, M. I. *J. Chem. Phys.* **2005**, *122*, 024706.
(294) Treglia, G.; Ducastelle, F. *J. Phys. F* **1987**, *17*, 1935.
(295) Gauthier, Y.; Joly, Y.; Baudoing, R.; Rundgren, J. *Phys. Rev. B* **1985**, *31*, 6216.
(296) De Boer, F. R.; Boom, R.; Mattens, W. C. M.; Miedama, A. R.; Niessen A. K. *Cohesion in Metals: Transition Metal Alloys*; Elsevier: Amsterdam, 1988.
(297) Watson, D. J.; Attard, G. A. *Surf. Sci.* **2002**, *515*, 87.
(298) Fiermans, L.; De Gryse, R.; De Doncker, G.; Jacobs, P. A.; Martens, J. A. *J. Catal.* **2000**, *193*, 108.
(299) Toshima, N.; Harada, M.; Yonezawa, T.; Kushihashi, T.; Kushihashi, K.; Asakura, K. *J. Phys. Chem.* **1991**, *95*, 7448.
(300) Toshima, N.; Yonezawa, T.; Kushiashi, K. *J. Chem. Soc., Faraday Trans.* **1993**, *89*, 2537.
(301) Wang, Y.; Toshima, N. *J. Phys. Chem. B* **1997**, *101*, 5301.
(302) Toshima, N.; Shiraishi, Y.; Shiotsuki, A.; Ikenaga, D.; Wang, Y. *Eur. Phys. J. D* **2001**, *16*, 209.
(303) Tong, Y. Y.; Yonezawa, T.; Toshima, N.; Van der Klink, J. J. *J. Phys. Chem.* **1996**, *100*, 730.
(304) Bemis, J. M.; Dahl, L. F. *J. Am. Chem. Soc.* **1997**, *119*, 4545.
(305) Massen, C.; Mortimer-Jones, T. V.; Johnston, R. L. *J. Chem. Soc., Dalton Trans.* **2002**, 4375.
(306) Lloyd, L. D.; Johnston, R. L.; Salhi, S.; Wilson, N. T. *J. Mater. Chem.* **2004**, *14*, 1691.
(307) Cheng, D.-J.; Huang, S.-P.; Wang, W.-C. *Chem. Phys.* **2006**, *330*, 423.
(308) Mallát, T.; Szabó, S.; Petró, J. *Appl. Surf. Sci.* **1990**, *40*, 309.
(309) Vrijen, J.; Radelaar, S. *Phys. Rev. B* **1978**, *17*, 409.
(310) Montejano-Carrizales, J. M.; Iniguez, M. P.; Alonso, J. A. *Phys. Rev. B* **1994**, *49*, 16649.
(311) Kittel, C. *Introduction to Solid State Physics*, 6th ed.; John Wiley: New York, 1986.
(312) Hultgren, R.; Desai, P. D.; Hawkins, D. T.; Gleiser, M.; Kelley, K. K.; American Society for Metals: Metals Park, OH, 1973.
(313) Alstrup, I.; Tavares, M. T. *J. Catal.* **1993**, *139*, 513.
(314) Yang, L.-Q.; DePristo, A. E. *J. Catal.* **1994**, *148*, 575.
(315) Ricardo-Chávez, J. L.; Pastor, G. M. *Comput. Mater. Sci.* **2006**, *35*, 311.
(316) Molenbroek, A. M.; Norskov, J. K.; Clausen, B. S. *J. Phys. Chem. B* **2001**, *105*, 5450.
(317) Van Ingen, R. P.; Fastenau, R. H. J.; Mittenmeijer, E. J. *J. Appl. Phys.* **1994**, *76*, 1871.
(318) Pabi, S. K.; Joardar, J.; Manna, I.; Murty, B. S. *Nanostruct. Mater.* **1997**, *9*, 149.
(319) Cattaruzza, E.; Battaglin, G.; Polloni, R.; Cesca, T.; Gonella, F.; Mattei, G.; Maurizio, C.; Mazzoldi, P.; D'Acapito, F.; Zontone, F.; Bertoncello, R. *Nucl. Instrum. Methods Phys. Res. B* **1999**, *148*, 1007.
(320) Damle, C.; Sastry, M. J. *Mater. Chem.* **2002**, *12*, 1860.
(321) Proux, O.; Regnard, J.; Manzini, I.; Revenant, C.; Rodmacq, B.; Mimault, J. *Eur. Phys. J.: Appl. Phys.* **2000**, *9*, 115.
(322) Portales, H.; Saviot, L.; Duval, E.; Gaudry, M.; Cottancin, E.; Pellarin, M.; Lermé, J.; Broyer, M. *Phys. Rev. B* **2002**, *65*, 165422.
(323) Boerma, D. O.; Dorenbos, G.; Wheatley, G. H.; Buck, T. M. *Surf. Sci.* **1994**, *307*−*309*, 674.
(324) Rousset, J. L.; Cadete Santos Aires, F. J.; Sekhar, B. R.; Mélinon, P.; Prevel, B.; Pellarin, M. *J. Phys. Chem. B* **2000**, *104*, 5430.
(325) Tran, N. T.; Kawano, M.; Powell, D. R.; Hayashi, R. K.; Campana, C. F.; Dahl, L. F. *J. Am. Chem. Soc.* **1999**, *121*, 5945.
(326) Garten, R. L.; Sinfelt, J. H. *J. Catal.* **1980**, *62*, 127.
(327) Sachtler, J. W. A.; Somorjai, G. A. *J. Catal.* **1983**, *81*, 77.
(328) *Metals Reference Book*, 5th ed.; Smithells, C., Brandes, E., Eds.; Butterworths: London, 1976.
(329) Van Langeveld, A. D.; Hendrickx, H. A. C. M.; Nieuwenhuys, B. E. *Thin Solid Films* **1983**, *109*, 179.
(330) Nosova, L. V.; Zaikovskii, V. I.; Kalinkin, A. V.; Talzi, E. P.; Paukshtis, E. A.; Ryndin, Y. A. *Kinet. Catal.* **1995**, *36*, 328.
(331) Fernández-Garcia, M.; Anderson, J. A.; Haller, G. L. *J. Phys. Chem.* **1996**, *100*, 16247.
(332) Zhu, L.; Liang, K. S.; Zhang, B.; Bradley, J. S.; DePristo, A. E. *J. Catal.* **1997**, *167*, 412.
(333) Gai, P. L.; Smith, B. C. *Ultramicroscopy* **1990**, *34*, 17.
(334) Gimenez, F.; Chapon, C.; Giorgio, S.; Henry, C. R. *Electron Microsc.* **1994**, *2A*, 351.
(335) Giorgio, S.; Chapon, C.; Henry, C. R. *Langmuir* **1997**, *13*, 2279.
(336) Gimenez, F.; Chapon, C.; Henry, C. R. *New J. Chem.* **1998**, *22*, 1289.
(337) Giorgio, S.; Graoui, H.; Chapon, C.; Henry, C. R. In *Metal Clusters in Chemistry*; Braunstein, P., Oro, L. A., Raithby, P. R., Eds.; Wiley-VCH: Weinheim, 1999; Vol. 2, p 1194.
(338) Kress, J. D.; DePristo, A. E. *J. Chem. Phys.* **1987**, *87*, 4700.
(339) Rubinovich, L.; Haftel, M. I.; Bernstein, N.; Polak, M. *Phys. Rev. B* **2006**, *74*, 035405.
(340) Toshima, N.; Wang, Y. *Langmuir* **1994**, *10*, 4574.
(341) Odenbrand, C. U. I.; Blanco, J.; Avila, P.; Knapp. C. *Appl. Catal. B* **1999**, *23*, 37.
(342) Zhou, S.-H.; Varughese, B.; Eichhorn, B.; Jackson, G.; McIlwrath, K. *Angew. Chem., Int. Ed.* **2005**, *44*, 4539.
(343) Khan, N. A.; Uhl, A.; Shaikhutdinov, S.; Freund, H.-J. *Surf. Sci.* **2006**, *600*, 1849.
(344) Wang, L. G.; Zunger, A. *Phys. Rev. B* **2003**, *67*, 092103.
(345) Patel, K.; Kapoor, S.; Purshottam Dave, D.; Mukherjee, T. *J. Chem. Sci.* **2005**, *117*, 311.
(346) Schmid, G.; Lehnert, A.; Malm, J.-O.; Bovin, J.-O. *Angew. Chem., Int. Ed. Engl.* **1991**, *30*, 874.
(347) Lee, A. F.; Baddeley, C. J.; Hardacre, C.; Ormerod, R. M.; Lambert, R. M.; Schmid, G.; West, H. *J. Phys. Chem.* **1995**, *99*, 6096.
(348) Takatani, H.; Kago, H.; Kobayashi, Y.; Hori, F.; Oshima, R. *Trans. Mater. Res. Soc. Jpn.* **2003**, *28*, 871.
(349) Nutt, M. O.; Hughes, J. B.; Wong, M. S. *Environ. Sci. Technol.* **2005**, *39*, 1346.
(350) Liu, H. B.; Pal, U.; Medina, A.; Maldonado, C.; Ascencio, J. A. *Phys. Rev. B* **2005**, *71*, 075403.
(351) Shiraishi, Y.; Ikenaga, D.; Toshima, N. *Australian J. Chem.* **2003**, *56*, 1025.
(352) Edwards, J. K.; Solsona, B. E.; Landon, P.; Carley, A. F.; Herzing, A.; Kiely, C. J.; Hutchings, G. J. *J. Catal.* **2005**, *236*, 69.
(353) Enache, D. I.; Edwards, J. K.; Landon, P.; Solsona-Espriu, B.; Carley, A. F.; Herzing, A. A.; Watanabe, M.; Kiely, C. J.; Knight, D. W.; Hutchings, G. J. *Science* **2006**, *311*, 362.
(354) Hilaire, A.; Légaré, P.; Holl, Y.; Maire, G. *Surf. Sci.* **1981**, *103*, 125.
(355) Nakagawa, T.; Nitani, H.; Tanabe, S.; Okitsu, K.; Seino, S.; Mizukoshi, Y.; Yamamoto, T. A. *Ultrason. Sonochem.* **2005**, *12*, 249.
(356) Toshima, N. *Pure Appl. Chem.* **2000**, *72*, 317.
(357) Wu, M.-L.; Chen, D.-H.; Huang, T.-C. *Langmuir* **2001**, *17*, 3877.
(358) Ascencio, J. A.; Liu, H. B.; Pal, U.; Medina, A.; Wang, Z. L. *Microsc. Res. Technol.* **2006**, *69*, 522.
(359) Paulus, P. M.; Goossens, A.; Thiel, R. C.; van der Kraan, A. M.; Schmid, G.; de Jongh, L. J. *Phys. Rev. B* **2001**, *64*, 205418.
(360) Lou, Y.-B.; Maye, M. M.; Han, L.; Luo, J.; Zhong, C.-J. *Chem. Commun.* **2001**, 473.
(361) Hostetler, M. J.; Zhong, C. J.; Yen, B. K. H.; Anderegg, J.; Gross, S. M.; Evans, N. D.; Porter, M.; Murray, R. W. *J. Am. Chem. Soc.* **1998**, *120*, 9396.
(362) Esparza, R.; Ascencio, J. A.; Rosas, G.; Ramirez, J. F. S.; Pal, U.; Perez, R. *J. Nanosci. Nanotechnol.* **2005**, *5*, 641.
(363) Liz-Marzán, L. M.; Philipse, A. P. *J. Phys. Chem.* **1995**, *99*, 15120.
(364) Henglein, A. *J. Phys. Chem. B* **2000**, *104*, 2201.
(365) Hodak, J. H.; Henglein, A.; Hartland, G. V. *J. Chem. Phys.* **2001**, *114*, 2760.
(366) Cao, L.-Y.; Tong, L.-M.; Diao, P.; Zhu, T.; Liu, Z.-F. *Chem. Mater.* **2004**, *16*, 3239.
(367) Ge, Q.; Song, C.; Wang, L. *Comput. Mater. Sci.* **2006**, *35*, 247.
(368) Maye, M. M.; Lou, Y.-B.; Zhong, C. J. *Langmuir* **2000**, *16*, 7520.
(369) Sudfeld, D.; Wojczykowski, K.; Hachmann, W.; Heitmann, S.; Rott, K.; Hempel, T.; Kämmerer, S.; Jutzi, P.; Hütten, A.; Reiss, G. *IEEE Trans. Magn.* **2002**, *38*, 2601.
(370) Zubris, M.; King, R. B.; Garmestani, H.; Tannenbaum, R. J. *Mater. Chem.* **2005**, *15*, 1277.
(371) Parks, E. K.; Kerns, K. P.; Riley, S. *J. Chem. Phys.* **2000**, *262*, 151.
(372) Parks, E. K.; Riley, S. J. *Z. Phys. D* **1995**, *33*, 59.
(373) Parks, E. K.; Kerns, K. P.; Riley, S. J. *J. Chem. Phys.* **2000**, *112*, 2479.
(374) Sahoo, S.; Rollmann, G.; Entel, P. *Phase Transit.* **2006**, *79*, 693.
(375) Eastham, D. A.; Qiang, Y.; Maddock, T. H.; Kraft, J.; Schille, J. P.; Thompson, G. S.; Haberland, H. *J. Phys.: Condens. Matter* **1997**, *9*, L497.
(376) Wang, J.-L.; Wang, G.-H.; Chen, X.-S.; Lu, W.; Zhao, J.-J. *Phys. Rev. B* **2002**, *66*, 014419.
(377) Wang, B.-L.; Chen, X.-S.; Chen, G.-B.; Wang, G.-H.; Zhao, J.-J. *Surf. Rev. Lett.* **2004**, *11*, 15.
(378) Longoni, G.; Manassero, M.; Sansoni, M. *J. Am. Chem. Soc.* **1980**, *102*, 3242.
(379) Pacchioni, G.; Krüger, S.; Rösch, N. In *Chemistry*; Braunstein, P., Oro, L. A., Raithby, P. R., Eds.; Wiley-VCH: Weinheim, 1999; Vol. 3, p 1392.
(380) Janssens, E.; van Hoof, T.; Veldeman, N.; Neukermans, S.; Hou, M.; Lievens, P. *Int. J. Mass Spectrom.* **2006**, *252*, 38.
(381) Zhurkin, E. E.; Van Hoof, T.; Hou, M. *Phys. Rev. B* **2007**, *75*, 224102.
(382) Carlsson, A. F.; Bäumer, M.; Risse, T.; Freund, H.-J. *J. Chem. Phys.* **2003**, *119*, 10885.
(383) Muñoz-Navia, M.; Villaseñor-González, P.; Dorantes-Dávila, J.; Pastor, G. M. *Comput. Mater. Sci.* **2006**, *35*, 302.
(384) Zitoun, D.; Respaud, M.; Fromen, M. C.; Casanove, M. J.; Lecante, P.; Amiens, C.; Chaudret, B. *Phys. Rev. Lett.* **2002**, *89*, 037203.

(385) Fromen, M. C.; Lecante, P.; Casanove, M. J.; Bayle, Guillemaud, P.; Zitoun, D.; Amiens, C.; Chaudret, B.; Respaud, M.; Benfield, R. E. *Phys. Rev. B* **2004**, *69*, 235416.
(386) Ellison, K. A.; Underhill, P. R.; Smeltzer, W. W. *Surf. Sci.* **1987**, *182*, 69.
(387) Sondón, T.; Guevara, J. *Physica B* **2004**, *354*, 303.
(388) Sondón, T.; Guevara, J.; Saul, A. *Phys. Rev. B* **2007**, *75*, 104426.
(389) Nagaki, D. A.; Badding, J. V.; Stacy, A. M.; Dahl, L. F. *J. Am. Chem. Soc.* **1986**, *108*, 3825.
(390) Kappes, M. M. *Chem. Rev.* **1988**, *88*, 369.
(391) Bromley, S. T.; Sankar, G.; Catlow, C. R. A.; Maschmeyer, T.; Johnson, B. F. G.; Thomas, J. M. *Chem. Phys. Lett.* **2001**, *340*, 524.
(392) Sun, S. H.; Murray, C. B.; Weller, D.; Folks, L.; Moser, A. *Science* **2000**, *287*, 1989.
(393) Ebert, H.; Bornemann, S.; Minár, J.; Dederichs, P. H.; Zeller, R.; Cabria, I. *Comput. Mater. Sci.* **2006**, *35*, 279.
(394) Park, J.-I.; Cheon, J. *J. Am. Chem. Soc.* **2001**, *123*, 5743.
(395) Park, J.-I.; Kim, M. G.; Jun, Y.-W.; Lee, J. S.; Lee, W.-R.; Cheon, J. *J. Am. Chem. Soc.* **2004**, *126*, 9072.
(396) Tan, C. Y.; Chen, J. S.; Liu, B. H.; Chow, G. M. *J. Cryst. Growth* **2006**, *293*, 175.
(397) Howard, L. E. M.; Nguyen, H. L.; Giblin, S. R.; Tanner, B. K.; Terry, I.; Hughes, A. K.; Evans, J. S. O. *J. Am. Chem. Soc.* **2005**, *127*, 10140.
(398) Stappert, S.; Rellinghaus, B.; Acet, M.; Wassermann, E. F. *J. Cryst. Growth* **2003**, *252*, 440.
(399) Tzitzios, V.; Niarchos, D.; Gjoka, M.; Boukos, N.; Petridis, D. *J. Am. Chem. Soc.* **2005**, *127*, 13756.
(400) Fortunelli, A.; Velasco, A. M. *J. Mol. Struct. (Theochem*) **1999**, *487*, 251.
(401) Yang, B.; Asta, M.; Mryasov, O. N.; Klemmer, T. J.; Chantrell, R. W. *Acta Mater.* **2006**, *54*, 4201.
(402) Kaszkur, Z. A.; Mierzwa, B. *Philos. Mag. A* **1998**, *77*, 781.
(403) Juszczyk, W.; Karpinski, Z.; Lomot, D.; Pielaszek, J.; Paal, Z.; Stakheev, A. Y. *J. Catal.* **1993**, *142*, 617.
(404) Saha, D. K.; Koga, K.; Takeo, H. *Eur. Phys. J. D* **1999**, *9*, 539.
(405) Paulus, P. M.; Bönnemann, H.; van der Kraan, A. M.; Luis, F.; Sinzig, J.; de Jongh, L. J. *Eur. Phys. J. D* **1999**, *9*, 501.
(406) Zhou, W. L.; Carpenter, E. E.; Lin, J.; Kumbhar, A.; Sims, J.; O'Connor, C. J. *Eur. Phys. J. D* **2001**, *16*, 289.
(407) Nashner, M. S.; Frenkel, A. I.; Somerville, D. M.; Hills, C. W.; Shapley, J. R.; Nuzzo, R. G. *J. Am. Chem. Soc.* **1998**, *120*, 8093.
(408) Liang, K. S.; Chien, F. Z.; Hughes, G. J.; Meitzner, G. D.; Sinfelt, J. H. *J. Phys. Chem.* **1991**, *95*, 9974.
(409) Wang, L.-L.; Khare, S. V.; Chirita, V.; Johnson, D. D.; Rockett, A. A.; Frenkel, A. I.; Mack, N. H.; Nuzzo, R. G. *J. Am. Chem. Soc.* **2006**, *128*, 141.
(410) Baranova, E. A.; Bock, C.; Ilin, D.; Wang, D.; MacDougall, B. *Surf. Sci.* **2006**, *600*, 3502.
(411) Fumagalli, A.; Martinengo, S.; Ciani, G.; Mascciocchi, N.; Sironi, A. *Inorg. Chem.* **1992**, *31*, 336.
(412) Wang, Z.; Ansermet, J.-P.; Slichter, C. P.; Sinfelt, J. H. *J. Chem. Soc., Faraday Trans. 1* **1988**, *84*, 3785.
(413) Li, X.; Kiran, B.; Li, J.; Zhai, H.-J.; Wang, L.-S. *Angew. Chem., Int. Ed.* **2002**, *41*, 4786.
(414) Pyykkö, P.; Runeberg, N. *Angew. Chem., Int. Ed.* **2002**, *41*, 2174.
(415) Autschbach, J.; Hess, B. A.; Johansson, M. P.; Neugebauer, J.; Patzschke, M.; Pyykkö, P.; Reiher, M.; Sundholm, D. *Phys. Chem. Chem. Phys.* **2004**, *6*, 11.
(416) Zhai, H.-J.; Li, J.; Wang, L.-S. *J. Chem. Phys.* **2004**, *121*, 8369.
(417) Parks, E. K.; Rexer, E. F.; J.; Riley, S. J. *J. Chem. Phys.* **2002**, *117*, 95.
(418) *The Crystal Structures of Intermetallic Alloy Phases*; U.S. Naval Research Laboratory, http://cst-www.nrl.navy.mil/lattice/alloys/.
(419) Massicot, F.; Schneider, R.; Fort, Y.; Illy-Cherrey, S.; Tillement, O. *Tetrahedron* **2000**, *56*, 4765.
(420) Parks, E. K.; Zhu, L.; Ho, J.; Riley, S. J. *J. Chem. Phys.* **1995**, *102*, 7377.
(421) Rexer, E. F.; Jellinek, J.; Krissinel, E. B.; Parks, E. K.; Riley, S. J. *J. Chem. Phys.* **2002**, *117*, 82.
(422) Bailey, M. S.; Wilson, N. T.; Roberts, C.; Johnston, R. L. *Eur. Phys. J. D* **2003**, *25*, 41.
(423) Wilson, N. T.; Bailey, M. S.; Johnston, R. L. *Inorg. Chim. Acta* **2006**, *359*, 3649.
(424) Rey, C.; García-Rodeja, J.; Gallego, L. J. *Phys. Rev. B* **1996**, *54*, 2942.
(425) Calleja, M.; Rey, C.; Alemany, M. M. G.; Gallego, L. J.; Ordejón, P.; Sánchez-Portal, D.; Artacho, E.; Soler, J. M. *Phys. Rev. B* **1999**, *60*, 2020.
(426) Polak, M.; Rubinovich, L. *Surf. Sci.* **2005**, *584*, 41.
(427) Moskovkin, P.; Hou, M. *Eur. Phys. J. D* **2003**, *27*, 231.
(428) Hambrock, J.; Schröter, M. K.; Birkner, A.; Wöll, C.; Fischer, R. A. *Chem. Mater.* **2003**, *15*, 4217.
(429) Cokoja, M.; Parala, H.; Schröter, M. K.; Birkner, A.; van den Berg, M. W. E.; Klementiev, K. V.; Grünert, W.; Fischer, R. A. *J. Mater. Chem.* **2006**, *16*, 2420.
(430) Cokoja, M.; Parala, H.; Schröter, M. K.; Birkner, A.; van den Berg, M. W. E.; Grünert, W.; Fischer, R. A. *Chem. Mater.* **2006**, *18*, 1634.
(431) Boyen, H.-G.; Ethirajan, A.; Kästle, G.; Weigl, F.; Ziemann, P.; Schmid, G.; Garnier, M. G.; Büttner, M.; Oelhafen, P. *Phys. Rev. Lett.* **2005**, *94*, 016804.
(432) Henglein, A. *Ber. Bunsen-ges. Phys. Chem.* **1980**, *84*, 253.
(433) Henglein, A.; Mulvaney, P.; Holzwarth, A.; Sosebee, T.; Fojtik, A. *Ber. Bunsen-ges. Phys. Chem.* **1992**, *96*, 754.
(434) Heiz, U.; Vayloyan, A.; Schumacher, E.; Yeretzian, C.; Stener, M.; Gisdakis, P.; Rösch, N. *J. Chem. Phys.* **1996**, *105*, 5574.
(435) Heiz, U.; Vayloyan, A.; Schumacher, E. *J. Phys. Chem.* **1996**, *100*, 15033.
(436) Kumar, V.; Kawazoe, Y. *Phys. Rev. B* **2001**, *64*, 115405.
(437) Durán Pachón, L.; Thathagar, M. B.; Hartl, F.; Rothenberg, G. *Phys. Chem. Chem. Phys.* **2006**, *8*, 151.
(438) Renouprez, A. J.; Faudon, J. F.; Massardier, J.; Rousset, J. L.; Delichere, P.; Bergeret, G. *J. Catal.* **1997**, *170*, 181.
(439) Paulus, U. A.; Wokaun, A.; Scherer, G. G.; Schmidt, T. J.; Stamenković, V.; Radmilovic, V.; Marković, N. M.; Ross, P. N. *J. Phys. Chem. B* **2002**, *106*, 4181.
(440) Coq, B.; Figueras, F. *J. Mol. Catal. A* **2001**, *173*, 117.
(441) Chang, J. R.; Chang, S. L.; Lin, T. B. *J. Catal.* **1997**, *169*, 338.
(442) Stanislaus, A.; Cooper, B. H. *Catal. Rev. Sci. Eng.* **1994**, *36*, 75.
(443) Yasuda, H.; Matsubayashi, N.; Sato, T.; Yoshimura, Y. *Catal. Lett.* **1998**, *54*, 23.
(444) Fujikawa, T.; Idei, K.; Ebihara, T.; Mizuguchi, H.; Usui, K. *Appl. Catal. A* **2000**, *192*, 253.
(445) Bazin, D.; Guillaume, D.; Pichon, Ch.; Uzio, D.; Lopez, S. *Oil Gas. Sci. Technol. Rev. IFP* **2005**, *60*, 801.
(446) Philips, J.; Auroux, A.; Bergeret, G.; Massardier, J.; Renouprez, A. *J. Phys. Chem.* **1993**, *97*, 3565.
(447) Choi, K. I.; Vannice, M. A. *J. Catal.* **1991**, *131*, 36.
(448) Greeley, J.; Mavrikakis, M. *Nat. Mater.* **2004**, *3*, 810.
(449) Bönnemann, H.; Endruschat, U.; Tesche, B.; Rufînska, A.; Lehmann, C. W.; Wagner, F. E.; Filoti, G.; Pârvulescu, V.; Pârvulescu, V. I. *Eur. J. Inorg. Chem.* **2000**, 819.
(450) Landon, P.; Collier, P. J.; Papworth, A. J.; Kiely, C. J.; Hutchings, G. J. *Chem. Commun.* **2002**, 2058.
(451) Turkenburg, D. H.; Antipov, A. A.; Thathagar, M. B.; Rothenberg, G.; Sukhorukov, G. B.; Eiser, E. *Phys. Chem. Chem. Phys.* **2005**, *7*, 2237.
(452) Han, Y.-F.; Wang, J.-H.; Kumar, D.; Yan, Z.; Goodman, D. W. *J. Catal.* **2005**, *232*, 467.
(453) Chen, M.; Kumar, D.; Yi, C.-W.; Goodman, D. W. *Science* **2005**, *310*, 291.
(454) Guo, T.; Nikolaev, P.; Thess, A.; Colbert, D. T.; Smalley, R. E. *Chem. Phys. Lett.* **1995**, *243*, 49.
(455) Deng, W.-Q.; Xu, X.; Goddard, W. A. *Nano Lett.* **2004**, *4*, 2331.
(456) Xiong, L.; Manthiram, A. *J. Mater. Chem.* **2004**, *14*, 1454.
(457) Raja, R.; Sankar, G.; Hermans, S.; Shepard, D. S.; Bromley, S. T.; Thomas, J. M.; Maschmeyer, T.; Johnson, B. F. G. *Chem. Commun.* **1999**, 1571.
(458) Midgley, P. A.; Weyland, M.; Thomas, J. M.; Johnson, B. F. G. *Chem. Commun.* **2001**, 907.
(459) Wasmus, S.; Küver, A. *J. Electroanal. Chem.* **1999**, *461*, 14.
(460) Liu, Z. L.; Ling, X. Y.; Su, X. D.; Lee, J. Y. *J. Phys. Chem. B* **2004**, *108*, 8234.
(461) Takasu, Y.; Itaya, H.; Kawaguchi, T.; Sugimoto, W.; Murakami, Y. *Stud. Surf. Sci. Catal.* **2003**, *145*, 279.
(462) Moore, J. T.; Chu, D.; Jiang, R. Z.; Deluga, G. A.; Lukehart, C. M. *Chem. Mater.* **2003**, *15*, 1119.
(463) Aberdam, D.; Durand, R.; Faure, R.; Gloaguen, F.; Hazemann, J. L.; Herrero, E.; Kabbabi, A.; Ulrich, O. *J. Electroanal. Chem.* **1995**, *398*, 43.
(464) Treglia, G.; Legrand, B. *Phys. Rev. B* **1987**, *35*, 4338.
(465) Wiltshire, R. J. K.; King, C. R.; Rose, A.; Wells, P. P.; Hogarth, M. P.; Thompsett, D.; Russell, A. E. *Electrochim. Acta* **2005**, *50*, 5208.
(466) Gasteiger, H. A.; Markovic, N.; Ross, P. N.; Cairns, E. J. *J. Phys. Chem.* **1994**, *98*, 617.
(467) Crabb, E. M.; Raviumar, M. K.; Thompsett, D.; Hurford, M.; Rose, A.; Russell, A. E. *Phys. Chem. Chem. Phys.* **2004**, *6*, 1792.
(468) Tong, Y. Y.; Kim, H. S.; Babu, P. K.; Waszczuk, P.; Wieckowski, A.; Oldfield, E. *J. Am. Chem. Soc.* **2002**, *124*, 468.
(469) Lyman, C. E.; Lakis, R. E.; Stenger, H. G., Jr. *Ultramicroscopy* **1995**, *58*, 25.
(470) Grgur, B. N.; Markovic, N. M.; Ross, P. N. *J. Electrochem. Soc.* **1999**, *146*, 1613.
(471) Wang, G.; Van Hove, M. A.; Ross, P. N.; Baskes, M. I. *J. Phys. Chem. B* **2005**, *109*, 11683.
(472) Delogu, F. *Nanotechnology* **2007**, *18*, 065708.

(473) Delogu, F. *Nanotechnology* **2007**, *18*, 235706.
(474) Allen, G. L.; Jesser, W. A. *J. Cryst. Growth* **1984**, *70*, 546.
(475) Shirinyan, A. S.; Gusak, A. M.; Wautelet, M. *Acta Mater.* **2005**, *53*, 5025.
(476) Yen, T. W.; Lai, S. K.; Jakse, N.; Bretonnet, J. L. *Philos. Rev. B* **2007**, *75*, 165420.
(477) Michaelian, K.; Garzón, I. L. *Eur. Phys. J. D* **2005**, *34*, 183.
(478) Chen, F. Y.; Curley, B. C.; Rossi, G.; Johnston, R. L. *J. Phys. Chem. C* **2007**, *111*, 9157.
(479) Montalenti, F.; Ferrando, R. *Phys. Rev. B* **1999**, *59*, 5881.
(480) Cheng, D.-J.; Huang, S.-P.; Wang, W.-C. *Phys. Rev. B* **2006**, *74*, 064117.
(481) Mottet, C.; Treglia, G.; Legrand, B. *Surf. Sci.* **1997**, *383*, L719.
(482) Aguado, A.; López, J. M.; Alonso, J. A.; Stott, M. J. *J. Phys. Chem. B* **2001**, *105*, 2386.
(483) Aguado, A.; González, L. E.; López, J. M. *J. Phys. Chem. B* **2004**, *108*, 11722.
(484) Reinhard, D.; Hall, B. D.; Berthoud, P.; Valkealahti, S.; Monot, R. *Phys. Rev. B* **1998**, *58*, 4197.
(485) Baletto, F.; Mottet, C.; Ferrando, R. *Phys. Rev. Lett.* **2000**, *84*, 5544.
(486) Baletto, F.; Mottet, C.; Ferrando, R. *Phys. Rev. B* **2001**, *63*, 155408.
(487) Baletto, F.; Doye, J. P. K.; Ferrando, R. *Phys. Rev. Lett.* **2002**, *88*, 075503.
(488) Ikeshoji, T.; Torchet, G.; De Feraudy, M.-F.; Koga, K. *Phys. Rev. E* **2001**, *63*, 031101.
(489) Chushak, Y. G.; Bartell, L. S. *J. Phys. Chem. B* **2001**, *105*, 11605.
(490) Valkealahti, S.; Näher, U.; Manninen, M. *Phys. Rev. B* **1995**, *51*, 11039.
(491) Kubachewski, O. *Trans. Faraday Soc.* **1950**, *46*, 713.
(492) Hansen, M.; Anderko, K. *Constitution of Binary Alloys*, 2nd ed.; McGraw Hill: New York, 1958.
(493) Yasuda, H.; Mori, H.; Komatsu, M.; Takeda, K. *Appl. Phys. Lett.* **1992**, *61*, 2173.
(494) Yasuda, H.; Mori, H. *Z. Phys. D* **1997**, *40*, 144.
(495) Yasuda, H.; Mori, H.; Furuya, K. *Philos. Mag. Lett.* **2000**, *80*, 181.
(496) Yasuda, H.; Mori, H. *Z. Phys. D* **1997**, *40*, 140.
(497) Pettifor, D. G. *Solid State Commun.* **1978**, *28*, 621.
(498) Lee, J.-G.; Mori, H. *Eur. Phys. J. D* **2005**, *34*, 227.
(499) Chushak, Y. G.; Bartell, L. S. *J. Phys. Chem. B* **2003**, *107*, 3747.
(500) Liu, H. B.; Pal, U.; Perez, R. ; Ascencio, J. A. *J. Phys. Chem. B* **2006**, *110*, 5191.
(501) Guirado-López, R. A.; Desjonqueres, M. C.; Spanjaard, D. *Phys. Rev. B* **2006**, *74*, 064415.
(502) Mariscal, M. M.; Dassie, S. A.; Leiva, E. P. M. *J. Chem. Phys.* **2005**, *123*, 184505.
(503) Kim, H. Y.; Kim, H. G.; Ryu, J. H.; Lee, H. M. *Phys. Rev. B* **2007**, *75*, 212105.
(504) Rubinovich, L.; Polak, M. *Surf. Sci.* **2002**, *513*, 119.
(505) Barrow, J. A.; Sordelet, D. J.; Besser, M. F.; Jenks, C. J.; Thiel, P. A.; Rexer, E. F.; Riley, S. J. *J. Phys. Chem. A* **2002**, *106*, 9204.
(506) Nanoalloys − From Theory to Applications, *Faraday Disc.* **2003**, 138.

CR040090G